Experimental Identification Of Blade Stall In Axial and Edgewise Flight Conditions

Alexander Daniel Croke

Submitted in fulfilment of the requirements for the
Degree of Doctor of Philosophy
Aerospace Engineering

James Watt School of Engineering
College of Science and Engineering
University of Glasgow

May 2025

Abstract

The recent resurgence of the airscrew propeller, growth in both military and civilian tiltrotor technology and successful operation of a rotorcraft on Mars has led to a reinvigoration of research surrounding blade stall in axial and edgewise conditions. Modern tiltrotor blades are designed to operate in both propeller and rotor mode, thus operating in underexplored regions of the operational flight envelope, where aerodynamic and aeroelastic instabilities may occur, leading to unfavourable and potentially fatal operational conditions. Despite several experimental investigations focused on blade stall over the past century, there is a clear lack of a comprehensive aerodynamic and aeroelastic experimental data set of sufficient resolution which can provide further insight into these complex phenomena and be used to validate high-fidelity numerical models. Therefore, within this body of work, state-of-the-art experimental test rigs were commissioned to develop a novel experimental methodology, primarily based on blade strain measurements, that can be utilised to identify operational conditions at which blades are stalled, for both axial and edgewise flight regimes.

Axial blade stall was investigated using the United Kingdom National Rotor Rig situated at the University of Glasgow De Havilland wind tunnel. A blade stall operational boundary was constructed for the MENtOR tiltrotor blade set through the use of key markers within the blade strain, wind tunnel velocity and motor data. It was shown for stalled conditions that the flap bending and torsional strain measurements departed from linear behaviour when increasing blade pitch with substantial growth in their standard deviation, up to twice the pre-stall value. Stall was also apparent in the strain spectra, exhibiting a significant non-harmonic content and large distribution of signal energy. Unsteady flow generated by the stall acted as a broadband forcing term for the blade structural dynamics resulting in the identification of blade eigenmode frequencies, particularly the first flap bending mode. To support the validity of the developed stall boundary identification criteria, a multi measurement approach was implemented to identify blade stall, using independent measurement techniques including stereoscopic Digital Image Correlation and load measurements. Flap bending deflection measurements and load remeasurements were shown to correlate strongly with the identified stall conditions obtained using the stall boundary identification criteria.

Subsequently, an investigation using a single bladed rotor was performed at the University of Maryland towing tank to assess the viability of utilising measurements of the blade strain

distribution to identify regions of reverse and separated flow in edgewise conditions. Reverse flow regions were identified through phase resolved measurements of rotor thrust, torque and pitching moment around the rotor azimuth. At large advance ratios where strong reverse flow effects occurred, phase resolved measurements of blade flap bending strain exhibited a strong agreement with load identified azimuthal locations at which the blade entered and exited the reverse flow region. Averaged and unsteady strain measurements displayed an identical trend to load measurements, demonstrating the applicability of strain distribution to identify stalled and reverse flow regions.

The results of this work have demonstrated the ability to use strain measurements to identify the presence of blade stall in both axial and edgewise conditions. Highlighting the capability to quickly, reliably and cost effectively develop blade stall boundaries when compared to more conventional experimental methods. Finally, the novel criteria developed within this work can be implemented across many technical readiness levels supporting academic and commercial blade testing activities.

Contents

List of Tables

List of Figures

Acknowledgements

Firstly, I would like to express my sincere thanks to my advisor Dr Richard Green, for his continuous support throughout the duration of my PhD and for sharing with me his wealth of knowledge on topics such as large scale wind tunnel facilities, experimental methods and rotary wing testing.

I would also like to express my gratitude to my co-supervisor Professor George Barakos, for his continued support over the years and for sharing his extensive knowledge and passion of rotorcraft with me.

I would also like thank and acknowledge Dr Daniele Zagaglia for his unwavering support, his time and advice throughout my PhD, it was very much appreciated. I must also thank Dr David Pickles for his support and advice throughout this process.

Furthermore, I would like to extend my thanks to Murray McKechnie, my numerical counterpart, whom it has been a pleasure working alongside.

My appreciation also extends to Dr Nicholas Bown of Dowty Propellers for his support and advice over the years. In addition, I wish to acknowledge the financial support provided by Dowty Propellers, allowing me to pursue this research.

My thanks also extends to Professor Anya Jones, for allowing me to undertake a visiting PhD post within her laboratory at the University of Maryland. I would also like to thank Dr Oliver Wild for being a great colleague during my period abroad.

I also want to thank all my friends, for their support, laughs and good times over the past few years. It has been crucial for me in the successful completion of this piece of work.

Last but not least, I would like to thank my family: particularity my parents and my brother Adam for the love and support they have shown me throughout my life. If not for them, I would not be where I am today.

Declaration

I certify that the thesis presented here for examination for a PhD degree of the University of Glasgow is solely my own work other than where I have clearly indicated that it is the work of others (in which case the extent of any work carried out jointly by me and any other person is clearly identified in it) and that the thesis has not been edited by a third party beyond what is permitted by the University's PGR Code of Practice.

I declare that the thesis does not include work forming part of a thesis presented successfully for another degree.

I declare that this thesis has been produced in accordance with the University of Glasgow's Code of Good Practice in Research.

I acknowledge that if any issues are raised regarding good research practice based on review of the thesis, the examination may be postponed pending the outcome of any investigation of the issues.

May 2025

.....

Alexander Daniel Croke

Scientific Output

Journal Publications

- **Alexander D. Croke**, Daniele Zagaglia, Murray McKechnie, Richard B. Green, and George N. Barakos. *"Experimental Investigation Into The Onset Of Stall On Tiltrotor Blades In Propeller Mode"*. Advances In Research, Development, Simulation, Design, Manufacturing, Testing and Operation Of Rotorcraft Special Issue, CEAS Aeronautical Journal, 2025.

Conference Proceedings

- **Alexander D. Croke**, Daniele Zagaglia, Richard B. Green, and George N. Barakos. *"Experimental Aerodynamic and Aeroelastic Characterisation Of A Propeller In Stalled Conditions"*. In Vertical Flight Society 81st Annual Forum, Virginia Beach, VA, USA, May 20-22, 2025.

- David J. Pickles, Daniele Zagaglia, **Alexander D. Croke**, Richard B. Green, and George N. Barakos. *"Experimental Investigation Into The Vortex Ring State Of Multi-Rotor Configurations"*. In 50th European Rotorcraft Forum, Marseille, France, 10-12 Sep, 2024.

- **Alexander D. Croke**, Oliver D. Wild, Anya R.Jones and Richard B. Green. *"Experimental Investigation Of Rotor Blade Structural Response In Hovering and Advance Flight At Low Reynolds Number Conditions"*. In Vertical Flight Society 80th Annual Forum, Montréal, Québec, Canada, May 7-9, 2024.

- **Alexander D. Croke**, Daniele Zagaglia, Mark A. Woodgate, Richard B. Green, and George N. Barakos. *"Experimental Investigation Into The Onset Of Stall Flutter On Tiltrotor Blades"*. In 49th European Rotorcraft Forum, Buckeburg, Germany, 05-07 Sep 2023.

- Daniele Zagaglia, **Alexander D. Croke**, Richard B. Green, and George N. Barakos. *"Development Of The UK National Rotor Rig For Aeroelastic Testing Of Rotary Wings"*. In 49th European Rotorcraft Forum, Buckeburg, Germany, 05-07 Sep 2023.

Conference Without Proceedings

- Daniele Zagaglia, **Alexander D. Croke**, Richard B. Green, and George N. Barakos. *"Wind Tunnel Investigation of Propeller Blades in Stalled Conditions"*. 9th UK Vertical Lift Network, Cheshire, England, United Kingdom, 20-21 May, 2024.

- **Alexander D. Croke**, Daniele Zagaglia, Richard B. Green, and George N. Barakos. *"Experimental Investigation Into The Stall Boundary Of Tiltrotor Blades"*. 7th UK Fluids Conference, Glasgow, Scotland, United Kingdom, 17-19 Oct 2023.

- David J. Pickles, Daniele Zagaglia, **Alexander D. Croke**, and Richard B. Green. *"The Vortex Ring State of Quadcopters"*. 7th UK Fluids Conference, Glasgow, Scotland, United Kingdom, 17-19 Oct 2023.

- **Alexander D. Croke**, Daniele Zagaglia, Richard B. Green, and George N. Barakos.*" Experimental Investigation Of Tiltrotor Blades At Stall Onset"*. 8th UK Vertical Lift Network, Cheshire, England, United Kingdom, 21-23 May 2023.

- **Alexander D. Croke**, Daniele Zagaglia, Richard B. Green, and George N. Barakos. *"Experimental Investigation Of Propeller Stall Flutter"*. 7th UK Vertical Lift Network, Cheshire, England, United Kingdom, 16-18 May 2022.

- Daniele Zagaglia, **Alexander D. Croke**, Richard B. Green, and George N. Barakos. *"A Novel Rig For The Study Of Propeller Stall Flutter"*. 7th UK Vertical Lift Network, Cheshire, England, United Kingdom, 16-18 May 2022.

Visiting Post

- Separated and Transient Aerodynamics Laboratory, College Park, University of Maryland, USA. 11 Sep - 20 Oct 2023.

Nomenclature

Latin Symbols

a	Local speed of sound, (m/s)
A	Disc area, πR^2, (m^2)
A	Axial force, (N)
A_{CS}	Wind tunnel cross sectional area, (m^2)
C	Blade chord, (m)
C_{root}	Chord at blade root, (m)
C_{tip}	Chord at blade tip, (m)
C_T	Coefficient of propeller thrust, $T/\left(\rho n^2 D^4\right)$, $(-)$
C_T	Coefficient of rotor thrust, $T/(\rho V_{tip}^2 A)$, $(-)$
C_Q	Coefficient of propeller torque, $Q/\left(\rho n^2 D^5\right)$, $(-)$
C_Q	Coefficient of rotor torque, $Q/(\rho V_{tip}^2 AR)$, $(-)$
C_M	Coefficient of rotor moments, $M/(\rho V_{tip}^2 AR)$, $(-)$
D	Blade diameter, (m)
DL	Disc loading, T/A, (N/m^2)
E_i	Fibre direction modulus, (GPa)
E_t	Transverse direction modulus, (GPa)
F_c	Centrifugal force, (N)
f	Frequency, (Hz)
f_m	Frequency of blade eigenmodes, (Hz)
f_n	Natural frequency, (Hz)
f_{res}	Frequency resolution, (Hz)
FoM	Figure of merit, $C_T^{3/2}/(C_Q\sqrt{2})$, $(-)$
$\mathscr{F}(\cdot)$	Fourier transform of function $\cdot$
(F_x, F_y, F_z)	Force components in the Cartesian axes system
G_{it}	Shear modulus, (GPa)
J	Propeller advance ratio, $U_\infty/(nD)$, $(-)$
J'	Equivalent propeller advance ratio, $U'/(nD)$, $(-)$
J_∞^{IND}	Induced wind tunnel recirculation advance ratio, $U_\infty^{IND}/(nD)$, $(-)$
k	Reduced frequency, $(-)$
l	Rolling moment, (Nm)
$\vec{L_0}$	Direct loads

$\vec{L_1}$	First order loads
$\vec{L_2}$	Second order loads
m	Mass, (kg)
m	Pitching moment, (Nm)
M	Mach number, U_∞/a , $(-)$
M_{tip}	Mach number at blade tip, V_{tip}/a , $(-)$
M_f	Magnification factor, (px/mm)
(M_x, M_y, M_z)	Moment components in the Cartesian axes system
n	Propeller rotational frequency, (Hz)
n	Yawing moment, (Nm)
N	Normal force, (N)
N_b	Number of blades, $(-)$
N_{rev}	Number of revolutions, $(-)$
P_o	Static pressure, (Pa)
P	Power, (W)
P_{IN}	Power input, (W)
P_{OUT}	Power output, (W)
q	Dynamic pressure, $\frac{1}{2}\rho U_\infty^2$, (Pa)
R	Blade radius, (m)
Re	Reynolds number, $(-)$
Re_{tip}	Reynolds number at blade tip, $(2\pi nRC_{tip})\,/\nu$, $(-)$
t_{TE}	Trailing edge thickness, (m)
t/c	Thickness to chord ratio, $(-)$
T	Thrust, (N)
T_o	Static temperature, (K)
$[T_0]$	Direct order interaction matrix
$[T_1]$	First order interaction matrix
$[T_2]$	Second order interaction matrix
U_∞	Freestream velocity, (m/s)
U'	Equivalent freestream velocity, (m/s)
U_{IND}	Propeller induced velocity, (m/s)
U_∞^{IND}	Induced wind tunnel recirculation velocity, (m/s)
V_{tip}	Blade tip velocity, ΩR, (m/s)
V_o	Voltage output, (V)
W_0	Weight tare, (N)
(x, y, z)	Cartesian axes system
x	Blade radial coordinate, (m)
x/c	x-coordinate normalised to blade chord, $(-)$
y/c	y-coordinate normalised to blade chord, $(-)$
Y	Side force, (N)

Greek Symbols

α_{eff}	Effective sectional angle of attack, (°)
$\beta_{0.75R}$	Propeller blade pitch angle at 75% radius, (°)
Γ_R	Lateral hub rotation, (°)
δT	Sectional thrust, (N)
δL	Sectional lift, (N)
δR	Sectional resultant force, (N)
$\delta Q/x$	Sectional in-plane force, (N)
δD	Sectional drag, (N)
δ	Flap bending deflection, (mm)
δ_R	Rigid flap displacement, (mm)
$\delta_{measured}$	Measured flap bending deflection, (mm)
$\Delta\theta$	Torsional twist, (°)
ΔP_{CON}	Pressure difference across contraction chamber, (Pa)
ΔP_{PROBE}	Pressure difference across Pitot-static probe, (Pa)
ΔU_∞	Freestream velocity resolution, (m/s)
ΔZ	Vertical displacement of load cell measuring surface and blade quarter chord, (m)
ε	Blockage factor, A/A_{CS}, $(-)$
ε_B	Bridge uncompensated strain, $(-)$
$\overline{\varepsilon_B}$	Bridge compensated strain, $(-)$
ζ	Damping ratio, $(-)$
η	Propeller efficiency, $\frac{1}{2\pi}\frac{C_T}{C_Q}J'$, $(-)$
θ	Rotor collective pitch angle, (°)
θ_t	Blade twist angle, (°)
θ_s	Stereoscopic angle, (°)
κ	Measured pressure ratio, $(-)$
κ_{ideal}	Theoretical pressure ratio, $(-)$
μ	Rotor advance ratio, $U_\infty/(\Omega R)$, $(-)$
ν	Kinematic viscosity, (m^2/s)
ν	Poisson's ratio, $(-)$
ρ	Density, (kg/m^3)
$\overline{\rho}$	Reference density, (kg/m^3)
σ	Rotor solidity, N_bc / (πR), $(-)$
σ_F	Axial strength in fibre direction, (MPa)
σ_T	Axial strength in transverse direction, (MPa)
$\sigma_{\overline{\varepsilon_B}}$	Standard deviation of bridge compensated strain, $(-)$
τ_{it}	Shear strength, (MPa)
τ_4	Weighted thrust, $T/\left(\rho A U_\infty^2\right)$, $(-)$
ϕ	Sectional inflow angle, (°)

ψ	Azimuthal position, ($^\circ$)
ω	Angular velocity, $2\pi f$, (rad/s)
Ω	Rotational frequency, (RPM)
$\overline{\Omega}$	Reference rotational frequency, (RPM)

Acronyms

AoA	Angle of Attack
ACDC	Alternating Current to Direct Current
ADC	Analogue to Digital Converter
ARA	Aircraft Research Association
BTEVS	Blunt Trailing Edge Vortex Street
CFD	Computational Fluid Dynamics
C.G	Centre of Gravity
CNC	Computer Numerical Control
CSD	Computational Structural Dynamics
DIC	Digital Image Correlation
EASA	European Union Aviation Safety Agency
EMA	Experimental Modal Analysis
EPSRC	Engineering and Physical Sciences Research Council
eVTOL	Electric Vertical Take-off and Landing
FAA	Federal Aviation Administration
FB	Flap Bending
FoM	Figure of Merit
FoV	Field of View
FRF	Frequency Response Functions
HMB3	Helicopter Multi-Block Code
LDA	Laser Doppler Anemometry
MAV	Micro Aerial Vehicles
MENtOR	Methods and Experiments for NOvel Rotorcraft
NACA	National Advisory Committee for Aeronautics
NASA	National Aeronautics and Space Administration
PCB	Printed Circuit Board
PID	Proportional-Integral-Derivative
PIV	Particle Image Velocimetry
PDSV	Primary Dynamic Stall Vortex
PSI	Pounds Per Square Inch
RAE	Royal Aircraft Establishment

RF	Radio Frequency
RFDSV	Reverse Flow Dynamic Stall Vortex
RFEV	Reverse Flow Entrance Vortex
RMS	Root Mean Square
RoI	Region of Interest
RPM	Revolutions Per Minute
RSB	Rotating Shaft Balance
SDSV	Secondary Dynamic Stall Vortex
SR	Single Rotation Series
STAL	Separated and Transient Aerodynamics Laboratory
TEV	Trailing Edge Vortex
T	Torsion
TV	Tip Vortex
UK	United Kingdom
UKNRR	United Kingdom National Rotor Rig
UKVLN	United Kingdom Vertical Lift Network
UMD	University of Maryland
UofG	University of Glasgow
UoM	University of Manchester
USAF	United States Air Force
USN	United States Navy
USNA	United States Naval Academy
UTRC	United Technologies Research Centre
WT	Wind Tunnel
WW2	World War Two
1-P	One Per Revolution
2-P	Two Per Revolution
2D	Two Dimensional
3D	Three Dimensional
2C	Two Component

Chapter 1

Introduction

1.1 Background and Motivation

Rotorcraft are complex machines that can provide the capability for operation in environments in which conventional fixed-wing aircraft cannot operate, as shown in Figure 1.1. With this in mind, the recent selection of the Bell V-280 tiltrotor aircraft by the United States Army as the replacement for the Sikorsky UH-60 Black Hawk and sudden growth in the development of electric Vertical Take-off and Landing (eVTOL) tiltrotor vehicles has led to a significant research interest within the rotary wing community to qualify the operating envelope of blades that are required to operate in both axial and edgewise flight regimes [1]. As a result, typical blades will be required to operate as both propellers and rotors in underexplored regions of the flight envelope, potentially leading to the probing of aerodynamic and aeroelastic boundaries [2].

Many eVTOL manufacturers have demonstrated a significant interest of the conventional airscrew propeller. The majority of the proposed eVTOL configurations will utilise an airscrew propeller, driven by electrical propulsion systems, thus promoting improved propulsive efficiencies when compared to that of a conventional gas turbine engine. However, in order to benefit from the improved propulsive efficiencies offered by a propeller, eVTOL manufacturers will be required to design and manufacture blades that use thinner aerofoil sections and incorporate non-conventional blade shapes including large twist distributions and sweep, thus altering the aerodynamic and aeroelastic operational envelope of the blades [3].

The design of such propellers is complex and requires the use of high-fidelity numerical codes to optimise blade aerodynamic performance and structural response. As extensively highlighted by the recent high-fidelity numerical work of Higgins et al. [3–9], the introduction of thinner and unconventional blade shapes, plus the use of lightweight carbon fibre composites, has been shown to lead to aeroelastic instabilities such as propeller stall flutter during operation at axial flight conditions where stall is present. Despite a significant numerical effort, state-of-the-art experimental datasets that are required to validate numerical models are extremely limited. Many of these investigations were undertaken prior to 1960 across the United Kingdom

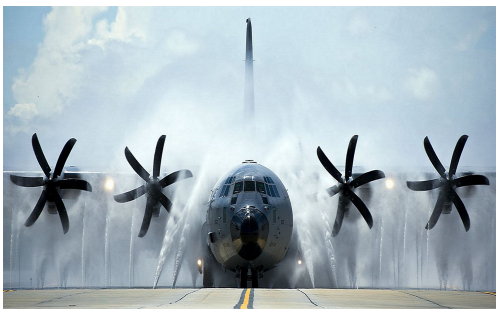

(a) Propellers: Lockheed Martin C-130 Hercules

(b) Helicopters: Sikorsky UH-60 Black Hawk

(c) Tilt-rotor: Bell V-280

(d) eVTOL: Joby Aviation

(e) MAV: Teledyne FLIR Black Hornet

(f) Martian Helicopter: NASA Ingenuity

Figure 1.1: Examples of conventional and non-conventional aircraft configurations that make use of rotary wings.

and United States, primarily utilising wooden blades. Large amounts of the experimental data collected during this period has been demonstrated to be disjointed and not suitable for modern validation. Thus imposing the need for a modern dataset that utilises a blade set with well defined blade structural and geometric properties. Furthermore, any proposed civilian aircraft configurations that wishes to be certified, will require reliable experimental data sets demonstrating a comprehensive testing regime and performance capability to satisfy regulatory bodies such as the European Union Aviation Safety Agency (EASA) and Federal Aviation Administration (FAA).

In addition to propeller stall in axial conditions, the recent growth of Micro Aerial Vehicles (MAVs) and notable success of the National Aeronautics and Space Administration (NASA) Martian helicopter, Ingenuity, has also led to a significant research interest in low Reynolds number and high advance ratio rotorcraft research at edgewise flight conditions. Similarly to that of propeller stall, there is a need for experimental datasets, particularly for separated flow

conditions and reverse flow regions, to enhance blade designs and performance capability.

To measure and develop the required datasets needed, bespoke experimental test rigs, that often utilise scaled down blade designs, are required to be tested within suitably sized experimental facilities such as wind tunnels and towing tanks. Conventionally, the identification of the presence of stall is highlighted through load measurements. However, this can be extremely complex and expensive to implement for rotary-wing applications and therefore can potentially limit the ability to obtain critical information from a testing campaign, such as blade stall boundaries. Therefore, to address the clear lack of comprehensive aerodynamic and aeroelastic measurements of a propeller at stalled conditions, this body of work will investigate the development of a novel stall identification methodology through means of experimental testing using a large scale state-of-the-art wind tunnel facility and national rotor rig.

1.2 Aim and Objectives

The motivation of this work stems from a significant lack of experimental aerodynamic and aeroelastic data sets concerning propeller and rotor blades operating in stalled conditions, for both axial and edgewise flight regimes. Therefore, to address this knowledge gap, the aim of this work is to:

Develop a novel experimental methodology, primarily based on blade strain measurements, that can be utilised to identify operational conditions at which blades are stalled, for both axial and edgewise flight regimes.

The key objectives of this work are as follows:

- Commission the United Kingdom National Rotor Rig (UKNRR) as a fixed pitch 1.25m diameter propeller capable of undertaking a series of wind tunnel test campaigns investigating propeller stall in axial flow conditions within the 9ft x 7ft DeHavilland wind tunnel situated at the University of Glasgow (UofG).
- Develop a stall boundary, primarily based on strain measurements using a clear set of criteria, for a blade design that is well defined both in geometric and structural properties, using state-of-the-art experimental instrumentation.
- Apply a multi measurement approach to identify blade stall through independent measurement techniques and support the validity of the stall boundary identification criteria developed.
- Assess the viability of utilising measurements of blade strain distribution to identify regions of reverse and separated flow in edgewise conditions.

1.3 Thesis Structure

Following the introduction provided in Chapter 1, the remainder of this thesis is structured as follows:

Chapter 2 provides an description of stall and its aerodynamic characteristics for both 2D and rotary wing flow conditions. Additionally, a comprehensive review of literature has been displayed highlighting the current state-of-the-art of experimental investigations where stall is present for both axial and edgewise conditions.

Chapter 3 provides a description of the experimental apparatus used to obtain the measurement results presented within this thesis. A description of the United Kingdom National Rotor Rig used to test a 1.25m diameter composite tiltrotor blade set in propeller mode at the University of Glasgow DeHavilland wind tunnel is provided. Details of rotor rig development, wind tunnel integration and instrumentation is outlined. Furthermore, a description is included of the experimental setup used to conduct experimental testing of a single bladed 0.625m diameter rotor operating at both hovering and high advance ratio conditions at the free surface water towing tank at the University of Maryland.

Chapter 4 presents a methodology of blade stall identification which has been developed to assess blade stall boundaries. A criteria has been defined based upon measurements of unsteady strain gauge and motor torque data. Additionally, blade eigenmode frequencies were experimentally identified and compared to that of numerical estimates.

Chapter 5 implements a multi-measurement approach, utilising performance measurements and measurements of blade tip deflections, to determine the identification of the blade stall boundary through independent measurement techniques and support the validity of the stall boundary identification criteria developed in Chapter 4.

Chapter 6 extends the methodology of blade stall identification to edgewise conditions to assess the viability of utilising measurements of blade strain distribution to identify regions of reverse and separated flow. Averaged and phase-averaged load and strain measurements are compared.

Chapter 7 outlines the main conclusions from this body of work and outlines recommendations of future work including required considerations for the development of a rotary wing test rig capable of providing state-of-the-art aerodynamic and aeroelastic measurements.

Chapter 2

Literature Review

Within this chapter a literature survey focused on experimental research regarding the presence of separated flows for rotary-wing applications in axial and edgewise flight conditions such as propellers and rotors is presented. An overview of stall and its aerodynamic characteristic for both two dimensional and three dimensional flows is presented within Section 2.1. Section 2.2 provides a review of propeller stall, detailing the development and application of experimental methods of large scale propeller testing, in-flight test campaigns and high speed propeller research. Similarly, Section 2.3 presents a review of experimental testing of rotors at low Reynolds conditions and with significant reverse flow regions. Section 2.4 provides a summary of available literature and research gaps are identified.

2.1 Stall

2.1.1 Two Dimensional Stall

2.1.1.1 Static Stall

Two dimensional aerodynamic coefficients can be analysed as a function of angle of attack (α) to provide insight into sectional lift (C_l), sectional drag (C_d) and sectional moment (C_m) properties for a given aerofoil. Considering the sectional lift coefficient, for low to moderate angles of attack, typically up to $\alpha \approx 12^\circ - 15^\circ$, the C_l grows linearly at a corresponding gradient of $\partial C_l / \partial \alpha$, where the flow around the aerofoil remains attached. The maximum lift coefficient ($C_{l_{max}}$) occurs at an angle of attack termed the static stall angle (α_s), where values of α immediately larger display a sudden loss of lift, as a consequence of large flow separation. Aerofoils operating in this condition are deemed to be *"stalled"*. Aerofoil stall can also be identified through a noticeable increase in drag, due to the presence of separated flow. Further to this, a strong nose down pitching moment is also observed, this is attributed to the shift in the centre of pressure towards the aerofoil trailing edge as a result of increased flow unsteadiness and separation. For α values immediately prior to α_s, there is a variation in the sectional gradients ($\partial C_l / \partial \alpha$, $\partial C_d / \partial \alpha$,

$\partial C_m/\partial\alpha$), indicating early stages of stall, this is defined as the *"stall onset"* region, where stall has not completely manifested but negative changes in sectional aerodynamics begin to appear.

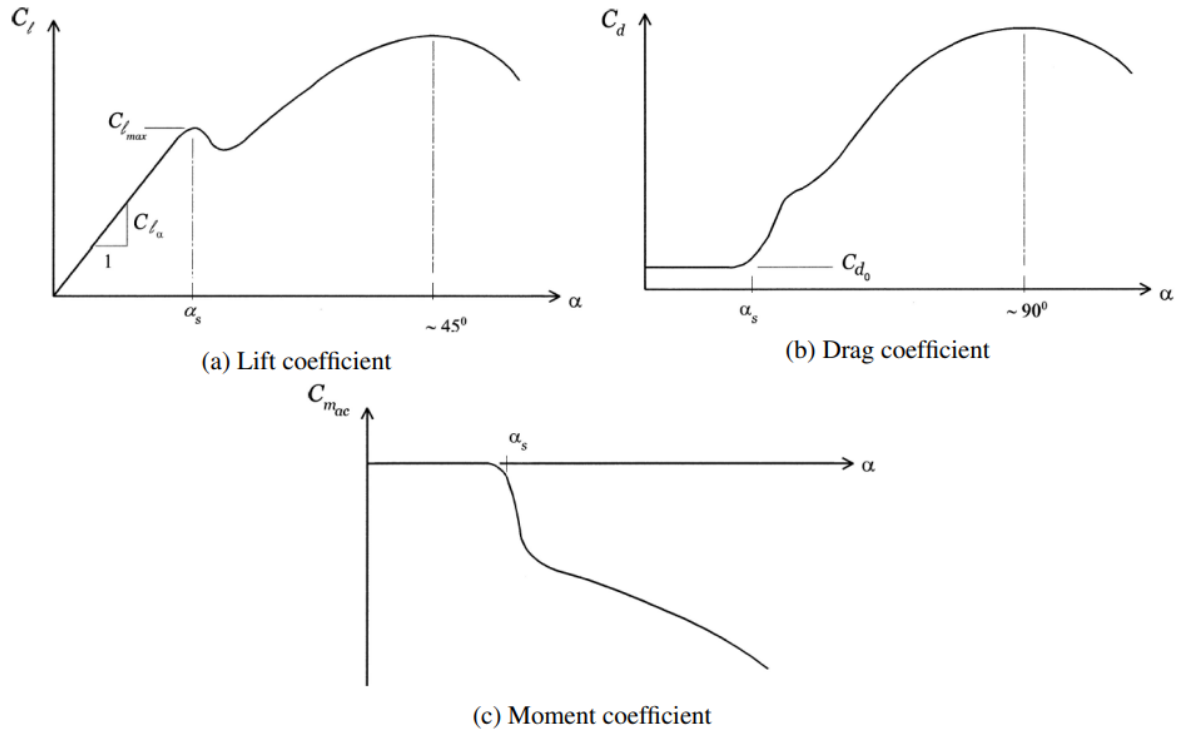

Figure 2.1: Two dimensional aerodynamic coefficients (C_l, C_d, C_m) as function of angle of attack (α). Figure taken directly from Higgins [4].

Flow separation occurs when the flow on the upper surface of the aerofoil detaches due to an increased boundary layer thickness as a consequence of a large adverse pressure gradient. Typically separation manifests as either an abrupt leading edge separation or a more gradual trailing edge separation. Trailing edge separation is the most common form of separation at low Mach conditions as the onset of stall is gradual. At even larger α values where the flow is deeply stalled, a secondary lift peak can occur. This lift peak is attributed to highly unsteady pressure fluctuations which can result in additional lift generation, peaking at approximately $\alpha \approx 45°$. Drag and moment measurements continue to demonstrate an increase as a consequence of deeply stalled flow.

2.1.1.2 Dynamic Stall

Dynamic stall is an unsteady aerodynamic phenomenon that presents itself in oscillating aerofoils. During dynamic stall, the angle of attack exceeds the static stall angle, resulting in complex aerodynamic conditions where excess lift is generated due to the formation of a vortical structure at the aerofoil leading edge, for an increasing angle of attack. To better appreciate the dynamic stall phenomenon, the development of the dynamic stall process is best described in five stages, as shown in Figure 2.2.

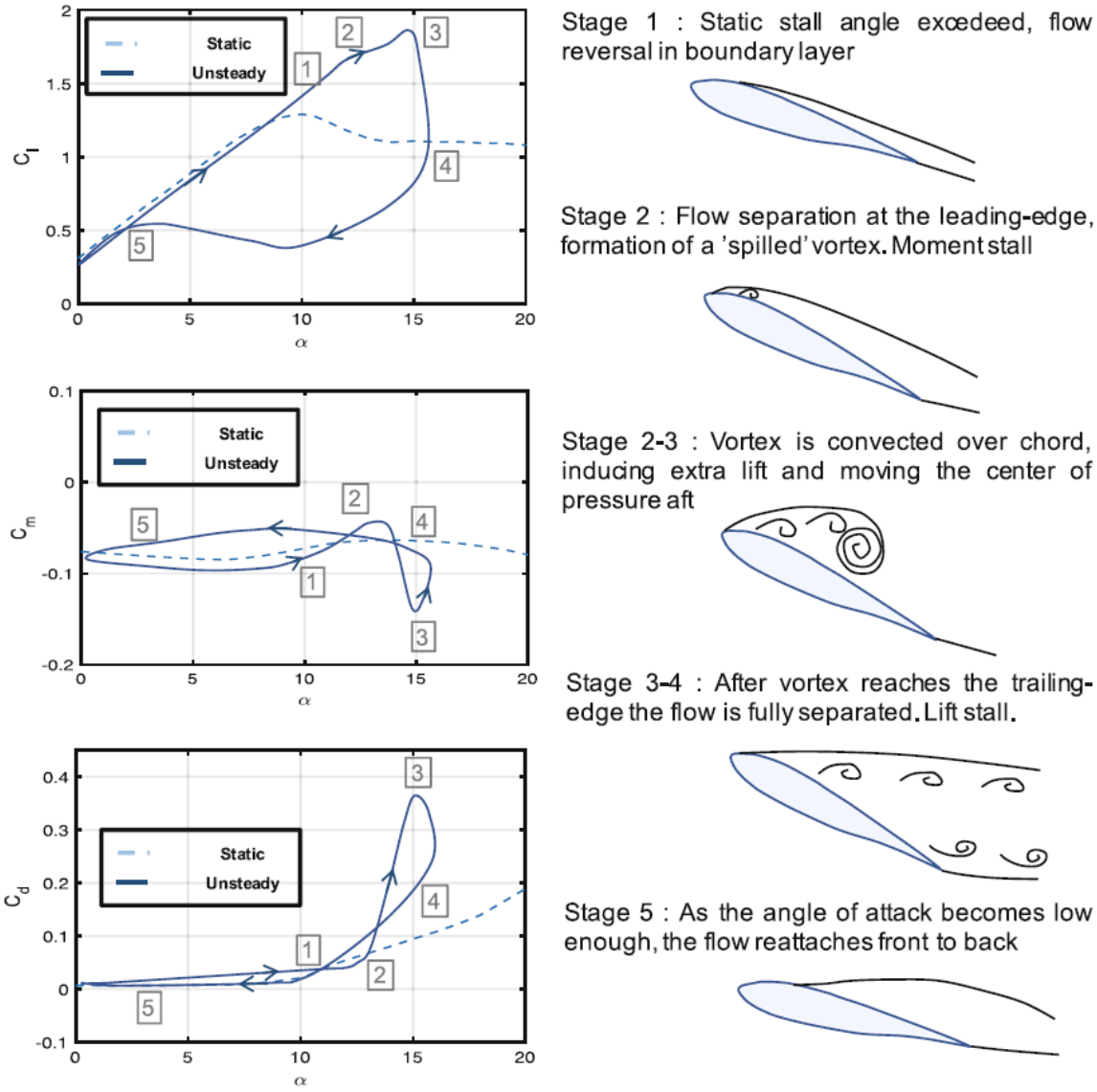

Figure 2.2: Stages of dynamic stall development. Figure taken directly from Santos Pereira [10].

During stage one, as the aerofoil angle of attack grows, the static stall angle is exceeded and flow reversal occurs within the aerofoil boundary layer. However, due to decreased adverse pressure gradients the location of the separation point moves further towards the leading edge, delaying the onset of flow separation to a larger angle of attack. As a consequence, a Leading Edge Vortex (LEV) develops and grows in strength. At stage two, leading edge flow separation occurs and the LEV separates, propagating along the chord towards the trailing edge resulting in a movement of the centre of pressure towards the trailing edge, thus resulting in a strong nose down moment, this is known as *"moment stall"*. However, due to the propagation of the LEV across the aerofoil upper surface, from the leading to the trailing edge, the aerofoil continues to generate lift. At stage three, where the LEV has reached the trailing edge, a sudden drop in lift and drag is observed, this occurs at a larger angle of attack when compared to moment

stall. Stage four occurs at the point when the upper surface of the aerofoil is fully separated as the LEV enters the aerofoil wake, passing the trailing edge. Leading to stage five, where flow reattachment occurs at an angle of attack significantly less than that of the static stall angle.

2.1.1.3 Stall Flutter

Aeroelastic instabilities such as stall flutter occur when aerodynamic damping is negative, resulting in work being transferred to the structure as a result of the aerodynamic forces and moments acting on the aerofoil. Consequently, this leads to structural excitation and growth in oscillatory amplitudes which can lead to structural failure.

Aerodynamic damping of an oscillating two dimensional aerofoil is obtained through analysis of the moment hysteresis loop, displayed in Figure 2.7, where the instantaneous angle of attack (α) is expressed in the form of $\alpha = \alpha_m + A^\circ \sin(2k\tau)$. Where α_m is the mean angle of attack, A is the amplitude of the oscillation, k is the reduced frequency and τ is the non-dimensional time.

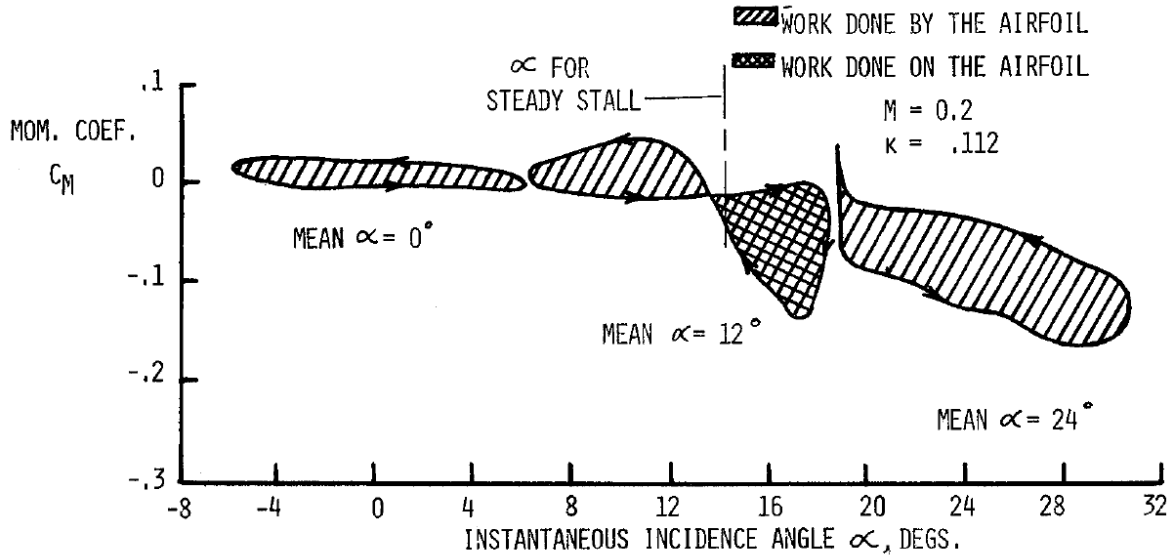

Figure 2.3: Effect of mean incidence angle on moment hysteresis loop for a NACA 0012 aerofoil oscillating $\alpha = \alpha_m + 6^\circ \sin(2k\tau)$ for $\alpha_m = 0^\circ, 12^\circ, 24^\circ$ at $k = 0.112$. Figure taken directly from McCormick [11].

Considering the $\alpha_m = 0^\circ$ case, the flow around the aerofoil remains attached as the angle of attack remains below the static stall angle. Additionally, the counter clockwise hysteresis loop demonstrates that work must be done by the aerofoil. However, when considering the $\alpha_m = 12^\circ$ case, there is both the presence of positive and negative aerodynamic work. This is a result of the aerofoil oscillating between attached and stalled flow states, thus the net area difference of the two moment loops displays negative damping highlighting the possible presence of a periodic

oscillation. The $\alpha_m = 24^\circ$ case represents an aerofoil operating continuously in completely stalled flow states where work must be done by the aerofoil.

Stall flutter is a periodic oscillation that is a consequence of partial or fully separated flow that usually takes the form of a purely torsional oscillation, therefore altering the effective angle of attack. Due to the presence of flow separation, the aerodynamic conditions are typically highly non-linear. Therefore, to counteract negative aerodynamic damping, there must be a favourable change in aerodynamic conditions or the introduction of positive structural damping.

2.1.2 Rotary Wing Stall

Unlike two dimensional flows, propellers and rotors encounter highly unsteady three dimensional flows, where sectional aerodynamic performance varies along the blade span resulting in variations of effective angle of attack. These variations in effective angle attack therefore require blades to be twisted to optimise inflow and induced velocity effects required to provide an efficient generation of aerodynamic forces such as lift, drag and thrust.

2.1.2.1 Propeller Stall

Consider a propeller in advancing flight conditions typical of cruise. The propeller rotates at a rotational frequency (Ω) and is subjected to an incoming freestream velocity (U_∞) parallel to the axis of rotation, as shown in Figure 2.4a. Propeller loading is on average axis-symmetric when operating in attached flow regimes. A significant parameter used to describe the operational condition of the propeller is the advance ratio (J), which relates the incoming forward velocity to the propeller rotational frequency (n) and propeller disc diameter (D).

$$J = \frac{U_\infty}{nD}$$

A schematic of a propeller blade section at spanwise location x is presented in Figure 2.4b. The relative velocity seen by the aerofoil section is composed of the rotational speed (Ωx), normal to the rotational axis and the induced velocity (U_{IND}) plus propeller advance velocity (U_∞), both of which are parallel to the rotational axis. The effective angle of attack (α_{eff}) at which the section operates at is dependent on both the blade pitch (β) and inflow angle (ϕ), i.e $\alpha_{eff} = \beta - \phi$.

At operational conditions where the blade α_{eff} becomes excessive (e.g very large blade pitch angles and low inflow angles, hence low advance velocities and advance ratios), propeller stall manifests, thus leading to regions of separated flow on the propeller blade. This leads to highly unsteady loading and complex aerodynamic flow conditions, ultimately degrading aerodynamic performance. In particular, there is an appreciable reduction in thrust generated by the propeller and increased in power demand, when this occurs the propeller is deemed to be stalled. Similar to a two dimensional aerofoil, stall onset can also be appreciated through a change in thrust and

torque gradients immediately prior to the stall. A breakdown of the force components can be appreciated when considering an individual propeller blade section, shown in Figure 2.4b.

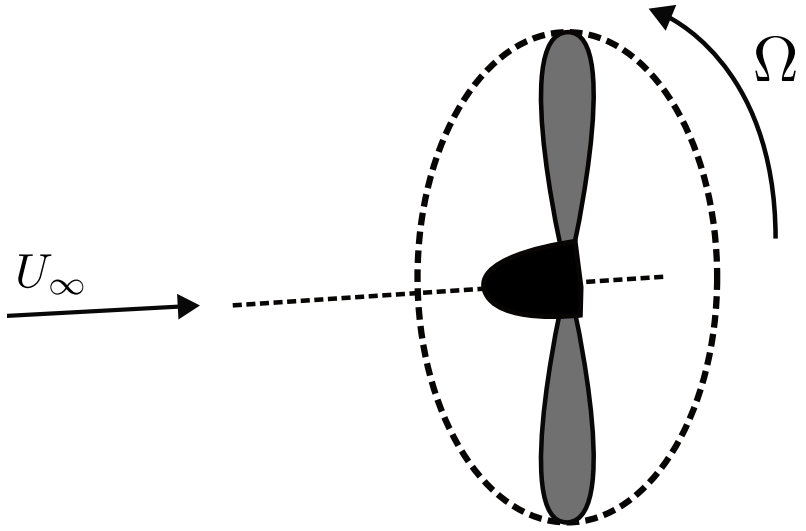

(a) Relationship between incoming advance velocity (U_∞) and propeller rotational frequency (Ω)

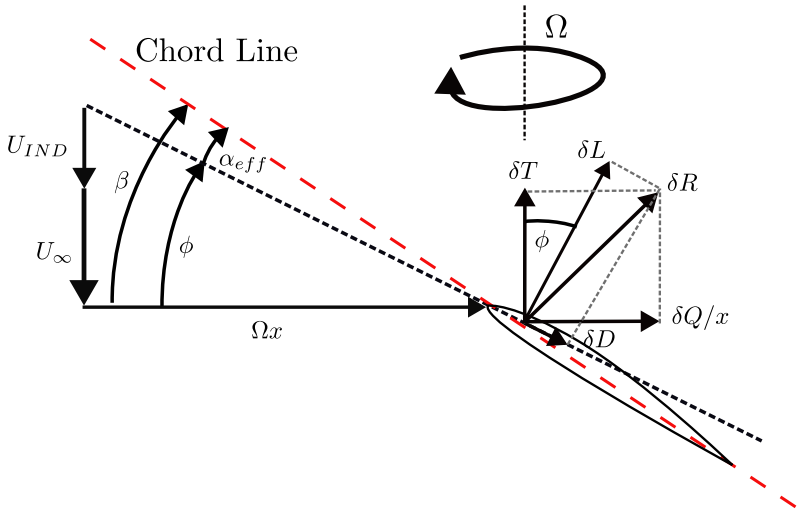

(b) Propeller blade element at the spanwise section x. β denotes the local blade pitch, ϕ the inflow angle and α_{eff} the effective angle of attack, where $\alpha_{eff} = \beta - \phi$

Figure 2.4: Schematic of propeller operating conditions during advancing flight.

Under certain conditions, the non-linear aerodynamic conditions the propeller is subjected to when a partial or complete flow separation occurs, can result in an adverse structural response. Many propeller blades incorporate geometries that are slender and make use of thin aerofoil sections to improve aerodynamic performance. However, this typically imposes very low stiffness properties thus leading to a weakened blade structure. Therefore, at stalled conditions when the aerodynamics become non-linear, shedding frequencies of the flow can potentially excite blade structural modes as a consequence of negative aerodynamic damping, leading to blade structural instabilities such as stall flutter. For conditions in which propeller stall flutter occurs,

a significant negative effect on blade aerodynamic performance is expected and can result in blade structural failure.

2.1.2.2 Rotors at High Advance Ratio

The aerodynamic environment of a rotor in the edgewise flight regime is very different to that of a rotor operating in hover due to the incoming forward velocity, U_∞. For a rotor revolving at a rotational frequency (Ω) with a blade radius (R), the dimensionless term for rotor forward speed named the advance ratio (μ) is defined as the in-plane forward velocity normalised with the rotor tip speed ($V_{tip} = \Omega R$).

$$\mu = \frac{U_\infty}{\Omega R}$$

Conventional helicopters typically have the capability to operate at a maximum advance ratio of 0.35 - 0.4, although it is not common for operation at greater forward speeds due to limitations of the rotor disc on both the advancing ($0^\circ < \psi < 180^\circ$) and retreating side ($180^\circ < \psi < 360^\circ$). At high advance ratio conditions, considering the blade tip on the advancing side of the rotor disc, large velocities leading to an increased tip Mach number are observed, thus resulting in aerodynamic conditions where compressibility effects can not be neglected, due to the occurrence of shock waves. For large advance ratio conditions, a phenomena on the retreating blade termed dynamic stall occurs. Dynamic stall manifests due to an increased velocity on the advancing blade and decreased velocity on the retreating blade results in an imbalance of the rotor. This imposes the requirement of trimming the rotor, which is performed through the implementation of a cyclic pitch. As a result, the retreating blade undergoes a time variant angle of attack which can exceed the static stall angle of attack for the blade aerofoils, resulting in flow separation and blade stall.

Furthermore, on the retreating side of the rotor disc a phenomenon called reverse flow can manifest, leading to unfavourable aerodynamic conditions that can result in unsteady blade and hub loading. For conditions at which reverse flow occurs, a portion of the rotor disc develops at the blade root, for which the forward velocity component becomes negative, resulting in a reversal of the flow direction, as shown in Figure 2.5a. The reverse flow region manifests itself as circle of diameter μR, with a centre point of radial distance $\mu R/2$ at an azimuthal position of $\psi = 270^\circ$. For example, considering a rotor at $\mu = 0.5$ as shown in Figure 2.5a, the reverse flow area will cover the inner 50% of the retreating rotor blade. Rotors operating at a large advance ratio will therefore have a larger portion of the total rotor disc area undergoing reverse flow. At forward flight conditions up to $\mu = 0.5$, the presence of the reverse flow region is not significant as the negative aerodynamic effects are deemed negligible due to the reduced area of the reverse flow region mainly effecting the blade root area, where the local dynamic pressure is low. Furthermore, the presence of a blade root cutout also contributes to the reduced negative effects as the portion of the blade does not positively contribute to the generation of meaningful

aerodynamic forces.

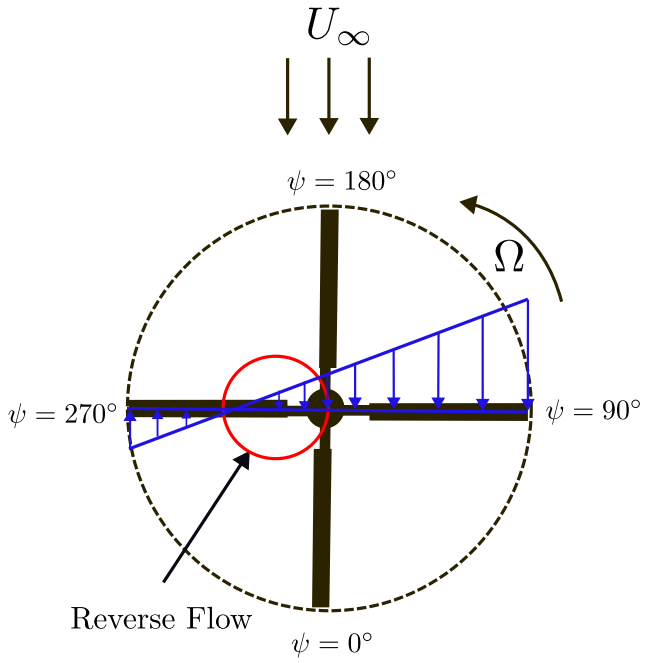

(a) Rotor azimuth during advancing flight

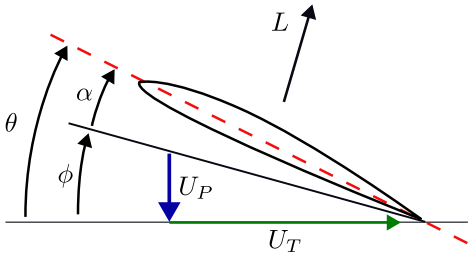

(b) Blade section during forward flow

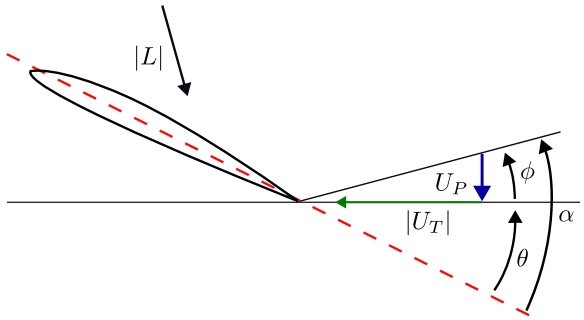

(c) Blade section during reverse flow

Figure 2.5: Aerodynamic environment of a rotor operating in forward flight conditions.

At locations along the blade radius where reverse flow occurs, the sectional aerodynamic conditions are altered significantly as the reversal of the flow direction, leads to negative thrusting conditions for regions of the blade subjected to reverse flow. A schematic highlighting the variation in blade loads for normal and reverse flow conditions is presented in Figure 2.5. Moreover, the sharp geometric trailing edge of the rotor blade acts as the aerodynamic leading edge, resulting in the development of strong vortical flow structures and separated flow regions, ultimately reducing rotor performance. For conditions of large advance ratio, $\mu > 0.5$, the influence of the reverse flow region is no longer insignificant as complex flow behaviours will lead to unsteady aerodynamic conditions that could result in a negative structural response.

2.2 Experimental State-Of-The-Art: Propeller Stall

2.2.1 Development of Novel Experimental Methods

Optical methods such as the light beam method, developed and implemented by Katzmayr [12], made use of photosensitive paper to measure flutter amplitudes and frequencies from light reflected off of the propeller blade tip. Analysis indicated a reduction in propeller efficiency with increasing amplitude and frequency of flutter. Moreover, Seewald [13] made use of a motion camera to capture bending and torsional deformations of rotating blades. Due to the restrictions of available camera technology, the experimental setup was limited by a lack of available light (exposure) which was required to ensure sufficient image resolution at high rotational speeds.

Further attempts to investigate propeller deflections were undertaken by Weick [14] by applying static loads to scaled models by means of weights and wires. To incorporate the large magnitude centrifugal forces expected from a full scale metal propeller, a metallic 2ft diameter scaled propeller model was developed to investigate deflections at take-off conditions, typical of stall flutter. Metal blades were used due to their homogeneous structure, resulting in uniform strength and stiffness. Weick highlighted that wooden blades could not be used to obtain any meaningful structural data. A later study by Weick [15] ascertained the material of propeller blade directly impacts the propulsive efficiency. Through experiment, Weick revealed that metal blades, in this case aluminium alloy, showed an improvement of between 4-7% when compared to equivalent wooden blades tested. At the largest pitch setting, the metal blade set was found to have a maximum propulsive efficiency of 86%. The blade deflections were recorded, however, due to inaccuracies of the experimental setup, the results were discarded.

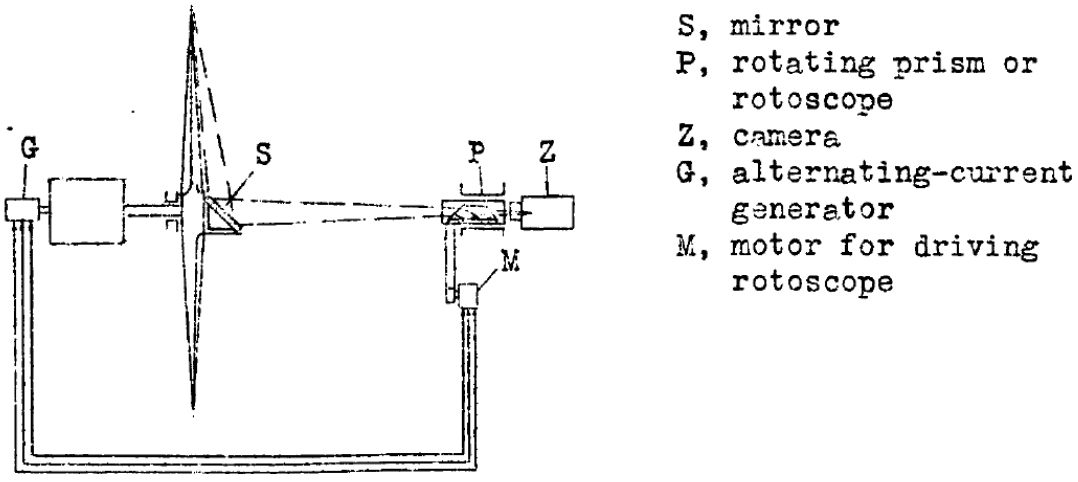

Figure 2.6: Experimental setup developed by Theodorsen to investigate propeller vibrations and centrifugal force effects. Image taken directly from Theodorsen [16].

Furthermore, Theodorsen [16] investigated propeller vibrations and the effect of centrifugal force on the propeller blade using a rotating prism mounted ahead of the propeller, both revolving about the same axis of rotation. As presented in Figure 2.6, the prism was used as an optical device to produce a viewpoint for the observer where the propeller appeared stationary, allowing for the correct orientation for observing the bending and torsional vibrations. Using a high frequency vibrator, variations in frequency were recorded, identifying three blade modes to be avoided during operation of the propeller. Data acquisition proved challenging as blade deflections were too fast for an observer to record manually, resulting in the use of a motion camera to capture images. However, similar to Seewald [13], the experimental setup was limited by available image exposure. Theodorsen noted, to yield a more reliable data set, a refinement of the experimental setup was required to remove damping from the supporting structure.

In 1932, Liebers [17] validated an analytical expression he had developed prior to determine the maximum bending deflection of a rotating propeller blade [18]. The maximum theoretical error was calculated to be 7%, yet experiments consisting of a variety of propeller models of various aerodynamic profiles and twist, were found to have an error no larger than 4%. Experimental testing focused on propeller tip flutter, for which two explanations of the phenomena where provided. First, a potential coupling between the torsional vibrations of the engine shaft at a resonant rotational frequency and the lowest frequency bending moment of the propeller. Second, periodic vibrations of the propeller caused by the unsymmetrical flow field.

To provide further insight, additional scrutiny was undertaken by Liebers [19] to study the resonance vibrations caused by propellers both analytically and experimentally. Lower and upper bending frequency limits were calculated using Rayleigh's principle. During experimental testing, it was observed that the frequency of the propeller bending is always less than the propeller rotational frequency and when the bending frequency is a low multiple of the rotational frequency, resonance cases are possible. Importantly, it was determined that propellers with the same ratio of hub radius to blade length at the same natural frequency have the identical bending frequencies when static and revolving, this was found to be true for different aerofoil shapes, materials and taper. Torsional and bending frequencies were exhibited to be orders of magnitude different from each other, with the torsional frequencies shown to be not significantly affected by aerodynamic forces acting on the propeller blade. Liebers concluded that the magnitude of the torsional vibrations are sufficiently larger than the rotational frequency of the propeller so that any potential coupling between the engine shaft was unlikely.

One year prior to the commencement of World War Two (WW2), Hartman et al. [20] measured the magnitude of propeller blade torsional and bending deflections at a range of rotational frequencies and radial stations along the blade span, using the light-beam method developed by Katzmayr [12]. Experimental results obtained at an advance ratio of 0.3, exhibited a more significant torsional deflection at x/R = 0.85 when compared to x/R = 0.7, in agreement with experimental data collected by Weick [14] ten years earlier in 1928. Further observations of the

test campaign included a shift in propeller coefficients and this was attributed to the torsional blade deflections changing the inclination of the aerofoil sections along the blade resulting in a non-optimal generation of lift. The torsional deflection was found to decrease as the advance ratio is increased. Moreover, during flutter, torque and thrust measurements became unsteady and a prominent audible sound was emitted, confirming an earlier prediction of negative acoustic effects made by Stowell [21].

Further tests by Hartman et al. [22] demonstrated violent flutter at low advance ratio, resulting in a reduction of propulsive efficiency of up to 18%. Previous findings of Borck [23] nearly two decades earlier also support the explanation that flutter of propeller blades could potentially lead to the blade oscillating in and out of stall, ultimately resulting in a reduced propulsive efficiency.

2.2.2 Large Scale Propeller Testing

During the early 1940s, investigations primarily driven by the outbreak of WW2, were undertaken both in the United Kingdom and United States to study propeller flutter of both attached and stalled flows. British investigations were conducted at the Royal Aircraft Establishment (RAE) spinning tower in Farnborough, England. Whereas, American investigations were conducted at various NACA facilities across the United States.

British testing [24–27] comprised of both static (J = 0) and low advance (0 < J < 0.3) inflow conditions, use of fixed and variable pitch settings propellers and operation across a range of rotational frequencies. The most common technique implemented to measure blade deformation was the placement of both axial and torsional strain gauges at various locations along the blade span and chord. Without the advantages of modern computing capabilities, strain gauge locations were determined using analytical methods such as the Rayleigh-Ritz method or cantilever beam theory. Moreover, an array of additional experimental methods were also implemented such as stroboscopic imaging and acoustic arrays. A summary of different experimental methods and test conditions of allied wartime propeller flutter investigations is presented in Table 2.1.

Similar to earlier work of Theodorsen [16], Shannon et al. [24] investigated the distribution of stress at edgewise resonance and its influence on other blade modes, making use of a non-rotating duralumin 10ft 10" diameter De Havilland variable pitch propeller, which was mounted to a torsionally elastic shaft with a vibrator and mass to emulate torsional vibrations applied to the propeller from an aircraft engine. For a fixed blade pitch of $\beta_{0.83R} = 25.4^o$, the fundamental edgewise frequency was 147 Hz and the 1st and 2nd flapping overtones occurred at 95 Hz and 168 Hz, respectively. It was observed that the 2nd flapping mode was excited with edgewise vibration.

Measurements of blade structural behaviour were obtained via strain gauges and a seismic unit integrated into the blade. Strain measurements indicated that stress at edgewise resonance

is primarily dependent on the coupling of flapping, leading to an unsymmetrical bending of the blade and a large deflection due to blade twist. Moreover, blade deflections were recorded every 3" along the blade from the tip. As the seismic unit was limited to recording relative values, the magnitude and phase were recorded from the reflection of light from four cylindrical mirrors on a camera film. Camera film results demonstrated the maximum value of the fundamental edgewise movement and second flapping overtone occurred concurrently. However, the magnitude of torsional deflection was inconsequential, as the torsional natural frequency was substantially larger than the frequencies reached during testing.

Table 2.1: Experimental propeller flutter test conditions and methodologies conducted in the UK and USA during WW2.*

Author(s)	Year	Country	Range of Test Conditions	Method
Shannon et al. [24]	1941	UK	$\beta_{0.83R} = 25.4^o$ RPM = 0 D = 10ft 10"	SU, LB, SG
Clifton et al. [25]	1943	UK	$\beta_{0.7R} = 11^o - 35^o$ RPM = 1200 - 1400 D = 10ft 9"	SG
Sterne et al. [26]	1943	UK	$\beta_{0.7R} = 5.2^o - 28^o$ RPM = 1350 - 1805 D = Not Defined	U
Sterne [27]	1945	UK	$\beta_{0.7R} = 8^o - 32^o$ RPM = 1000 - 1800 D = 10ft 9"	AU
Theodorsen et al. [28]	1945	USA	$\beta_{0.7R} = NotDefined$ RPM = Not Defined D = 3ft 9"	ST, PR

In 1943, Clifton et al. [25] tested a four blade wooden spitfire propeller of diameter 10ft 9" at the No.3 spinning tower at the RAE and a two blade version at the onsite wind tunnel facility. The aim of the investigation was to characterise the flutter boundary of the blades by making use of blades instrumented with flexural (bending) and torsional strain gauges to detect oscillations and strains of the blade during flutter. Five out of the six tests at the spinning tower displayed the presence of flutter at the pitch angle range tested. During wind tunnel testing, at $\beta_{0.7R} = 27^o$, flutter occurred at 1300 RPM, with the failure of bending strain gauges occuring at 1350 RPM. Testing indicated that a sudden increase in the vibration amplitude is a prominent feature of flutter and at small angles of attack the flutter encountered is classical flutter as the strain gauges show both flexural and torsional oscillations, inferring the flow is still attached to the blades and no separation has occurred.

Continuing the use of wooden propeller blades, Sterne et al. [26] investigated the strength

*AU = Aurally, LB = Light Beam, PR = Pressure Probe, SG = Strain Gauge, ST = Stroboscopic Imaging, SU = Seismic Unit, U = Unknown

and flutter characteristics of the blades during operation through $\beta_{0.7R} = 5.2^o - 28^o$. Large sections of the operating envelope were found to be susceptible to extreme flutter, leading to modifications of the blade design. At operating conditions at which $\beta_{0.7R} > 20^o$, violent flutter was encountered and for cases at which $\beta_{0.7R} < 20^o$ no characteristics of flutter observed. Increased severity of flutter was obtained by increasing the rotational frequency beyond the minimum required for flutter, where the blade oscillations became more violent. In pursuit to reduce flutter, blades were modified to remove a section of the leading edge and the under camber of the blade, moving the centre of pressure rearward on the blade. The modified blade was tested through a range of $\beta_{0.7R} = 5.2^o - 22^o$, where no flutter was observed at rotational frequencies significantly higher than the required rotational frequency to excite flutter of the unmodified blade. The modified blade was observed to have less vibrations than equivalent blades of similar thickness and material at the same operating conditions.

Further testing by Sterne [27], using the blade set tested by Clifton et al. [25], was conducted on two, three and four bladed propellers to investigate the effect of the number of blades on flutter boundaries. During testing of the two, three and four bladed configurations, both classical and stall flutter occurred. For the four bladed case, displayed in Figure 2.7, the presence of stalled flow around the blades, $\beta_{0.7R} = 20^o - 28^o$, resulted in excitation of the torsional blade mode caused by negative torsional damping, thus resulting in the instability in the torsional degree of freedom. Once testing had concluded, it was noted that the blades became warm to touch after flutter occurred, with the area of greatest warmth close to the blade tip. During classical flutter, the critical flutter speed for a three bladed propeller was found to be 90 RPM larger than the equivalent two and four blade configurations. Moreover, the two and four blade configurations were found to have the same critical flutter speed with the onset of heavy flutter found to occur at the same operating condition, thus suggesting that the critical flutter speed is independent of the number of blades. However, during stall flutter, the critical flutter speed of the three bladed propeller was found to be less than that of both the two and four bladed propeller.

Sterne concluded that compressed wooden blades are not suitable to collect meaningful structural information, particularly as structural failure can result from heavy flutter for blades with a thickness to chord ratio of less than 10% at 0.7R. Sterne also observed that the critical flutter speed is different in the stalling and low incidence ranges, whilst also noting that the critical flutter speed is a function of blade design and the number of propeller blades as there was found to be little variation of critical flutter speed at low incidence range between propellers of the same design. Subsequently, there is however a large variation in severity of flutter above the critical flutter speed. Furthermore, in agreement with the findings of Theodorsen [16], Sterne noted that structural failure of propeller blades in flutter in the low incidence flutter range, take the form of longitudinal and traverse cracks, indicating that flutter is a result of both classical bending and torsional vibrations.

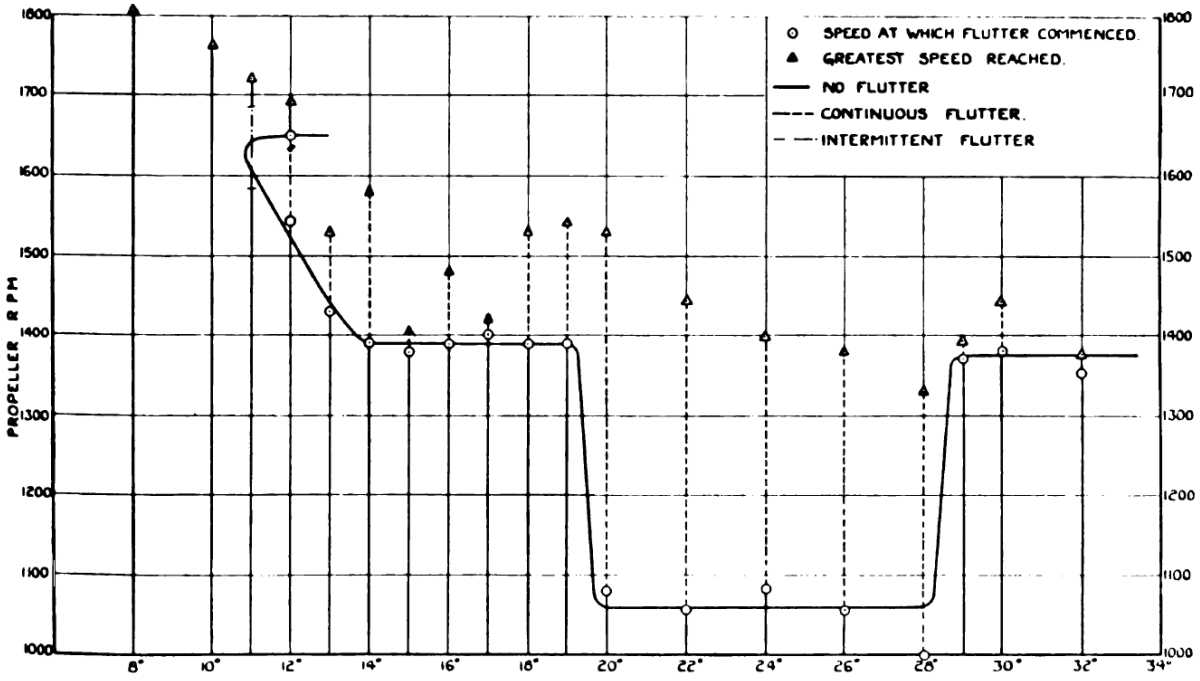

Figure 2.7: Blade flutter boundary map as a function of RPM and $\beta_{0.7R}$. Figure taken directly from Sterne [27].

Further work performed by Theodorsen et al. [28], investigated the effect of the lift coefficient on propeller flutter. It was exhibited prior to the commencement of flutter, the blade twists to a critical position at which point flutter begins and at which the angle of attack at which flutter occurs was found to be independent of the initial blade pitch setting. It was noted that calculations required to adequately predict flutter proposed great difficulty, as the speed at which the blade will stall is lower than the speed at which flutter will occur. Theodorsen et al. implemented stroboscopic observation techniques to confirm the divergence speed and stall flutter speed is approximately the same. This observation was explained by the presence of centrifugal effects and the propeller blade twisting to a stalled condition at the divergence speed, which occurs before flutter begins. It was also revealed that an appropriate camber results in the flutter speed converging close to the stall speed. In addition, as the lift coefficient is increased the flutter speed is reduced. Theodorsen et al. determined that propellers operating at zero lift will induce self excited torsional vibrations at frequencies which are integer multiples of the operating RPM, this phenomena is called wake flutter, however was shown not to be a concern during normal operating limits.

Following the conclusion of the second world war, Haines et al. [29] studied the performance during stalled conditions of a two bladed Rotol hydulignum spitfire propeller using the Royal Aircraft Establishment (RAE) 24ft wind tunnel, by obtaining measurements of propeller thrust and torque. Making use of the blade design tested earlier by Clifton et al. [25], four blade pitch settings were investigated ($\beta_{0.7R} = 10.1^o, 15.1^o, 22^o$ and 27^o). $\beta_{0.7R} = 10.1^o$ and 15.1^o were tested through a range of advance ratio's, ranging from 0 to 0.6 in 0.1 increments. Test-

ing was stopped at $J = 0.6$, as the blade tip speed was approximately the local speed of sound. Larger blade pitch angles of 22^o and 27^o saw severe flutter occur, especially at test conditions corresponding to stall, resulting in testing being halted. The maximum available rotational frequency was dictated by a previous experimental campaign conducted by Sterne [27], of which maximum blade stress was ascertained using flexural and shear strain gauges. The two bladed hydulignum propeller configuration was shown to have an improved aerodynamic performance when compared to the metal equivalent. This was attributed to the larger thickness ratio of the hydulignum propeller, resulting in the delay of stall at higher power settings.

Sterne et al. [30] developed the work of Haines et al. [29] by instrumenting the blades with strain gauges. Both flexural and shear strain gauges were mounted at both 50% and 80% along the blade span. Blade cabling was placed under a cellulose blade coating to ensure that the boundary layer was not tripped and the airflow across the blade surface did not separate. Three wind tunnel freestream velocities were tested (40,80 and 100 ft/s) to ascertain the influence of larger advance ratios on the classical and stall flutter boundaries. At a freestream of 40 ft/s, torsional flutter was observed at 1200 RPM resulting in an almost sinusoidal motion of the blade as the rotational frequency was increased to 1250 RPM. Both the 50% and 80% radial locations, highlighted the torsional strains measurements were in phase and agreed with the static test data, therefore demonstrating that the blades were oscillating at the fundamental torsional frequency of 120 Hz and at this condition stall flutter was observed. For the 80ft/s case, no vibrations were recorded as the blade was operating outwith the stall region. However, increasing the rotational frequency to 1350 RPM, resulted in torsional flutter excitation. Moreover, for the 100ft/s case, the rotational frequency was increased to 1450 RPM where both the torsional and flexural vibrations were recorded. The amplitudes and strains were not repeating with time and displayed an irregular pattern, highlighting a non-linearity in the aerodynamics. Stall flutter was observed for all cases and the rate of flutter became excessive, testing was stopped due to violent oscillations.

Finalising the experimental work on propeller stall flutter at the RAE [24–27, 29, 30], Ewing et al. [31] investigated flutter characteristics of two to five bladed propeller configurations, all of identical blade profiles. All propeller blades were manufactured using duralumin, an aluminum alloy, as a prior investigation by Haines et al. [29] demonstrated that severe flutter can occur within typical operating ranges of wooden propellers, due to reduced torsional stiffness. Blades were tested through a large range of blade pitch angles, both above and below the stall angle. Stall flutter was the only type of flutter encountered and was purely torsional, with the maximum amplitude of vibratory stress occurring at approximately 0.7-0.74R, agreeing with earlier experiments of Weick [14, 15]. At cases of low angle of attack, flutter was not found to occur, even at large rotational frequencies. Despite this, the phase relation was found to be significantly impacted by the rotational frequency and the number of propeller blades, in addition to influencing the amplitude of vibrations. Moreover, in agreement with the experimental work of Clifton et

al. [25] using wooden blades, the flutter characteristics of duralumin blades were also found not to be influenced by the number of propeller blades.

Testing of a single wooden propeller blade with a Clark Y-section was conducted by Baker et al. [32] at zero advance conditions within the National Advisory Committee for Aeronautics (NACA) Langley vacuum sphere. Positive and negative blade pitch settings ranging from 25^o to -25^o were tested at several atmospheric pressures ranging from 32.5 kPa to 101.3 kPa to simulate the effect of varying altitude. During testing, flutter was not observed. However, for several test cases the flutter speed was found to be larger than the safe operating speed of the propeller, explained by the incorporation of a significant safety factor into the blade design. Measurements demonstrated that at large magnitude of both positive and negative blade pitch angles, the flutter frequency tends towards the natural torsional frequency. As a result, the stall flutter speed is significantly lower than the classical flutter speed due to the influence of the blade stall. It was therefore concluded by Baker et al. that at both large positive and negative blade pitch angles, if the critical flutter velocity was achieved then the aeroelastic behaviour excited would be stall flutter due to the presence of flow separation.

Until 1951, the work on stall flutter both experimentally and analytically was extremely disjointed, with the majority of large scale studies performed on wartime propeller blade designs or over simplified blade geometries. Furthermore, due to the complexity of the aerodynamics as a consequence of the presence of flow separation, the use of well understood theories such as potential flow theory could not be implemented and therefore this imposed an increasing requirement to perform experimental test campaigns.

To address this, Baker [33] performed another experimental study at the NACA Langley vacuum sphere to observe the effect of varying key blade parameters on the stall flutter boundary of a propeller blade. Parameters investigated included; torsional stiffness, thickness, sweep, length-chord ratio, sectional C.G location, blade taper, blade twist, Mach number, fluid density and sectional lift coefficient. Rotational frequency was increased until flutter was observed with several attempts made to transition through the flutter region. However, oscillations proved too violent, ultimately resulting in blade failure and termination of the testing. Blade frequencies, obtained via wired strain gauges, were recorded using an oscillograph for both the torsional and bending modes, alongside propeller rotational frequency and total-pressure measurements of the propeller wake, 0.17D downstream from the rotor disk. The experiment concluded that torsional stiffness, blade taper, blade twist, length-chord ratio and density have no significant impact on the minimum flutter speed. Furthermore, an increase of the section thickness from 6% to 9% resulted in a 20% increase in flutter speed. Although, increasing the blade thickness was shown to potentially result in a reduction of blade aerodynamic efficiency as the aerofoil approaches and exceeds trans-sonic speeds. Introduction of backwards sweep was shown to result in an small increase in the flutter speed. Nevertheless, the significance of this finding was overshadowed by the difficulties imposed during the blade manufacture to appropriately incorporate a swept

blade geometry. Forward movement of the sectional C.G location results in large increases in the flutter speed. However, if moved too far forward the negative pitching moment would grow in magnitude due to radial loading, resulting in a larger torsional deflection. It was therefore concluded that forward movement of the C.G location at low blade pitch angles would have a significant positive effect on the minimum flutter speed. In addition, Baker demonstrated that an increase in torsional frequency gives a proportional rise in flutter velocity whilst highlighting that a reduction in blade length or increased section thickness of the aerofoil, increases the blade torsional frequency.

A further investigation was undertaken by Gray et al. [34] at the Langley 16ft wind tunnel facility to measure torsional deflections of multiple propeller blades at a variety of operating conditions. Four constant chord two-bladed propellers built from aluminium alloy with varying thickness and camber were studied for a fixed blade pitch of $\beta_{0.75R} = 45^o$. Testing was conducted through a range of advance ratios, where rotational frequency was held constant and the free stream velocity of the tunnel was altered. Measurements of blade twist were obtained at three radial locations ($x/R = 0.45, 0.7, 0.9$) along the blade to improve reliability of the blade twisting behaviour. Moreover, Gray et al. did note that their intention was also to obtain pressure distribution measurements at the nine locations across the blade span, but this was not feasible at the time. Results demonstrated that the largest deflection occurred on the thinnest propeller where the blade deflected over a range of 4.9^o for both positive and negative deflection angles at a radial location 90% along the blade, 10% from the blade tip. In agreement with the findings of Baker [33], blade torsion was shown to have a sizeable effect on the radial loads of the blade, altering the local blade pitch angle and the overall propeller efficiency. A theoretical approximation developed by Gray et al. to calculate the total torsional deflection along the blade span, agreed with the experimental results collated for the majority of cases within a tolerance of 0.2^o. However, test cases at which the blade was operating at highly loaded conditions could not be adequately captured.

Subsequently, an investigation into the effect of blade-section camber on the static characteristics of different NACA propellers was performed by Wood et al. [35] using the static test stand at NACA Langley. Blade pitch angles ranging from 0^o to 16^o were tested in 4^o increments through a rotational frequency range of 600-2200 RPM, in increments of 100 RPM. To avoid the possibility of the excitement of whirl flutter, rotational frequencies greater than 2200 were not exceeded. For the 16^o blade pitch case, flutter occurred at a rotational tip speed of 248 m/s for NACA 10-(5)(066)-03 section blades. In comparison, flutter was observed for the NACA 10-(0)(066)-03 section blades at a tip velocity of 169 m/s. The torsional rigidity of both blades was investigated with both blade sets found to have the first torsional frequency occur between 151-156 Hz, highlighting no apparent structural difference between the blades in torsion. Testing was achieved for all rotational frequencies across all blade pitch angles except for the 16^o case, due to the presence of flutter.

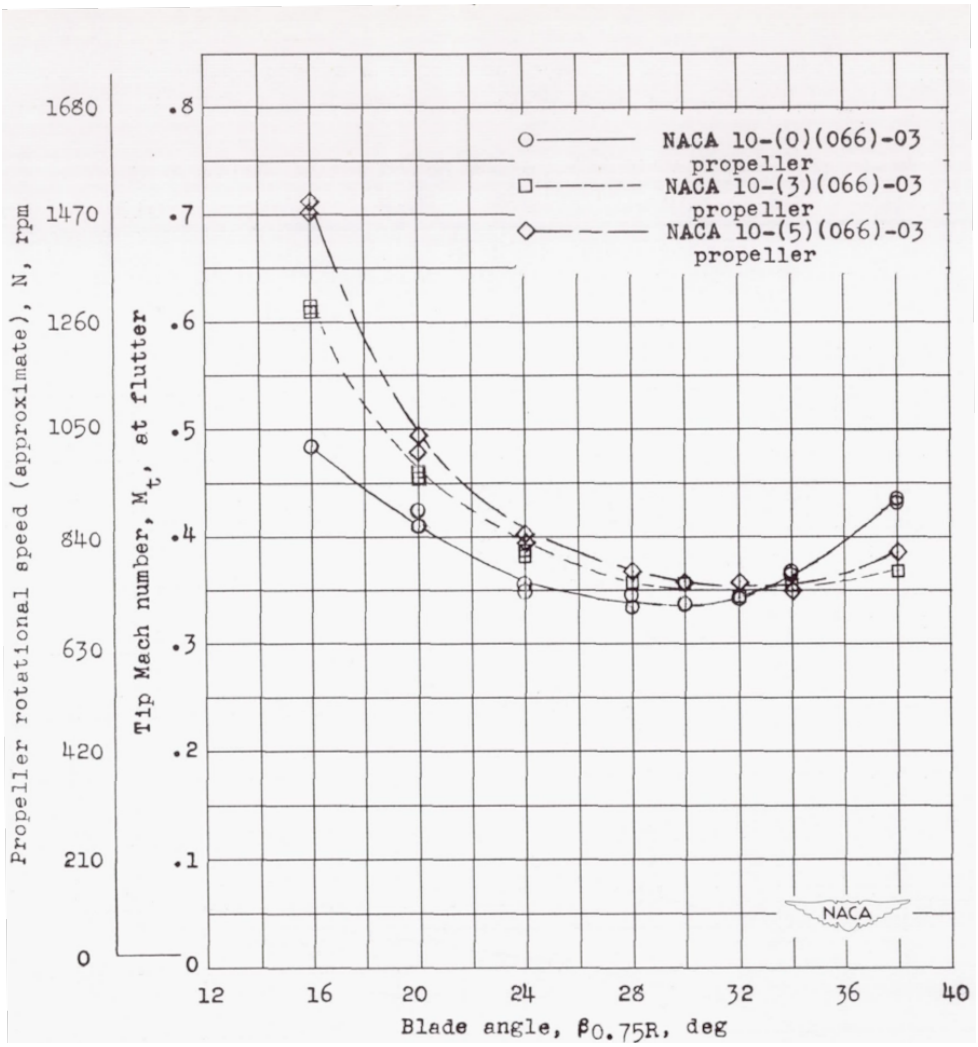

Figure 2.8: Variation of tip Mach number at flutter as function of $\beta_{0.75}$. Image taken directly from Allis et al. [36].

Allis et al. [36] continued the work of Wood et al. [35] by conducting a experimental test campaign to investigate the effect of blade-section camber on stall flutter characteristics at zero advance ratio. Three propeller sections were tested at blade pitch angles ranging from 16^o to 38^o, all with a diameter of 3.048m (10ft) and a constant design sectional lift coefficients of 0, 0.3 and 0.5 respectively, from root to tip. Propeller rotational frequency was increased until flutter was observed. Measurements of thrust, torque, blade torsional deflection, torsional and bending stresses were recorded at equal increments of increasing rotational frequency, until a maximum tip Mach number of 0.72 was reached, as displayed in Figure 2.8, where high levels of torsional stress were recorded. Results demonstrated that an increase in blade section camber increases the flutter speed coefficient up to a blade pitch angle of 28^o. At 16^o, an increase in blade section lift coefficient resulted in a 36% increase in thrust coefficient during flutter conditions. Flutter speed, thrust and power coefficients were recorded to an accuracy of 5% and the blade pitch angle was set to an accuracy of $+/-0.05^o$ with torsional deflections measured to an accuracy

of $+/-0.1^o$.

Later that year, Heath [37] investigated torsional damping characteristics of laminated beams within the application to the problem of propeller stall flutter. The focus of the investigation was to develop an understanding of the effect of number of laminations and the effect of various bonding materials used to construct the models, with respect to the structural damping and behaviour of the torsional mode. Eight models were constructed and tested. During the testing of model five, it was observed that the 2nd bending mode and 1st torsional mode were interacting in a coupled manner. To resolve this, weights were added to separate the natural frequencies of the coupled modes, a method demonstrated analytically in 1935 by Theodorsen [28]. The torsional stiffness measurements obtained were averaged due to the non-uniformity of material stiffness over the length of the beams. It was shown that stall flutter vibrations are mainly torsional and that the rise of the minimum flutter parameters, calculated from aerodynamic coefficients, infer an increase in the minimum flutter speed.

To assess the flutter characteristics of thin propeller blades, Hubbard et al. [38] undertook an experimental investigation at the NASA Langley vacuum sphere to systematically identify key parameters that result in the excitement of propeller stall flutter. Three propeller blades were tested, each with varying blade thickness percentages. Model 1 had a blade thickness of 2% and was intended for supersonic operation. Model 2 was a 6% blade thickness propeller blade that was tested through a range of Mach numbers by altering the speed of sound using various mixture ratios of Freon-12 and air. Higher Mach numbers were of greater interest than that of lower Mach numbers so that the compressibility effects of outer sections of the blade could be studied. In addition, the shape of the flutter boundaries were also of interest. Model 3 was manufactured twice as model 3(a) and 3(b). Both model 3 variations were identical in shape and had a 3% blade thickness, however the internal structure was varied to investigate the effects of structural damping and blade stresses. Model 3(a) was manufactured from solid steel and had a lower internal damping than that of model 3(b) which was constructed using a laminated design to increase damping. All blades were tested for a given atmospheric pressure and blade angle for a variety of rotational frequency values until flutter occurred multiple times to establish a defined flutter boundary. During testing, in order to navigate the flutter boundary safely, a controllable pitch hub was used so that the blade pitch and rotational frequency could be changed during testing, to ensure the ability to enter and exit the flutter condition with relative ease. Strain gauge measurements at the blade root were logged during testing to monitor and measure the bending and torsion strains of the blade. At the same time, an oscillograph was used to record the frequency of the oscillations of the blade, whilst a phase locked stroboscopic light was used to measure the blade pitch as the propeller rotated. To correctly identify flutter and not confuse it with stable vibrations, flutter speed is defined as

"The velocity at which structural oscillations diverge resulting in a sudden growth in

oscillation amplitude".

Model 1 testing demonstrated that simply increasing the flow velocity (Mach number) at a fixed rotational frequency and blade angle until flutter occurred, resulted in several resonance peaks that required appropriate acceleration to safely transition through rotational frequencies close to resonance peaks. However, oscillations became too significant resulting in testing to be stopped. On one instance the blade did fail and this occurred when operating near the flutter boundary. Effects of Mach number on model 2 showed that generally the flutter region is reduced as the sound-speed coefficient is increased. Moreover, at higher Mach numbers flutter occured at smaller blade angles. Furthermore, increasing torsional damping of model 3 from 0.004 to 0.022 was found to increase minimum flutter speed by 40%, whilst increased internal damping was found to reduce the magnitude of vibratory stresses of model 3 during flutter.

Rogallo et al. [39] examined the stall flutter characteristics of a duralumin three bladed 10ft diameter supersonic type propeller at the NASA Ames 40ft by 80ft wind tunnel. Similar to the earlier works of Baker et al. [32], the effect of stall flutter on a propeller operating in negative and positive thrusting conditions was investigated. Moreover, propeller operation with an inclined thrust axis and vibratory blade stresses as the flutter boundary is approached and exceeded were also investigated. Measurements of propeller thrust and power were logged for all test cases, whilst wake and inflow measurements were recorded for selected operational cases. Moreover, blade stress measurements were also acquired using strain gauges to capture the blade flutter and bending response. Each blade was instrumented with a bending gauge placed 20" and a torsion gauge 42" from the thrust axis. To investigate the radial flapwise bending of the blade, the master blade had extra bending gauges placed at 30", 40" and 50" from the thrust axis. An extra torsional gauge was placed at 24" to investigate the torsional mode. The maximum flutter stress appeared to be a function of the maximum thrust, typically occurring around the 0.8R position. An attempt to correlate 2D and 3D aerodynamic data was made to provide an insight into stall flutter prediction. However, this was unsuccessful due to significant differences in the 2D and 3D results. With respect to the 2D case, known stall angles were between 6^o and 8^o. Equivalent blade locations for the 3D data resulted in angles of attack as large as 20^o with no stall present. Additionally, flutter was found not to effect the thrust or power of the propeller and thrust axis inclination up to 15^o appeared to have no effect on flutter. For cases which flutter was observed, the divergence from linearity of the thrust variation at outboard sections was noted as shown in Figure 2.9. At 0.78R and 0.9R, the divergence occurred at the same time as flutter onset. There was no stall found inboard of 0.64R for all test conditions, resulting in the conclusion that the divergence is believed to be a result of complete flow separation at or in some cases, partial separation prior to the onset of blade sectional stall angle, typical of stall flutter.

In 1964, Rogallo [40] patented a flow control system that was intended to control the loads acting on operating propeller blades. Rogallo theorised that implementing lateral blowing to

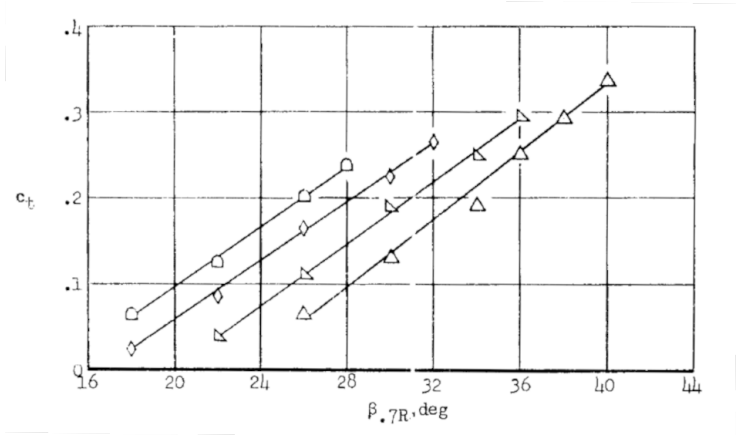

(a) 0.64R

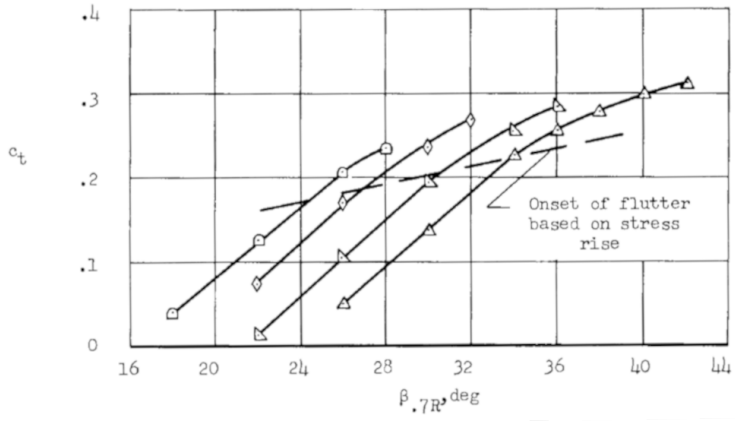

(b) 0.78R

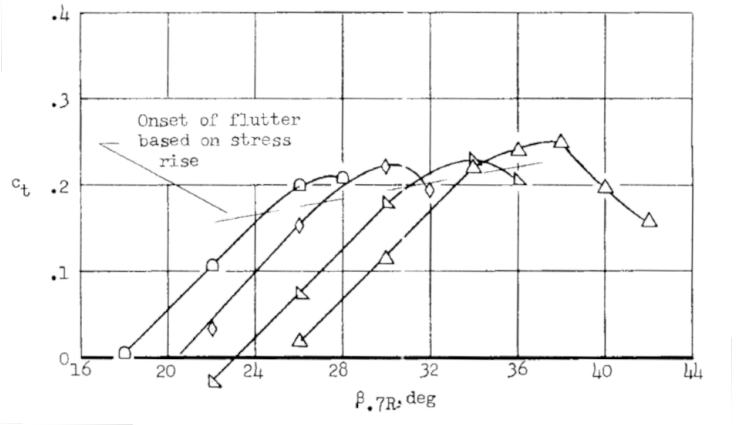

(c) 0.9R

Figure 2.9: Variation of sectional thrust coefficient (C_t) as a function of $\beta_{0.7R}$. Image taken directly from Rogallo et al. [39].

redirect the air flow back towards the blade tip would result in the fluid flow through the propeller being worked upon by a more efficient part of the propeller. Unlike guide vanes or a propeller shroud, the blowing system was not represented by a physical structure meaning there would be an expected reduction of drag, as the redirected flow does not encounter the air frame. As a

result of this, the ability to reduce or eliminate the effect of stall flutter on propeller blades was discussed. However, the device was never manufacture or tested.

Throughout the 1960s and 1970s, the development of propeller aircraft was on the decline, due to the dawn of the jet age, thus experimental propeller works became extremely scarce. At the end of the 1970s, Burton [41] of Dowty Rotol undertook a series of strain gauge tests on a type(c) R.305/3-82-F/6 propeller to investigate vibratory and torsional stresses. Identical to a British wartime investigation by Clifton [25], testing was conducted using the spinning tower at the RAE. The purpose of the test campaign was primarily to determine propeller strength through the measurement of both vibratory and torsional stress levels. Moreover, strain gauges were used to investigate flutter characteristics of the fixed-pitch blade over a range of rotational frequencies and different blade pitch settings. Strain gauges were cemented onto the blade surface at distances ranging between 0.2 - 0.95 R, with torsional gauges placed at an increased resolution of 0.05R between 0.6-0.95 R. During initial test runs, testing was terminated due to excessive noise signifying flutter, a finding observed decades earlier both by Weick [14] and Stowell [21]. Upon inspection of the propeller crosshead following runs that encountered flutter, the crosshead was deemed to have failed as a result of fatigue at a blade pitch setting of $27^o40'$. Moreover, propeller power was found to exceed the normal operating ratings of the engine. In addition, severe torsional stresses were also monitored, further indicating the presence of stall flutter. Following, a redesign of the crosshead, acceptable levels of torsional stress were recorded using a blade pitch angle range of $-22^o40'$ to 34^o and no unexpected prominent noise was detected.

2.2.3 Experimental Flight Testing

Between 1956 and 1958, O'Bryan [42–44] lead a joint effort between the United States Air Force (USAF), United States Navy (USN) and NACA to investigate the vibratory bending and torsional stresses of a new series of NACA propeller blades at varying flight conditions. A summary of the investigated parameters is presented in Table 2.2. As already shown by Gray et al. [34], O'Bryan also established that the use of thin propeller blades generates a greater degree of blade flexibility resulting in a reduction of the bending and torsional natural frequencies, meaning the blades are more susceptible to stall flutter. Subsequently, a particular focus was placed on the 1-P (once per revolution) stress and stall flutter stress. O'Bryan defined the 1-P stress as

"The stress that occurs due to the oscillating aerodynamic load imposed on the propeller as a result of an inclined thrust axis".

The inclination angle, computed from both wind tunnel and flight pressure data, was obtained using a pressure probe with an estimated accuracy of $\pm 0.02^o$. The pressure readings ob-

tained during flight, both static and total, were recorded using a Kollsman type 651 pitot-static probe, one propeller tip chord length ahead of the aircraft wing tip. Additionally, the Mach number was obtained using radar with an estimated accuracy of ± 0.005. Using a USAF McDonnell XF-88B aircraft, three varying spinner shapes were investigated to observe any potential change in the propeller inflow, a summary of experimental parameters is displayed in Table 2.2.

Table 2.2: Summary of in-flight experimental test campaigns undertaken by O'Bryan between 1956-1958 to investigate propeller blade stress at large inflow conditions [42–44]

Investigation	1956 [42]	1958a [43]	1958b [44]
Maximum Mach Number, M	0.95	0.95	0.96
Maximum Advance Ratio, J	2.2	3.6	4.9
Propeller Material Type	SAE 4340 Solid Steel	SAE 4340 Solid Steel	SAE 4340 Solid Steel
Thickness to Chord Ratio, t/c	2-4 %	2-5.4%	2-7.7%
Aerofoil Section	Symmetrical NACA 16 Series	Symmetrical NACA 16 Series	Cambered NACA 16 Series
Planform Shape	Tapered	Tapered	Rectangular
Propeller Configuration	3 blade	3 and 4 blade	3 blade
Propeller Diameter, ft	7.2	9.8 and 10	6.85
Bending Strain Gauge Location, %R	0.37 / 0.394	0.314 / 0.331 / 0.382	0.35 / 0.375 / 0.387 / 0.411
Torsion Strain Gauge Location, %R	0.78	0.739	0.725
Test Altitude(s), ft	5,000 / 20,000 / 30,000	5,000 / 25,000	25,000
Spinner Shape	Spherical	Conical	Elliptical

During flight and static ground tests, strain gauges were placed along the blade centre line to monitor the bending and torsional stresses as displayed in Figure 2.10. All blades were manufactured using heat treated SAE 4340 solid steel, which has a ultimate tensile strength of 180,000 psi and a working endurance of 56,000 psi. During the first investigation [42], no flutter was detected throughout the entirety of the test matrix. The magnitude of the bending stress was the lowest of both modes and peaked at 11,500 psi during an engine start at 5,000ft at 250mph. A sharp rise in bending stress was observed at 750 RPM, however, decreased to 4,000 psi before the rotational speed of the engine reached 1000 RPM or within 3 seconds. Whilst conducting an emergency feathering test at Mach 0.95, Torsional stress peaked at 2,000 psi, otherwise values remained between 500 and 1,500 psi. The maximum torsional stress from static testing was 670 psi. Investigation two [43] was a continuation of prior work [42], however, tailored the investigation towards the effects of propeller shape, configuration and spinner shape.

The three blade configuration had a 9.8ft propeller whereas the four blade configuration required a 10ft propeller due to the requirement of a larger hub. Flight and ground tests were undertaken and strain gauge data was recorded using an oscillograph. During static ground tests of the three blade configuration, stall flutter was observed at a blade pitch angle of 19.5^o, resulting in a sharp rise in torsional stress at 100 Hz, agreeing with the calculated result of 100 Hz. No further cases displayed behaviour of flutter during ground testing. However, as the maximum engine temperature was reached, a blade pitch angle of 19.6^o was not surpassed. Investigation three [44] highlighted that for mach numbers greater than 0.84, the bending vibration wave shape becomes complex. Below 0.84, the variation of stress with excitation factor indicates a wave shape similar to that of 1-P stress. Additionally, bending stresses were also found to increase with Mach number whilst the ratio of bending stress to excitation factor decreased as

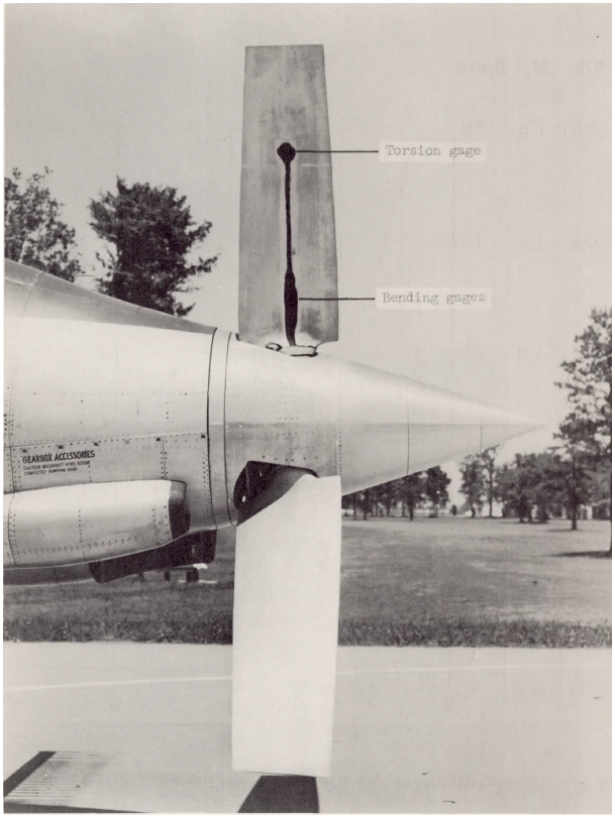

Figure 2.10: Propeller blade instrumented with torsional and bending strain gauges prior to an experimental test flight. Figure taken directly from from O'Bryan [43]

Mach number increased from 0.68 to 0.84, the explanation reached was due to a reduction in lift at outboard sections as a consequence of a resultant Mach number larger than 0.9 . During flight the maximum torsional stress was no greater than 1,000 psi. Ground tests saw a larger torsional stress up to 5,000 psi however this was whilst the blade was stalled and was not of concern due to ample stiffness.

2.2.4 High Speed Propeller Concepts

During the mid to late 1970s, large rises in international fuel costs [45] and the increasing dependency on the newly developed turbofan engine, resulted in the National Aeronautics and Space Administration (NASA) to begin the development of a high speed propeller concept, in an attempt to utilise the high propulsive efficiency of a propeller to mitigate fuel costs. Conventional propeller designs until this time period were known for the ability to operate at high efficiencies up to Mach 0.6 [46]. For larger Mach conditions, there was a noticeable drop in propulsive efficiency due to the influence of compressibility effects on the outer sections of the blades, where higher resultant velocities occur due to a larger rotational velocity component. To counter this, NASA's turboprop program became the focus of propeller research as a new set of highly swept, highly twisted and highly loaded propeller blades were developed. These blades were named the Single Rotation series, also commonly referred to as SR blades, shown in Figure

2.11.

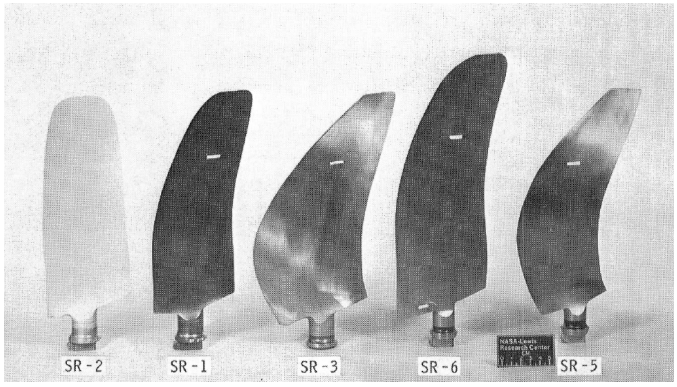

(a) SR - 2/1/3/6/5 series blade shapes

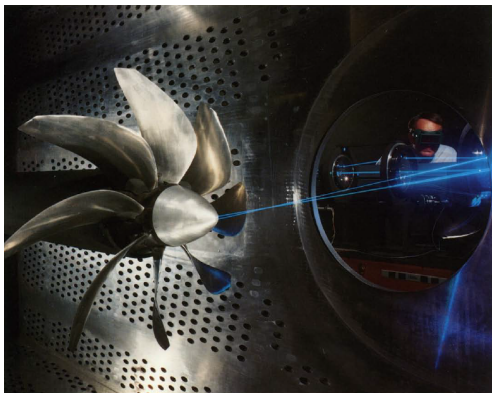

(b) 8 bladed SR-5 propeller configuration

Figure 2.11: SR blades used during the NASA advanced turboprop project at NASA Lewis. Images taken directly from Whitlow et al. [45] and Hager [47].

Extensive testing of the SR blades was undertaken by NASA throughout the 1980s, primarily at the Lewis research centre 8 x 6 ft wind tunnel [47]. Typical propfan propeller configurations consisted of 8 to 10 blades and a variation in sweep, all of which were tested at various operating conditions. The blades were extensively researched, particularly in the areas of aerodynamics, structures and acoustics [48]. In addition to strain gauges, non-intrusive optical methods such as Laser Doppler Anemometry (LDA) were utilised to measure the surrounding flow field during both stall flutter and classical flutter.

In 1981, Mehmed et al. [49] undertook a testing campaign of two, five and ten bladed titanium prop-fan models operating between Mach 0.36 to 0.85, through blade pitch angles $\beta_{0.8R} = 47^o$ and 75^o, to investigate aeroelastic stability boundaries to aid the development of numerical codes that could be validated for predicting blade flutter. Experiments of the SR-5 blade were undertaken at NASA Lewis 6ft x 8ft wind tunnel using three 1/7th scaled models, all of which were not aeroelastically scaled. The details of the design point operating condition are presented in Table 2.3. Blades were instrumented with strain gauges to measure both bending and torsional stresses. Propeller vibrations were captured via a stroboscopic camera system and flow visualisation methods such as tufts and pressure sensitive paint where employed to provide a qualitative assessment of the flow behaviour. Moreover, radial pressure profiles were obtained using a total pressure probe downstream of the propeller. Throughout the pitch range tested, cases for Mach numbers larger than 0.6, flutter occurred. Results obtained were also shown to support the explanation that aerodynamic cascade effects have a significant negative impact on the flutter limitations, as coupling of blades saw a significant stress rise for a small increase in rotational frequency. Both five and ten bladed configurations demonstrated this instability at velocity conditions surrounding the sonic barrier, relative tip Mach numbers of 0.95 and 1.10, respectively. Despite the increased occurrence of instability, no effect on propeller aerodynamic performance was recorded. Futhermore, classical flutter in the form of coupled bending and

torsional motion was observed. However, stall flutter was ruled out due to low blade incidence angles. Experimental flutter speed data did not correlate well with the corresponding analytical data, most likely due to effects such as trans-sonic flow, blade mistuning, blade sweep, aerodynamic coupling, separated flow regions or non-linearities of blade properties.

Table 2.3: Design point operating conditions of the SR-5 model for use in the Lewis wind tunnel by Mehmed et al. [49]

Parameter	**Symbol**	**Value**	**Units**
Mach Number	M	0.8	-
Static Pressure	P_o	76.6	kN/m^2
Static Temperature	T_o	292	K
Rotational Frequency	Ω	7950	RPM
Tip Velocity	V_{Tip}	259	m/s
Power	P	388	kW
Thrust	T	1112	N
Blade Pitch Angle at 0.8R	$\beta_{0.8R}$	61.6	^{o}

Bansal et al. [50] conducted a collaborative test program between NASA Lewis and NASA Ames, to investigate the 1-P dynamic response and stability of three advanced turbo prop models. Three individual campaigns were undertaken over a range of parameters, defined in Table 2.4. A 1-P dynamic response was excited by altering the propeller shaft angle to provide angular inflow conditions. In contrast to stability tests, the shaft angle was held constant at 0^o and excitation was attributed to tunnel turbulence or a nitrogen gas stream behind the propeller disc. To further simulate conditions typical of in-flight operation, the propeller was installed onto a semi-span fuselage/wing/nacelle model to provide realistic inflow conditions to the propeller. The SR-5 model, identical to that used by Mehmed et al. [49], demonstrated flutter during testing. However, both SR-2 composite model (SR-2C) and SR-3 models did not flutter. The SR-5 flutter boundary was found to reduce with increasing Mach number, number of blades and blade pitch angle. Moreover, the SR-3 model was found to have larger damping in the four bladed configuration when compared to that of the eight bladed model. 1-P inboard stresses of the SR-2 blade, demonstrated a parabolic variation with the fuselage reference angle to the incoming free-stream velocity. It was concluded that data obtained from both NASA Ames and NASA Lewis displayed very good consistency in stress behaviour, both in terms of magnitude and slope, with small differences attributed to wing circulation and nacelle interference.

Smith investigated the dynamic stability of the SR-2, SR-3 and SR-5 advance turbo-prop blade sets at static [51]. Both SR-2 and SR-3 blade sets were comprised of eight blades, whilst the SR-5 model was a ten bladed configuration. The SR-3 and SR-5 blade sets were manufactured from solid titanium, whereas the SR-2 was constructed from solid steel. All three models were manufactured at a 1/8th scale, corresponding to a propeller diameter of 0.62m. Blade pitch range varied across all blades tested with a minimum blade pitch for SR-2, SR-3 and SR-5

Table 2.4: Test matrix of dynamic response and stability campaign undertaken by Bansal et al. [50]

Facility	Test Type	Prop-fan Model	Number of Blades	Wind Tunnel Mach Number	RPM	Reference Blade Angle (^{o})	Shaft Tilt Angle (^{o})	Fuselage Angle of Attack (^{o})
NASA Lewis	1-P	SR-2C	8	0.36 - 0.90	4000 - 9000	38.1 - 59.7	0 to 15	-
8x6 ft	Response	SR-3	8	0.35 - 0.85	3800 - 9000	45.0 - 80.7	0 to 15	-
Wind Tunnel		SR-5	10	0.36 - 0.85	2700 - 9000	49.1 - 72.9	-1 to 15	-
NASA Lewis	Stability	SR-2C	8	-	-	-	-	-
8x6 ft		SR-3	4	0.8 - 0.85	7000 - 9000	59.0 - 60.8	0	-
Wind Tunnel			8	0.8 - 0.85	7000 - 9000	57.7 - 61.0	0	-
		SR-5	2,5,10	0.7 - 0.85	4700 - 6750	69.0 - 73.0	0	-
NASA Ames	Installed	SR-2C	8	0.6 - 0.85	6430 - 9000	50.7 - 57.0	-	-3 to 5
14x14 ft	Response			0.8 - 0.85	7000 - 9000	59.0 - 60.8	-	-
Wind Tunnel				0.8 - 0.85	7000 - 9000	57.7 - 61.0	-	-
				0.7 - 0.85	4700 - 6750	69.0 - 73.0	-	-

of $\beta_{0.78R} = -14.3^o$, -8^o and 11^o, respectively. The maximum blade pitch for all blades was $\beta_{0.78R} = 80^o$. Static testing was performed in the United Technologies Research Centre (UTRC) large subsonic wind tunnel. Measurements obtained showed, SR-5 blades with a larger blade sweep suppressed stall flutter better than both the un-swept SR-2 blades and the less swept SR-3 configurations. Blade vibratory stresses were measured, using strain gauges, highlighting a reduction in stress amplitude with increasing sweep across a variety of pitch angles and rotational frequencies, including areas of deep stall. To avoid confusion, Smith defined the total vibratory stress as,

"The maximum stress peak that repeats itself two or three times during the stress data sample period".

It was noted that for all models the largest vibratory stress occurred at the maximum rotational frequency and pitch angle, leading to the understanding this is a forced response as a consequence of vortex shedding and aeroelastic buffet, an aeroelastic excitation as a result of presence of separated flow. Measurements from the static investigation by Smith, demonstrated the analytical predictions to estimate the flutter boundaries matched the experimental data well for the SR-2 and SR-3 blades, with SR-2 flutter occurring in the torsional mode as predicted. Moreover, flutter occurred for the SR-3 and SR-5 blade sets, primarily excited by the 2nd bending mode. In contrast, the SR-5 blade was found not to flutter during any of the experimental tests.

Smith developed his work on static testing by undertaking an experimental test campaign at low advancing conditions [52] for Mach numbers between 0 and 0.35. Similar to the findings of the static tests carried out [51], an increased blade sweep angle and increased advance velocity were demonstrated to significantly increase the stall flutter boundary of the blade, due to the reduction in blade stress due to the elevation of blade loads as a consequence of increased advance ratio. Moreover, the reduction of the effective angle of attack significantly reduced the occurrence of partial or complete flow separation. As expected, measurements of blade stress

at Mach 0.1 were considerably less than that of static test results. In addition, the propeller was tilted relative to the flow, introducing an angular inflow to the propeller disc, highlighting a linear increase in blade stress with tilt angle. Moreover, blade stress sensitivity (stress divided by excitation factor) was shown to increase with increased blade pitch, increased rotational frequency and decreasing advance ratio. During operation within the stalled region, typically between $\beta_{0.78R} = 30^o$ to 45^o, a clear spike in stress was observed. In deep stall conditions, typically greater than 50^o, the SR-5 blade set exhibited behaviour of the buffet phenomenon. At the same operating conditions, both SR-2 and SR-3 models displayed a coupled excitation of both bending and torsional modes in stalled flow, indicating the presence stall flutter.

To include all aspects of propeller design into the aeroelastic testing campaign of the SR blades. Mehmed et al. [53] investigated classical bending-torsion flutter of composite SR3C-X2 propfan blades at relative subsonic flows around the blade tip. Four and eight blade configurations were tested at tunnel Mach numbers between 0.36 to 0.75 for rotational frequencies up to 8000 RPM for blade pitch angles ranging from $\beta_{0.8R} = 56.6^o$ to 68.4^o. It was demonstrated that for increased blade pitch settings and propellers with a larger number of blades, aerodynamic coupling, also termed cascading effects, lead to instabilities. Strain gauge measurements obtained for propellers with blade numbers greater than six, demonstrated the need for evaluation of cascade effects, as the thin and flexible blades are prone to deflections due to large centrifugal and aerodynamic loads. Moreover, due to the highly swept and twisted geometric properties of the SR-blades, coupling of the bending and torsional modes is likely, as documented previously by Smith [51]. Classical flutter was identified, across a range of small to large blade pitch settings, at a frequency between that of the first and second mode, suggesting an aerodynamic coupling between the modes. Moreover, a flutter response was noticed on the four bladed propeller when the rotational frequency crossed the 2-P order line. This response was understood to be a result of low damping near the flutter condition and the matching of the inter-blade phase angle of the flutter mode and the 2-P response. Furthermore, a prior investigation by Mehmed et al. [49] demonstrated that classical flutter onset of a 10 bladed titanium prop-fan was unexpected. However, in the case of the SR3C-X2 propfan, the blade first mode frequency was close to that of the flutter frequency , this was likely attributed to the composite nature of the blade material offering lower stiffness, thus less structural damping.

To further investigate the dynamic response and stability of composite prop-fan blades Smith et al. [54] manufactured and tested a composite SR-3 blade, named SR-3C-3. The composite blades were manufactured using carbon fibre cloth layers in an epoxy matrix. To remove blade instabilities, the ply layers were positioned in an orientation of $\pm 45^o$ in an attempt to match the structural response of the existing titanium SR-3 model. Testing was performed at the NASA Lewis 8x6 ft wind tunnel, at an air density equivalent to a standard day altitude of between 5000ft and 7000ft. Blades were operated at rotational frequencies ranging between 3730 to 10000 RPM. In an attempt to probe the flutter boundary at Mach 0.9, the rig rotational limit

of 9000 RPM was exceeded. Despite the attempt to excite flutter, the SR-3C-3 blade proved to be free of flutter at all conditions tested. However, the strain sensitivity of composite blades was larger than that of their metal equivalent, most likely due to variation in blade stiffness and properties of inertia. Furthermore, in agreement with Mehmed et al. [53], due to non-linear effects as a result of flexible thin sections and swept blades, the maximum strain value was found to occur at approximately 8000 RPM, the critical speed of first mode/2-P crossover. Moreover, the 1-P strain increased with larger rotational frequencies for both the inboard and mid blade bending gauges, with the inboard strain always larger. Identical behaviour was exhibited by the shear gauges until Mach 0.7, at which point there was a reduction in 1-P vibratory stress for an increasing rotational frequency. This reduction was attributed to the movement of the aerodynamic centre, thus altering the torsional response whilst the bending response would not be effected.

Developing existing work on composite blades, Smith et al. [55] investigated the installed response of eight bladed SR-2C and SR-3C-3 propellers mounted onto a fuselage structure. Both models were evaluated at fuselage reference angles ranging from -1^o to 4^o up to a tunnel Mach number 0.85, for rotational frequencies ranging between 3740 to 7000 RPM for SR-3C-3 and 5677 to 8532 for SR-2C. P-order and modal responses were measured using strain gauges to investigate the first mode/2-P crossover critical speed, as this condition has been shown to excite blade dynamic response. Furthermore, due to the presence of the fuselage, during testing resonant frequencies were encountered which required appropirate accelerations to avoid excitation of the overall structure, a similar encounter was noted previously by Hubbard et al. [38]. Comparison of the dynamic response of both the installed and uninstalled propeller models using earlier data obtained by Bansal et al. [50], highlighted the pressure interaction due to the presence of the wing, demonstrated a 1-P response twice that of an uninstalled model, whilst the 2-P blade strain was found to change linearly with the lift produced by the wing. It was also observed that higher order harmonic responses were of interest near critical speeds due to interactions between the blade tips and wing leading edge as a result of their close proximity.

Kaza et al. [56] investigated the concept of intentionally mistuning eight bladed composite SR3C-X2 and SR3C-3 propellers, as a potential method of controlling the blade structural response, thus increasing the flutter boundary. Mistuning can take the form of small differences applied to the blade design or can result from discrepancies during manufacturing process, leading to small blade to blade variations. Both blade sets were identical geometrically, however, variation of the ply angle of the composite layers was introduced. Both blade sets had 80% of ply's oriented in the pitch axis (0^o), the remaining 20% were oriented at $\pm 22.5^o$ and $\pm 45^o$ for the SR3C-X2 and SR3C-3 blades, respectively. Strain measurements were taken to capture strain amplitudes, flutter speed, flutter frequency and flutter inter-phase blade angles, concluding that the variation in ply angles resulted in a variation in response, ultimately giving rise to the idea that ply angles can be optimised to define the blade flutter boundary. Testing was conducted

up to rotational frequencies of 8000 RPM for tunnel Mach numbers ranging between 0.36 to 0.75. Flutter was detected for the SR3C-X2 blade, however, the SR3C-3 showed no indication of flutter excitation.

As the NASA SR series propeller blades program began to come to an end, Oral Mehmed - the engineer who oversaw the aeroelastic testing of the SR blades - wrote a summary document [57] to capture the key findings of over 1000 hours of wind tunnel testing. He noted that classical flutter of propeller blades is understood sufficiently and propeller designs can be tuned during the design process to avoid such a phenomenon. In contrast, stall flutter was deemed much more complex due to the non-linear aerodynamic conditions due to the presence of separated flow. However, many useful insights were ascertained, particularly the reduction of the flutter response by increasing of both blade sweep and forward speed, independently of each other.

Since the late 1980s very little experimental work has been carried out on propeller stall flutter. The last significant propeller flutter investigation made publicly available was conducted by Podboy et al. [58], investigating stall flutter of a counter rotating propfan with forward swept front rotor blades. Testing was undertaken at a constant free-stream Mach number of 0.2 for both rotational frequencies were tested, 5600 RPM and 5900 RPM. Large individual blade loading occurred as a result of 30^o forward sweep, due to large torsional deformation at the blade tips. Flutter was only observed for the 5900 RPM case, however, stall flutter was not observed as LDA measurements indicated no flow separation around the blades.

2.2.5 Summary of Literature

Following an extensive survey of experimental works conducted on propeller aerodynamic and aeroelastic behaviour in both attached and stalled conditions, the following key points have been extracted to adequately summarise the current state-of-the-art.

- There is a clear lack of modern experimental data of sufficient resolution in the public domain that can be used to to validate newly developed high-fidelity prediction methods, whilst also providing further insight into the development of blade stall and aeroelastic phenomenon such as stall flutter.
- Past works on this area of research tend to be quite dated (mostly conducted prior to 1960), utilising wooden or metal-alloy propeller blades of unknown geometry and structural properties, thus rendering the data collected as not suitable for validation of newly developed numerical models.
- Despite what appears a large number of experimental investigations, there has been no clear testing strategy on how to appropriately investigate the phenomenon of stall flutter, thus resulting in largely disjointed data sets. Experimental investigations undertaken were conducted on a vast range of blade shapes, sizes, material types, operational conditions using an array of various different experimental techniques.

- Experimental methods implemented on prior investigations are applied with excellent scientific rigour. However, due to technological limitations of the time, particularly data acquisition systems and optical methods, many of the data sets are treated with reduced confidence.

- No experimental work on this area of propeller research has been conducted in decades. Likely due to the fact that large scale propeller test rigs are complex to design, manufacture, setup and operate.

To address the current gap in knowledge within this area of research. At present, there is not an experimental data set for a blade set of known geometry and well defined structural properties that has made use of modern experimental apparatus to measure blade aerodynamic performance and aeroelastic behaviour for a well defined test matrix.

2.3 Experimental State-Of-The-Art: Rotors At High Advance Ratio

Low Reynolds number rotorcraft research ($Re \leq 10^4$) has been re-invigorated following the recent success of the Martian helicopter, Ingenuity [59]. In addition, there has been a significant increase in low Reynolds number and high advance ratio rotor research due to the ongoing development of novel rotorcraft concepts including electric Vertical Take-off and Landing (eVTOL) vehicles, Micro Air Vehicles (MAVs) and high speed helicopters [60].

2.3.1 Micro Air Vehicles

The growth of low Reynolds research can be attributed largely to the development and use of both military and commercial MAVs. This growth has therefore refocused low Reynolds rotorcraft research towards topics surrounding blade aerodynamics and aeroelasticity, in an effort to improve the efficiency of thrust generation whilst providing insight into structural response. Multiple experimental investigations have been undertaken to assess the Figure of Merit (FoM) of a MAV rotors at hovering conditions [61–64], all of which show significantly degraded FoM values (FoM ≤ 0.45) when compared to that of a full scale rotor (FoM $\approx 0.5 - 0.8$).

Bohorquez et al. [61, 62] designed and developed a MAV test rig to assess both a single and coaxial rotor configuration. Single rotor tests were performed for both twisted and untwisted blades at rotational frequencies ranging between 3,000 and 4,500 RPM for a range of collective angles between $\theta = 6^\circ - 18^\circ$ in 3° increments. Coaxial testing was performed at the same rotational frequency range as the single rotor tests with combinations of upper and lower blade collective angles of $\theta = 15^\circ$ and 18°. Results from the twisted single rotor tests displayed a maximum FoM of 0.42 for a rotational frequency of 4,500 RPM at $\theta = 15^\circ$ with a corresponding tip chord Reynolds number of 25,000. Poor performance was attributed to an increased profile drag, blade geometry, surface roughness, viscous drag effects and elastic deformation of the blades. Furthermore, it was highlighted that reduction of the blade induced power at low Reynolds conditions cannot be alleviated to the same extent as a full scale rotor by twisting the rotor blade.

Hein et al. [63] investigated a two bladed MAV rotor for total combination of six aerofoil shapes with varying camber and leading edge profiles at a tip chord Reynolds number of 40,900. Measurements of rotor thrust and torque were obtained to assess rotor performance in hover whilst flow visualisation was used to assess the inflow profile. Results indicated that the maximum FoM = 0.526 was obtained for a camber of 6.75%, this corresponds to a 57% increase when compared to an equivalent flat plate with a FoM = 0.335. Moreover, a sharp leading edge flat plate was shown to improve FoM by up to 19% when compared to a blunt leading edge flat plate. This was attributed to the significant reduction in the blade thickness

ratio and slight geometric introduction of a camber. Furthermore, flow visualisation highlighted that large vortex sheets were shed from the rotor blades, forming turbulent regions towards the blade root, thus tampering with the rotor inflow, ultimately reducing performance. A similar study was performed by Ramasamy et al. [64] to assess MAV hovering performance for various blade shapes, twist distributions, aerodynamic profiles and leading edge shapes operating at a tip Reynolds number of 35,000. Measurements of rotor thrust and torque were obtained via a load cell to characterise aerodynamic performance demonstrated that blades with sharper trailing and leading edges demonstrated a performance improvement due to a reduction in profile drag and wake area. Moreover, Particle Image Velocimetry (PIV) was implemented to assess the flow structures whilst also computing the circulation to provide an estimate of sectional lift and drag contributions. Findings also highlighted that length of time for the tip vortex roll up increased when compared to that of a standard rotor thus increasing the influence of the tip vortex on aerodynamic performance.

2.3.2 Reverse Flow

Wild et al. [65–67] continued to progress work on blade leading and trailing edge geometries by comparing both blunt and sharp aerofoil shapes. Blade load measurements were obtained using a six axis force balance, whilst similar to Ramasamy et al. [64], measurements of flow structures were obtained using PIV, assessing velocity and vorticity to assess prominent wake features. A single bladed rotor investigation conducted by Wild et al. [65] at a hovering tip Reynolds number of 26,000 was undertaken to compare an elliptical blunt edge trailing edge with that of a sharp edge for a NACA 0012 aerofoil section. Measurements showed that the blunt trailing edge in an attached flow regime reduced the magnitude of blade thrust and no effect on thrust occurred when operating in separated conditions. Furthermore, the blunt edge trailing edge showed a reduction in blade pitching moments by up to 29% when compared to the sharp edge equivalent, this is explained by the delay in flow separation in regions of reverse flow.

Prior investigations by Wild et al. [66, 67] made use of two component (2-C) PIV to assess the development of flow structures within the reverse flow region when comparing a blunt and sharp trailing edges for a four bladed NACA 0012 constant chord rotor. Four individual vortex structures were observed: tip vortex (TV), reverse flow entrance vortex (RFEV), blunt trailing edge vortex street (BTEVS) and reverse flow dynamic stall vortex (RFDSV). The RFDSV was shown to be critical in the development of unsteady loading on the blade and also highly dependant to the tip vortex at the aerodynamic leading edge. Moreover, the blunt trailing edge demonstrated that the RFDSV reduces the wake area as a result of the vortical structure moving closer to the blade surface, as shown in Figure 2.12.

Furthermore, a series of works by Lind et al. [68–73] investigated the reverse flow region for both static and rotating aerofoil sections for Reynolds number ranges between $10^5 - 10^6$. Areas of study included blade trailing edge geometries, thicker aerofoil sections, flow field char-

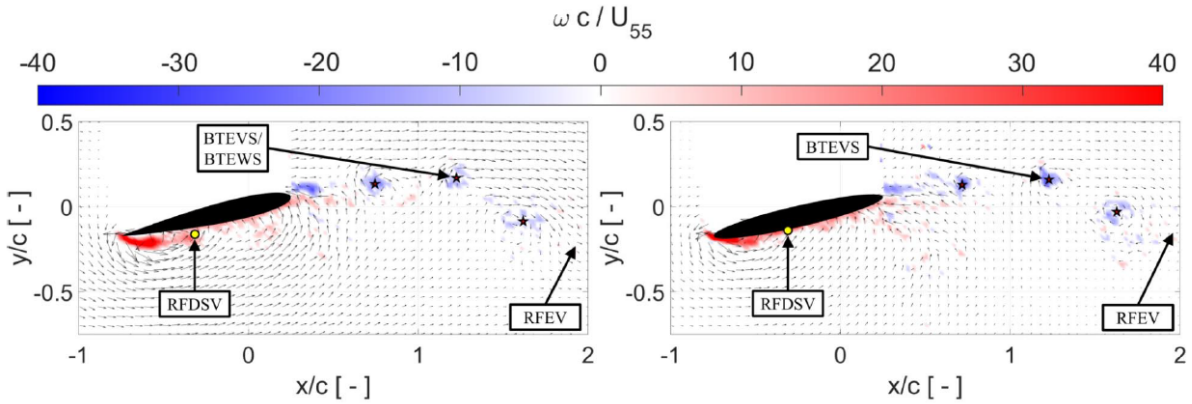

Figure 2.12: Identification of key vortex structures highlighted through averaged vorticity fields obtained via PIV for sharp edge NACA 0012 (left) and ecliptical blunt edge (right) at $\mu = 1.00, \theta = 13^{\circ}, \psi = 270^{\circ}$. Figure taken directly from from Wild et al. [67]

acterisation using 2D PIV, influence of shaft angle on the RFDSV and unsteady surface pressure measurements. Lind et al. [68] investigated the effect of both sharp and blunt trailing edges in reverse flow at static angles of attack for three different aerofoil sections at a chord based Reynolds number of 110,000, for a corresponding chord length of 0.071 m. A NACA 0012 section was used to investigate sharp trailing edge behaviour whilst an elliptical and Sikorsky DBLN-526 section were used to investigate blunt trailing edge geometries. Unsteady and time-averaged load measurements were obtained. Moreover, 2-C PIV was implemented to assess prominent flow features such as separation points and wake features. Drag measurements of the NACA 0012 in a reverse flow configuration were recorded to be greater than twice that of non-reversed conditions for angle of attack values less than 10°. Furthermore, drag results demonstrated a decrease for blunt aerofoil sections in reverse flow between $5 - 16^{\circ}$. However, lift and pitching moments were shown to increase, thus no blunt trailing edge showed better performance across lift, drag and pitching moment.

Making use of the three aerofoil sections tested previously by Lind et al. [68], a further investigation was conducted by Lind et al. [69] using 2-C PIV and force measurements to assess the vortex shedding behaviour of sharp and blunt trailing edge aerofoils at chord based Reynolds numbers of $45,000/110,000/165,000$. Three flow regimes were identified when the aerofoils were in a reverse flow configuration: slender body vortex shedding, turbulent wake and deep stall vortex shedding. The slender body vortex shedding was shown to manifest as a von Karman vortex sheet in the aerofoil wake, with a typical thickness of 12% of the chord, a consequence of separation at the rear portion of the aerofoil towards the blunt trail edge, prior to which the flow remained attached. Within the turbulent wake regime, separation is shown to occur abruptly after the aerodynamic leading edge. Furthermore, the wake region was demonstrated to be largely aperiodic and is significantly dependent on the geometric trailing edge shape, where a blunt trailing edge results in a smaller wake than a sharp trailing edge in the turbulent wake

regime when compared to the slender body vortex shedding regime, hence the reduction in measured drag. In the deep stall regime, separation was observed to occur at similar locations as the turbulent wake regime. Large coherent vortical structures of similar magnitude to the aerofoil chord were shown to form at the trailing edge and shed into the wake region.

Developing earlier works [68, 69], Lind et al. [70] conducted a series of wind tunnel test campaigns at the United States Naval Acadamey (USNA) 1.07 m x 1.52m low-speed closed loop wind tunnel and the 0.51 m x 0.71 m low-speed open loop wind tunnel at the University of Maryland to investigate the Reynolds effects in both reverse and non-reversed flow configurations representative of a full scale helicopter rotor at an advance ratio of 0.77. Four aerofoil sections, two sharp edge trailing edge (NACA 0012 and NACA 0024) and two blunt trailing edge (24% t/c ellipse and a cambered ellipse 26% t/c and 4% camber) were tested at chord based Reynolds numbers of $330,000/660,000/1,000,000$. Measurements of aerofoil loads were obtained. In addition, surface oil flow visualisation was performed on both the pressure and suction sides of the aerofoils to identify prominent regions in the flow such as separation bubbles, recirculation regions plus regions of attached and separated flow. Findings indicate that for the NACA 0012 in reverse flow conditions their is no dependency on Reynolds number. However, the NACA 0024 showed a dependency up until a angle of attack of 13°, angles exceeding this were shown to be insensitive due to the presence of significant or complete flow separation. Moreover, blunt trailing edge aerofoil sections demonstrated a strong dependency on Reynolds number, particularly at low angles of attack, which is likely induced by the strong variation in the movement of the separation point.

Lind et al. [71] further develop prior work [70] by obtaining time resolved pressure measurements along the upper and lower aerofoil surfaces. Lift and drag load components were calculated by implementing a panel based integration scheme. It was noted that due to low spatial resolution of pressure transducer locations, prominent features such as pressure and suction peaks were not adequately captured towards the leading edge. Furthermore, an estimation of pressure at the geometric trailing edge was obtained via a linear extrapolation. Nonetheless, pressure based load measurements were shown to correlate very well with that of load measurements obtained via a force balance both in forward and reverse flow regimes.

Lind et al. [72] expanded their previous work by commissioning a custom dynamic stall rig in the 0.51 m x 0.71 m low-speed open loop wind tunnel at the University of Maryland. The development of such a rig allowed for the study of a NACA 0012 aerofoil to be tested in both forward and reverse flow regimes whilst undergoing a sinusoidal pitching motion. Three reverse flow mean pitch angles of $5°, 10°$ and $15°$ were tested for two pitch amplitudes of $5°$ and $10°$. The oscillation frequency was varied to correspond to five reduced frequencies ranging from $k = 0.1 - 0.511$ whilst free stream velocity was altered to test three chord based Reynolds numbers, $165,000/330,000/500,000$. Pressure based loads were obtained using the panel based integration scheme developed previously [71]. Furthermore, to assess the viability of the method

in dynamic stall conditions, a qualitative correlation was performed using the well establish 2D aerofoil section tests conducted by McAlister et al. [74], highlighting a successful implementation of the method. Moreover, 2-C PIV was performed to determine prominent flow features. Key features such as the Primary Dynamic Stall Vortex (PDSV), Trailing edge Vortex (TEV) and Secondary Dynamic Stall Vortex (SDSV) were clearly identified when analysing both velocity and vorticity fields. In addition, pressure transducer measurements were shown to adequately capture chord wise locations at which these flow features exist, correlating very well with the optical measurement.

Following the extensive 2D investigations by Lind et al. [68–72], an experimental investigation to assess the flowfield of a 1.7m diameter slowed rotor using 2-C PIV was performed in the Glenn L. Martin wind tunnel at the University of Maryland focusing on the azimuthal angle of 270° at the 40% radial location [73]. The rotor was tested at four advance ratios ($\mu = 0.6, 0.7, 0.8, 0.9$) all of which had a constant rotational frequency of 900 RPM. Each test case maintained a blade pitch collective angle of 10° whilst three shaft tilt angles (−4°,0°,4°) were investigated. Results indicated that a positive shaft tilt angle resulted in an a stronger RFDSV and as a consequence a larger angle of attack distribution in region of reverse flow.

Datta et al. [75] tested a full scale UH-60A rotor at slowed RPM (40% and 60% nominal) conditions to investigate blade aerodynamic and aeroelastic performance at large advance ratios. For slowed conditions where $\mu \geq 0.8$, dynamic loads when compared to nominal rotor loads at $0.3 \leq \mu \leq 0.4$ were demonstrated to range significantly from equivalent to extremely larger magnitudes. This observation within the data was attributed to significant differences in loading at outboard and inboard blade sections on the advancing side of the rotor disc, as a consequence of the required rotor trim state that is imposed by large regions of reverse flow on the retreating side of the rotor disc. Furthermore, measurements of unsteady pressure were used to identify the presence of the RFDSV on the retreating side of the disc, highlighting the shift of the centre of pressure towards the geometric quarter chord, thus reducing the peak blade torsional loading. This observation was also observed by Lind et al. [73]. At present, the dataset collected by Datta et al. [75] is by far the most comprehensive aerodynamic and aeroelastic dataset for a rotor at reverse flow conditions. Despite, this vast dataset, limited investigations have been undertaken in experimental rotor aeroelasticity at reverse flow conditions.

2.3.3 Summary of Literature

Following a thorough review of experimental works conducted on rotor aerodynamic and aeroelastic behaviour whilst operating at high advance ratios at both low and high Reynolds conditions, the following statements have been highlighted to condense the current state-of-the-art appropriately.

- Several investigations have been undertaken to assess rotor aerodynamic performance of

MAVs in hovering conditions through measurements of global blade loads and PIV. Poor performance when compared to large scale rotors was shown to be attributed to an increased blade profile drag, non-optimised blade geometries, increased surface roughness, prominent viscous drag effects and elastic deformation of the blades. As a result of the reduced rotor scale, there is an inability to perform aeroelastic measurements without significantly disrupting the aerodynamic behaviour of the blades. Furthermore, there is a severe lack of data for MAVs operating in the forward flight regime.

- Reverse flow investigations have been performed at both low and high Reynolds conditions, ranging from small scale rotors to full scale slowed RPM helicopters. Prominent flow features such as the RFDSV have been clearly identified for both blunt and sharp trailing edge blades using an array of experimental methods such as unsteady pressure measurements and PIV, thus leading to a very good understanding of the aerodynamic environment. Despite this, there is still a clear lack of aeroelastic experimental data sets that can be used to provide detailed insight into blade structural response when operating in the reverse flow region.

There is a clear need to address the current gap of an experimental dataset of a rotor operating in reverse flow at low Reynolds conditions that provides both aerodynamic and aeroelastic measurements.

2.4 Chapter Summary

Within this chapter a literature survey detailing experimental investigations of blade stall in both axial propeller mode and edgewise rotor mode was presented. A description of stall and stall onset are provided in Section 2.1 and the aerodynamic characteristics as a consequence of stall were outlined for both two dimensional and three dimensional flows. Section 2.2 provides a review of propeller stall and stall flutter. Despite a significant amount of prior testing, much of this testing was disjointed, following no clear testing strategy and was conducted prior to 1960, making use of wooden or metal-alloy blades with undefined geometric and structural properties. Furthermore, many of the test campaigns did not adequately capture data of sufficient resolution for modern high-fidelity numerical model validation. Thus, there is a need for a state-of-the-art propeller dataset that utilises a blade set with clearly defined geometric and structural properties. Similarly, Section 2.3 presents a review of experimental testing of rotors in edgewise conditions at low Reynolds numbers and with significant reverse flow regions. Generally, at the smaller scale, aerodynamic phenomena have been well documented using optical methods such as PIV. However, there is a clear lack of experimental data that can provide detailed insight into blade structural response at stalled and reverse flow conditions.

Chapter 3

Experimental Test Rigs and Instrumentation

Within this chapter a description of the test rigs, instrumentation and measurement techniques utilised during two individual test campaigns to investigate propeller stall and rotor reverse flow are described. The United Kingdom National Rotor Rig (UKNRR) was utilised to investigate a large scale fixed pitch propeller configuration in stalled conditions due to its large available motor power capability. Section 3.1 details the experimental setup of the UKNRR and supporting measurement systems within the De Havilland low speed wind tunnel situated at the University of Glasgow (UofG). To characterise propeller strain behaviour, which allows for the detection of operational conditions at which stall onset and fully developed stall are observed, the experimental measurement principles and apparatus that allow for testing across a range of range of advance ratios (J) and blade pitch angles ($\beta_{0.75R}$) are outlined. A secondary investigation was performed to measure both the aerodynamic performance and blade strain distribution of a single bladed fixed collective rotor blade in both hovering and edgewise flight conditions. Testing was performed within the University of Maryland (UMD) free surface water towing tank facility allowing for testing at low Reynolds and high advance ratio (μ) conditions. A description of the experimental setup is provided in Section 3.2.

3.1 Propeller Stall

3.1.1 United Kingdom National Rotor Rig

The United Kingdom National Rotor Rig (UKNRR) is a large-scale direct drive propeller test rig that is permanently located at the UofG De Havilland wind tunnel. The UKNRR was initially commissioned and designed as part of a UK wide research initiative led by the Aircraft Research Association (ARA). UK academic institutions involved throughout the project included: University of Glasgow, University of Manchester, University of Bristol, University of Liverpool,

University of Leicester, University of Bath and Cranfield University. The scope of the rig was to provide the United Kingdom with a large-scale tiltrotor test rig, allowing for horizontal to vertical transition of the rotor plane during operation. However, due to unforeseen technical complexities and funding limitations, the project was scrapped in 2016 and the rig was placed in storage before being fully commissioned. UofG acquired the UKNNR in February 2020, as part of the Engineering and Physical Sciences Research Council (EPSRC) funded Methods and Experiments for NOvel Rotorcraft (MENtOR) project, undertaken within the UK Vertical Lift Network (UKVLN), with the intention to utilise the large publicly backed investment made in both the UKNRR and supporting systems plus instrumentation. Therefore, the decision was made to convert the UKNRR to a conventional propeller/rotor rig by removing the ability to transition through the conversion corridor. Significant time and investment from UofG was undertaken to achieve this goal. As a result, UofG houses the largest operational propeller/rotor test rig within in the UK academic community.

3.1.1.1 Description of UKNRR

The UKNRR was originally designed to allow for testing of both helicopter and tiltrotor configurations. Therefore a gearbox was required to allow for transition from propeller mode to rotor mode. The propeller shaft was powered by an electric motor which could provide a maximum power of 77 kW, allowing for a maximum rotational frequency of 3000 RPM for propeller blades of diameter 1.4m or for a larger blade diameter of 1.8m, a maximum rotational frequency of 2300 RPM could be achieved. However, due to vibratory issues during the operation of the gearbox, operation of the UKNRR was severely limited.

Nonetheless, due to the requirement at The University of Glasgow to possess the ability to test propeller and rotor blades in deeply stalled conditions, imposing the need for a larger maximum available power, the gearbox was removed, converting the UKNRR into a direct drive system, shown in Figure 3.1. The maximum operating limits of the UKNRR post conversion to a direct drive propeller are shown in Table 3.1. Further details of the development of the UKNRR at The University of Glasgow can be found in Zagaglia et al. [76].

Table 3.1: Maximum allowable operating conditions of UKNRR.

Maximum Operational Limit	Quantity	Units
Thrust	3400	N
In-Plane Forces	550	N
Torque	350	Nm
In-Plane Moments	250	Nm
Available Power	125	kW
Rotational Frequency	3000	RPM
Pitch Angle Range	[-5,40]	$^\circ$

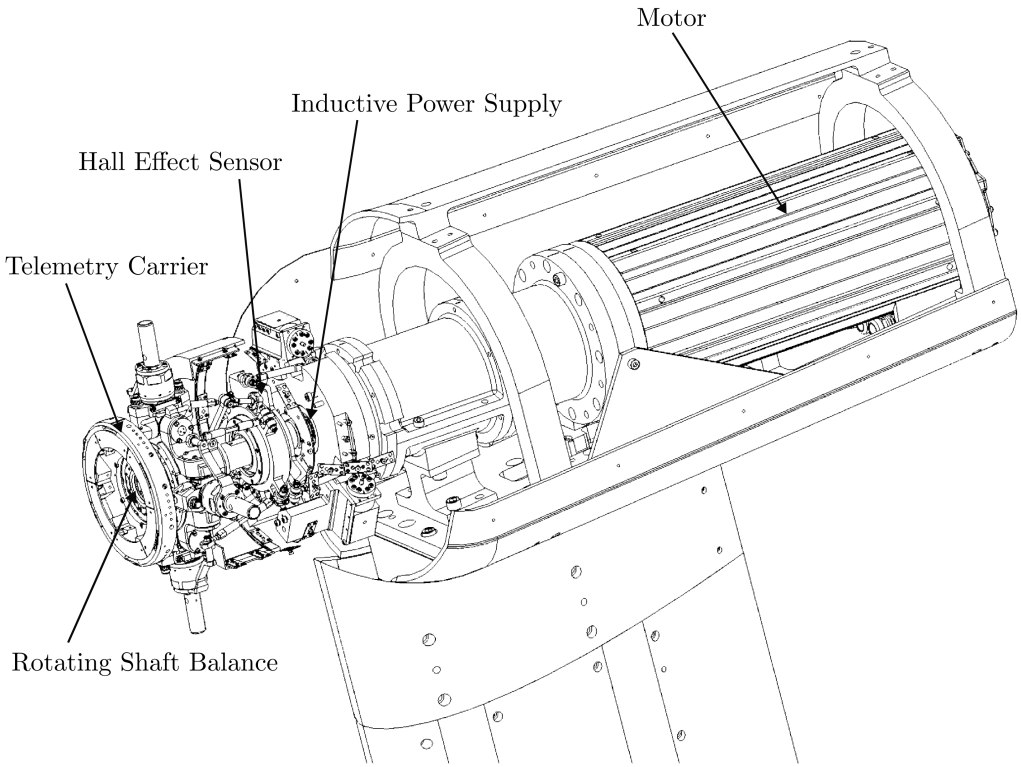

(a) Schematic of the UKNRR highlighting main components and instrumentation.

(b) UKNRR installed in the De Havilland wind tunnel.

Figure 3.1: United Kingdom National Rotor Rig (UKNRR) after conversion to direct drive configuration at the University of Glasgow.

3.1.1.2 Integration of UKNRR into De Havilland Wind Tunnel

A schematic of the rotor rig installed inside the test section (2.74m width x 2.1m height x 5.64m length) of the UofG De Havilland wind tunnel is presented in Figure 3.2. Due to the presence of the turntable, the rig was installed so that the propeller plane would lie upstream of the centre of the test section, approximately 1 m downstream from the end of the contraction.

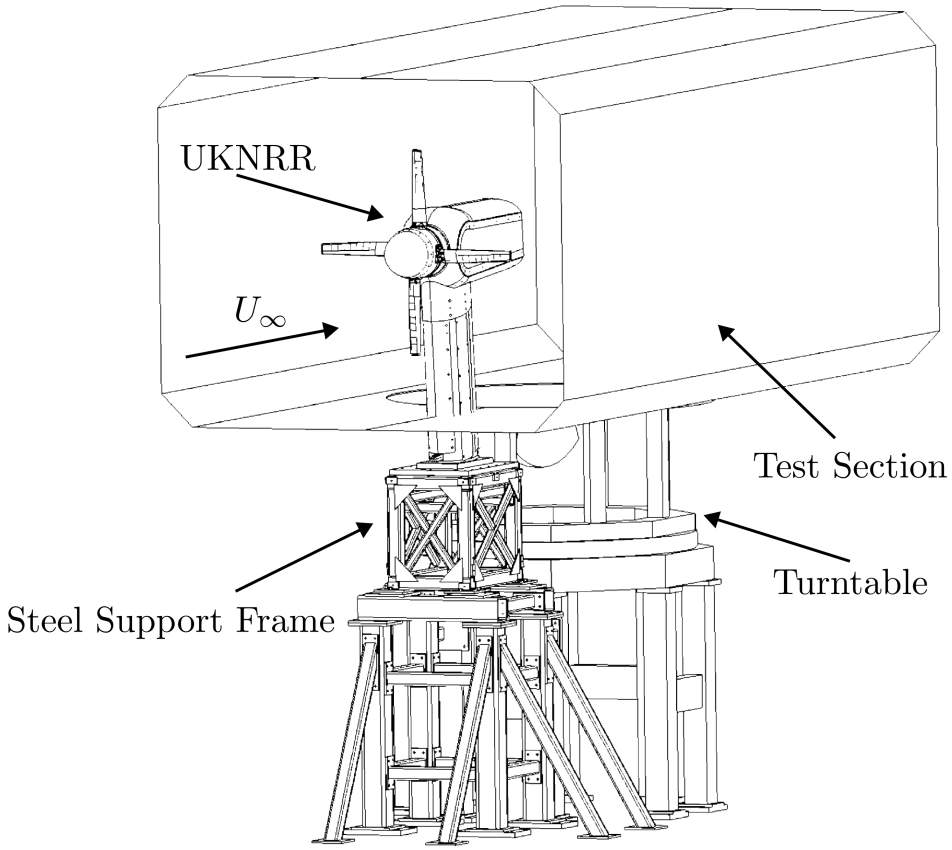

Figure 3.2: Schematic highlighting the integration of the UKNRR when installed within the UofG De Havilland tunnel.

The rig sits on top of a steel framework which is bolted to the ground and connected to the turntable behind. An aluminium wing section provides a streamlined support to the motor, that spins the rotor through a direct drivetrain. The centre line of the motor-drivetrain-shaft-hub assembly is positioned in the centre of the wind tunnel working section and the rig is free from any contact with the tunnel floor. Due to the relatively slender nature of the upper part of the rotor rig and the presence of very heavy components at the top of the supporting structure, a modal test campaign was carried out by Tatar et al. [77] to assess the modal characteristics and the resonances that the rig may have to cross during the spin-up and spin-down procedures. Despite a successful characterisation of rig mode shapes, rig modal testing did not include the installation of blades and the telemetry carrier. Therefore, a small deviation in identified mode frequencies was expected during rig operation.

3.1.1.3 Rotor Hub Modifications

Flap and lag stops were designed, manufactured and installed onto the UKNRR rotor hub. Unlike a helicopter rotor, where flap and lag angles change as a function of azimuthal position, the addition of flap and lag stops prevents the movement of the blades in the flap-wise and lag-wise directions, therefore altering the rotor hub configuration from a fully articulated rotor to a fixed pitch propeller as shown in Figure 3.3.

Flap stops were manufactured from 1.2316 tool steel. The material of choice was selected to withstand the expected large flap-wise loading at positively aerodynamically loaded blade configurations and large rotational speeds, typically between 1800 to 3000 RPM (30 to 50 Hz). Lag stops were manufactured from Nylon 6 as steel lag stops were not required. This is a result of the magnitude of forces in the lag direction being significantly less than that of flap-wise loading, as lag-wise movement is not the primary direction of blade loading. Both the steel and nylon 6 flap stops were manufactured to strict tolerances of ± 0.05 mm, to ensure a secure fit when installed onto the rotor hub. Despite the change in mass distribution of the rig when flap and lag stops are installed, the C.G location remains unaltered as the flap and lag stops are of a consistent weight for each pitch shaft. The mass of each stop component are shown in Table 3.2. Once all flap and lag stops were installed onto the rotor hub, the pitch mechanism becomes fully restricted. Testing was carried out to ensure all stops work as intended, resulting in no failures of any critical components on the rotor rig, particularly the rotor hub.

Table 3.2: Masses of stop components.

Component	Material	Mass (g)
Front Flap Stop	1.2316 Tool Steel	89.99
Rear Flap Stop	1.2316 Tool Steel	45.19
Lag Stop	Nylon 6	3.47

To accurately set the blade pitch angle whilst in propeller mode, 3D printed collar structures fore and aft of the swashplate were installed to restrict swashplate movement along the main shaft. Due to the non-linear kinematics of the swashplate, collar sets were manufactured to fix the swashplate in a precise position along the shaft (to set the blade collective pitch) and parallel to the rotor plane (to set the longitudinal and lateral cyclic angles to zero). The available blade pitch range at which the blades can be set ranges from -5° to 40°. Measurements of angles corresponding to each collar set were checked using an inclinometer, to a precision of $\pm\ 0.1^{o}$. Locations of the stops and collars positions on the rotor hub are shown in Figure 3.3.

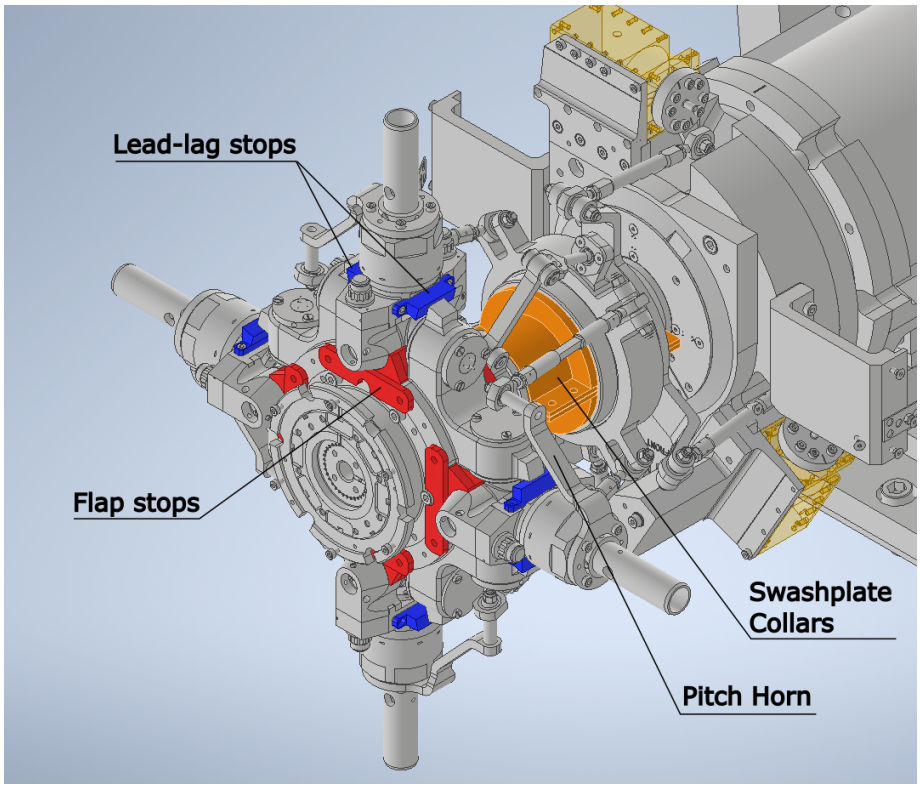

Figure 3.3: Rotor hub with flap, lead-lag stops and swashplate collars installed.

3.1.2 MENtOR Blade Set

Four bespoke composite tiltrotor blades were designed at the UofG CFD laboratory, within the in the framework of the MENtOR project, to investigate blade performance at stalled conditions [78]. The blades were instrumented with both fully bridged axial and shear strain gauges to obtain measurements of local bending and torsion. The blade design was adapted from an earlier blade set developed by the University of Manchester (UoM) in order to satisfy the new rig limitations following rig modifications to propeller mode.

3.1.2.1 Geometry and Aerofoil Profiles

Tiltrotor blades are designed to operate both as propellers and also as rotors, therefore they require a moderate twist to provide meaningful production of thrust throughout their intended operating envelope. The UofG MENtOR blades incorporate an overall non-linear twist of 19.3° and a root chord of 84.2 mm which linearly tapers to 60 mm at the tip, the distribution of twist and chord can be appreciated in Figure 3.4.

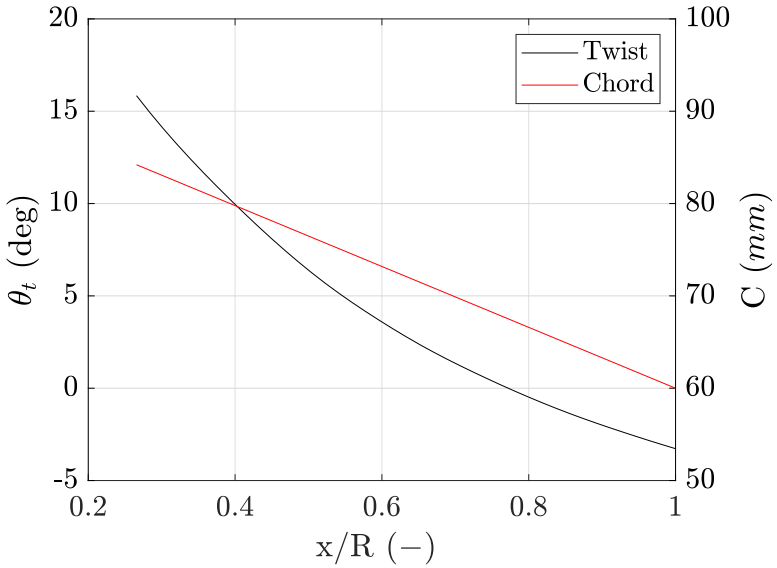

Figure 3.4: MENtOR blade twist (θ_t) and chord (C) distribution as a function of radial position from the centre of rotation (x/R).

Moreover, the rotor disc is 1.25m in diameter, corresponding to a blade span of 0.625m. Blades were designed to operate at a tip Mach-scaled condition of 0.6 at a rotational frequency of 3000 RPM. To impose this design requirement, the following blade sections were selected at their respective radial stations to ensure suitable blade performance: NACA 64_128 at the root ($x/R = 0.26$), Vertol V43015_2.48 ($x/R = 0.6$) and Vertol V23010_1.58 at the tip ($x/R = 1$). Blade aerofoil sections are displayed in Figure 3.5, highlighting the blade thickness variation from root to the tip. A summary of the maximum blade design parameters are displayed in Table 3.3.

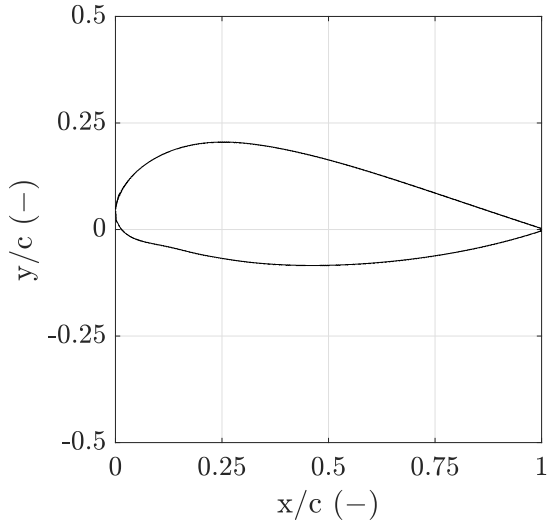

(a) NACA 64-128

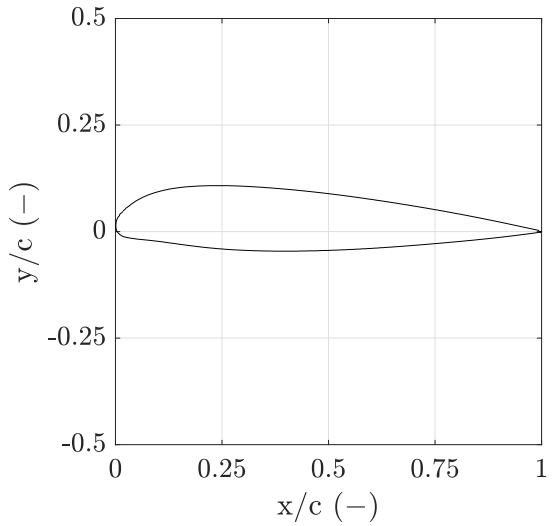

(b) Vertol V43015-2.48

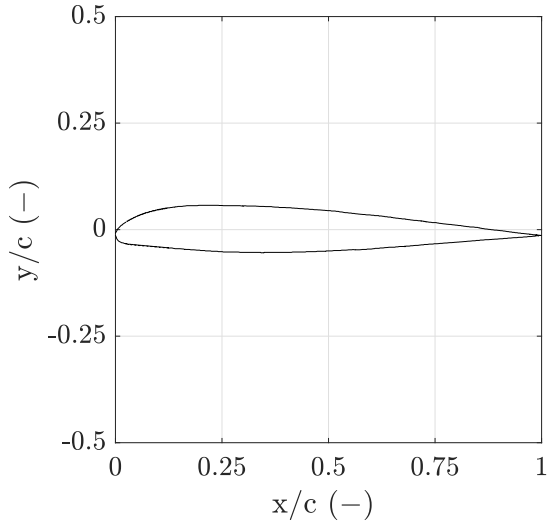

(c) Vertol V23010-1.58

Figure 3.5: MENtOR blade aerofoil section profiles used at corresponding radial locations: (a) Root (b) Midspan (c) Tip.

Table 3.3: Maximum design conditions of the UofG MENtOR blade set.

Parameter	Symbol	Quantity	Units
Number of Blades	N_b	4	-
Freestream Velocity	U_∞	38	m/s
Propeller Rotational Frequency	Ω	3000	RPM
Tip Mach Number	M_{tip}	0.6	-
Tip Reynolds Number	Re_{tip}	0.864×10^6	-
Tip Chord	C_{tip}	60	mm
Radius	R	625	mm
Trailing Edge Thickness	t_{TE}	0.47	mm
Blade Pitch	$\beta_{0.75R}$	36	$^\circ$

3.1.2.2 Blade Manufacture and Structural Properties

The MENtOR blade set is comprised of 4 carbon-fibre composite blades that were designed and manufactured to provide a modern blade design for experimental testing from which the blade geometry and structural properties are well defined. Multiple components are required to manufacture a blade design that is suitable for the aeroelastic testing required, each component material and properties are presented in Table 3.4.

3.1.2.2.1 Blade Root

The blade root serves two critical functions. First, the attachment of the blades to the pitch shaft on the rotor hub. This requires a very high tolerance cylindrical extrusion to be placed within the root fitting to ensure that the blade rigid deflection is limited when aerodynamically loaded. Second, the carbon-fibre composite aerofoil skin is attached to the blade root fitting by means of an adhesive film to ensure sufficient strength and geometric properties of the blade. To ensure tolerance, weight and strength requirements, the blade root was manufactured from an aerospace grade aluminium alloy (AA7075-T651) using high precision CNC machining.

3.1.2.2.2 Aerofoil Skin and Tip Cap

The aerofoil skin and tip cap were manufactured from a carbon-fibre composite material (TC250-AS4C-3K), using four layers of plain weave carbon epoxy prepreg resin with individual ply orientations varied as follows: (0/90) / (+45/-45) / (+45/-45) / (0/90), that were then vacuum bagged and cured in an autoclave to create the required laminate. A four layer composite design was implemented to ensure a uniform 1mm skin thickness across the entire span of the blade whilst also sufficiently increasing the stiffness of the aerofoil skin without compromising the weight. Moreover, to allow for mass balancing if required, the blade tip cap design incorporates mass balancing holes that can be used to apply additional blade mass should there be a large discrepancy during manufacture.

3.1.2.2.3 D-Spar and Core

The blade spar is responsible for sustaining the majority of the blade load. Therefore, similar to the aerofoil skin, the blade spar was manufactured from a carbon-fibre composite material (TC250-AS4C-3K), using four layers of plain weave carbon epoxy prepreg resin with individual ply orientations varied as follows: (0/90) / (0/90) / (0/90) / (0/90). The spar was manufactured as a D shaped spar to allow for an internal ROHACELL® 71HERO foam core, ensuring sufficient strength whilst minimising component weight. Incorporation of a foam core allows for the carbon-fibre aerofoil skin and metal blade root fitting to be attached to the blade spar using Redux 312/5 adhesive film.

3.1.2.2.4 Collar Ring and Shear Pin

The blades are required to be easily removable from the rotor hub without compromising the reliability of the blade mounting connection. Therefore, a maraging steel shear pin is used to secure the blade root fitting to the rotor hub pitch shaft. To ensure this connection is not a potential point of failure, maraging steel collar rings were manufactured and installed within the blade root fitting and shear pin interface, to increase the load bearing strength. Once the shear pin is in place, securing the blade to the pitch shaft in the correct location, a grub screw is used to prevent the pin from sliding.

Table 3.4: Material properties of each of the MENtOR blade components.*

Component	Material	Orientation	$\rho[kg/m^3]$	$E_i[GPa]$	$E_t[GPa]$	$G_{it}[GPa]$	$\nu[-]$	$\sigma_F[MPa]$		$\sigma_T[MPa]$		$\tau_{it}[MPa]$
								Tensile	Compression	Tensile	Compression	
Aerofoil Skin	TC250-AS4C-3K	[(0/90) / (+45/-45) / (+45/-45) / (0/90)]	1.57	63.64	58.41	3.93	0.06	967.4	752.2	766.5	739.8	105
D-Spar Skin		[(0/90) / (0/90) / (0/90)/ (0/90)]	-	-	-	-	-	-	-	-	-	-
D-Spar Core	ROHACELL® 71HERO	-	0.075	0.123	-	-	0.4	-	-	-	-	-
Root Fitting	AA7075-T651	-	2.81	71.7	-	-	0.33	435	-	-	-	-
Collar Ring Shear Pin	Maraging Steel	-	8	190	-	-	0.3	1860	-	-	-	-
Pitch Shaft Adhesive	Redux 312/5	-	1.2	4.5	-	-	0.7	-	-	-	-	38

* ρ - Density; E_i - Fibre direction modulus; E_t - Transverse direction modulus; G_{it} - Shear modulus; ν - Poisson's ratio; σ_F - Axial strength in fibre direction; σ_T - Axial strength in transverse direction and τ_{it} - Shear strength

3.1.2.3 Mass and Centre of Gravity Locations

After the blades were manufactured, assembled and wired, a quality check was carried out to assess their mass properties and how similar the four blades were with respect to one another. The individual blades masses are reported in Table 3.5, showing a mass deviation of of 1 g (0.3%). The position of the centre of mass was found to be 123mm outboard and 13 mm towards the trailing edge with respect to the centre-axis of the collar rings. as represented in Figure 3.6. Measurements of C.G locations were taken 3 times per blade and found to be very consistent amongst each of the four blades.

Table 3.5: Measurements of individual MENtOR blade masses with electrical tag strips, connectors and strain gauges installed as per testing conditions.

Blade	Mass (g)
1	324
2	325
3	324
4	326

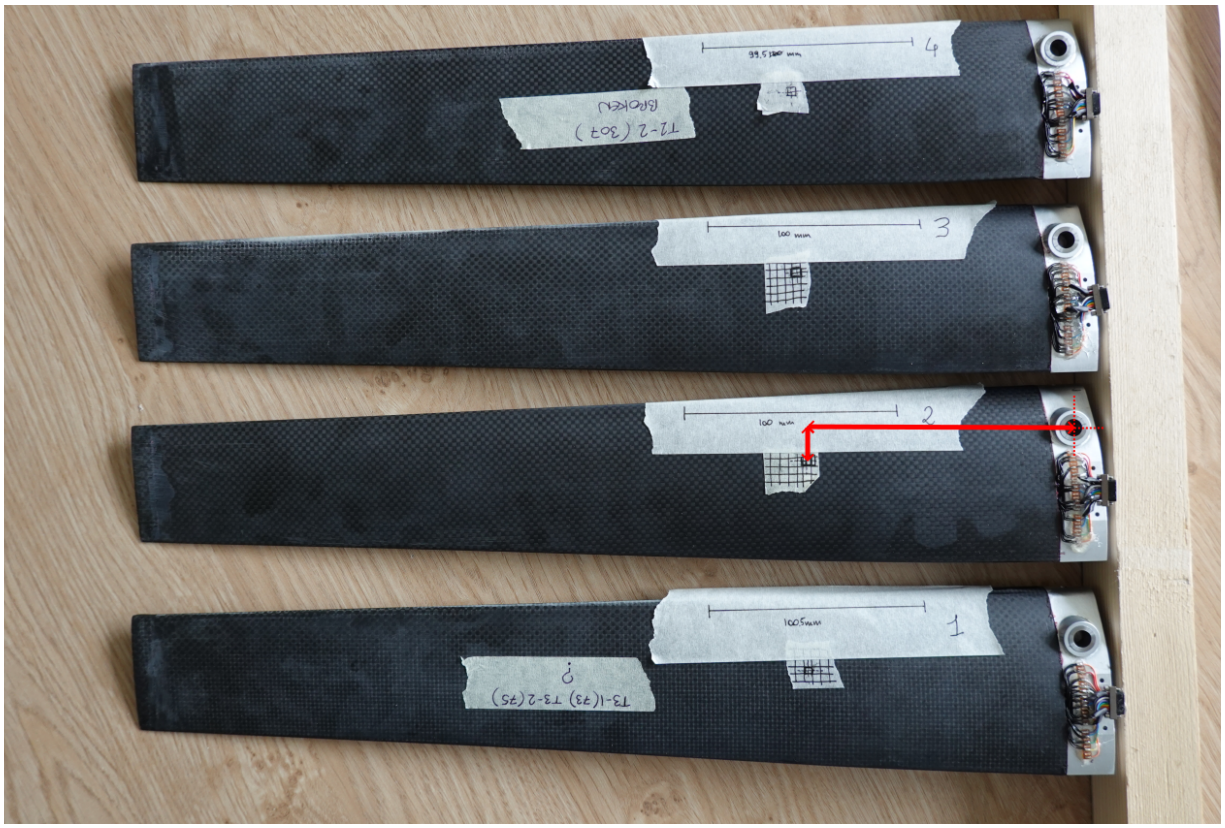

Figure 3.6: Measured centre of gravity locations of MENtOR blade set.

3.1.2.4 Experimental Modal Analysis

Experimental Modal Analysis (EMA) was performed on the MENtOR composite blade set by the University of Bristol to identify the rigid and elastic blade mode shapes and their corresponding modal parameters [79], including natural frequency (f_n) and damping ratio (ζ). Free-free testing (shown in Figure 3.7) was performed for a frequency range of 0-1500 Hz with the blade suspended so that primary vibrations were in the perpendicular plane to the blade chord. A single 0.8g highly sensitive accelerometer was placed at the trailing edge of the the blade tip and a modal impact hammer was used to provide an excitation at 10 locations to allow for sufficient spatial resolution. Accelerometer Frequency Response Functions (FRF) were determined using the frequency domain PolyMAX method [80]. Tests were conducted on each blade six times to ensure a meaningful degree of repeatability. Experimental results of blade modal tests identifying the first 5 elastic modes are presented in Table 3.6.

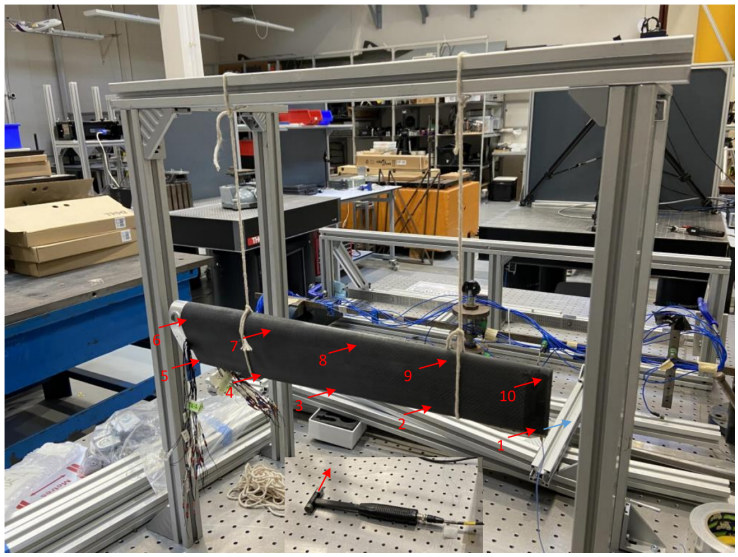

Figure 3.7: Test rig at University of Bristol used to perform Experimental Modal Analysis (EMA) of MENtOR blade set. Figure taken directly from Wu et al. [79].

Table 3.6: Summary of individual MENtOR blade modal parameters including natural frequency (f_n) and damping ratio (ζ) as per the free-free boundary condition results of University of Bristol blade modal testing [79].

	Blade Number	1		2		3		4	
Mode Shape	Mode Number	f_n (Hz)	ζ (-)	f_n (Hz)	ζ (-)	f_n (Hz)	ζ (-)	f_n (Hz)	ζ (-)
Bending	1	261.3	0.0030	258.3	0.0049	258.2	0.0033	257.7	0.052
Bending	2	743.2	0.0038	735.6	0.0045	736.0	0.0031	733.6	0.0038
Torsion	3	933.4	0.0051	934.4	0.0057	916.3	0.0055	931.2	0.0066
Bending-Torsion	4	1295.7	0.0038	1301.9	0.0039	1288.8	0.0041	1270.0	0.0042
Bending	5	1412.4	0.0047	1401.9	0.0051	1408.0	0.0052	1397.1	0.0053

3.1.2.5 Numerical Modal Analysis

To provide insight into the blade aeroelastic response, numerical finite element calculations were performed by McKechnie et al. [81] at the UofG CFD laboratory using MSC-NASTRAN to identify prominent mode shapes and corresponding eigenfrequencies. The blade structural model consists of six parts (root fitting, skin, D-spar, spar filler, rear filler and tip cap), all of which were individually meshed, with the full mesh consisting of 1.9M tetrahedral elements. The non-matching mesh interfaces between parts were bonded using the MSC-NASTRAN glue feature. This structural model has been validated in the past against experimental modal test results in free-free conditions [81]. To best replicate the physical constraints of the blades mounted on the hub in the current configuration, a fixed root boundary condition was applied to the first 2 mm in the span-wise direction of the blade. An implicit, non-linear, MSC-NASTRAN SOL400 method was used to conduct the eigen-analysis and the results are shown in Table 3.7 (Summary of mode shapes and their non-rotating frequencies), Figure 3.8 (Mode shapes) and Figure 3.9 (Campbell diagram).

The first three modes, with eigenfrequencies starting at 113 Hz for the non-rotating case, are mainly flap bending modes, whereas the fourth is a combination of torsion and flap bending. As shown in the Campbell diagram of Figure 3.9, all modes undergo some level of centrifugal stiffening as the propeller rotational frequency increases. However, this effect is not prominent due to the large intrinsic rigidity of scaled down blades, such as the ones adopted in this study, and the fact that the blades are clamped at the root, as opposed to standard fully-articulated rotors with flap hinges.

Table 3.7: Summary of numerical main blade eigenfrequencies and mode shapes at 0 RPM with a the fixed root boundary applied.

Mode Shape	Mode Number	f_m at 0 RPM (Hz)
1st Flap Bending	1	113
2nd Flap Bending	2	384
3rd Flap Bending	3	513
1st Torsion - Flap Bending	4	944

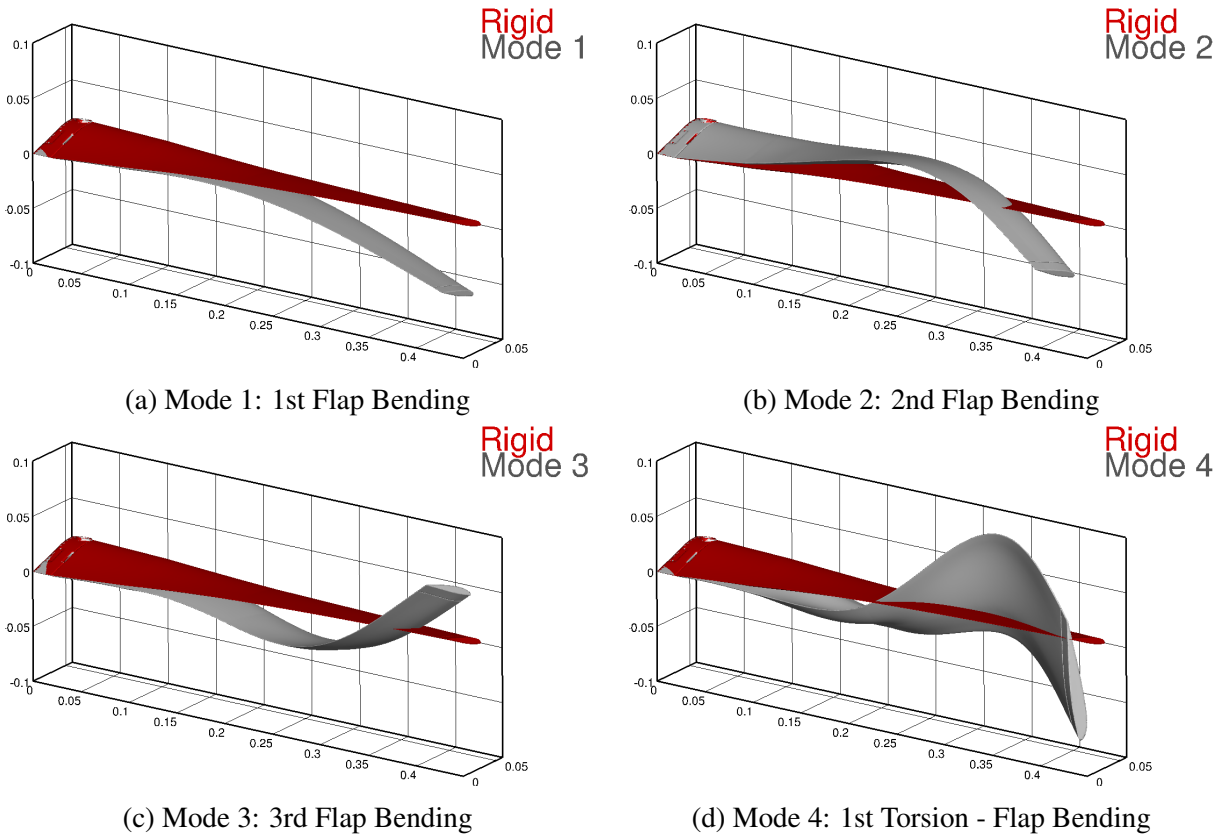

(a) Mode 1: 1st Flap Bending

(b) Mode 2: 2nd Flap Bending

(c) Mode 3: 3rd Flap Bending

(d) Mode 4: 1st Torsion - Flap Bending

Figure 3.8: Visualisation of the first four computed mode shapes at 0 RPM. The undeformed blade is represented in red, the mode shapes in grey.

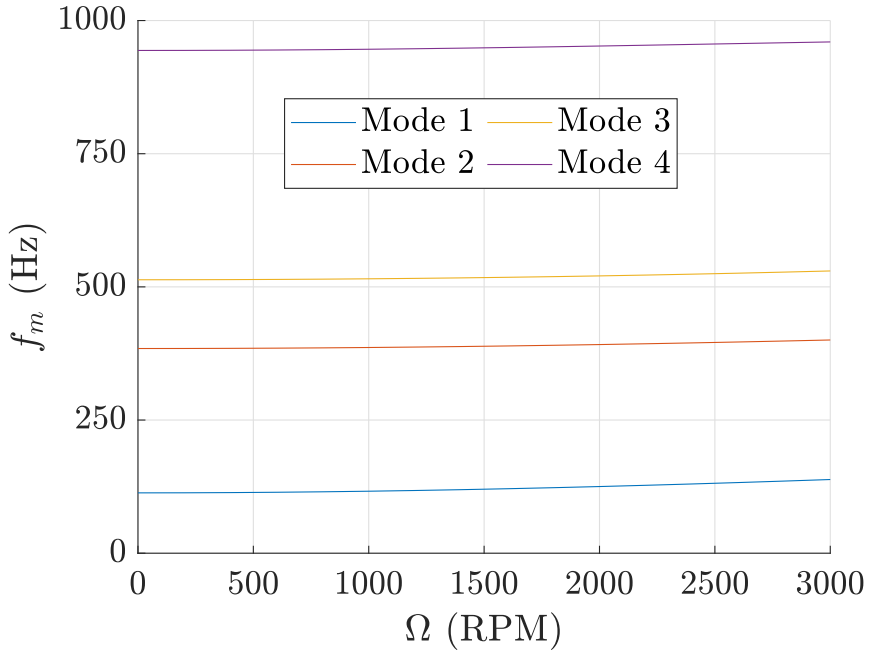

Figure 3.9: Campbell diagram showing modal frequencies (f_m) as a function of the rotational frequency (Ω).

3.1.2.6 Strain Gauges

Each blade is instrumented with fully bridged shear and axial strain gauges, totalling four bridges per blade. Strain gauges were installed on the internal surface of the blade skin to allow for review of bridge time histories plus spectral content of the blade structural response at various test points within the test matrix and to provide an affirmation of stalled flow conditions within the test matrix. Strain gauge bridges have been placed at various locations along the spanwise and chordwise directions, shown on Figure 3.10, to measure flap bending (FB) and torsional twist (T). Bridge locations were determined during the design of the blade which made use of coupled CFD and CSD simulations [78].

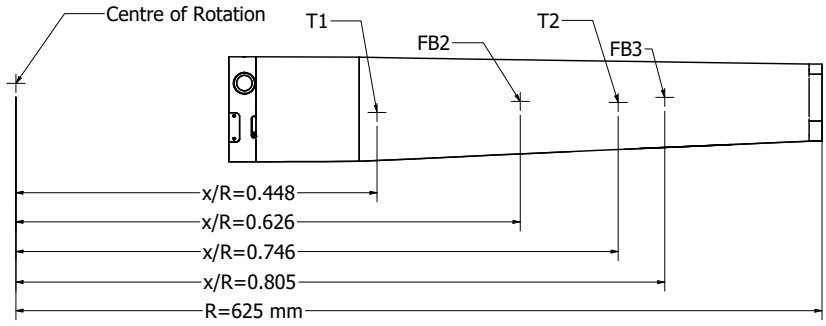

Figure 3.10: Location of flap bending (FB2, FB3) and torsional (T1,T2) strain gauge bridges on the instrumented blade.

Flap bending bridges were composed of four axial strain gauges (1000Ω OMEGA SGD-7/1000-DY13) oriented in the spanwise direction, of which two gauges are co-located on the upper blade surface and two on the lower, at the same spanwise location. For measurements of torsional strain, shear gauges are required to form torsional bridges (1000Ω OMEGA SGT-3D/1000-SY13), also with two gauges co-located on both the upper and lower blade surfaces, respectively. This full-bridge arrangement compensates for centrifugal loading and thermal deformation, so that the bridge reading ε_B is representative of the difference in strain between the upper and lower surface of the blade, $\varepsilon_B = \varepsilon_{LOW} - \varepsilon_{UP}$. Positive values of ε_B are to be expected when the blade is normally loaded (i.e. with moderately positive blade pitch angles) since ε_{UP} is negative (e.g. the upper fibres are compressed) and ε_{LOW} is positive (e.g. the bottom fibres are under tension).

In order to correctly compare strains obtained at different flow densities and rotational frequencies, a corrected strain measurement $\overline{\varepsilon_B}$ has been implemented throughout this thesis, defined as:

$$\overline{\varepsilon_B} = \varepsilon_B \frac{\overline{\rho}}{\rho} \left(\frac{\overline{\Omega}}{\Omega} \right)^2 \tag{3.1}$$

where $\overline{\rho}$ is the reference density (i.e. 1.225 kg/m^3), $\overline{\Omega}$ is the reference rotational frequency, i.e. 1800 RPM and ε_B is the non corrected strain reading.

3.1.3 Telemetry System

Data from sources on the rotating frame were obtained using a custom built Datatel digital telemetry system. The Datatel system allows for the transmission of data signals from the rotating frame to the stationary frame, in addition to providing the required power and signal conditioning for the instrumentation.

3.1.3.1 Signal Conditioning and Processing

The telemetry system comprises 60 channels (six transmitters of 10 channels each) and is configured to transmit data from both the RSB and instrumented blade, measuring hub loads and blade strain gauges, respectively. The telemetry hardware required is housed in a telemetry carrier which hosts six component groups, shown in Figure 3.11. Each component group consists of a transmitter module, alternating current to direct current (ACDC) converter, RSB or blade connector, all of which are connected via a Printed Circuit Board (PCB).

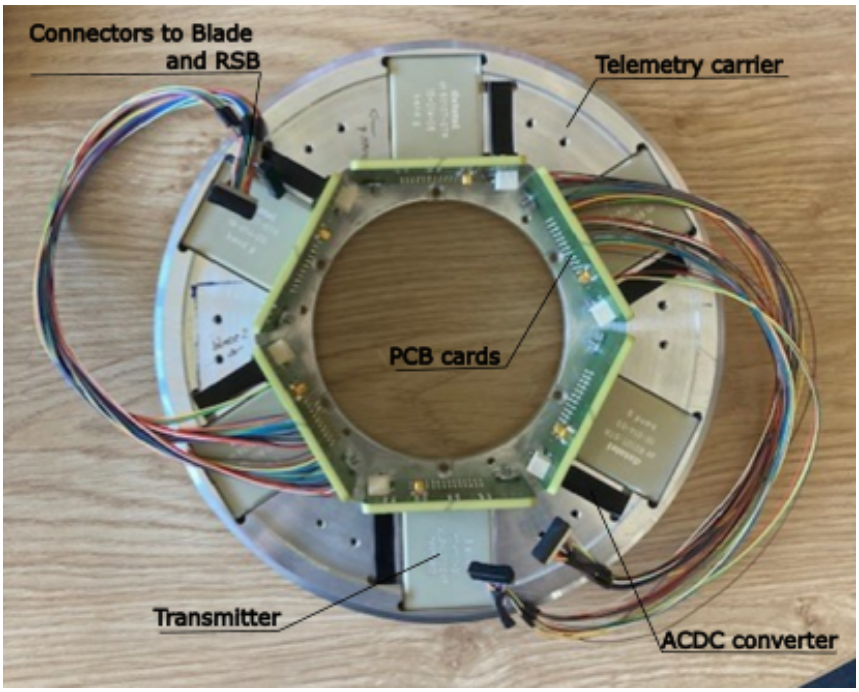

Figure 3.11: Datatel telemetry carrier that is mounted on the rotating side of the hub and houses telemetry hardware components.

Transducers are provided with an highly stable individual current supply, with the current value determined during the signal optimisation of the system, which remains unchanged throughout operation. Transducer signals are then amplified by a pre determined gain, also determined during the system optimisation, ensuring that the measuring range is adequate and the signal is not clipped. The analogue to digital converter (ADC) digitises the amplified and conditioned signal prior to signal processing from which a serial data stream is generated. To

pass the data from the rotating to stationary frame, data are modulated using a radio frequency (RF) modulator on the rotating side before being allocated to a transmitting antenna. On the stationary frame the receiving antenna allocates the radio frequency signal to the receiver, where the signal is demodulated. Data packets are then decoded and spilt from the serial data stream to parallel output signals which are then assigned to the digital output Ethernet connections. A schematic diagram outlining this process is presented in Figure 3.12.

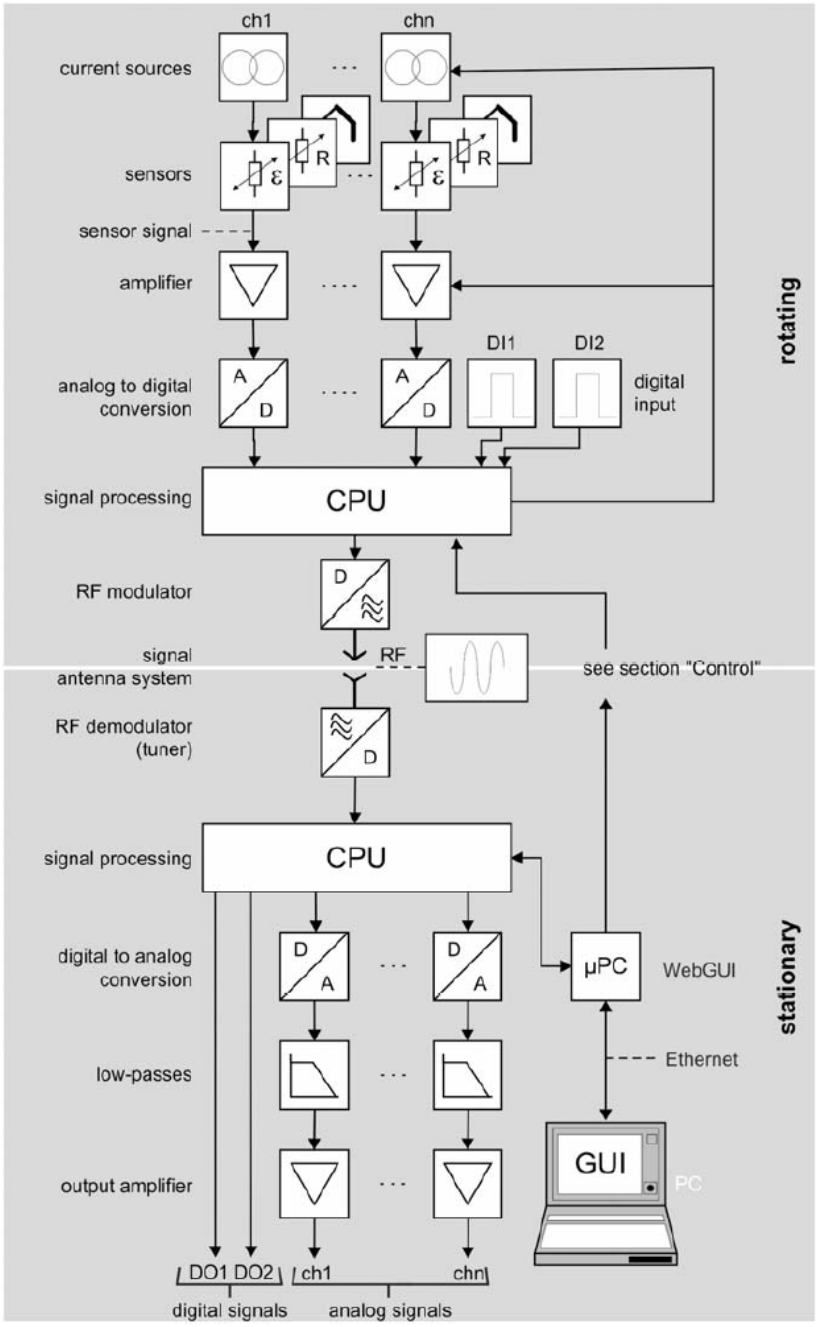

Figure 3.12: Block diagram of the signal processing required to transmit data from the rotating to stationary frame. Image taken directly from Datatel helicopter main telemetry manual [82].

3.1.3.2 Inductive Coil System

Power to the transducers and data signals back to the receiver are transmitted from the rotating part of the rig to the stationary part by means of an inductive coil system, endowed with a transmitting and receiving antenna. The rotor and stator coils are spaced 2mm apart, ensuring undisturbed transmission of both power and data signals. Power and signal cables soldered to the rotor coil are immediately passed into and run the entire length of the propeller shaft, where power and signal connections are then made to the PCB cards within the telemetry carrier as shown in Figure 3.13.

An alternating current power generator generates a sinusoidal current which supplies the transmitter. A control signal is modulated and sent from the micro PC, determining the current amplitude. To ensure operation of the inductive coil system at low impedance values, the AC voltage is amplified. Within the adapter box, the matching element consists of a transformer to vary the impedance and a resonance capacitor allowing for sufficient energy to pass power and data signals across the contact free gap. To ensure correct operation of the inductive coil system, the spacing between the rotor and stator coil must remain fixed, otherwise the current provided to the transmitter will vary resulting in a measurement bias. The ACDC module within the telemetry carrier converts the AC voltage to a stable DC voltage which provides power to the transmitter and instrumentation. Signals from the transmitter are modulated and received by the antenna system at which point the RF signals are amplified, balancing signal attenuation for the long antenna cabling.

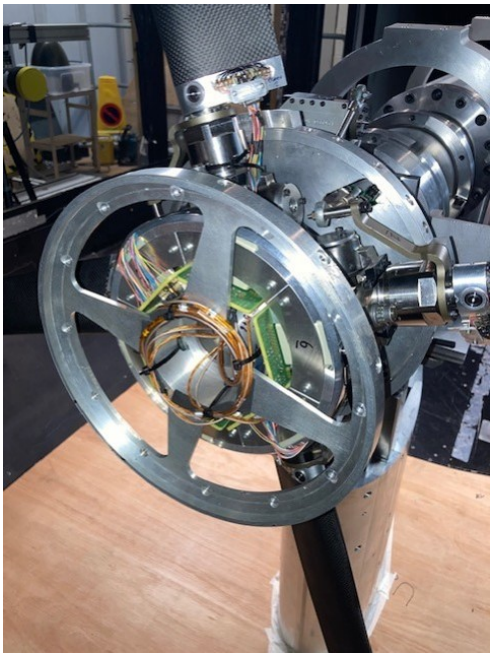

Figure 3.13: Telemetry carrier mounted on the rotor hub attached to power and signal cables that run through the propeller shaft from the inductive coil system.

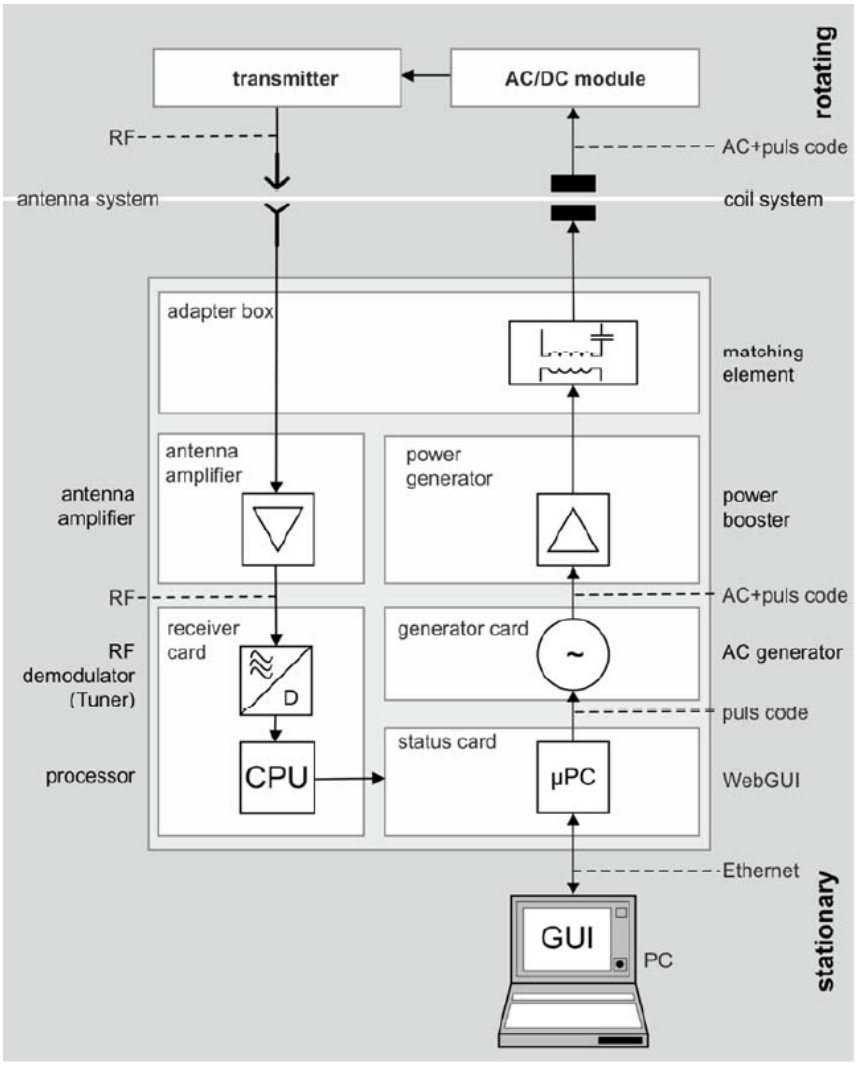

Figure 3.14: Block diagram outlining the power and signal transmission from the rotating to stationary frame using an inductive coil system. Image taken directly from Datatel helicopter main telemetry manual [82].

3.1.4 Rotating Shaft Balance

Rotor loads are measured via a custom built Rotating Shaft Balance (RSB), which is installed within the rotor hub of the UKNRR. The RSB was manufactured by the Aircraft Research Association (ARA) and was calibrated using a custom made calibration jig. Prior to arrival in Glasgow, the RSB was never wired, physically installed or tested under load. This section will provide a description of the balance design, verification of calibration matrices and post-processing considerations to obtain rotor loads.

3.1.4.1 Axes System

The RSB is a custom design six component rotating balance that is capable of obtaining all three forces (F_x, F_y, F_z) and three moments (M_x, M_y, M_z) produced by the rotor. To obtain rotor loads in the appropriate frame of reference, the balance axes system was defined independently from the Cartesian balance axes (x, y, z). The balance axes system is shown for both forces and moments are presented in Figure 3.15a and Figure 3.15b, respectively. Moreover, RSB force and moment limitations in addition to RSB axes notation is displayed in Table 3.8.

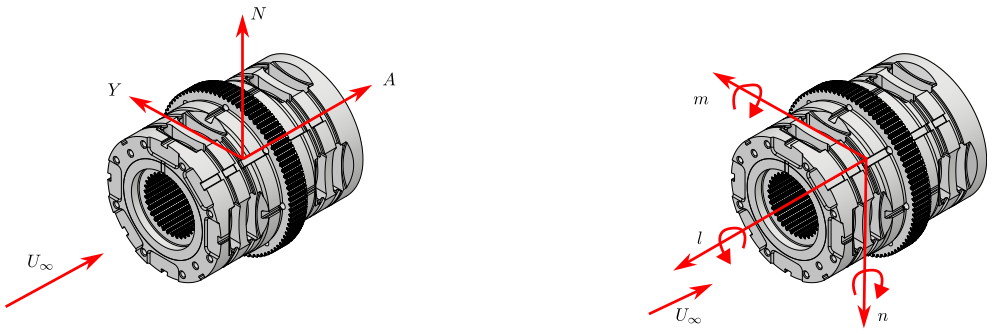

(a) Force axes

(b) Moment axes

Figure 3.15: Force and moment axes system for the custom Rotating Shaft Balance (RSB) when installed on the United Kingdom National Rotor Rig (UKNRR) at an azimuthal position of $\psi = 0°$.

Table 3.8: Maximum allowable loads for RSB and definition of axes system notation.

Notation	Axes	Maximum Load	Units
Y	Side force	550	N
N	Normal force	550	N
A	Axial force	3400	N
m	Pitching moment	250	Nm
l	Rolling moment	250	Nm
n	Yawing moment	350	Nm

3.1.4.2 Balance Reduction Method

The RSB is instrumented with 48 strain gauges, positioned on balance flexures at various positions around the balance (shown in Figure 3.16), that are arranged to form 12 full bridge configurations. Eight full bridges are required to obtain a measurement of three forces and three moments, with the remaining four bridges used to monitor balance thermal effects.

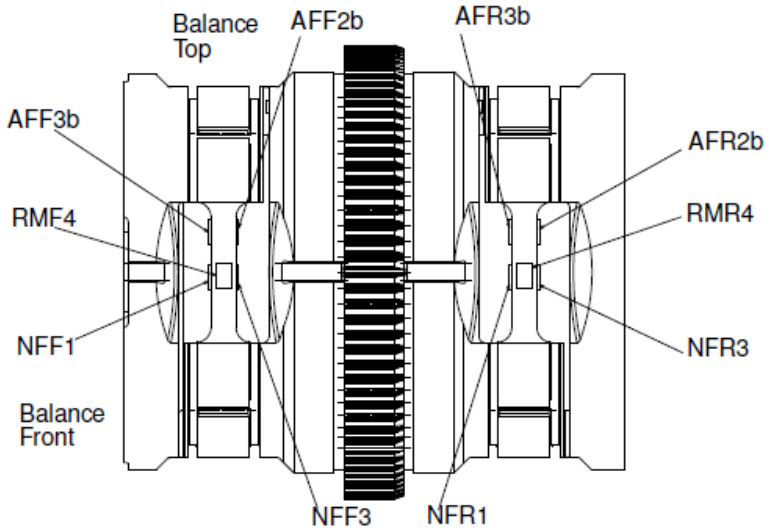

Figure 3.16: Port View of the RSB displaying the distribution of strain gauges on balance flexures at multiple locations around the RSB. Figure taken directly from Smith [83].

The balance is compromised of eight output channels which deliver the fully bridged strain gauge output voltage (V_o) corresponding to each channel, in an $[8 \times 1]$ vector. A reduction from an eight channel output to a six channel output, $[6 \times 1]$ vector, representing the corresponding voltages in the form of a six component load system of three forces (Y, N, A) and three moments (m, l, n) was implemented.

Forces and moments were obtained using a second order Taylor series expansion, which is based upon a method first proposed by Cook [84]. Direct $[T_0]$, first $[T_1]$ and second $[T_2]$ order interactions matrices were obtained during the calibration procedure. Both a first and second order expansion can be used to ascertain load measurements which account for channel cross-coupling. Direct loads, $\vec{L_0}$ illustrate the proportion of the load passing through an individual channel. First order loads, $\vec{L_1}$, relative to direct loads can appear to be significant due to the formation of the balance coefficients, as first order loads incorporate direct loads and their respective components from other gauges. Second order loads, $\vec{L_2}$, also include cross-coupling and demonstrated a significant reduction in percentage difference relative to direct loads.

The calibration of the RSB required the manufacture of a bespoke calibration jig and was performed by ARA [83]. Calibration matrices were obtained for both propeller and helicopter mode, showing little to no difference in interaction matrices. A sample calculation of load reduction and both calibration matrices are presented in Appendix A.

3.1.4.3 Weight Tare

Unlike a conventional non-rotating balance, a rotating balance is mounted between the propeller shaft and the hub, rotating at the propeller rotational frequency, resulting in both fluctuating and mean load components. Measurement of the mean and fluctuating load components are composed of weight, centrifugal and aerodynamic terms.

To account for the fluctuating weight component during balance operation, a weight tare was performed to characterise the weight distribution measured on the active side of the balance around the rotor azimuth. Ensuring balance zeros were measured with the normal force oriented in positive vertical sense, static (non-rotating) measurements of side and normal force were logged as a function of balance azimuthal position (ψ) at a resolution of $\psi = 10°$, as displayed in Figure 3.17. Clarification of azimuthal position and RSB balance axes orientation, with respect to the propeller rig structure, is presented in Figure 3.18. Measurements of normal force highlight a maxima at $\psi = 180°$, which corresponds to a reading of two times the weight ($2W_0$) of the mass on the active side of the RSB. Therefore, the normal force distribution around the azimuth does not average to zero. However, readings of side force are sinusoidal in nature with the maxima and minima of identical magnitude occurring at $\psi = 90°$ and $\psi = 270°$, respectively. Moreover, the side force distribution around the azimuth does average to zero and is highlighted by a reading of zero side force at $\psi = 180°$. As per the testing conditions where the blades, telemetry system and hub spinner are all mounted on the active side of the balance, the mass on the rotating side was measured to be 14.4 kilograms at a fore centre of gravity location of 0.02m.

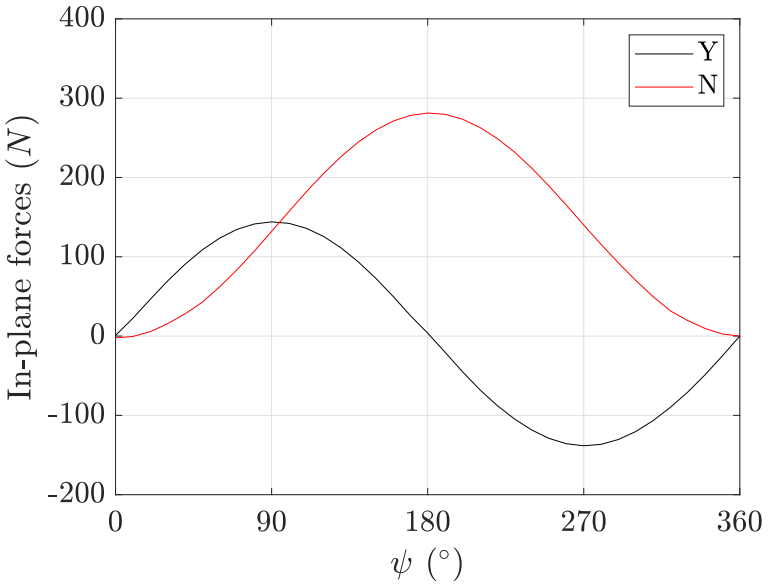

Figure 3.17: Distribution of side (Y) and normal (N) force measurements around the rotor azimuth for a static (non-rotating) case at a resolution of $\Delta\psi = 10°$ required to perform a balance weight tare.

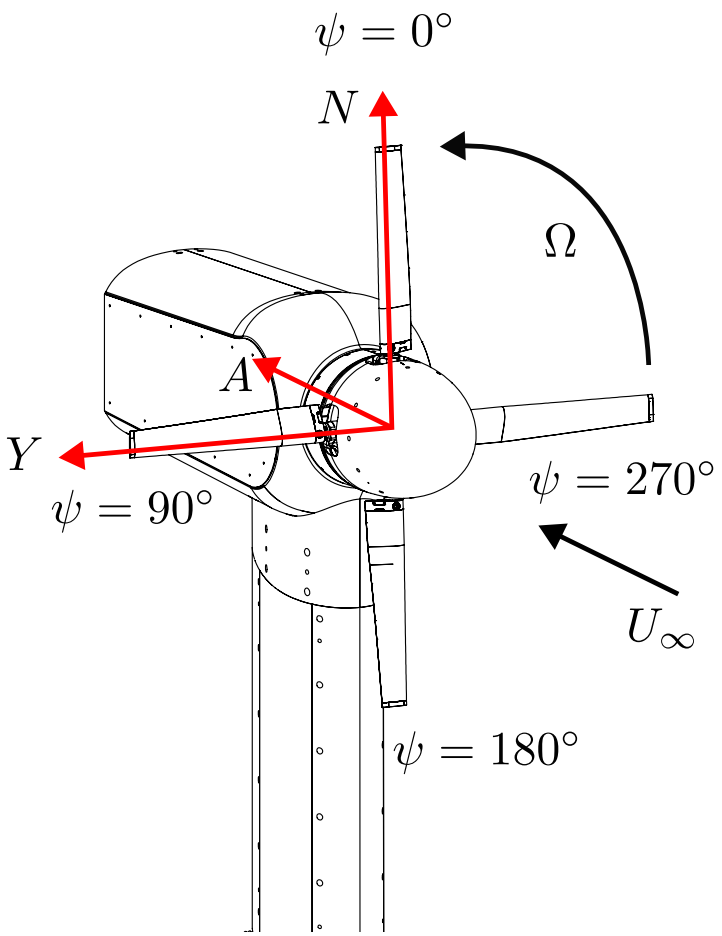

Figure 3.18: Definition of propeller azimuthal position (ψ) and RSB axes orientation with respect to the propeller rig structure.

3.1.4.4 Dynamic Behaviour Characterisation

Installation of the RSB within the rotor hub resulted in the removal of the larger mass solid steel dummy balance from the rotor hub, thus introducing a larger degree of flexibility of the rig structure as a whole. Additionally, for the RSB to work as intended, by definition there must be some degree of flexibility within the RSB to allow the balance to deform during operation. Therefore, both the variation in the rigidity and mass of the entire rotor rig structure will ultimately lead to movement of the rig structural mode frequencies, thus changing the rig dynamic behaviour. Consequently, to assess the dynamic behaviour of the rig and the balancing of the rotor hub, a dynamic (rotating) RSB characterisation was performed with no blades mounted on the hub.

Hub balancing is fundamental to safe operation of a rotary wing mechanism as a small offset of centre of mass with respect to the axis of rotation can result in extremely large in-plane centrifugal forces, even at moderate rotational frequencies. As an example, assuming an offset of the centre of mass with respect to the axis of rotation of 1mm, for a hub mass of 14.4 kg at 1800 RPM, results in a significant in-plane force of approximately 512 N. Therefore, to position the hub centre of mass as close as feasibly possible to the axis of rotation, mass balancing was

undertaken by making use of ballast screws mounted on outer ring of the spinner support, with a total mass of 16g. To assess the mass balancing of the hub, RSB measurements of in-plane loads were assessed as a function of rotational frequency, as shown in Figure 3.19. It is clear that the loading behaviour is parabolic, as expected, until a rotational frequency of 1560 RPM. It is understood that at 1560 RPM and very close surrounding frequencies, a rig resonance is excited and thus the measurement provided by the RSB at rotational frequencies larger than 1560 RPM are deemed unreliable due to the possibility of the measurement of inertial force terms such as rig/balance motion due to resonance. However, it should noted that successful hub balancing was achieved as the peak in-plane force of approximately 80 N observed at 1560 RPM corresponds to a centre of mass radial offset of approximately 0.2 mm. This behaviour can also be appreciated from the in-plane moments that arise due to in-plane forces acting at a distance at which the centre of mass and the RSB centre are offset in the axial direction. The values of moments observed are relatively small as the centre of the RSB is approximately at the centre of the rotor hub.

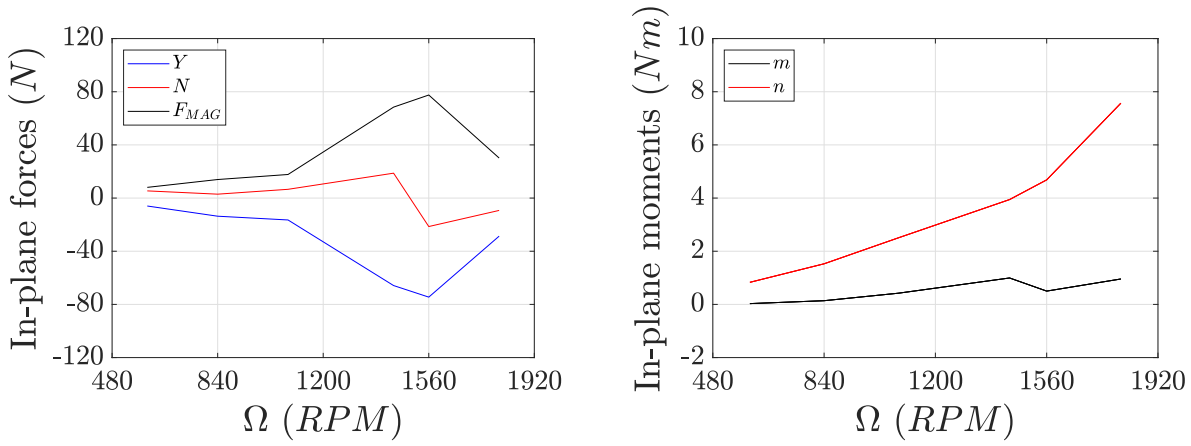

(a) In-plane forces

(b) In-plane moments

Figure 3.19: RSB measurements of in-plane loads as a function of rotational frequency to assess rotor hub mass balancing and rig dynamic behaviour.

3.1.5 Stereoscopic Digital Image Correlation

To better understand the fluid-structure interaction of propeller blades operating in off-design conditions such as stall and negative aerodynamic loading, measurements of blade deformations can provide a useful insight into further understanding aeroelastic behaviour of propeller blades.

3.1.5.1 Configuration of Experimental Apparatus

Measurements of phase-locked blade tip flap bending and torsional twist were carried out by means of stereoscopic Digital Image Correlation at a fixed azimuthal position of $\psi = 270°$. A randomised speckle dot pattern was applied to the propeller blade tip using a white chalk marker, shown in Figure 3.20, to ensure sufficient contrast to the blade surface for adequate pattern identification.

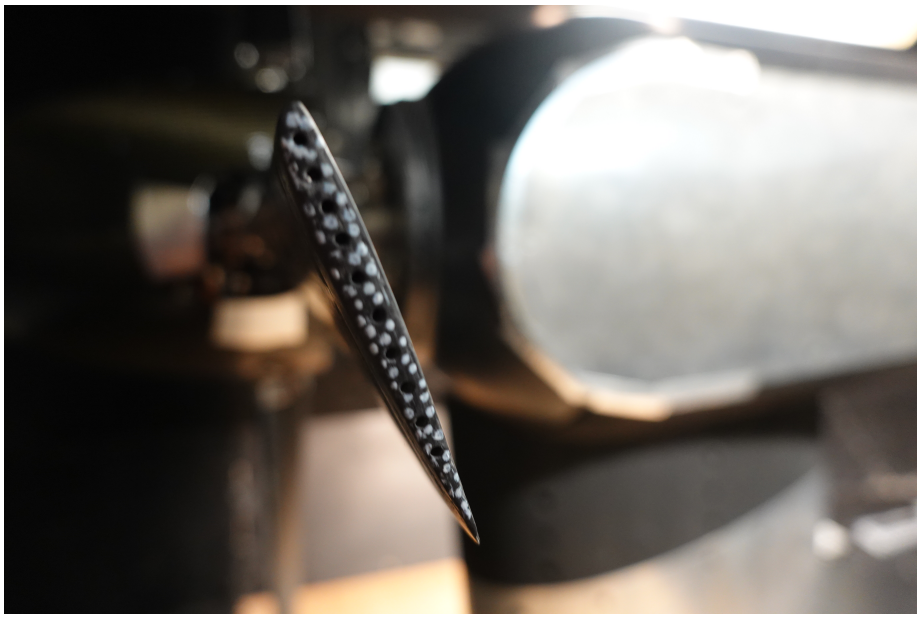

Figure 3.20: Enhanced image of the randomised speckle dot pattern applied to the blade tip of the MENtOR composite blade set using a white chalk marker to ensure sufficient contrast between the pattern and blade surface.

200 images pairs were acquired for each test point using two GigE-Prosilica GT2450 cameras with an image resolution of 5 Mpixels, making use of optical lenses with a 17mm focal length. An appropriate Region of Interest (ROI) at which the blade tip remains visible within the Field of View (FoV) of each camera for all test conditions is shown in Figure 3.21, with dimensions of 0.259 m x 0.09 m, corresponding to $0.414R$ x $0.138R$. Camera 1 and 2 were oriented at $\pm 12.5°$ from the horizontal axis (parallel to the wind tunnel floor) to ensure a stereoscopic angle of $\theta_s = 25°$ resulting in an improved in-plane measurement accuracy, highlighted in Figure 3.22. Calibration of the measurement volume was performed using a Dantec Dynamics 15mm 9x9 chequered calibration target, determining a magnification factor of $M_f = 7.35 px/mm$.

Furthermore, to accurately synchronise the rotor position and camera acquisition, required

use of a timing box. A 1/rev signal was provided to the timing box from a Hall effect sensor installed on the swashplate, ensuring accurate rotor position information required to implement the correct time delay.

An additional magnet of opposite polarity was placed on the rotor hub at an azimuthal offset of 180°, to ensure that mass balancing of the hub was preserved. During image acquisition, exposure time was set to the minimum of the system, corresponding to $25\mu s$ to minimise streaking at high RPM conditions. For larger rotational frequencies sub-sampling was implemented to ensure adequate image quality for correlation. Contextual illumination was provided by a Drello stroboscopic 4037 handlamp with a reflector and quartz-glass flashtube, using a Drelloscop 3018 supply unit, to maximise luminosity of the acquired pictures. Image correlation and visualisation was performed using Dantec Dynamics ISTRA 4D with maximum facet sizing and grid spacing of 31 pixels and 15 pixels, respectively.

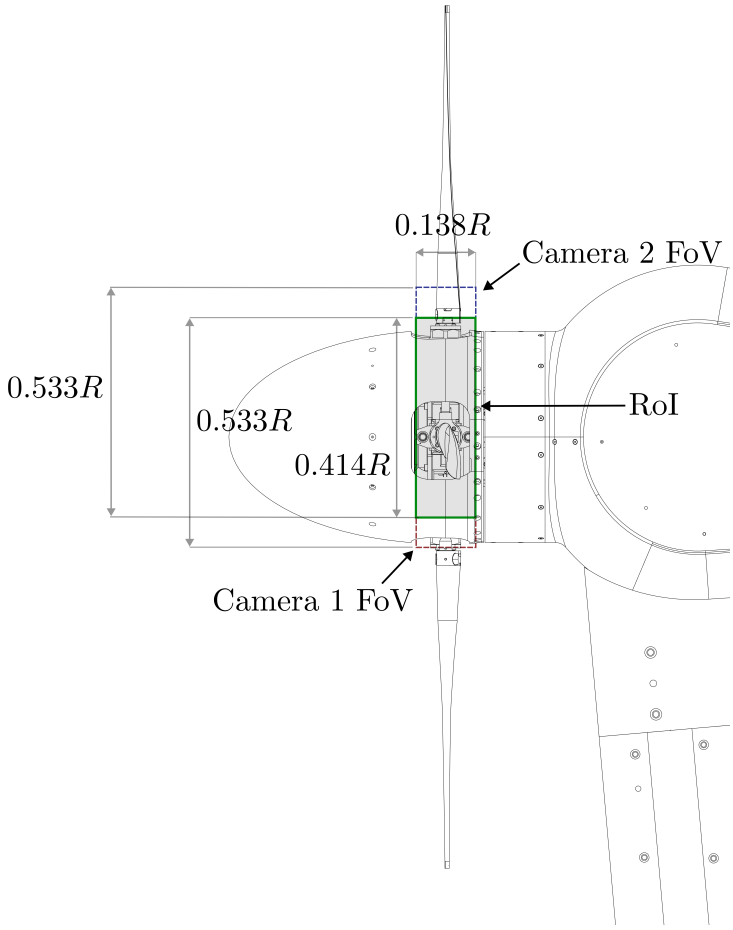

Figure 3.21: Schematic diagram showing the Field of View (FoV) for each of the cameras in the stereoscopic DIC setup and the corresponding Region of Interest (RoI) investigated to measure propeller blade tip deformations.

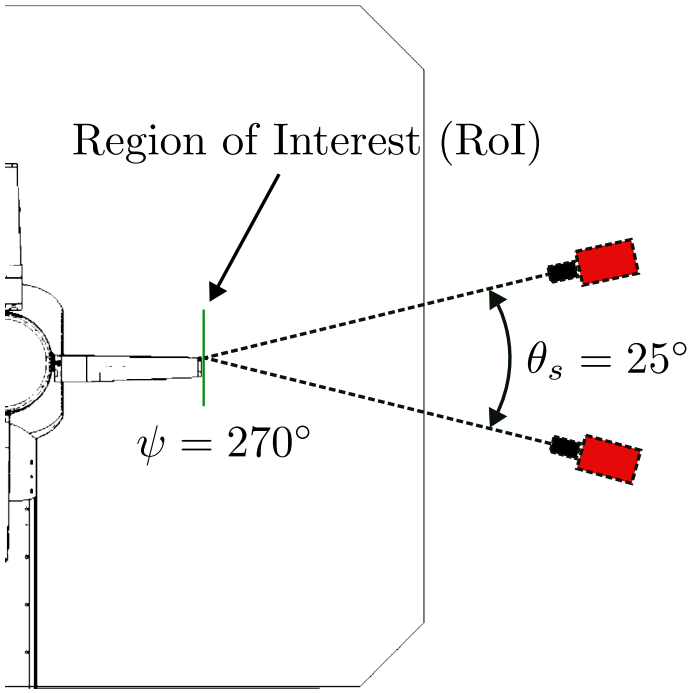

Figure 3.22: Schematic diagram showing the orientation of the stereoscopic DIC setup and the corresponding Region of Interest (RoI) investigated at an azimuthal position of $\psi = 270°$ for phase-locked measurements of propeller blade tip deformation.

3.1.5.2 Measurement Evaluation and Post Processing

Measurements obtained during testing are evaluated within the ISTRA 4D software using the DIC reference frame, which is designated during the calibration procedure, based upon the orientation of the calibration target. Therefore, during post-processing a reference system transformation was performed, shown in Figure 3.23, to define a more meaningful axes system, termed the blade reference system. The blade reference system axes were prescribed so that deformation measurements correspond to positive values of magnitude for both a growth in blade flap bending and nose up twist.

$$X = Y_{DIC} \qquad Y = -X_{DIC} \qquad Z = Z_{DIC}$$

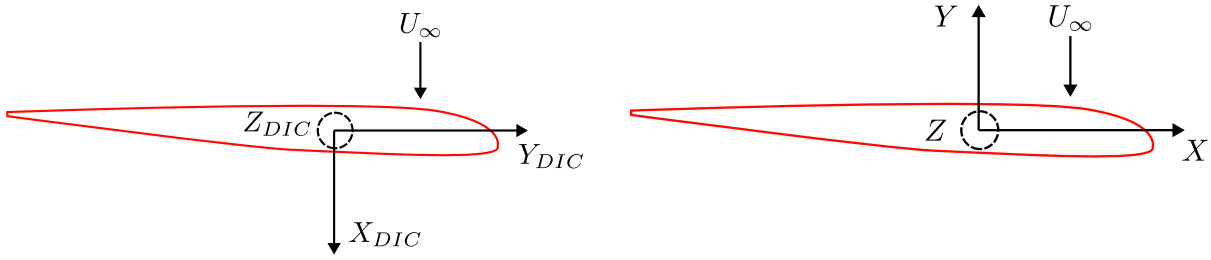

(a) DIC reference frame

(b) Blade reference frame

Figure 3.23: Definitions of both the DIC and blade reference frame used to evaluate blade tip deformation.

All deformations were computed using the blade reference system, where X and Y coordinates are assigned both a subscript and superscript. The subscript notes the point on the blade (A or B) and the superscript notes the image counter, where N represents the image number and R the reference image. This is demonstrated visually in Figure 3.24. Furthermore, expressions of torsional twist ($\Delta\theta$) and flap bending deflection (δ) have been expressed below in terms of image number and point locations. Point locations were determined using existing balancing holes on the tip cap. Blade flap bending deflection was measured with respect to the $0.25C_{tip}$, whereas torsional twist was determined using the balancing holes closest to the trailing edge and leading edge to improve measurement reliability.

$$\Delta\theta = \theta_N - \theta_R = tan^{-1}\left(\frac{Y_A^N - Y_B^N}{X_A^N - X_B^N}\right) - tan^{-1}\left(\frac{Y_A^R - Y_B^R}{X_A^R - X_B^R}\right)$$

$$\delta = \delta_N - \delta_R = Y_A^N - Y_A^R$$

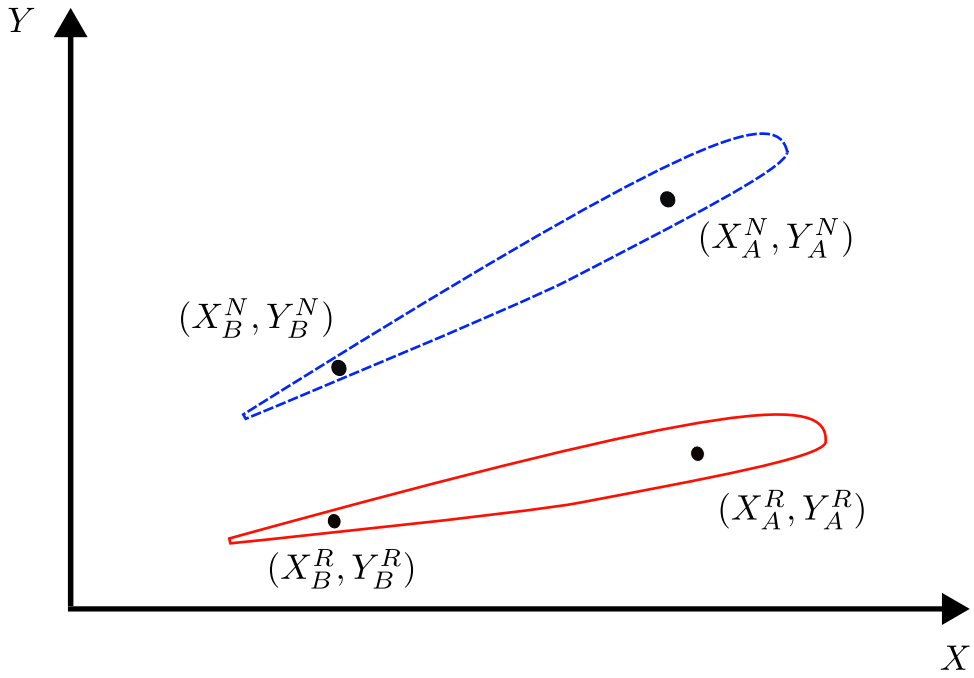

Figure 3.24: Schematic diagram highlighting the coordinates of a blade reference image (shown in red) and a blade at a given image count (shown in blue), required to ascertain the blade deformation.

3.1.6 De Havilland Wind Tunnel

The De Havilland wind tunnel is a subsonic closed return wind tunnel, with a 2.74m $\times$ 2.10m $\times$ 5.64m (Width $\times$ Height $\times$ Length) test section, shown in Figure 3.25. The contraction ratio from the settling chamber to the test section entrance is 5:1. The wind tunnel fan has a diameter of 3m and operates at the required rotational speeds to provide a maximum freestream velocity (U_∞) of $\approx$ 70 m/s. The freestream dynamic pressure together with environmental data (Temperature and Barometric pressure) is measured using a Pitot-static probe and thermocouple, located on the port side in an upstream position of the working section. For applications where the probe is not influenced by the wind tunnel model, the freestream velocity, measurements from the probe and thermocouple can be used to set to a desired freestream velocity using both a manual dial or a Proportional-Integral-Derivative (PID) based controller. Appropriate controller gains are set using the Ziegler-Nichols method. The flow entering the test section is uniform in nature and has a turbulence intensity level of $\approx$ 0.4% [85]. Breather vents at the test section outlet are incorporated into the wind tunnel design to ensure wind tunnel static pressure measurements and atmospheric pressure outwith the tunnel are approximately at equilibrium.

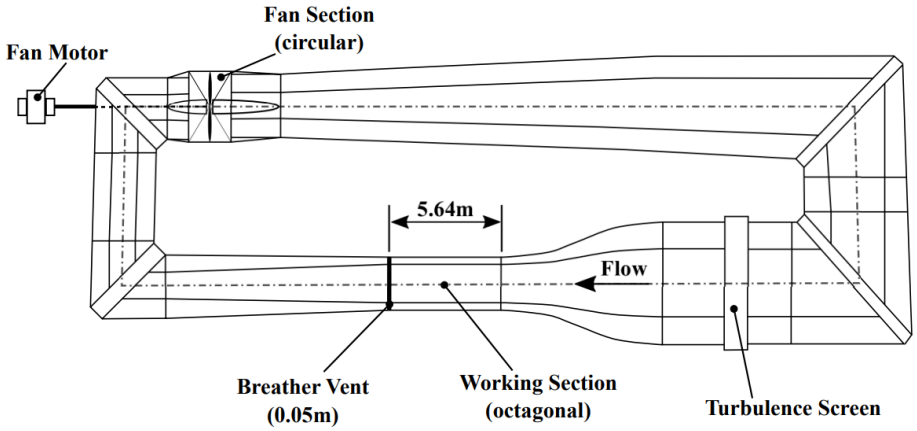

Figure 3.25: Schematic of the De Havilland wind tunnel structure from a top-down view. Figure taken directly from Skinner [86].

3.1.6.1 Velocity Calibration

The integration of the UKNRR in the De Havilland wind tunnel presented a challenge in how to accurately and reliably determine the wind tunnel speed at which the propeller was subjected to. The presence of the model positioning system in the working section, forced the rig to be installed upstream of where models are usually located in the test section, in a position where the propeller plane was aligned with the main Pitot-static probe. This prevented the sole use of the Pitot-static probe to accurately measure the freestream velocity, due to the influence of the propeller streamtube on the probe. Therefore, to provide a reliable reference pressure measurement

that could be used to accurately set the wind tunnel speed, a differential pressure transducer was used to measure the pressure difference across two rings of pressure tappings at the entrance and exit of the contraction section. This measurement was deemed to be less affected by the influence of the propeller. Figure 3.26 shows the location of the Pitot-static probe (P), in addition to the locations of the pressure tapping rings at the entrance (A) and exit (B) of WT contraction.

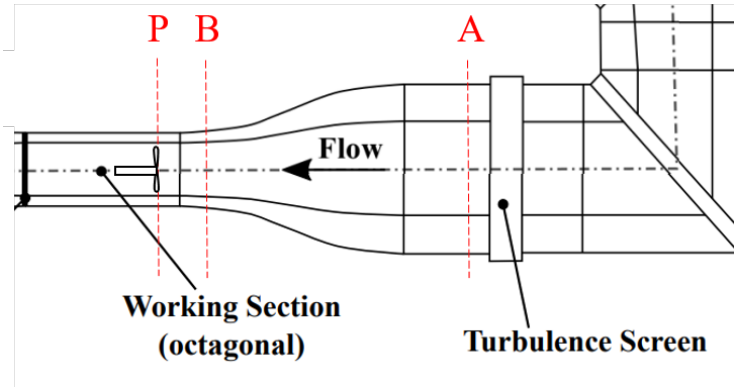

Figure 3.26: Schematic of the wind tunnel test section and contraction, with the position of the propeller plane and Pitot-static probe (P), and the locations of the pressure tap rings at the entrance (A) and exit (B) of the contraction. Figure adapted from Skinner [86].

To ensure the wind tunnel velocity measurements obtained by measuring the pressure difference across the contraction were meaningful, a wind tunnel calibration was performed with the UKNRR situated within the working section with all four blades removed. The calibration was performed by measuring the pressure difference across the contraction ($\Delta P_{CON} = P_A - P_B$) and the dynamic pressure of the Pitot-static probe (ΔP_{PROBE}) within the working section for a series of wind tunnel fan settings. Measurements were obtained between $U_\infty = 0 - 40$ m/s at a resolution of $\Delta U_\infty = 2.5$ m/s. Calibration results are presented in Figure 3.27 in terms of the pressure ratio between the two measurement source, $\kappa = \Delta P_{CON}/\Delta P_{PROBE}$ as a function of freestream velocity (Figure 3.27a) and contraction pressure difference as a function of the dynamic pressure measured using the Pitot-static probe (Figure 3.27b).

It is shown that the average pressure ratio across the range of freestream velocities is $\kappa = 0.9471$, which is within a sensible range of the theoretical value of $\kappa_{Ideal} = 24/25 = 0.96$ that can be obtained when considering a contraction ratio of 5:1. Values of κ at $U_\infty \leq 7.5$ m/s display some level of drift from the average ratios due to the dynamic pressure being relatively small and being more affected by measurement noise. Furthermore, a linear regression of both pressure sources was performed, confirming $\kappa = 0.9471$ with a deviation of 0.0465 Pa. Once the calibration was completed, the reference dynamic pressure used to set the wind tunnel speed was set to be $q = \Delta P_{CON}/\kappa$, where $q = \frac{1}{2}\rho U_\infty^2$.

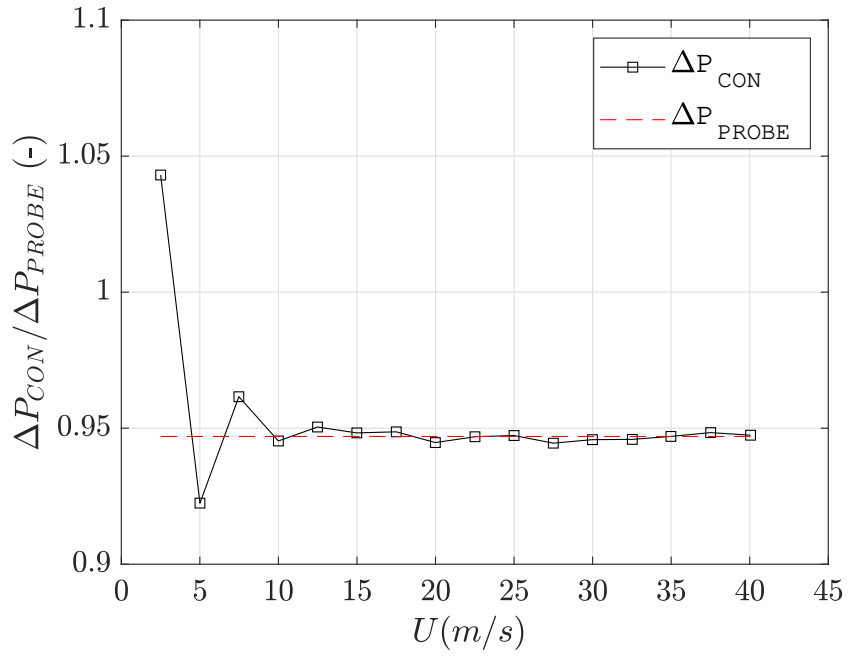

(a) Average Velocity

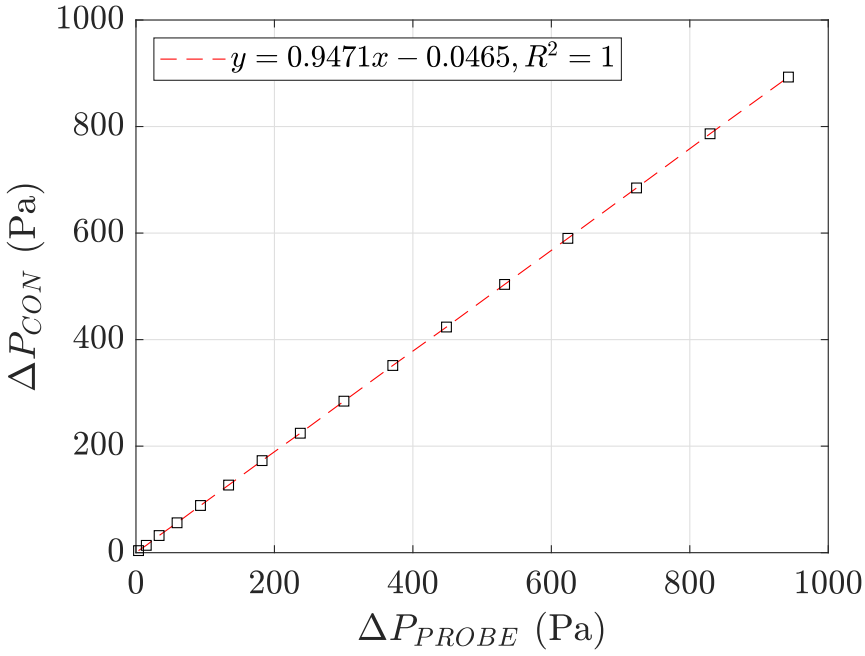

(b) Linear Regression

Figure 3.27: Calibration of the De Havilland wind tunnel using pressure measurements from the wind tunnel Pitot-static probe and contraction ring.

3.2 Rotor At High Advance Ratio

3.2.1 Free Surface Water Towing Tank

Testing was performed in the free surface water towing tank facility, where the tank dimensions are 1.5m x 1m x 7m (Width x Height x Length). The rotor rig was situated on the centre line of the towing tank with the blade submerged 0.225m from the blade quarter chord with respect to the tank water level of 0.9m, to reduce rotor-wall interactions. As shown in the schematic of the experimental setup, presented in Figure 3.28, the blade is mounted onto the rotor hub which is connected to two control rods which are driven by a motor located on the tow carriage to provide rotational motion of the blade. The tow carriage is driven by a separate motor to provide a translation movement of the blade within the tank. Unlike a wind tunnel, desired motion profiles such as translational and rotational velocities plus accelerations are pre programmed and allocated to the motor controllers prior to execution of the test. Between test runs adequate time is required to allow for the tank to settle so that future runs are not biased, typically 10 minutes between runs was allocated to allow for the tank to return to a state of equilibrium.

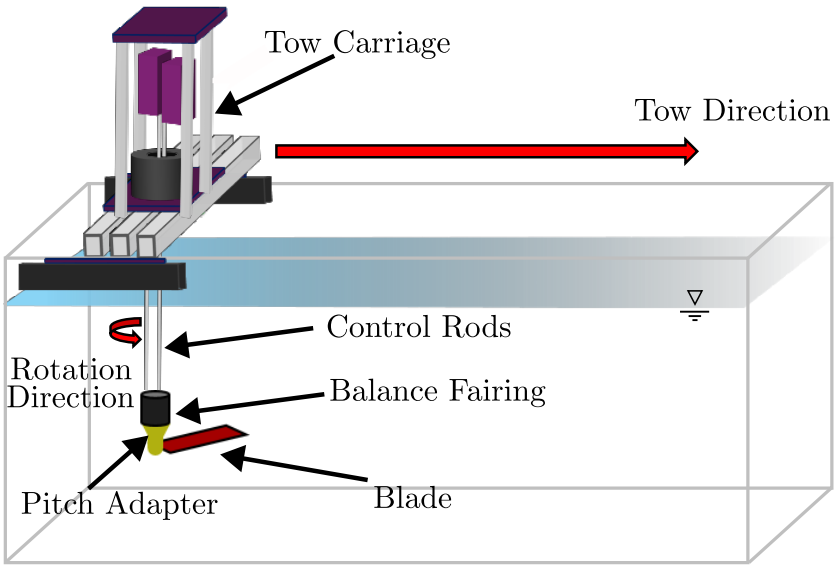

Figure 3.28: Schematic of the single bladed rotor rig within the free surface water towing tank. Figure adapted from Wild et al. [65].

3.2.2 Rotor Rig

A single bladed fixed collective rotor rig, shown in Figure 3.29, was used to investigate rotor aerodynamic and structural response at large advance ratio conditions. Making use of adapters with attachment points at pre-defined angles, the collective was set to an accuracy of less than 0.1°. Two collective blade pitch angles were investigated, one representative of attached flow ($\theta = 7^{o}$) and another to represent a rotor operating in separated conditions ($\theta = 25^{o}$).

The rotor rig allows for force and moment data from the rotor blade to be measured, making use of the ATI six degree-of-freedom (6-DOF) Mini-40 IP68 force/torque sensor (SI-40-2). Balance calibration was performed to ensure the sensing range of the balance force channels are $F_x, F_y = 40N$, $F_z = 120N$ and and moment channels are $M_x, M_y, M_z = 2Nm$. Corresponding to a channel resolution of $F_x, F_y = 0.01N$, $F_z = 0.02N$ and $M_x, M_y, M_z = 0.00025Nm$. Load data obtained by the load cell was corrected by means of a moment transfer to account for the offset in the vertical displacement (ΔZ) of the load cell measuring surface and the blade quarter chord. Load data was acquired at a sampling rate of 1 kHz and synchronised with the towing tank motor encoders. Sampling periods were dependant on rotor advance ratio, ranging from approximately 15 to 240 seconds per run. To ensure repeatability and accuracy of the experimental data logged, five runs were performed for each advance ratio per collective. Removal of any hub effects from the raw measurements, were corrected for by means of aerodynamic tare (blade-off) runs.

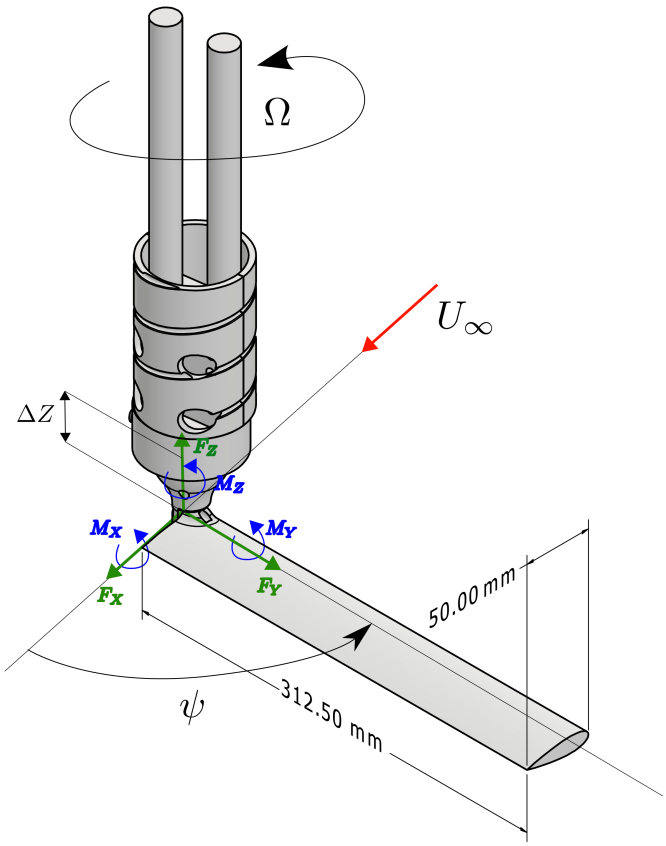

(a) Schematic highlighting axis system, rotational direction and freestream velocity directions.

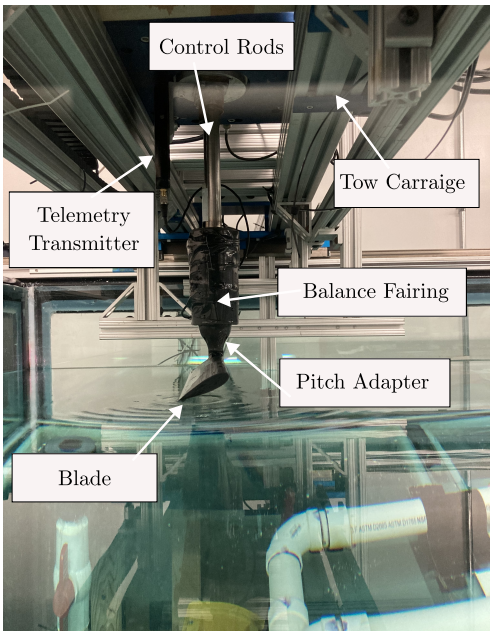

(b) Image of single rotor highlighting rig components.

Figure 3.29: Single bladed rotor rig within the towing tank at the University of Maryland.

3.2.3 Blade Design and Instrumentation

Testing of a single constant chord rotor blade of 0.3125m radius and 0.05m chord was undertaken. The blade design incorporates a NACA 0024 profile across the entirety of the span. This profile was chosen to allow for the installation of wired strain gauges into the internal sections of the blade, ensuring no influence on the flow behaviour on the blade surface. Furthermore, the NACA 0024 series aerofoil is a very well understood aerofoil with an abundance of experimental data across a range of Reynolds numbers.

Moreover, the blade was manufactured at the University of Maryland using a precision 3D printer. During the manufacture of both the upper and lower blade skins, carbon fibre composite layers were included to strengthen the blade and act as a blade spar, thus making the tested blade representative internally of a conventional rotor blade design. Sufficient internal spacing was left for the installation of blade instrumentation, wiring and waterproofing material prior to bonding. A summary of blade features and fluid properties is shown in Table 3.9.

Table 3.9: Main features of the rotor blade and experimental setup.

Characteristic	Symbol	Value	Units
Aerodynamic Profile	-	NACA 0024	-
Aspect Ratio	-	6.25	-
Taper	-	Non-tapered	-
Twist Distribution	-	Non-twisted	-
Radius	R	0.3125	m
Diameter	D	0.625	m
Chord	C	0.05	m
Number of Blades	N_b	1	-
Solidity	σ	0.051	-
Disk Area	A	0.3067	m^2
Collective	θ	7/25	^{o}
Kinematic Viscosity	ν	1.004×10^{-6}	m^2/s
Fluid Density	ρ	998	kg/m^3

The rotor blade was instrumented with fully bridged axial strain gauges, totalling 3 bridges across the blade. The bridges were arranged to measure the flap bending (FB) of the blade and were located at the following radial locations (y/R) 0.25, 0.5 and 0.75 as shown in Figure 3.31. Two gauges were co-located on the upper blade surface and two on the lower, at the same radial location. This full-bridge arrangement compensates for centrifugal loading and thermal deformation, so that the bridge reading ε_B is representative of the difference in flap bending strain between the upper and lower surface of the blade. Measurements of local bending were transmitted from the rotating frame to the stationary frame via the Parker-Lord V-Link-200 telemetry system from which strain time histories were sampled at a frequency of 1024 Hz.

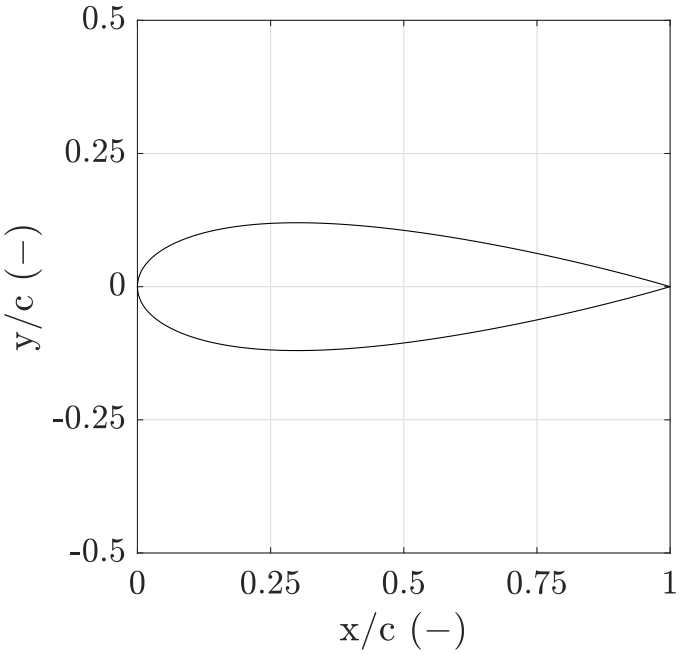

Figure 3.30: NACA0024 aerofoil profile used at all blade sectional spanwise positions.

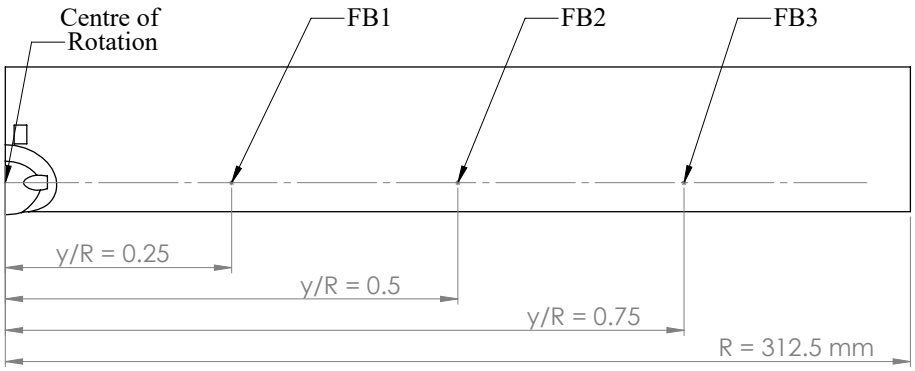

Figure 3.31: Span wise location of flap-bending (FB) strain gauge bridges on the instrumented blade.

3.3 Chapter Summary

A description of the experimental test rigs, instrumentation and measurement techniques implemented for experimental test campaigns investigating propeller stall and rotors at high advance ratio conditions have been documented within this chapter. Section 3.1 focused on the development, configuration and integration of the UKNRR within the De Havilland closed loop low speed wind tunnel, outlining critical pieces of the experimental setup such as: instrumented blades including blade geometry and structural properties; Datatel telemetry system and inductive power supply; rotating shaft balance and a steroscopic digital image correlation system. In addition, descriptions of measurement corrections required for suitable data analysis were presented. Key corrections implemented include: measurements of blade strain; RSB normal and side force components during dynamic operation and a wind tunnel velocity calibration. Section 3.2 outlines the design and configuration of a single bladed rotor rig within the free surface towing tank at the University of Maryland. Details of the blade design, configuration of instrumentation such as a six-component load cell to obtain blade force measurements and strain gauge positions to measure blade strain distribution are documented.

Chapter 4

Stall Boundary Identification Criteria

This chapter presents the strain characterisation of the MENtOR tiltrotor blade set, operating in fixed pitch propeller mode, at varying rotational frequencies, blade pitch angles and advance ratio's. A novel methodology of stall identification has been developed to identify the presence of stall onset through the measurement of unsteady blade strain, motor torque and wind tunnel velocity data. A description of the test conditions is presented in Section 4.1. Measurements required to assess the onset of blade stall are described within relevant sections, including the wind tunnel recirculation velocity (Section 4.2); averaged strain (Section 4.3) and unsteady blade strain measurements (Section 4.4) and motor torque demand (Section 4.5). Furthermore, a stall boundary determined through the established criteria presented is displayed in Section 4.6. Results presented in this chapter were obtained prior to the installation of the RSB where a steel dummy balance was installed within the rotor hub.

4.1 Test Matrix

The test matrix used to determine the operating boundary of this blade set was varied using three parameters: propeller rotational frequency Ω, advance ratio $J = U_\infty/(nD)$ and blade pitch $\beta_{0.75R}$ measured at 75% of the propeller radius. As the rotor has been configured to operate as a fixed pitch propeller, the pitch angle was fixed during each test with only rotational frequency and advance velocity varying. Testing was performed at a range of blade pitch angles between $\beta_{0.75R} = 15.9^o$ to 35.6^o. All tests were performed for a range of rotational frequencies between 1080 RPM and 1800 RPM in increments of 120 RPM. This corresponded to a maximum tip Mach number of $M_{tip} = 0.35$ and a maximum tip chord based Reynolds number of $Re_{tip} \approx 0.48$ million.

Due to the nature of the closed loop wind tunnel, in cases when the tunnel was not turned

Elements of this chapter are published in Croke et al. "Experimental Investigation Into The Onset Of Stall On Tiltrotor Blades In Propeller Mode", Advances In Research, Development, Simulation, Design, Manufacturing, Testing and Operation Of Rotorcraft Special Issue, CEAS Aeronautical Journal, 2025.

on ("No WT"), the propeller would still induce a recirculating flow around the tunnel loop that acted as a *de facto* advance velocity. The magnitude of the recirculation is dependent on $\beta_{0.75R}$, as for attached cases an increasing blade pitch will result in a larger induced flow and therefore an increased advance ratio. "No WT" tests, when the wind tunnel fan was not turned on, were performed for every pitch angle to assess the minimum advance ratio at which the propeller could be tested. At "wind on" conditions the wind tunnel was turned on to introduce an oncoming wind to the propeller. Each test was run at constant advance ratio and blade pitch angle, requiring the magnitude of the wind tunnel speed to be adjusted as the propeller rotational frequency was varied.

Moreover, for each blade pitch angle, the maximum advance ratio values that could be tested increased with blade pitch, as a higher $\beta_{0.75R}$ would allow for a larger reduction in the angle of attack caused by the advance speed before encountering negative thrust. The most outboard bending strain gauge, FB3, and the motor torque were monitored throughout testing to determine at what advance ratio the outboard section of the blade entered negative loading. The advance ratio was limited to 1.4 for the large pitch angle tests due to the maximum achievable wind tunnel speed. A visual representation of the test matrix is shown in Table 4.1.

Table 4.1: Test matrix as a function of blade pitch ($\beta_{0.75R}$) and advance ratio (J). Each test was performed at rotational frequencies varying from 1080 RPM to 1800 RPM in 120 RPM increments. X = Point tested, Blank = Point not tested.

$\beta_{0.75R}$	No WT	J=0.3	J=0.4	J=0.5	J=0.6	J=0.7	J=0.8	J=0.9	J=1.0	J=1.1	J=1.2	J=1.3	J=1.4
15.9^o	X	X	X	X									
17.4^o	X	X	X	X	X								
19.2^o	X	X	X	X	X	X							
20.9^o	X	X	X	X	X	X	X						
22.5^o	X		X	X	X	X	X	X					
24.2^o	X		X	X	X	X	X	X	X				
25.8^o	X		X	X	X	X	X	X	X	X			
27.3^o	X		X	X	X	X	X	X	X	X	X		
28.9^o	X			X	X	X	X	X	X	X	X	X	
30.5^o	X			X	X	X	X	X	X	X	X	X	X
32.2^o	X			X	X	X	X	X	X	X	X	X	X
33.9^o	X			X	X	X	X	X	X	X	X	X	X
35.6^o	X			X	X	X	X	X	X	X	X	X	X

4.2 Measured Recirculation Around the Wind Tunnel Loop

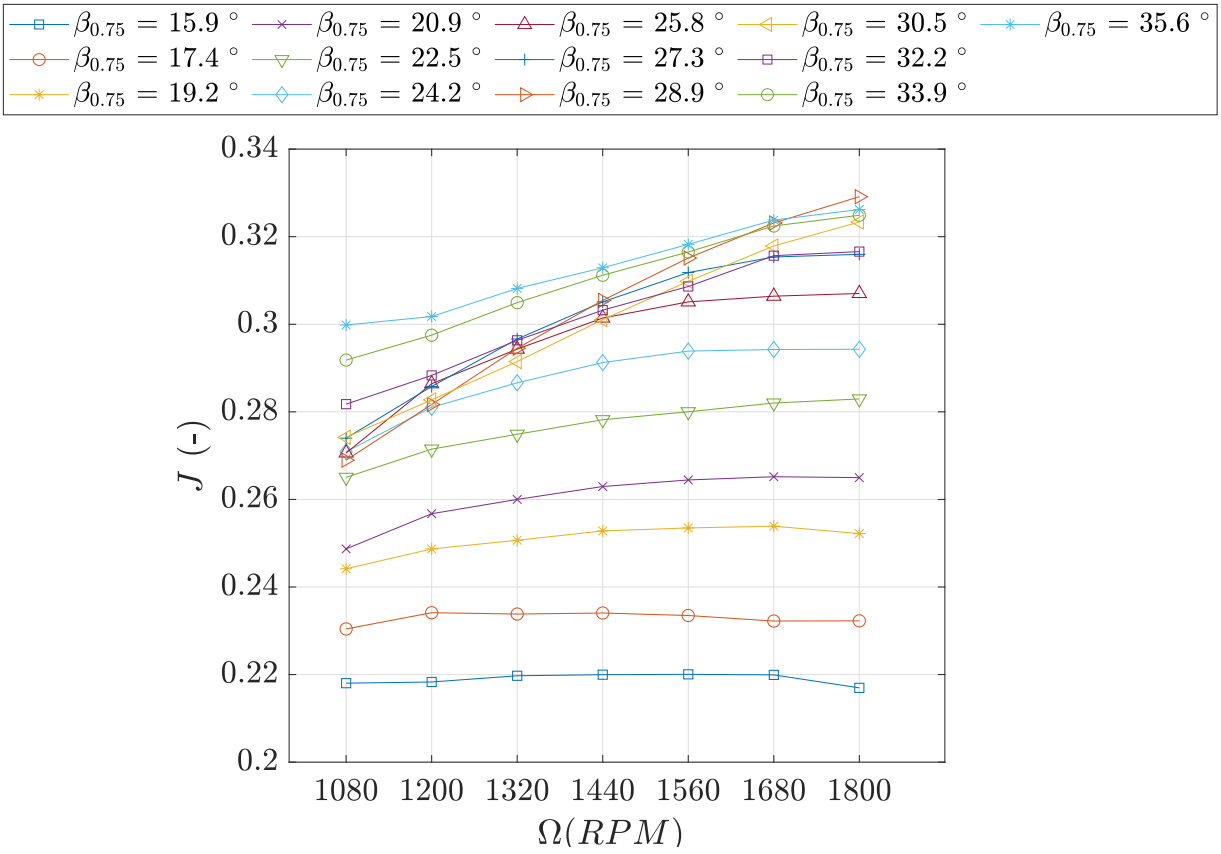

Figure 4.1: Propeller induced J vs RPM at "No WT" condition, for various pitch settings.

As previously stated in Section 4.1, the minimum speed at which the wind tunnel could be set is dependent on the magnitude of the recirculation around the tunnel loop caused by the propeller. Figure 4.1 shows the advance ratio induced by such recirculation when the tunnel was not turned on as a function of the propeller rotational frequency, for a series of blade pitch angles. At low $\beta_{0.75R}$, the induced advance ratio is constant with respect to Ω, implying that the propeller works at constant thrust coefficient throughout the range of RPM investigated. This can be appreciated more clearly when estimating the induced velocity at the propeller disc by means of momentum theory:

$$v_i = \sqrt{\frac{T}{2\rho A}} = \sqrt{\frac{\rho n^2 D^4 C_T}{2\rho D^2/4}} = nD\sqrt{\frac{2}{\pi}C_T}$$

where $T = \rho n^2 D^4 C_T$ and $A = D^2/4$. It can be reasonably assumed that the induced wind tunnel recirculation velocity (U_∞^{IND}) is proportional to v_i ($U_\infty^{IND} \propto v_i$). Thus when scaled by nD, an expression relating (J_∞^{IND}) as a function of the thrust coefficient (C_T) is obtained.

$$J_{\infty}^{IND} \propto \frac{v_i}{nD} \propto \sqrt{\frac{2}{\pi} C_T}$$

Which shows that the advance ratio is proportional only to the C_T. As the blade pitch is increased, the J curves move upwards as the thrust grows. They also start to bend down in the low RPM range, until they collapse on one another, e.g in the range $22.5° \leq \beta_{0.75R} \leq 30.5°$ at 1080 RPM. This is evidence that the thrust generated by the propeller stops to grow, suggesting the onset of stall. This translates to a lower intensity recirculation around the wind tunnel loop, quantifiable for the $\beta_{0.75R} = 22.5°$ case with a difference of about 0.018 in J, or 6%, between the 1080 RPM case (stalled) and the 1800 RPM case (not stalled). This can also be appreciated from Figure 4.2 displaying the variation in J as a function of blade pitch angle for various rotational frequencies. It is expected for stall to affect low RPM cases first as the lower blade Reynolds number promotes flow separation at lower angles of attack. As the pitch angle is further increased, the collapse point moves to higher RPMs, suggesting that stall starts to affect cases with higher blade Reynolds numbers also.

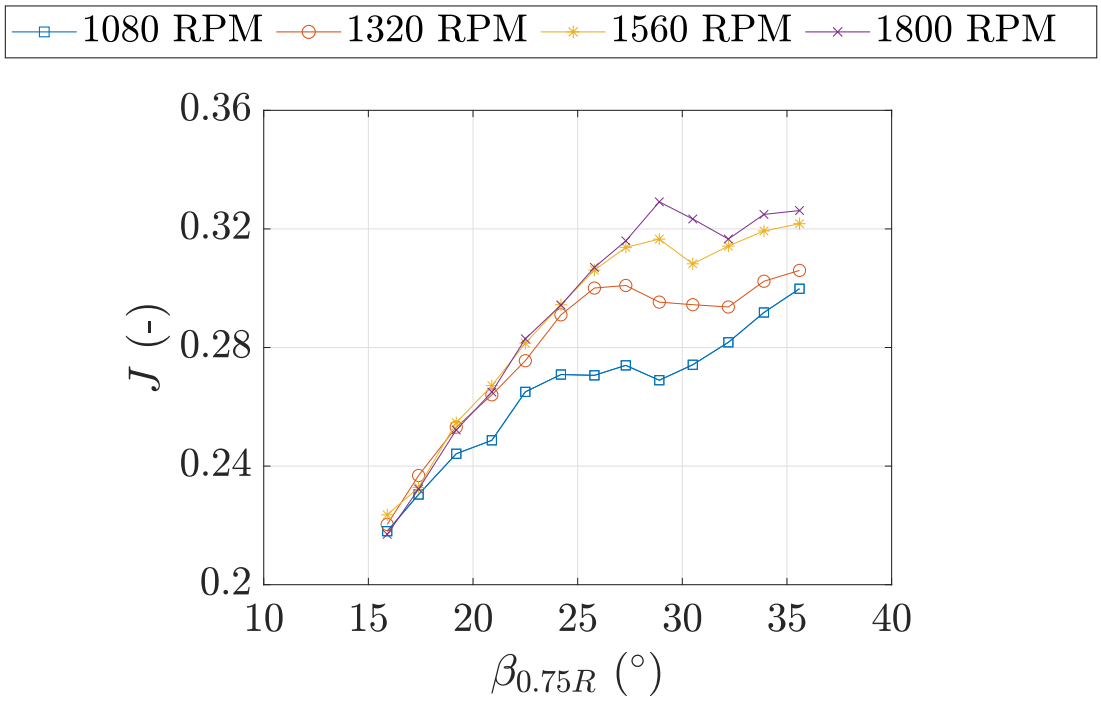

Figure 4.2: Propeller induced J vs $\beta_{0.75R}$ for various rotational frequencies at "No WT" conditions.

4.3 Averaged Strain Measurements

4.3.1 Corrected Blade Strain

Stall onset can be appreciated by looking at the blade strain measurements. FB2 and FB3 are flap bending (FB) bridges positioned at $x/R = 0.62$ and $x/R = 0.8$ respectively, as shown in Figure 3.10. Since the flapping motion of the blade was constrained by flap stops, the blade acted as a cantilever beam, hence readings for FB2 which is closer to the root, were generally higher than those for FB3. Figure 4.3 presents the corrected strain for bridges FB2 and FB3 at 1080 RPM for the following advancing conditions: J = “No WT" case, 0.5, 1.0 and 1.4, as a function of the blade pitch angle. Considering the “No WT" case shown in Figure 4.3a, the advance velocity is not fixed and varies with blade pitch angle for a given rotational frequency. The variation in advance velocity is driven by the increasing induced velocity (U_{IND}) generated by the propeller. This variation in advancing speed is only present in the “No WT" case with larger J values set using the wind tunnel fan.

Considering the “No WT" case, a noticeable departure from linear behaviour can be appreciated for both FB2 and FB3 bridges starting at $\beta_{0.75R} = 22.5°$, marking the stall onset at this rotational frequency, as already appreciated when looking at the advance ratio curves of Fig. 4.1 collapsing on one another. This is further confirmed by evaluating the standard deviation of the bridge measurements (represented as an error bar in Figure 4.3), that sees a sharp increase in magnitude for $\beta_{0.75R} \geq 22.5°$, owing to the much more unsteady aerodynamics of the stalled blades. This behaviour observed in the FB2 and FB3 strain gauge measurements during the “No WT" case is also identifiable at conditions of advance velocity where stall is present. Figure 4.3b shows deviation from linear behaviour for both FB2 and FB3 bridges starting at $\beta_{0.75R} = 28.9°$ for J = 0.5 at 1080 RPM. The delay in stall onset is to be expected and can be explained by a reduced effective angle of attack at larger advance conditions and a thinner sectional boundary layer as a result of a larger Reynolds number.

Moreover, larger advance ratio conditions of J = 1.0 and 1.4, shown in Figures 4.3c and 4.3d, respectively, present a linear growth in both FB2 and FB3 bridge measurements across all blade pitch angles. No indication of deviation from linear behaviour is observed and bridge standard deviations remain constant with growing blade pitch, highlighting no large growth in measurement unsteadiness. It should however be noted that the magnitude of the bridge unsteadiness for a given J value where no stall is present remains relatively constant but does increase for larger values of J, this can be explained by larger dynamic pressure values promoting larger flow oscillations within the bridge content, even for conditions where the flow remains attached.

Considering that the bending bridges measure the strain caused by the overall load acting from their position until the end of the blade (i.e. $0.8 \leq x/R \leq 1$ for FB3 and $0.62 \leq x/R \leq 1$

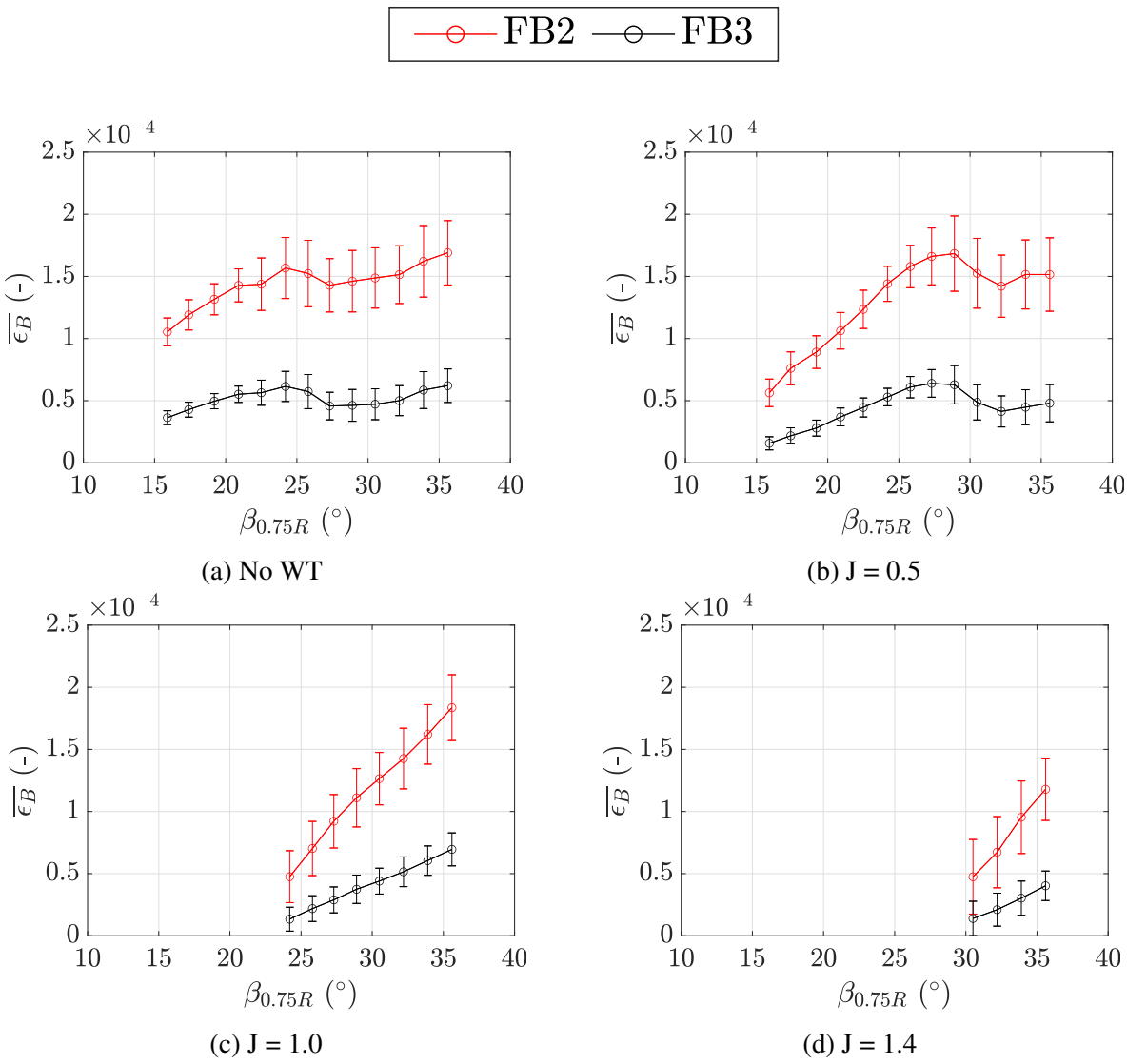

(a) No WT

(b) J = 0.5

(c) J = 1.0

(d) J = 1.4

Figure 4.3: Corrected strain for bridges FB2 and FB3 at 1080 RPM as a function of the blade pitch angle. Standard deviation of the measurements has been added as error bar.

for FB2), and after the stall onset both FB2 and FB3 readings drop by roughly the same amount, this suggests that most of the stall develops towards the blade tip.

This can be better quantified by looking at Figure 4.4a, where the standard deviation of the flap bending bridges is presented against the blade pitch. Prior to stall, the standard deviation remains roughly constant and approximately doubles after stall onset for both flap bending bridges. This holds true also at higher advance ratios such as the $J = 0.5$ case where stall is still present, as shown in Figure 4.4b. Furthermore, at large advance ratio cases where there is no presence of separation, shown in Figure 4.4, the standard deviation remains relatively constant.

Torsional strain measurements were obtained using torsional (T) bridges T1 and T2 positioned at $x/R = 0.45$ and $x/R = 0.75$ respectively, as shown in Figure 3.10. Readings of the corrected strain for bridges T1 and T2 at 1080 RPM for the following advancing conditions: J

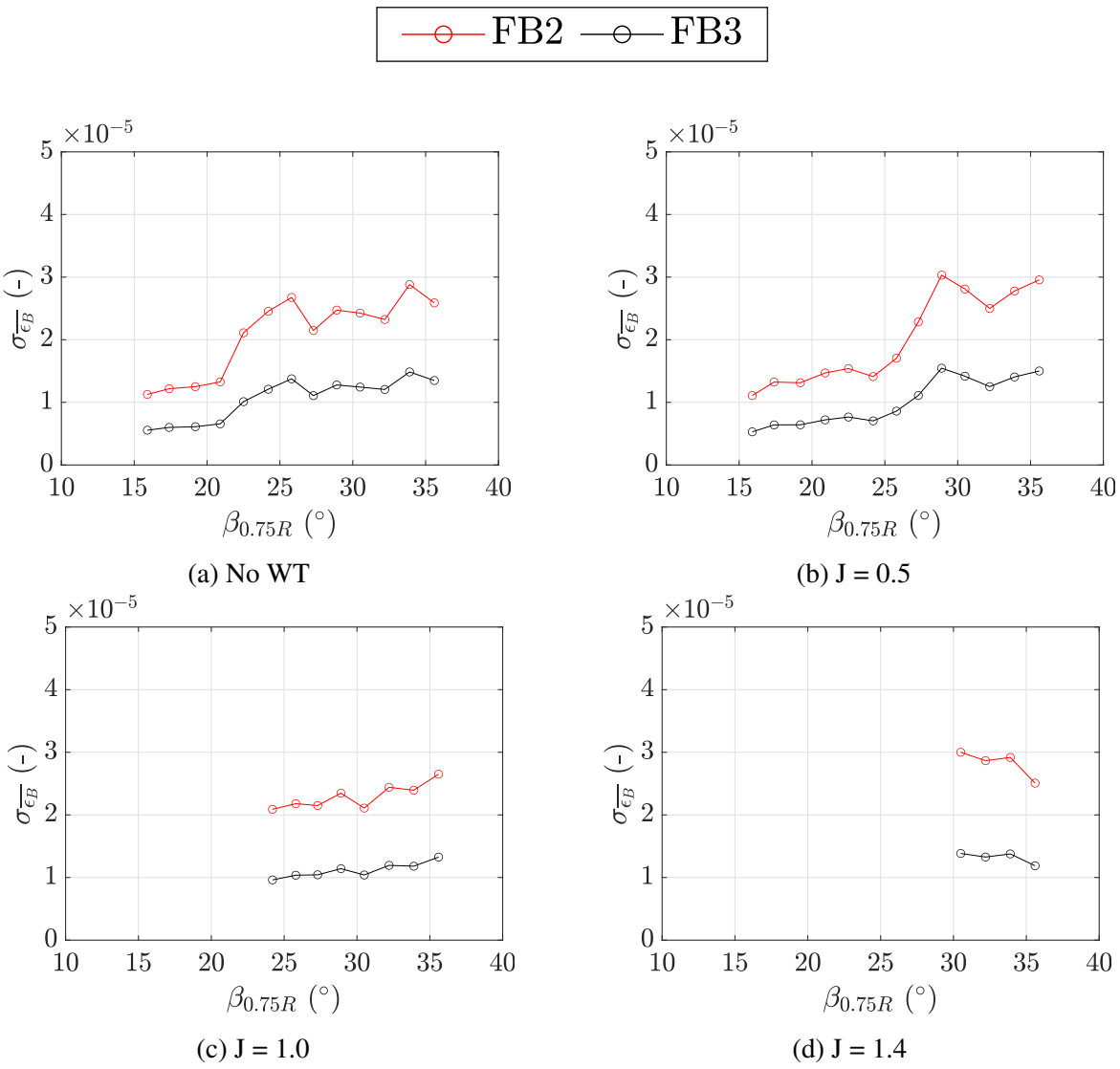

(a) No WT (b) J = 0.5

(c) J = 1.0 (d) J = 1.4

Figure 4.4: Standard deviation of corrected strain ($\sigma_{\overline{\epsilon_B}}$) for bridges FB2 and FB3 at 1080 RPM as a function of the blade pitch angle.

= “No WT" case, 0.5, 1.0 and 1.4, as a function of the blade pitch angle are displayed in Figure 4.5. Similar to the flap bending bridges, departure from linear behaviour of the torsional strain can be used to indicate the onset of stalled flow. It can be observed that for all J cases shown within Figure 4.5, torsional bridges T1 and T2 have opposing signs, indicating that they are under strain in opposing directions. In a physical sense, this means that the more outboard bridge T2 is twisting in a nose down direction as opposed to the more inboard bridge, T1, rotating in a nose up direction.

Focusing firstly on the “No WT" case shown in Figure 4.5a, it is clear from measurements of T2, that there is an abrupt change in the strain magnitude at $\beta_{0.75R} > 22.5°$ indicating an onset of stall. This explanation of the behaviour of the T2 bridge, can be supported by a growth in the standard deviation of the measurement, similar to that of the flap bending bridges. Furthermore,

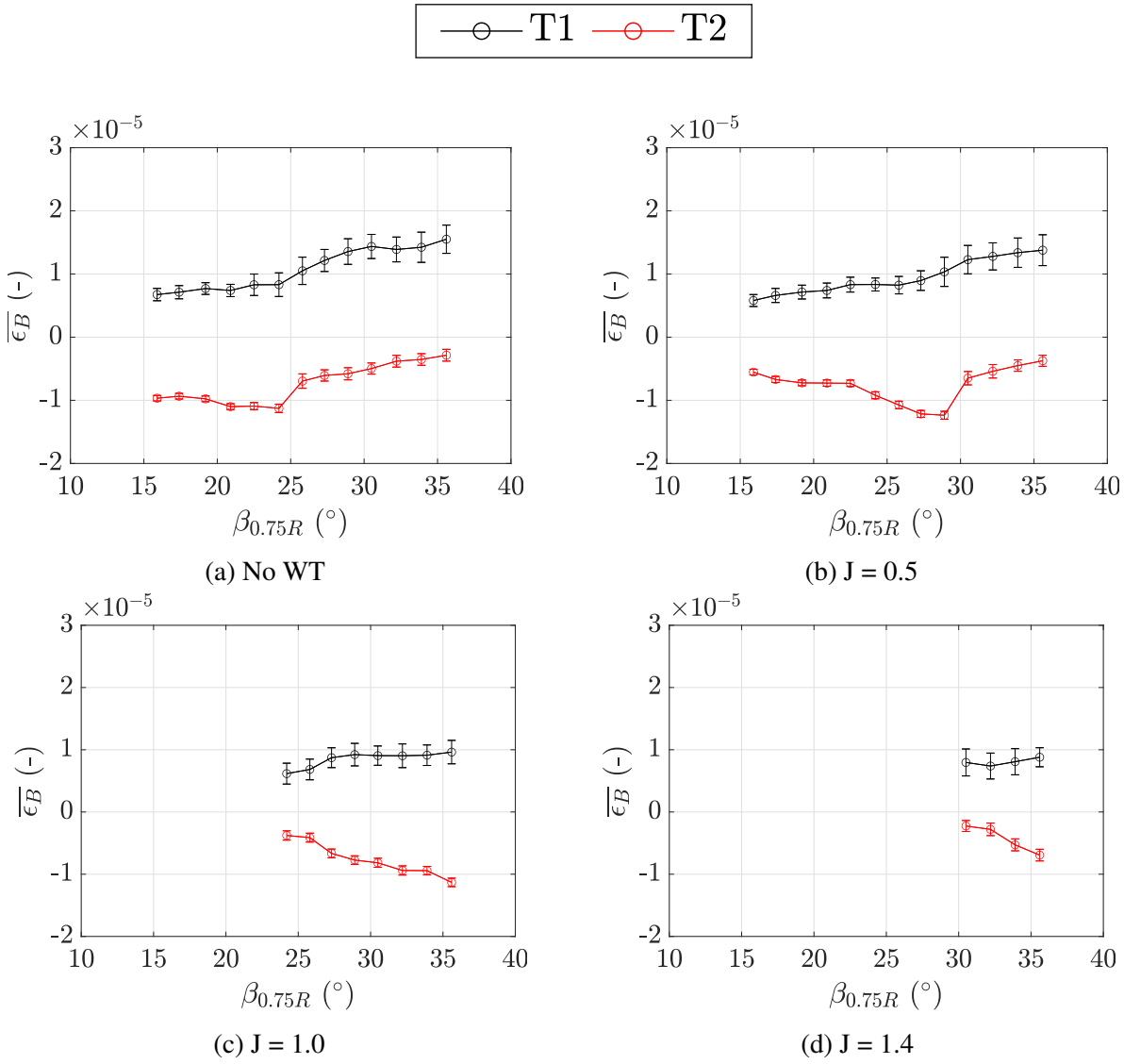

(a) No WT (b) J = 0.5

(c) J = 1.0 (d) J = 1.4

Figure 4.5: Corrected strain for bridges T1 and T2 at 1080 RPM as a function of the blade pitch angle. Standard deviation of the measurements has been added as error bar.

for $\beta_{0.75R} \geq 22.5°$, the reduction in negative strain (tending towards zero in absolute terms) shows the blade section is twisted in the upwards direction to a less nose down position. Alternatively, T1 is shown to grow positively in strain, relatively linearly, representing a increasing nose up position for an increasing blade pitch. Moreover, similar to T2, T1 shows a growing in standard deviation measurements for $\beta_{0.75R} \geq 22.5°$, further supporting the presence of stalled flow. Figure 4.5b shows a similar behaviour to that of the “No WT" case with deviation from linear behaviour for T2 occurring at a larger blade pitch of $\beta_{0.75R} = 28.9°$ for J = 0.5 at 1080 RPM. Again, similar to the flap bending bridge measurements, this can be attributed to increased advance velocity conditions, delaying the onset of stall.

In addition, Figures 4.5c and 4.5d show larger advance conditions of J=1.0 and 1.4, respec-

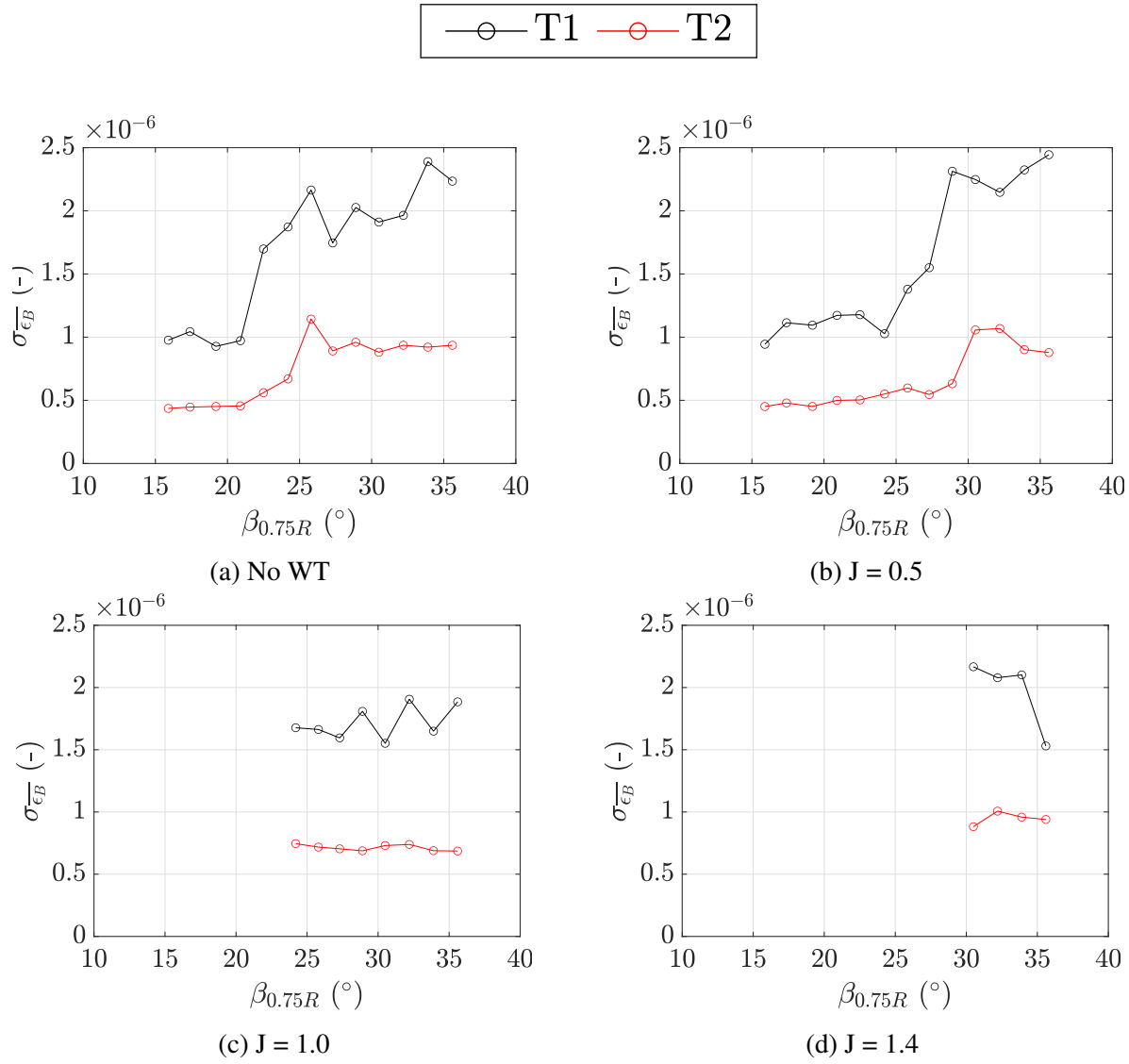

(a) No WT (b) J = 0.5

(c) J = 1.0 (d) J = 1.4

Figure 4.6: Standard deviation of corrected strain ($\sigma_{\overline{\epsilon_B}}$) for bridges T1 and T2 at 1080 RPM as a function of the blade pitch angle.

tively. It is clear from both of these plots that both T1 and T2 bridges continue to follow a linear trend with increasing blade pitch. Moreover, a consistent standard deviation indicates that the follow has limited unsteadiness and remains largely attached, thus demonstrating a similar behaviour as the flap bending bridges. Measurements of torsional standard deviation, shown in Figure 4.6, highlight an identical behaviour to that of the flap bending bridges. Furthermore, when considering the behaviour of both the torsional and flap bending strain measurements as a function of blade pitch, it can be inferred that the blade stall manifests towards the tip and moves further inboard towards the root with cases of deep stall.

4.3.2 Effect of Advance Ratio on Corrected Blade Strain

Propeller aerodynamic loading varies with change in advancing velocity at which it is operating. Therefore, an effect on propeller structural behaviour is to be expected. The effect of varying the propeller advance ratio is displayed using the strain readings from the FB2 and FB3 bridges, presented in Figures 4.7 and 4.8, respectively. Firstly, it should be reminded that the "No WT" curve, differently from the other advance ratios, was not obtained at constant advance ratio, as this would depend on the specific pitch setting ($0.22 \leq J \leq 0.30$ for 1080 RPM and $0.22 \leq J \leq 0.33$ for 1800). The J ranges for alternative RPM values can be obtained from Figure 4.1.

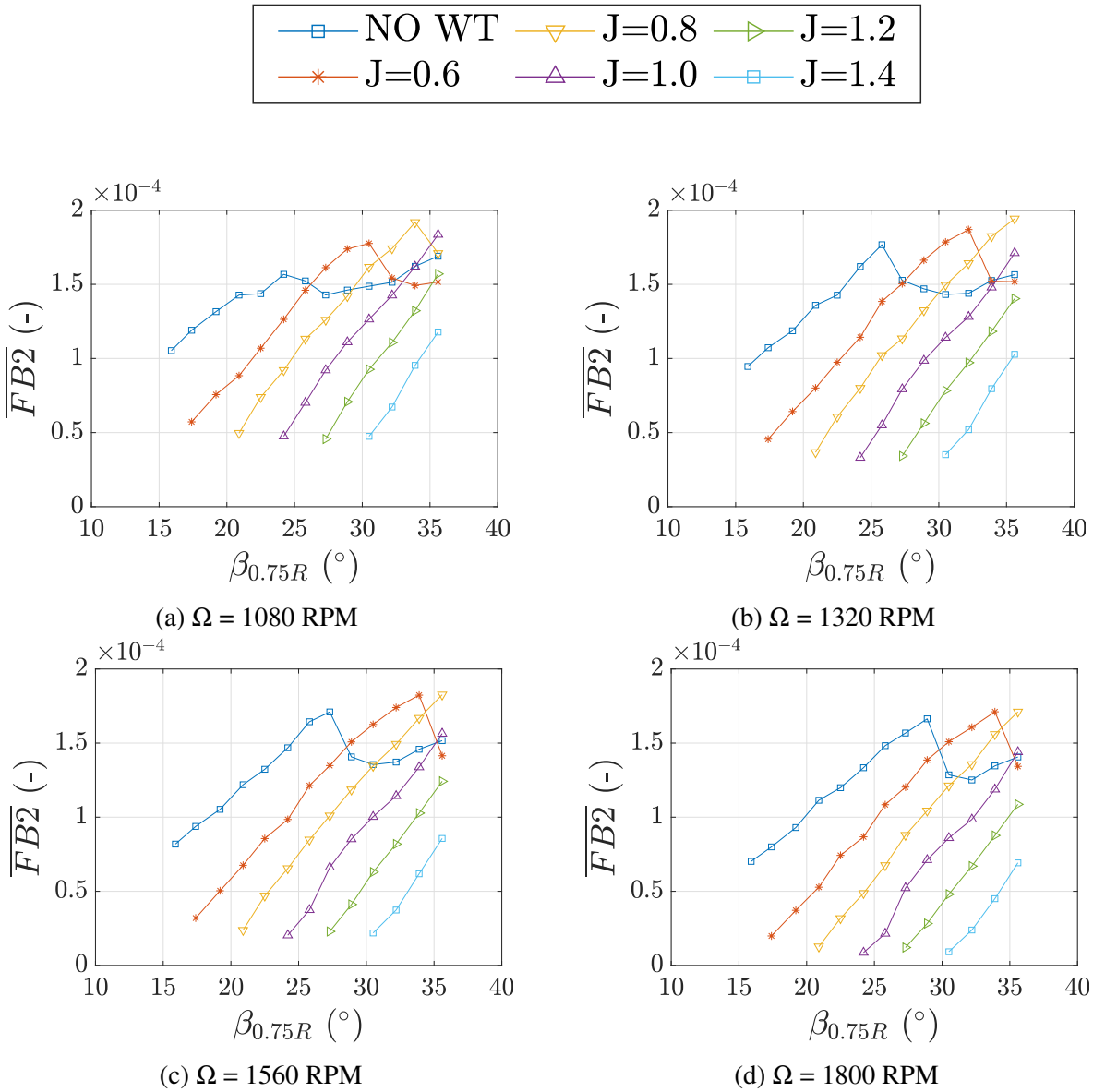

(a) Ω = 1080 RPM

(b) Ω = 1320 RPM

(c) Ω = 1560 RPM

(d) Ω = 1800 RPM

Figure 4.7: Corrected strain for bridge FB2 as a function of the blade pitch for various J.

Figure 4.7 displays the measurements of bending obtained from the FB2 bridge across the rotational frequency range tested ($\Omega = 1080 - 1800$ RPM). At rotational frequencies before stall, an increase in forward speed causes a decrease in the bending reading, as the effective AoA the blade is subjected to decreases. This can be seen clearly when looking at 1080 RPM (Figure 4.7a) and 1800 RPM (Figure 4.7d) in isolation, with many J conditions at 1800 RPM approaching a zero value, with any negative reading indicating a reversal of bending direction.

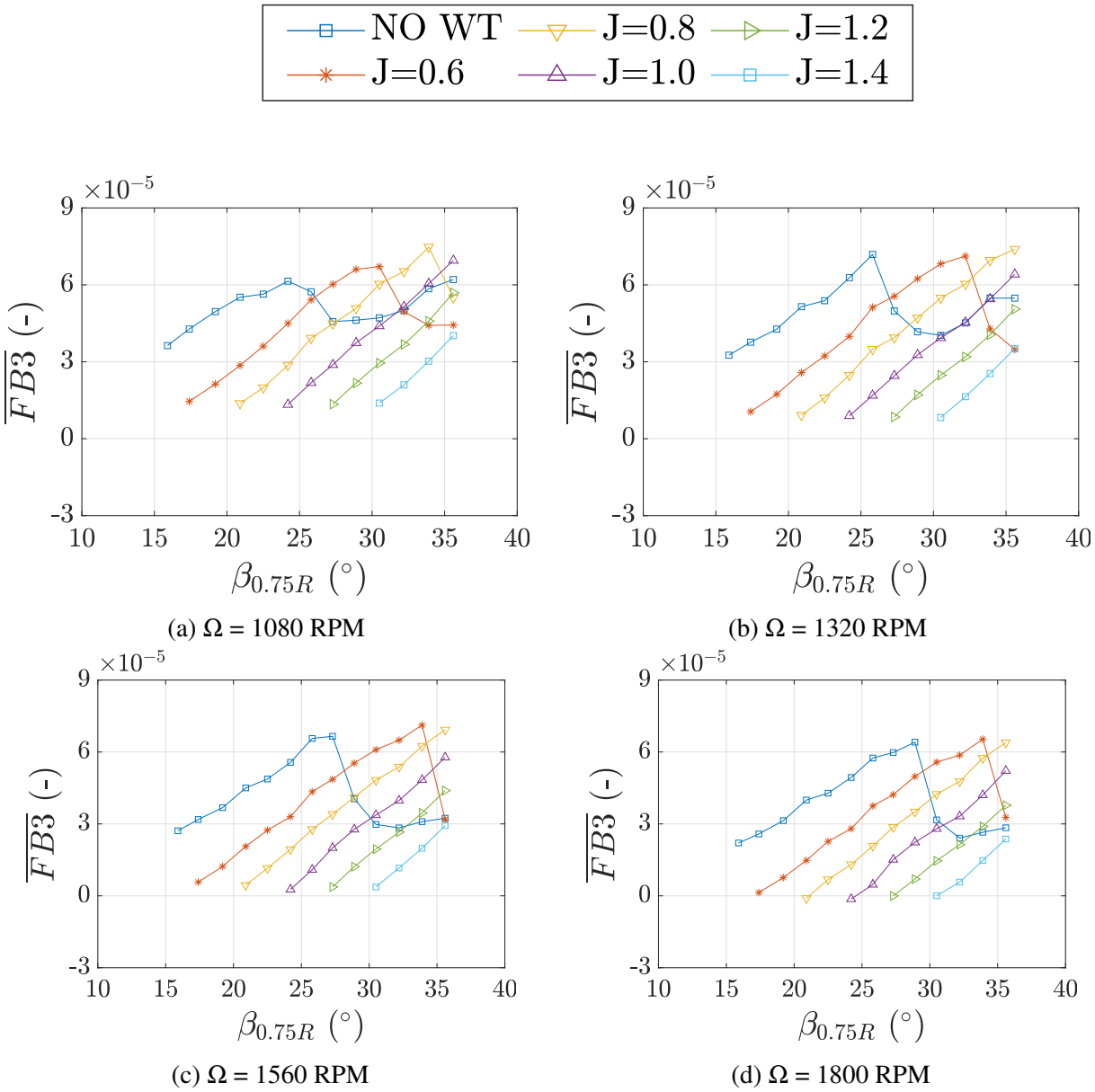

(a) Ω = 1080 RPM

(b) Ω = 1320 RPM

(c) Ω = 1560 RPM

(d) Ω = 1800 RPM

Figure 4.8: Corrected strain for bridge FB3 as a function of the blade pitch for various J.

A reversal of bending direction is explained by a negative local AoA, resulting in a reversal of the direction of aerodynamic loading due to an excessive freestream velocity at a given rotational frequency. This is apparent when focusing on FB3 (Figure 4.8), located more outboard towards

the blade tip, as the local resultant velocity seen by the blade is larger due to an increased contribution from the rotational frequency. Focusing on measurements of FB3 at a rotational frequency of 1800 RPM (Figure 4.8d), it is clear for advance conditions of J > 0.6, readings of FB3 are zero or negative, indicating thrust reversal at this section of the blade. It should be noted that the blade as a whole can continue to produce positive thrust. However, during testing negative FB3 readings were used as a marker to indicate the negative thrust boundary of the aerodynamic section at the FB3 radial location on the blade and therefore testing was stopped to prevent the scenario where the entire blade was operating in a reverse thrusting condition.

Moreover, an increasing advance ratio also results in the growth of the angle of attack at which the blade sees flow separation and at which stall occurs. As displayed in Figures 4.7 and 4.8, the peak of the strain curve moves to larger $\beta_{0.75R}$ values, delaying the onset of the stall. Furthermore, for both FB2 and FB3 measurements, at an equal advance ratio, the stall angle is always smaller in the 1080 RPM case with respect to the 1800 RPM case, reinforcing again the idea that low RPM propellers tend to stall sooner, even at larger advance ratios.

Torsional measurements presented in Figures 4.9 and 4.10, respectively, also support the notion that the introduction of an advance velocity delays the onset of stall. Measurements of torsional strain obtained from the T1 bridge are presented in Figure 4.9. At first glance, the data presented could easily be misinterpreted to suggest that the T1 bridge cannot be used to identify the presence of stall onset. However, similar to that of the flap bending bridges, the T1 bridge is located closer to the blade root than that of T2. Therefore, the T1 measurement shows the contribution of torsional strain from the T1 bridge radial location to the blade tip, which is larger than that of T2. This means that any structural torsional strain at inboard locations is more nuanced and therefore more difficult to visually appreciate when compared to the results of T2, shown in Figure 4.10.

Considering the "No WT" curve of T1 and T2 bridges for the 1080 RPM case, it is clear from the T2 behaviour (Figure 4.10a) that the blade pitch angle at which stall onset begins to occur is $\beta_{0.75R} \geq 24.2^{\circ}$ as there is a prominent change in magnitude in the measured strain. When focusing attention on T1 (Figure 4.9a), the blade pitch at which stall onset is identified is also shown to be $\beta_{0.75R} \geq 24.2^{\circ}$. However, when considering this behaviour in the context of the flap bending bridges, there is a disagreement between flap and torsion bridges on where stall onset manifests. The pitch angle at which stall onset presents itself has been shown to be larger for torsional bridges, implying that a noticeable change in the torsional behaviour of the blade is present only for more developed stages of the blade stall. A further explanation that supports this observation is that the blades have a larger torsional stiffness than that of flap bending stiffness, thus the flap bending behaviour of the blade will dominate when the blade is subjected to aerodynamic loads.

Therefore, focusing on measurements obtained from the T2 bridge, shown in Figure 4.10, it is clear that the torsional measurements can also be used to appreciate the delay in onset of

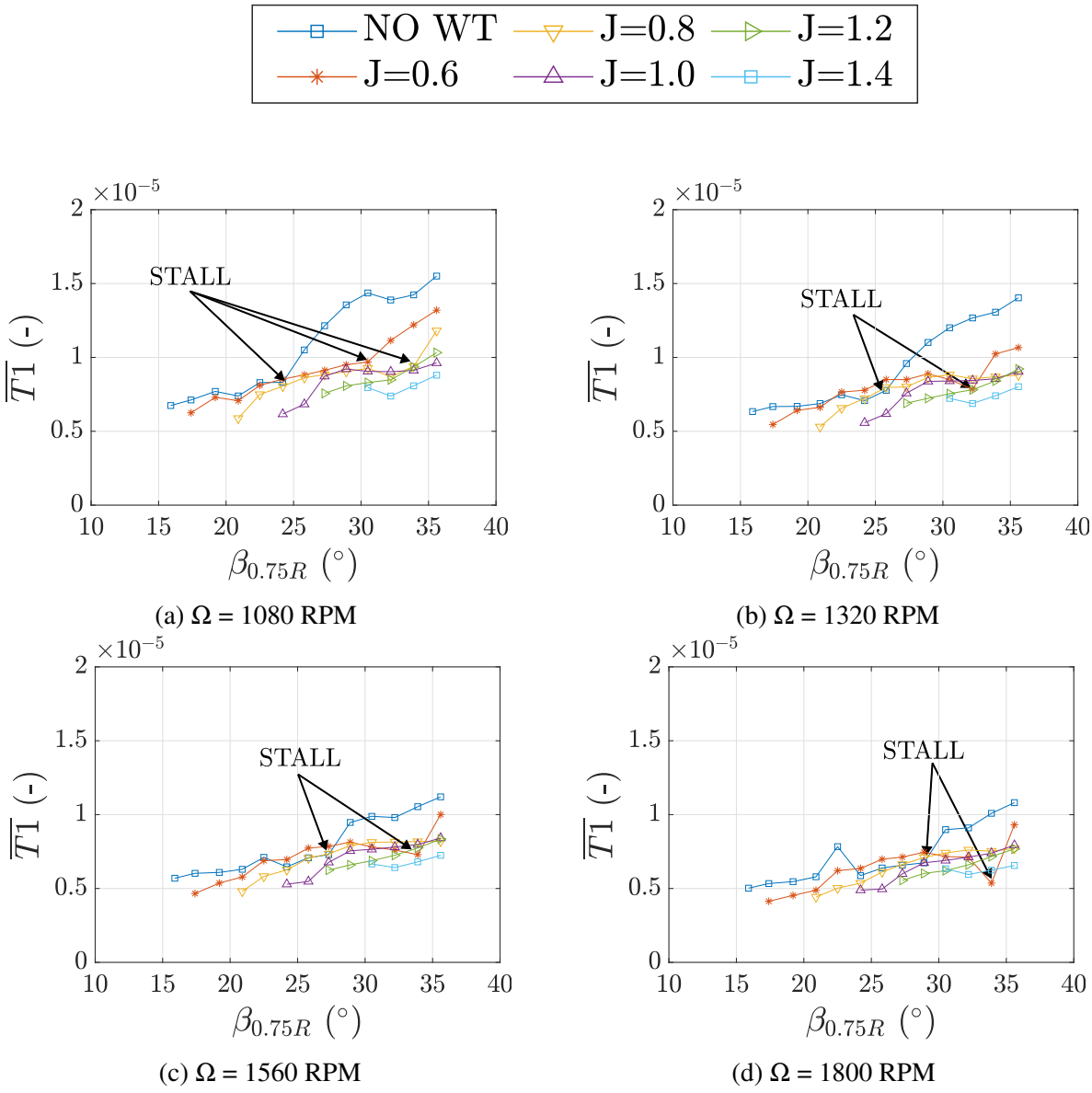

(a) Ω = 1080 RPM

(b) Ω = 1320 RPM

(c) Ω = 1560 RPM

(d) Ω = 1800 RPM

Figure 4.9: Corrected strain for bridge T1 as a function of the blade pitch for various J.

stall with increasing advance ratio. Despite the ability to capture the behaviour similar to the results of the flap bending bridges, torsional bridges appear less reliable in detecting stall onset than that of the flap bending, as torsional bridges displayed large variations only in deeper stall conditions.

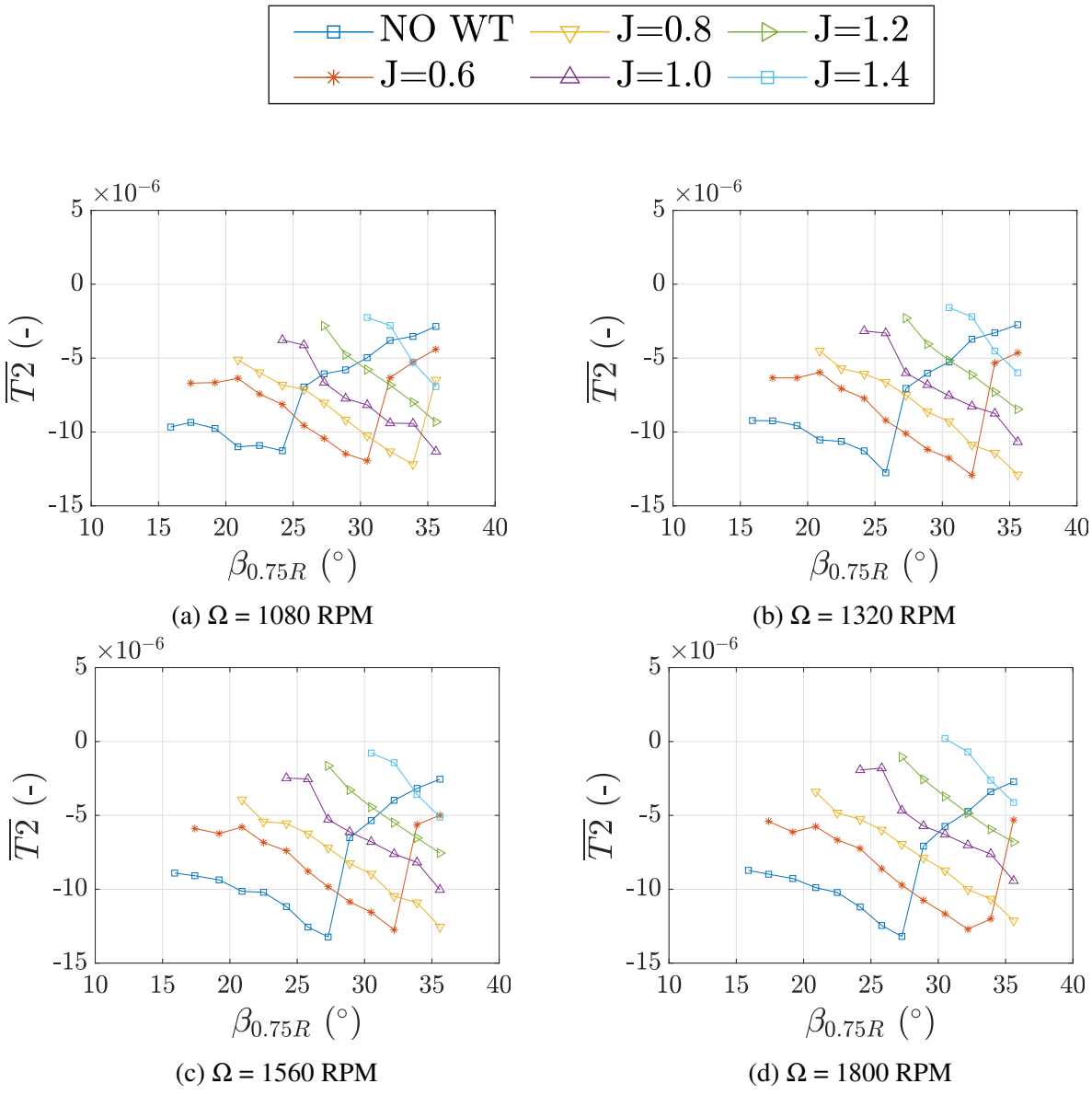

(a) Ω = 1080 RPM

(b) Ω = 1320 RPM

(c) Ω = 1560 RPM

(d) Ω = 1800 RPM

Figure 4.10: Corrected strain for bridge T2 as a function of the blade pitch for various J.

4.3.3 Effect of Rotational Frequency on Corrected Blade Strain

The notion that low RPM propellers tend to stall sooner than high RPM propellers, even at larger advance ratios can also be appreciated from Figures 4.11 and 4.12, highlighting the effect of varying RPM for a given advance ratio, for both FB2 and FB3 bridges, respectively.

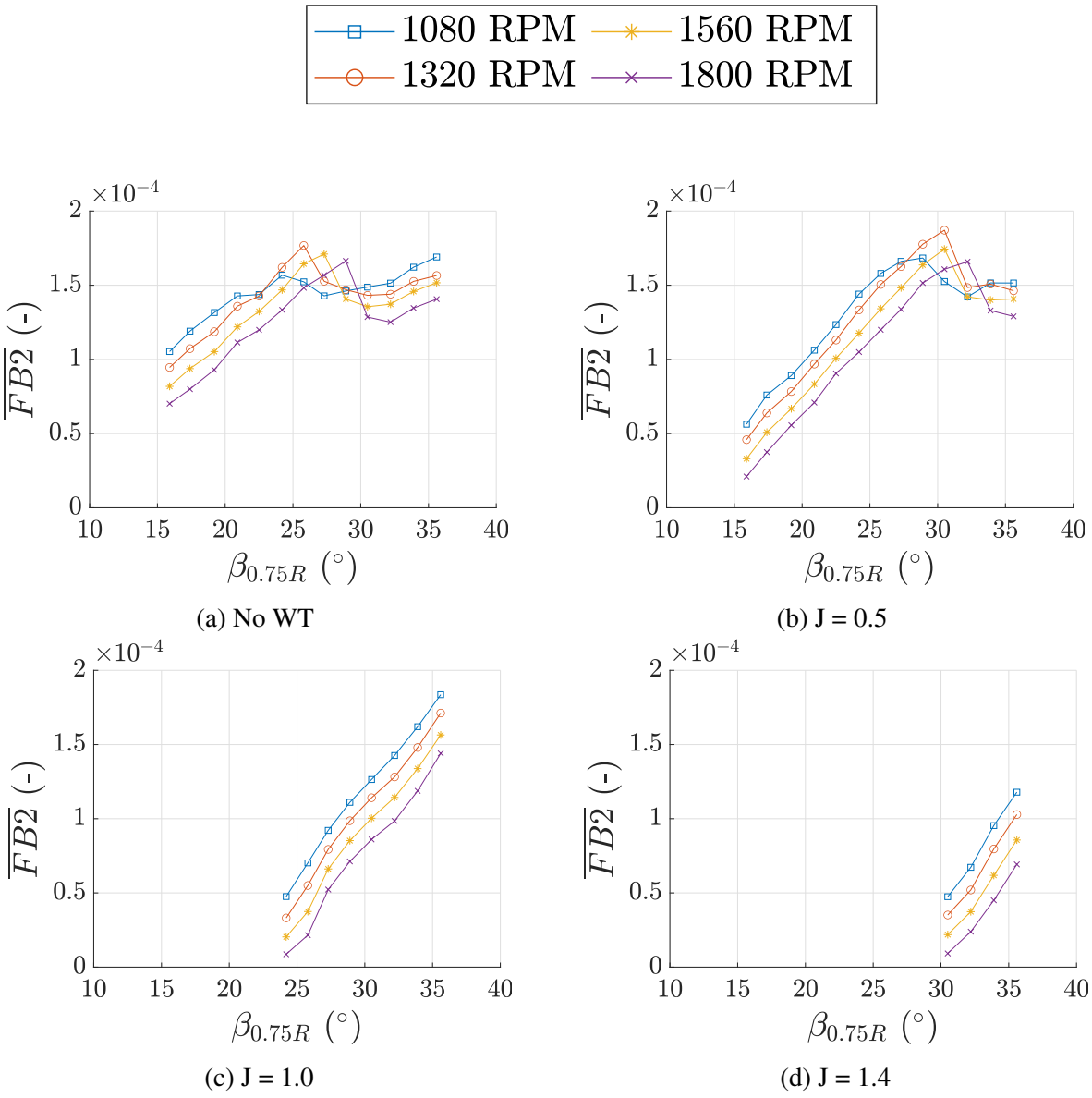

(a) No WT

(b) J = 0.5

(c) J = 1.0

(d) J = 1.4

Figure 4.11: Corrected strain for bridge FB2 as a function of the blade pitch for various RPM.

It should be noted that if the strain data were not corrected, the curves for different rotational frequencies would be on completely different scales due to the change in the dynamic pressure seen by the blade, hence different aerodynamic loading. Therefore, by applying the compensation, the results are effectively compared as if the same dynamic pressure were present on the blades. In the not stalled region this allows for the appreciation of the centrifugal stiffening of

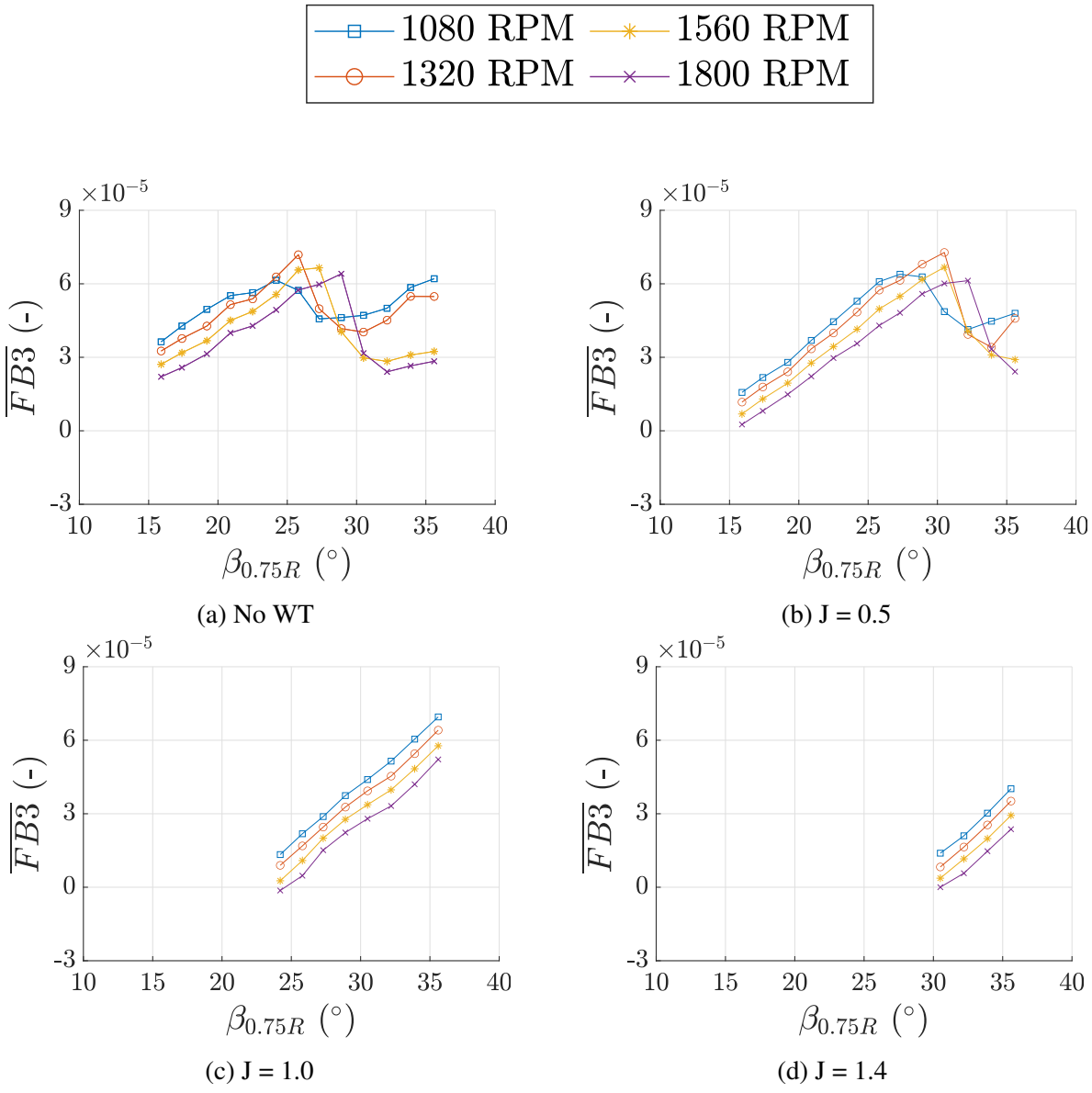

(a) No WT

(b) J = 0.5

(c) J = 1.0

(d) J = 1.4

Figure 4.12: Corrected strain for bridge FB3 as a function of the blade pitch for various RPM.

the blades, that causes smaller corrected deformations for larger rotational speeds.

Focusing on the "No WT" flap bending results shown in Figures 4.11a and 4.12a, as expected, it is clear for an increasing rotational frequency the blade pitch at which stall onset occurs is delayed. Corrected FB2 and FB3 results indicate an identical stall onset angles for all rotational frequencies tested, despite the non-constant advance ratio. However, to isolate the effects of increased rotational frequency, a constant advance ratio of J = 0.5 is presented in Figures 4.11b and 4.12b to highlight the influence of RPM for conditions which are both attached and stalled. It is apparent when compared to their respective "No WT" curves that the trend of the FB2 and FB3 curves prior to the stall angle, appear more linear than that of the wind off cases. Furthermore, as blade centrifugal force (F_c) grows with the square of the rotational frequency,

it is therefore expected that the centrifugal loading will reduce the blade deformation imposed by the aerodynamic loading without the presence of rotation and therefore a reduction in strain is expected for increased rotational frequencies. This effect can be clearly appreciated for both FB2 and FB3 bridge measurements at values of advance ratio greater than one, where stall is not present.

This delay in the development of stall for larger rotational frequency conditions can be explained by an increased Reynolds number at which the blade aerodynamic sections are operating. This increase in Reynolds number can be attributed to the larger relative velocity at which the individual aerofoil sections are subjected to, as a result of an increased Ωx velocity component. Furthermore, the increase in relative velocity further energises the sectional boundary layer, imposing the necessity for an increased adverse pressure gradient to promote flow separation, when compared to lower Reynolds number cases. To further support earlier onset of stall at lower RPM conditions, 2D aerodynamic lift and drag polars of the Vertol 23010-1.58 aerofoil section, displayed in Figure 4.13, were obtained using XFOIL. The Vertol 23010-1.58 aerofoil, shown in Figure 2.4b, was selected for analysis as it is the aerofoil utilised at the blade tip of the MENtOR blade set. Reynolds numbers were computed for both $Re = 288 \times 10^3$ (1080 RPM) and $Re = 481 \times 10^3$ (1800 RPM) conditions at the blade tip, using the 60 mm blade tip chord as the length scaling parameter.

Figure 4.13 presents the C_l vs α polar through an angle of attack range of 0° to 18°. Upon inspection, it is shown that there is some small delay in the point at which the aerofoil stall angle occurs, approximately at $\alpha = 13^\circ$ to 14°. For the $Re = 481 \times 10^3$ case, this subtle postponement of the stall can be better appreciated by the increased C_l value for conditions at which $\alpha = 10^\circ$ to 13°. Furthermore, the $Re = 288 \times 10^3$ case at $\alpha = 10^\circ$ displays a reduction in the $C_l - \alpha$ gradient, thus suggesting an earlier stall onset when compared to a larger Reynolds number condition. It is also observed for both $Re = 288 \times 10^3$ and $Re = 481 \times 10^3$ at $\alpha = 1^\circ$ to 3° there is a noticeable kink from the anticipated linear trend suggesting the presence of a laminar separation bubble and turbulent reattachment. However, it should be noted that this observation is less significant at the $Re = 481 \times 10^3$ condition. This prominent variation in lift can be explained by the use of the Vertol 23010-1.58 aerofoil section at low Reynolds numbers for which operation is not optimised. The MENtOR blade set was designed and optimised using high-fidelity CFD for operation at 3000 RPM [78], with a corresponding tip Reynolds number of $Re = 864 \times 10^3$, 3 times larger than the 1080 RPM value, thus again highlighting the delay in stall onset for propellers operating at larger rotational frequencies.

Analysis of torsional results, presented in Figures 4.14 and 4.15, highlights an identical behaviour pattern with that of the flap bending bridges. However, just like the effect of increasing advance ratio, the torsional results appear less reliable in determining the onset of the stall due to the very small magnitude changes in the torsional measurements that are a direct consequence of the increased torsional stiffness of the blades.

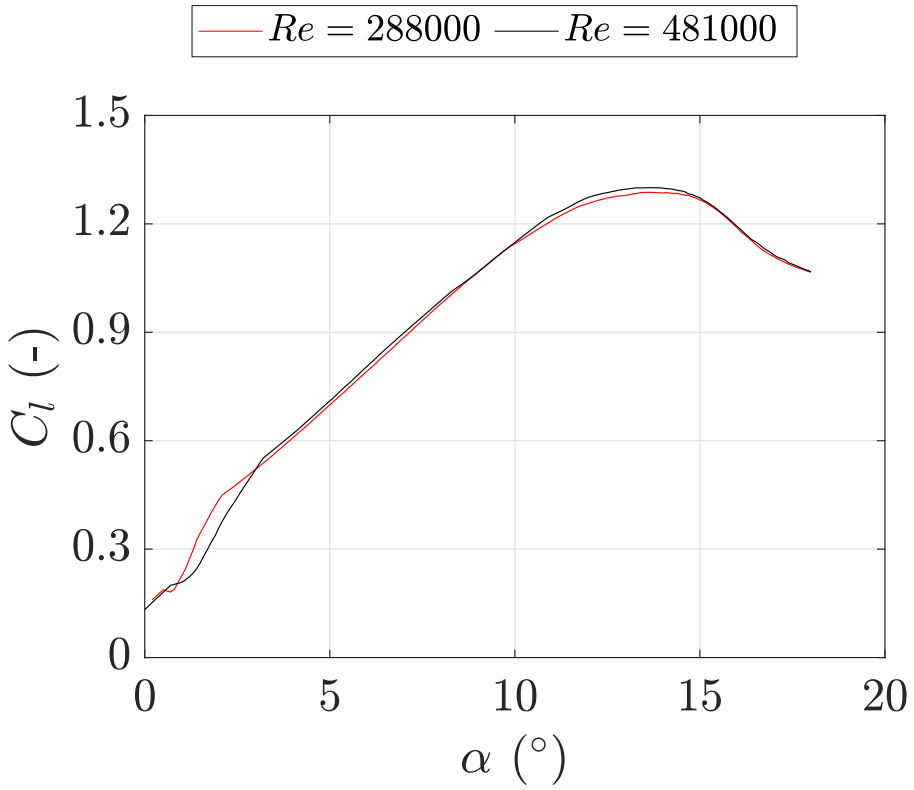

Figure 4.13: Coefficient of lift (C_l) polar for angle of attack (α) values ranging between 0° to 18° for a Vertol 23010-1.58 aerofoil implemented at the blade tip. Computations performed using XFoil for Reynolds numbers that represent the blade tip conditions at $Re = 288 \times 10^3$ (1080 RPM) and $Re = 481 \times 10^3$ (1800 RPM) $Re = 481 \times 10^3$.

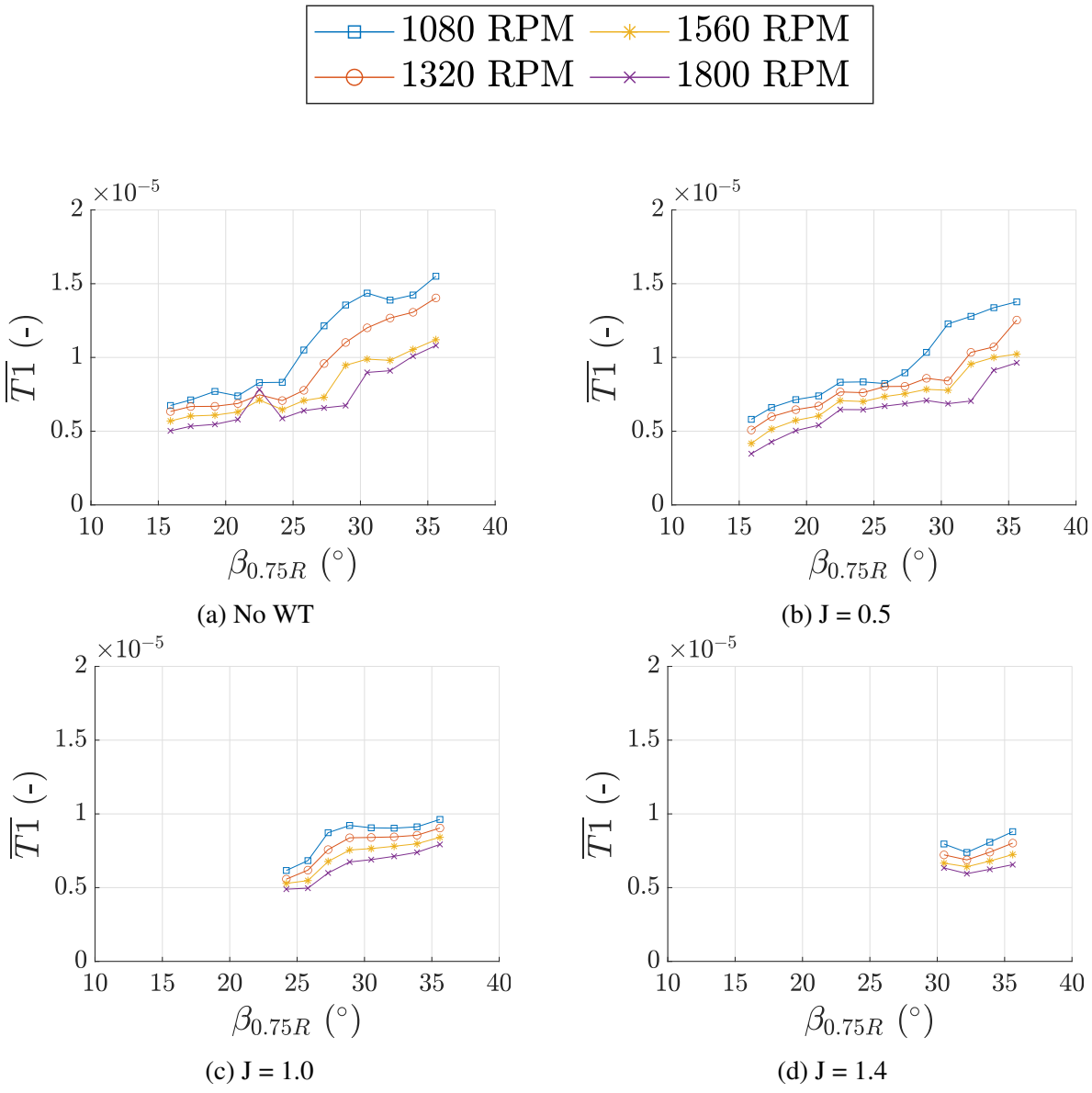

(a) No WT

(b) J = 0.5

(c) J = 1.0

(d) J = 1.4

Figure 4.14: Corrected strain for bridge T1 as a function of the blade pitch for various RPM.

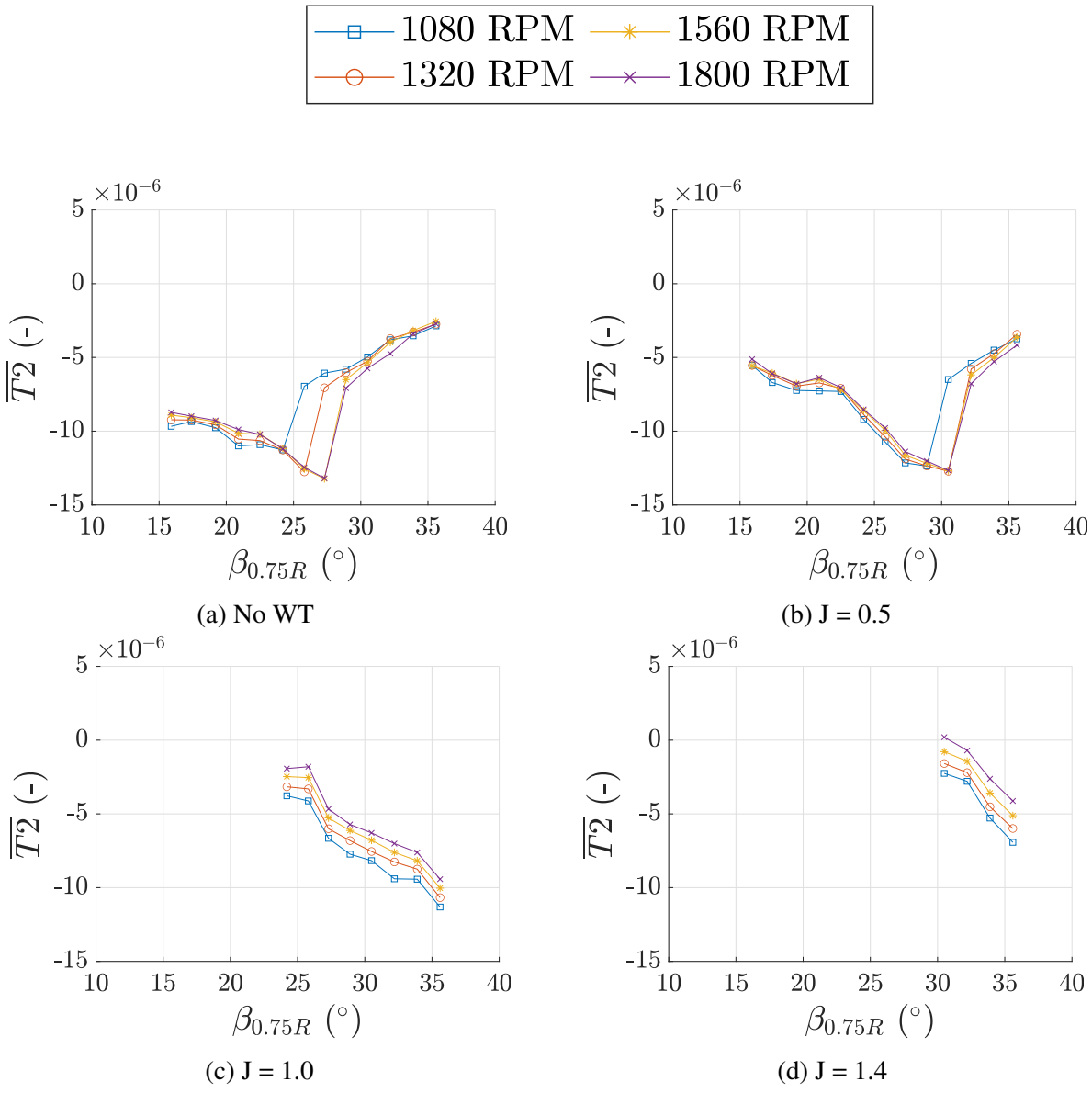

(a) No WT

(b) J = 0.5

(c) J = 1.0

(d) J = 1.4

Figure 4.15: Corrected strain for bridge T2 as a function of the blade pitch for various RPM.

4.4 Spectral Content and Time Histories

To further indicate the presence of operating conditions at which the propeller is stalled, analysis of the strain gauge spectral content and its time history was performed. Results for both flap-bending and torsional bridges are presented in Figures 4.16 - 4.19. All data analysed within Section 4.4 corresponds to a blade pitch of $\beta_{0.75R} = 30.5^o$, as this blade pitch case has already been identified to include cases at both stalled and non-stalled conditions based on the steady strain measurements. Plots of time history are shown as a function of the number of full propeller revolutions (N_{rev}), with 20 revolutions shown for both rotational frequencies of 1080 and 1800 RPM. It should be noted for the 1800 RPM case, the time taken to achieve 20 revolutions is smaller than that of the 1080 RPM case, therefore the timescales are not equivalent. Spectral content was also analysed by means of a Fast Fourier Transform (FFT). This was performed for all test points with data obtained over a 19.5 second sampling time, allowing for a frequency resolution (f_{res}) of 0.05.

Focusing attention to both the FB2 and FB3 bridges, displayed in Figures 4.16 and 4.17. Three advance velocities of J= “No WT”, 0.5 and 1.0 are presented to highlight cases which are stalled, partially stalled or at stall onset and cases which are attached showing no indication of stalled flow. Firstly, analysing the spectra content of FB2, Figure 4.16b clearly displays a large non-harmonic content across a broadband of frequencies for both 1080 and 1800 RPM, super-imposed to the underlying propeller harmonics at multiple integers of its rotational frequency. The amplitude of this broadband content is of the order of 10 to 20% of the maximum harmonic content.

Alternatively, Figure 4.16d presents the same rotational frequencies and blade pitch, however for an increased advance ratio of 0.5. Upon inspection, it is clear that the 1080 RPM case exhibits a similar behaviour to that of the corresponding "No WT" case (Figure 4.16b), whereas the 1800 RPM does not appear to show a large broadband content and is represented by the propeller harmonics only. This can be explained by the propeller not being stalled for the 1800 RPM case. It is expected that the spectral content of a propeller blade operating at a stalled condition will exhibit a significant non-harmonic content, where the signal energy is distributed amongst a large range of frequencies. This behaviour is driven by stall induced vortical structures being shed in the wake at frequencies that vary along the blade span x as the section relative velocity Ωx increases, which are not necessarily synchronised with the propeller harmonics, this is apparent in Figure 4.16d for the 1800 RPM case. Opposingly, a propeller rotating in a non-stalled condition should mainly display a content that is comprised of the fundamental frequency and its harmonics, this behaviour can be observed in the spectra content of FB2 at J=1.0, displayed in Figure 4.16f.

To corroborate this observation, the time histories of the strain signals over 20 revolutions are shown in Figures 4.16a, 4.16c and 4.16e. Focusing on the “No WT” case (Figure 4.16a), it is

clear that whenever the blade is stalled, no repeatable pattern and consistency in the amplitude of the oscillation can be found in the time histories, with aperiodic bursts present throughout the signal. Conversely, upon inspection of the 1800 RPM case at J = 0.5, Figure 4.16c, the signal clearly shows a repetitive pattern of consistent amplitude, as the 1/rev signal is apparent as a prominent downwards spike at equally spaced time intervals. This dominant 1/rev signal is believed to be an indicator of the influence between the measuring blade passing the rotor rig aerofoil strut, as measurements are obtained at a constant rotational frequency. Taking into consideration the J=1.0 case (Figure 4.16e), where the flow is understood to be attached, further evidence of a dominant 1/rev signal is apparent, thus supporting the belief that the dominant spike can be attributed to the influence of the rotor rig strut.

Shifting the focus to FB3 (Figure 4.17), it is clear that the explanation provided for the identification of stall using FB2 data can also be applied to that of FB3. The key difference is the variation in magnitude of the strain measurements, with measurements of FB3 smaller than that of FB2 by approximately one order of magnitude. Moreover, it is apparent from analysis of the time histories of FB2 and FB3 that the fluctuation from the mean measurement value is larger for FB2 than that of FB3. This is in agreement with the data presented in Figure 4.3, of which the error bars indicate the standard deviation. The Root Mean Square (RMS) is not required to further inform the behaviour of the measurement fluctuations as the measurement error is smaller than that of the unsteadiness observed, this can be understood from the excellent repeatability of the measurements.

Through observation of time histories and spectral content of FB2 and FB3 bridges, that unsteady strain data can be used in conjunction with steady strain measurements to identify cases at which the blades are operating in a stalled condition. Unsteady measurements of T1 and T2 bridges, shown in Figures 4.18 and 4.19, were also shown to agree with the unsteady flap bending measurements, therefore indicating the suitability to use strain measurements as a method to identify the aerodynamic boundaries of a propeller blade set.

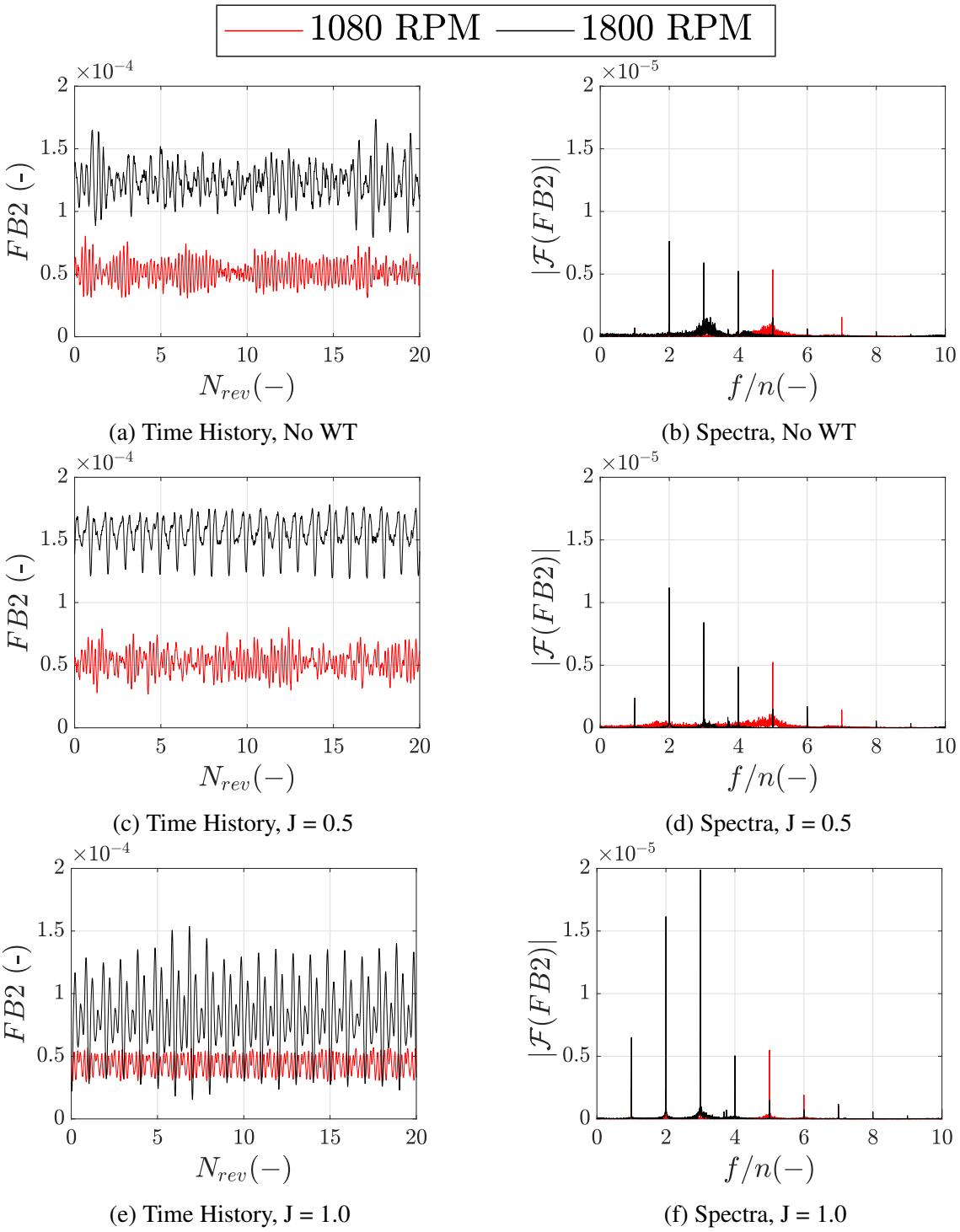

(a) Time History, No WT

(b) Spectra, No WT

(c) Time History, J = 0.5

(d) Spectra, J = 0.5

(e) Time History, J = 1.0

(f) Spectra, J = 1.0

Figure 4.16: Amplitude of the Fourier transform (as a function of the non dimensional frequency f/n) and time histories (as a function of the number of revolutions) of the uncorrected strain measurements for FB2 at $\beta_{0.75R} = 30.5°$.

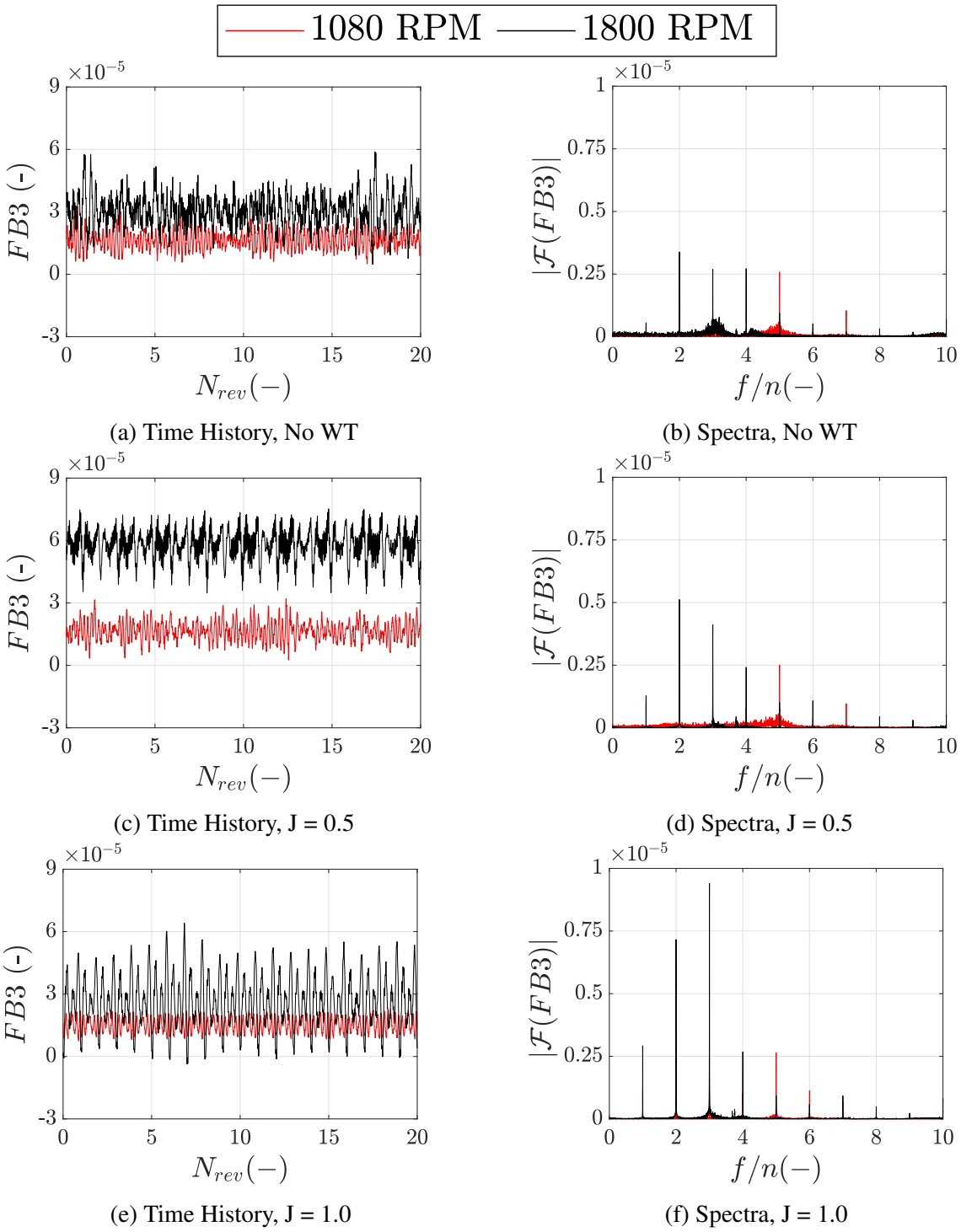

(a) Time History, No WT

(b) Spectra, No WT

(c) Time History, J = 0.5

(d) Spectra, J = 0.5

(e) Time History, J = 1.0

(f) Spectra, J = 1.0

Figure 4.17: Amplitude of the Fourier transform (as a function of the non dimensional frequency f/n) and time histories (as a function of the number of revolutions) of the uncorrected strain measurements for FB3 at $\beta_{0.75R} = 30.5°$.

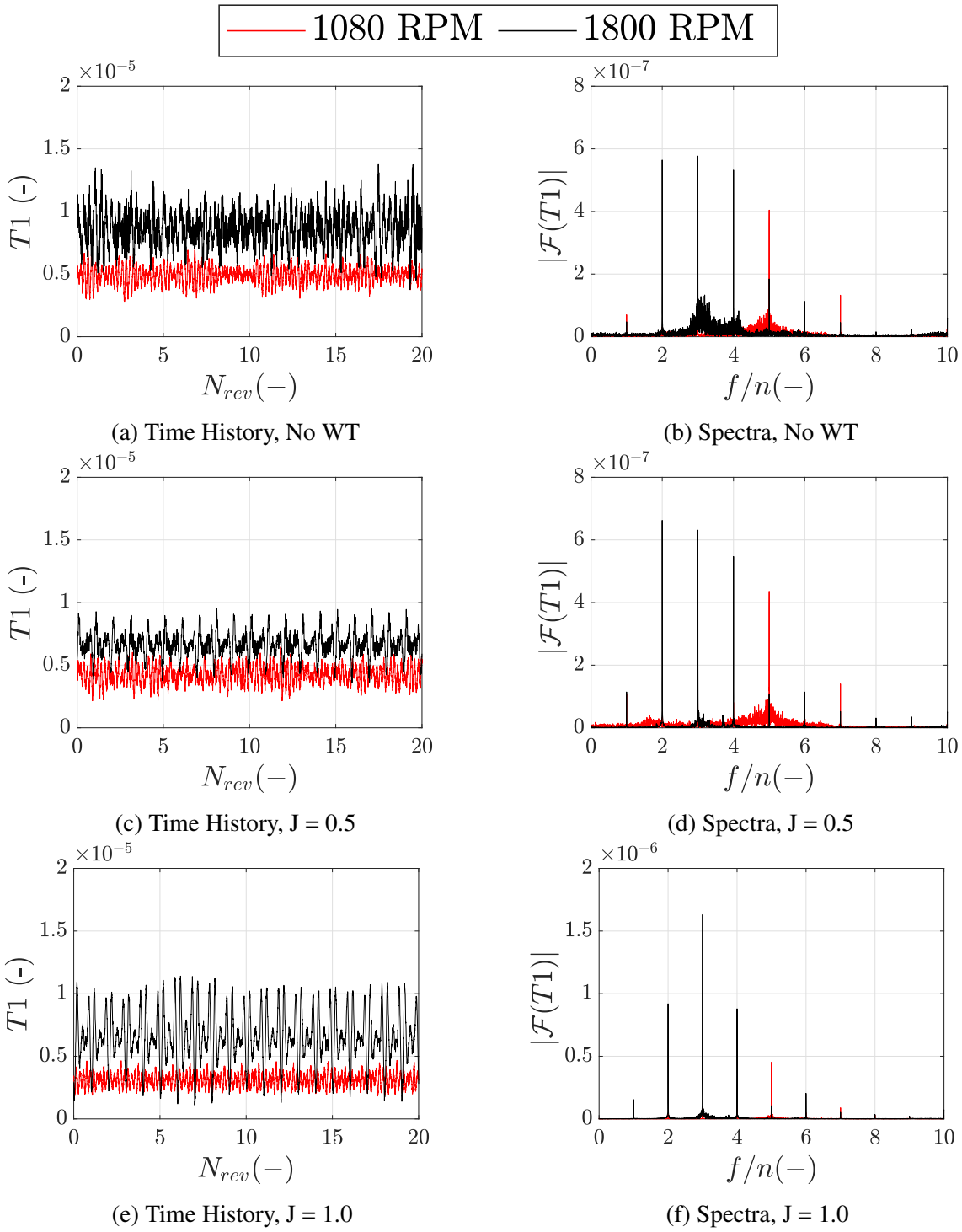

(a) Time History, No WT

(b) Spectra, No WT

(c) Time History, J = 0.5

(d) Spectra, J = 0.5

(e) Time History, J = 1.0

(f) Spectra, J = 1.0

Figure 4.18: Amplitude of the Fourier transform (as a function of the non dimensional frequency f/n) and time histories (as a function of the number of revolutions) of the uncorrected strain measurements for T1 at $\beta_{0.75R} = 30.5°$.

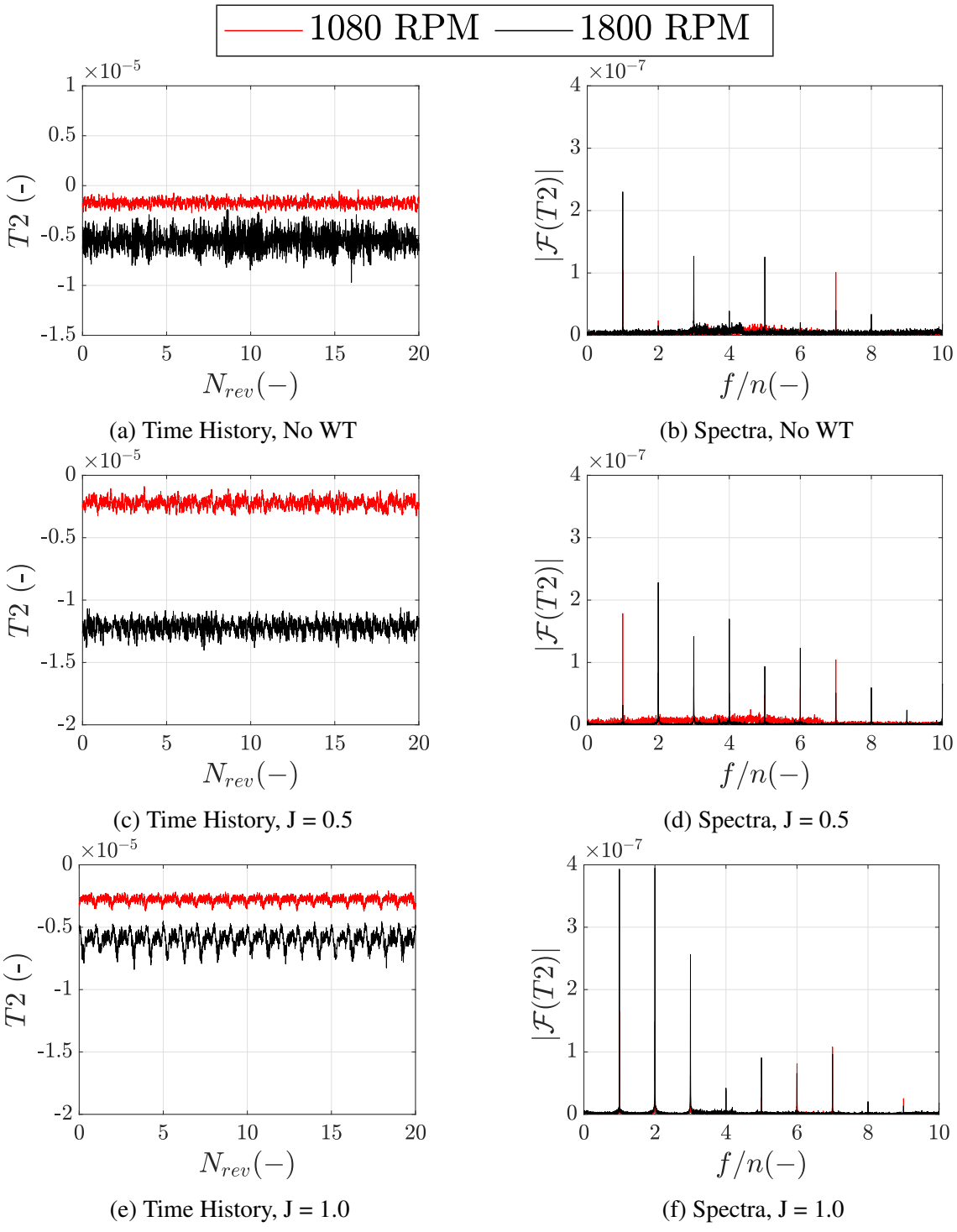

(a) Time History, No WT

(b) Spectra, No WT

(c) Time History, J = 0.5

(d) Spectra, J = 0.5

(e) Time History, J = 1.0

(f) Spectra, J = 1.0

Figure 4.19: Amplitude of the Fourier transform (as a function of the non dimensional frequency f/n) and time histories (as a function of the number of revolutions) of the uncorrected strain measurements for T2 at $\beta_{0.75R} = 30.5°$.

4.4.1 Blade Modal Identification

Until this point, strain data presented has been primary discussed in the aerodynamic context regarding stall identification. However, due to the nature of strain gauge measurements providing insight into the blade structural response, this subsection will shift the focus to the blade structural response, primarily through the identification of blade elastic mode eigenfrequencies.

Therefore, to address the blade structural response in context of the blade aerodynamics, returning to Figure 4.16b, it can be appreciated that the peak of the non-harmonic content is located just past the 3/rev for the 1800 RPM case and just past the 5/rev for the 1080 RPM case, which translate to the same dimensional frequency of approximately 90 to 100 Hz. This is very close to the numerically estimated 1st flap bending frequency (113 Hz), which suggests that the blade structural response to the broadband content of the stall cell shedding mainly manifests as an excitation of the first flap bending mode.

To better highlight the blade structural response, the spectral content is also presented for both flap bending and torsional bridges against a larger range of dimensional frequency (up to 1200 Hz) using a logarithmic scale, as shown in Figures 4.20 and 4.21. Vertical lines have been included in correspondence of the numerical (solid) and estimated experimental (dashed) mode frequencies. The choice of the logarithmic scale allows us to show the contribution of less energetic modes which would not be discernible from the background noise using a linear scale. Looking at Figure 4.20a, the main non-harmonic peak corresponding to the first flap bending mode is clearly present at approximately 90 to 100 Hz and is well captured by the numerical estimate. A secondary peak, whose amplitude is approximately one order of magnitude less than the first, is shown to occur at approximately 300 Hz and is expected to represent the second flap bending mode. The agreement between the numerical and experimental estimate of the mode frequency is found to be strong for the first, more energetic, flap bending mode. However, for higher order modes, this correlation is shown to degrade. This can be attributed to how the physical constraints on the blades are enforced, both numerically and on the experimental rig. Some small level of flexibility of the hub kinematics was observed during the rig operation, which could have affected the clamped constraint at the blade root, so that the conditions would slightly differ from the idealised constraint in the numerical simulations.

Table 4.2: Summary of the main blade eigenfrequencies identified via experimental measurements of strain gauge bridges.

Mode Shape	Mode Number	Range of f_m (Hz)
1st Flap Bending	1	90-100
2nd Flap Bending	2	295-305
3rd Flap Bending	3	452-462
1st Torsion - Flap Bending	4	804-814

Shifting the focus back towards stalled and non-stalled conditions, it can be observed for larger advance ratio cases such as the $J = 0.5$ case, shown in Figure 4.20a, that there is an increase in the signal amplitude at the lower frequency range at 1080 RPM, at which stall is present, with respect to the 1800 RPM case, as already noticed in the linear scale plots. This effect becomes less prominent at larger frequencies where higher order modes occur. Furthermore, it should be noted that both the flap bending bridges (FB2 and FB3), identify the same experimental modal eigenfrequencies, presented in Table 4.2.

When considering torsional bridge data it appears more difficult to appreciate the first three blade mode shapes, all of which possess flap bending shapes. However, mode four which is a torsion-bending mode is very well captured when looking at both T1 and T2 bridges, with the identified modal peak in clear agreement with mode 4 estimation obtained from the flap bending bridge data. Ultimately, further supporting the prior finding that flap bending bridges provide a better insight into blade stall identification as the blade first flap bending mode typically occurs at a lower eigenfrequency, therefore stall induced vortical structures excite this mode prior to higher order torsional modes.

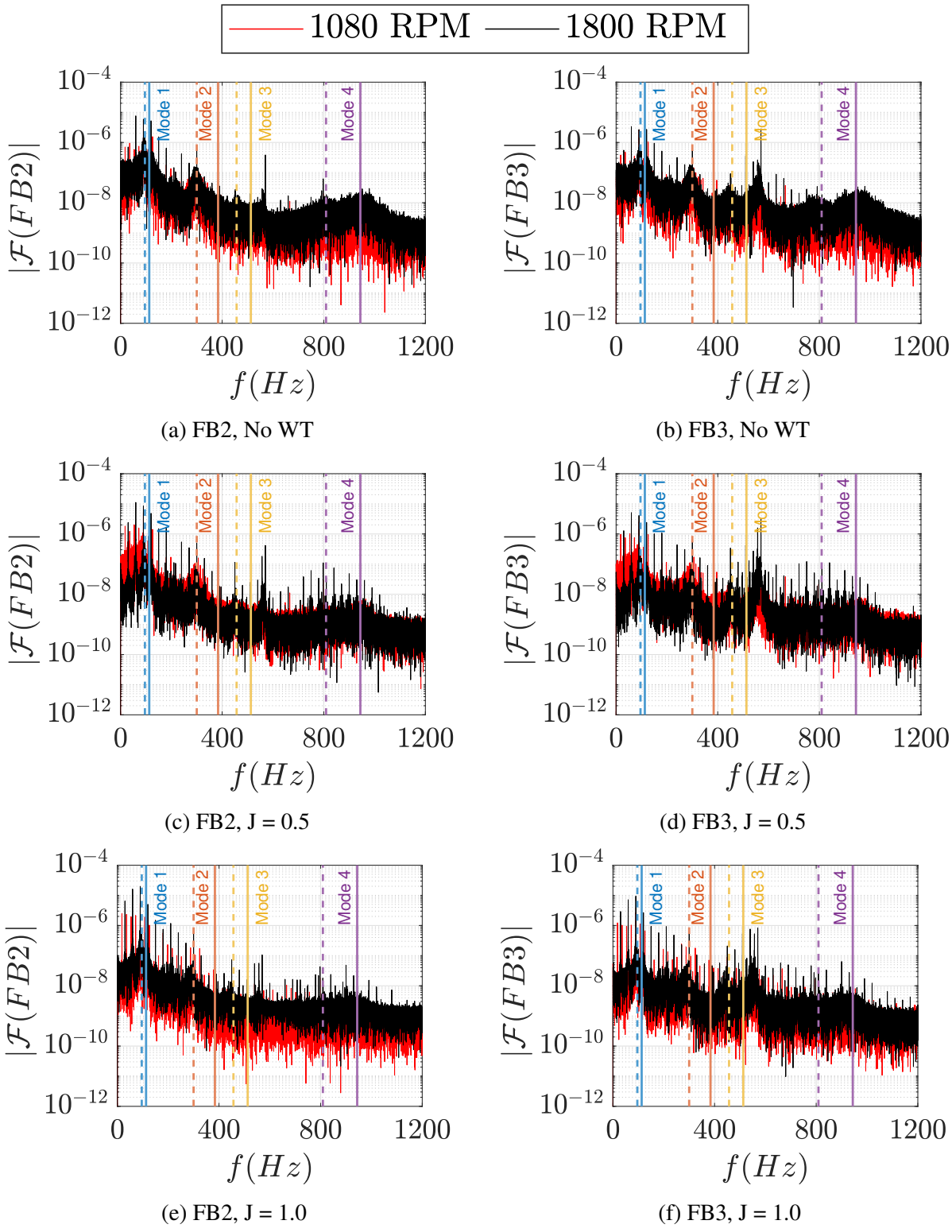

(a) FB2, No WT

(b) FB3, No WT

(c) FB2, J = 0.5

(d) FB3, J = 0.5

(e) FB2, J = 1.0

(f) FB3, J = 1.0

Figure 4.20: Amplitude of the Fourier transform of flap bending bridges (FB2 and FB3) uncorrected strain measurements at $\beta_{0.75R} = 30.5°$, plotted in logarithmic scale as a function of the dimensional frequency. Numerical (solid) and identified experimental (dashed) modal frequencies are added as vertical lines.

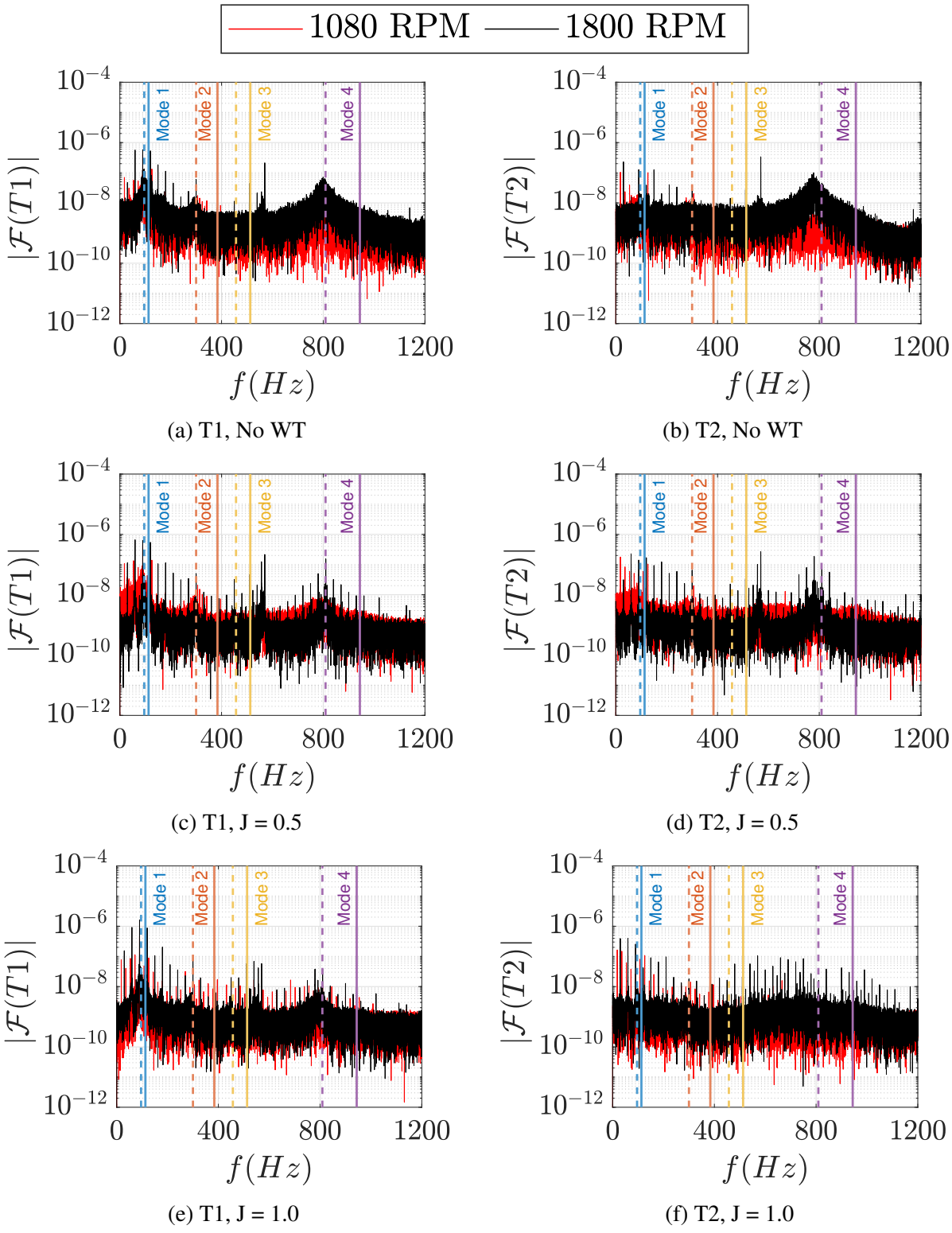

(a) T1, No WT

(b) T2, No WT

(c) T1, J = 0.5

(d) T2, J = 0.5

(e) T1, J = 1.0

(f) T2, J = 1.0

Figure 4.21: Amplitude of the Fourier transform of flap bending bridges (T1 and T2) uncorrected strain measurements at $\beta_{0.75R} = 30.5°$, plotted in logarithmic scale as a function of the dimensional frequency. Numerical (solid) and identified experimental (dashed) modal frequencies are added as vertical lines.

4.5 Torque Measurements

The propeller rig is endowed with a rotational shaft balance, which at the time of testing was not yet fully commissioned and installed. Therefore, to estimate the blade torque, the feedback torque from the motor controller was used. This included other sources of torque other than the blade aerodynamic torque, such as internal frictions and the torque arising from the hub and spinner. To compensate for this, blade-off measurements at several rotational frequencies and advance ratios were acquired and subtracted to the corresponding blade-on measurements. Torque coefficients (C_Q) were computed using the standard definition for propellers:

$$C_Q = \frac{Q}{\rho n^2 D^5}$$

Subtraction of blade-off measurements were computed in coefficient form to ensure that the data points are not skewed or influenced by any variation in density between blade-on and blade-off measurements. Despite what appears to be relatively small changes in density in absolute terms, variations of even a few percent can alter the measurement tare by an appreciable amount and thus result in biased data measurements.

$$C_Q = C_{Q,ON} - C_{Q,OFF}$$

Further insight on the stall development can be achieved though analysis of the torque. Figure 4.22 presents the torque coefficient as a function of the advance ratio for several blade pitch angles, at four different rotational frequencies. Until stall, all curves behave as expected, with a gradual reduction in propeller torque for an increasing advance ratio as the effective AoA of the blade is decreased, resulting in a reduced thrust and therefore a reduced induced power. Moreover, an increase in the blade pitch angle promotes a consistent shift to larger torque values, with the curves almost evenly spaced. In the top-left corner of both plots, where the stalled cases are present, a large change in the slope of the $C_Q - J$ curves can be observed as opposed to the flat behaviour of the curves for the non-stalled cases. This can be explained by the large increase in parasitic drag arising from the stalled regions. However, not all the stalled cases show a noticeable variation in slope in that region. For example, at 1080 RPM (Figure 4.22a), all cases with $\beta_{0.75R} \geq 22.5^\circ$ at sufficiently low J have been identified as stalled cases using the other criteria adopted up to this point. However, the curves for $\beta_{0.75R} = 22.5^\circ$ and 24.2° in Figure 4.22a do not show a remarkable change in gradient. This is believed to be caused by the increase in parasitic power being partially compensated for by a decrease in the induced power due to a reduction in thrust at stall onset. Hence while a strong change in the slope can be effectively be used to assess the presence of fully developed stall in a particular test point, early-stage stall might still be present in cases that show no such behaviour. This behaviour is also apparent for the other rotational frequencies tested, as shown in Figure 4.22.

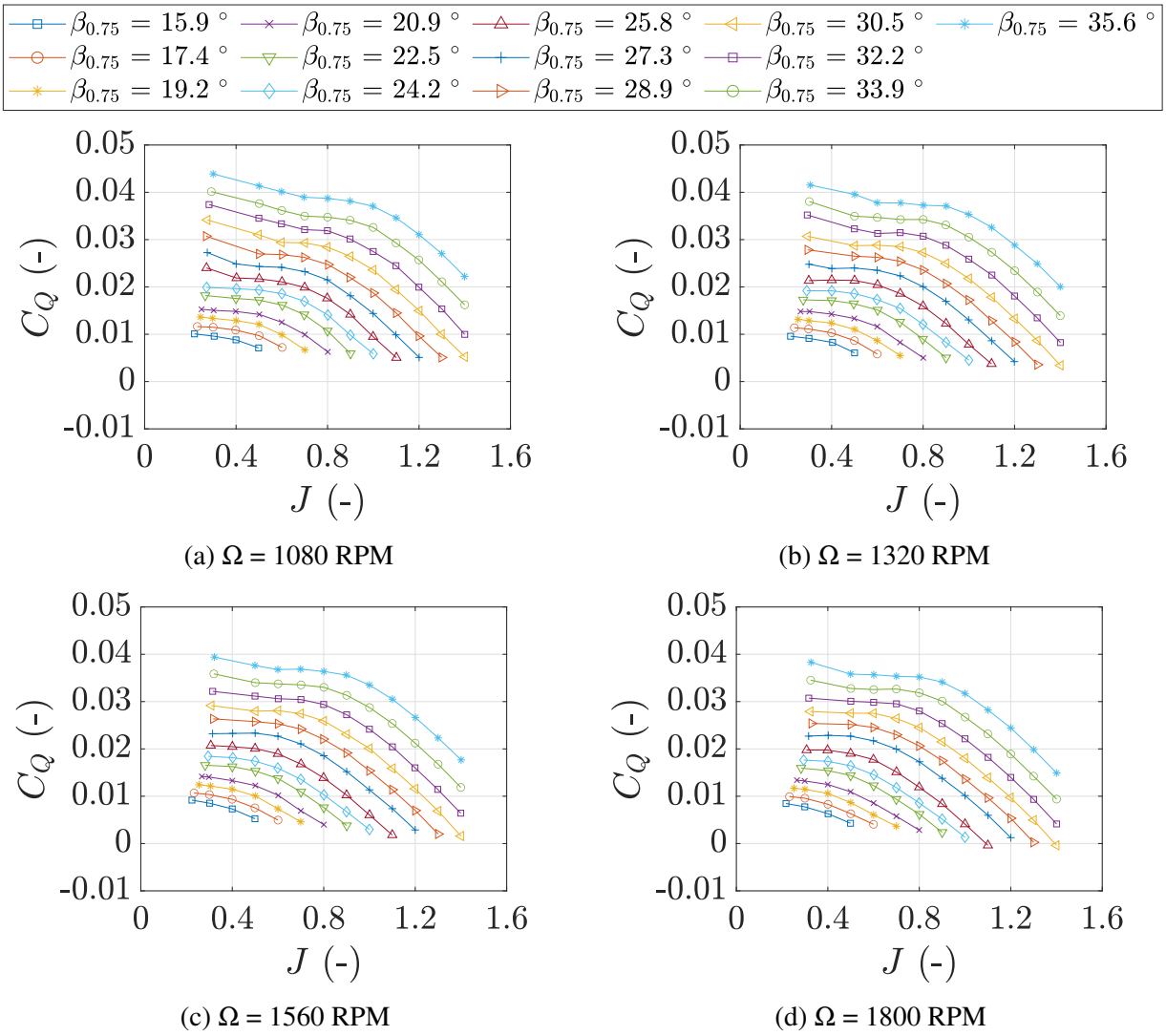

(a) Ω = 1080 RPM

(b) Ω = 1320 RPM

(c) Ω = 1560 RPM

(d) Ω = 1800 RPM

Figure 4.22: Torque coefficient C_Q as a function of the advance ratio J, various pitch settings.

4.6 Stall Boundary Identification Criteria

As detailed in section 4.2, stall has been identified at a variety of test points within the test matrix, using the following criteria:

- Collapse of the induced velocity around the wind tunnel loop for increasing pitch angles when the wind tunnel fan is not in operation.
- Departure from linear behaviour of the flap bending strain vs blade pitch curves.
- Marked increase of the standard deviation of the flap bending strain, up to twice the pre stalled conditions.
- Presence of non-harmonic content in the strain spectra, up to 20 % in amplitude of the corresponding harmonic content.
- Non consistent oscillation amplitude in the strain time history.
- A more pronounced increase in torque for fully developed stall (even if not so evident at stall onset).

Testing was performed at varying rotational frequencies Ω, advance ratios J and blade pitch angles $\beta_{0.75R}$ as described in Section 4.1 to characterise the stall envelope of the tiltrotor blade set. The overall test points and the subset of cases where stall was identified using the criteria above are presented in Figure 4.23 and slices of the boundary presented as a function of RPM and J in Figures 4.24 and 4.25, respectively. Although not the focus of this thesis, it should be noted that cases at high advance ratio were also investigated to qualify the opposite end of the propeller operational envelope, where the negative angle of attack induced by the advance speed creates negative thrust towards the blade tip. The maximum advance ratio that could be tested increased with the blade pitch angle. Therefore, $\beta_{0.75R} = 15.9^o$ could be tested up to and including J = 0.5, while $\beta_{0.75R} \geq 30.5^o$ could be tested up to and including J = 1.4.

By looking at Figure 4.23, stall was primarily observed at a lower advance ratio, lower rotational frequencies and large blade pitch angles, as expected. The smallest pitch angle at which stall was identified was $\beta_{0.75R} = 22.5^\circ$ during a "No WT" test performed at a corresponding J = 0.265 and at 1080 RPM, with all cases prior to this showing no evidence of stalled flow. However, it is clear that looking at $\beta_{0.75R} = 22.5^\circ$ and 24.2° at 1080 RPM and 1200 RPM, both indicate presence of early onset of stall as even a small increase in advance ratio to J = 0.4 results in the re-attachment of the flow. As $\beta_{0.75R}$ was increased, the number of rotational frequencies at which stall was present for low advance ratios grew in a discontinuous manner. For the ”No WT” cases between $22.5^\circ \leq \beta_{0.75R} \leq 27.3^\circ$, stall was only present at $\Omega \leq 1200$ RPM. At $\beta_{0.75R} = 28.9^\circ$, there was a sudden growth in rotational frequencies at which stall was present up to 1560 RPM. Eventually, for $\beta_{0.75R} \geq 28.5^\circ$, stall was present at all Ω tested, up to and including 1800 RPM.

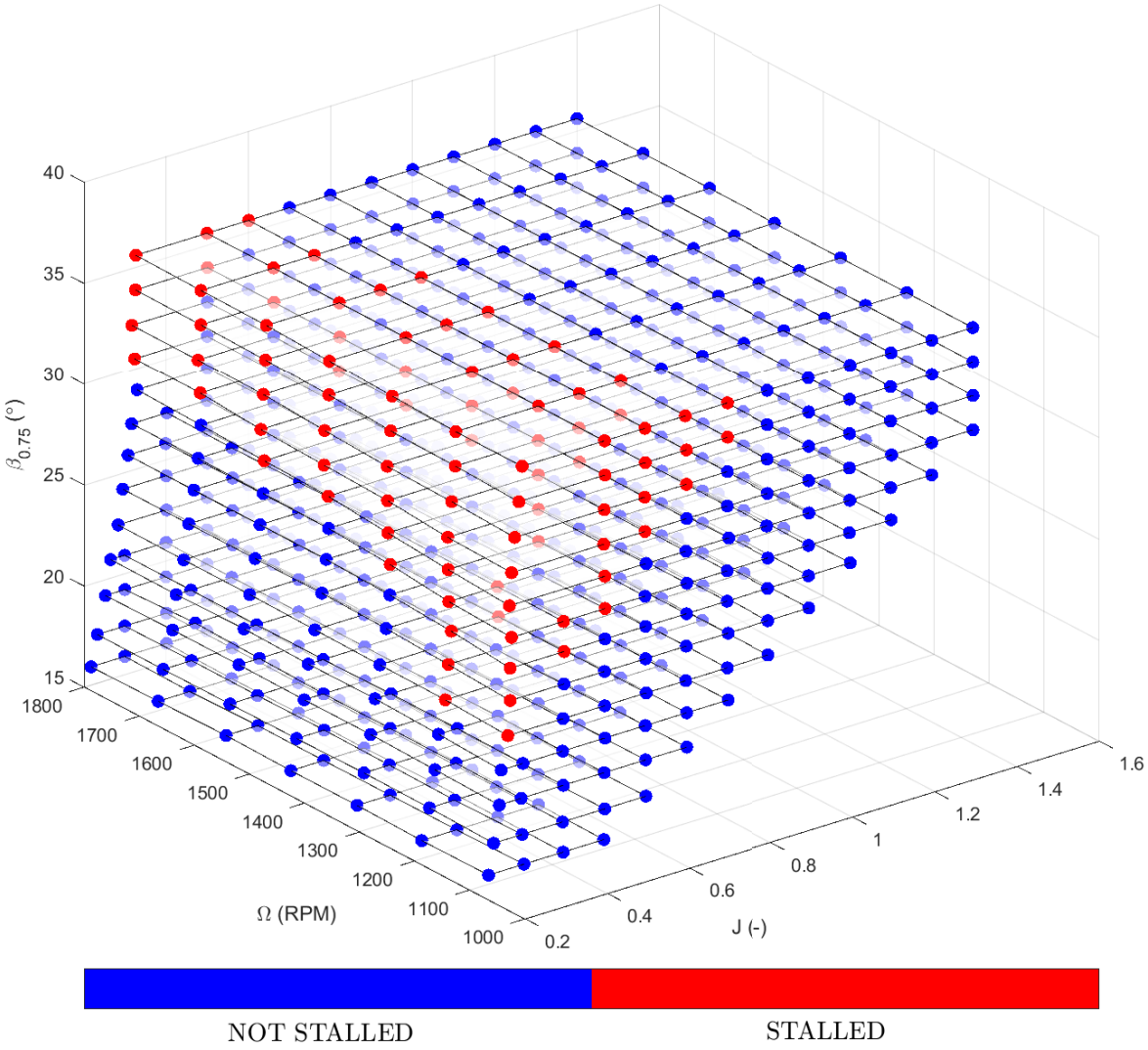

Figure 4.23: Stall boundary, as a function of rotational speed, advance ratio and blade pitch angle. Each dot correspond to a test point: red indicates evidence of stall, blue otherwise.

This behaviour is also observed at low advance ratio conditions up to $J = 0.5$, which can be more easily appreciated from Figure 4.24a. For an increased advance ratio of $J = 0.7$ (Figure 4.24b), a reduction in the number of identified stall points is observed, highlighting that low RPM and high blade pitch conditions develop stall sooner, until eventually the advance ratio becomes excessive enough to eliminate the presence of stall, as shown in Figures 4.24c and 4.24d. This sudden growth in the range of RPMs at which stall is present is a direct consequence of the effect of the Reynolds number on stall development: for how large the Reynolds number can be, there will be always a point when the AoA will be excessive and stall will develop. This behaviour was observed for both the ”No WT” case, where a small variation in J was present by varying the RPM, and for J=0.4 and J=0.5, where J was kept constant across the RPM range.

On the contrary, the influence of J on the presence of stall was observed to be more gradual

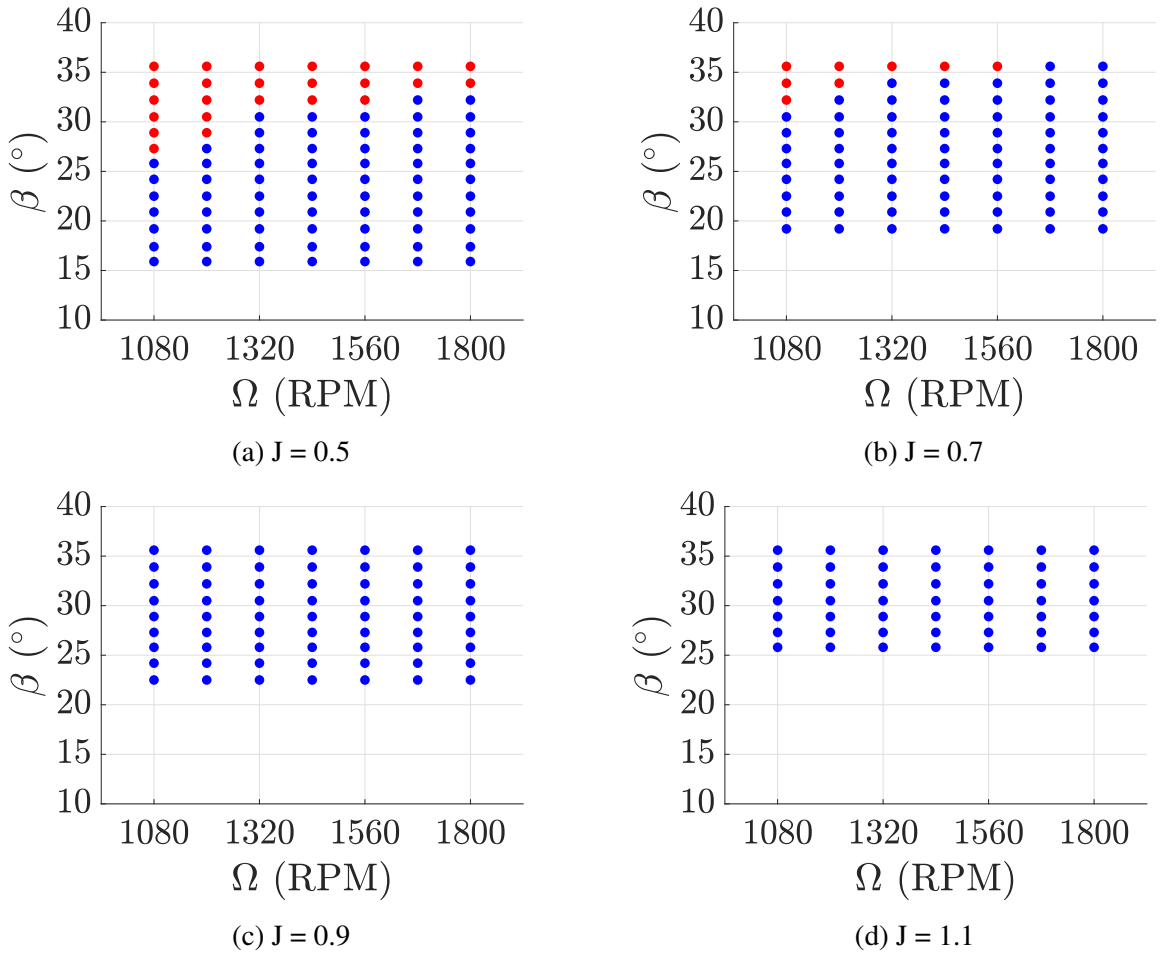

(a) J = 0.5

(b) J = 0.7

(c) J = 0.9

(d) J = 1.1

Figure 4.24: Stall identification as a function of RPM and blade pitch angle for a fixed advance ratio. Each dot correspond to a test point: red indicates evidence of stall, blue otherwise.

and approximately linear. This observation can be better appreciated in Figure 4.25, where there is a noticeable reduction in the number of stalled conditions at which the propeller operates when comparing the 1080 RPM (Figure 4.25a) and 1800 RPM (Figure 4.25d) conditions for a given value of J. At the lowest rotational frequency of 1080 RPM, the minimum J at which stall was observed ranged from J = 0.25 at $\beta_{0.75R} = 22.5°$ to J = 0.8 at $\beta_{0.75R} = 35.6°$. However, for an increased RPM, e.g 1320 RPM, shown in Figure 4.25b, the stalled range reduces to J = 0.29 at $\beta_{0.75R} = 27.3°$ to J = 0.7 at $\beta_{0.75R} = 35.6.3°$. A similar gradual behaviour was observed at higher RPM values of 1560 RPM and 1800 RPM, even if for a smaller range of J and pitch angles, as the volume of stalled points reduces in size, again supporting that lower RPM propellers stall sooner.

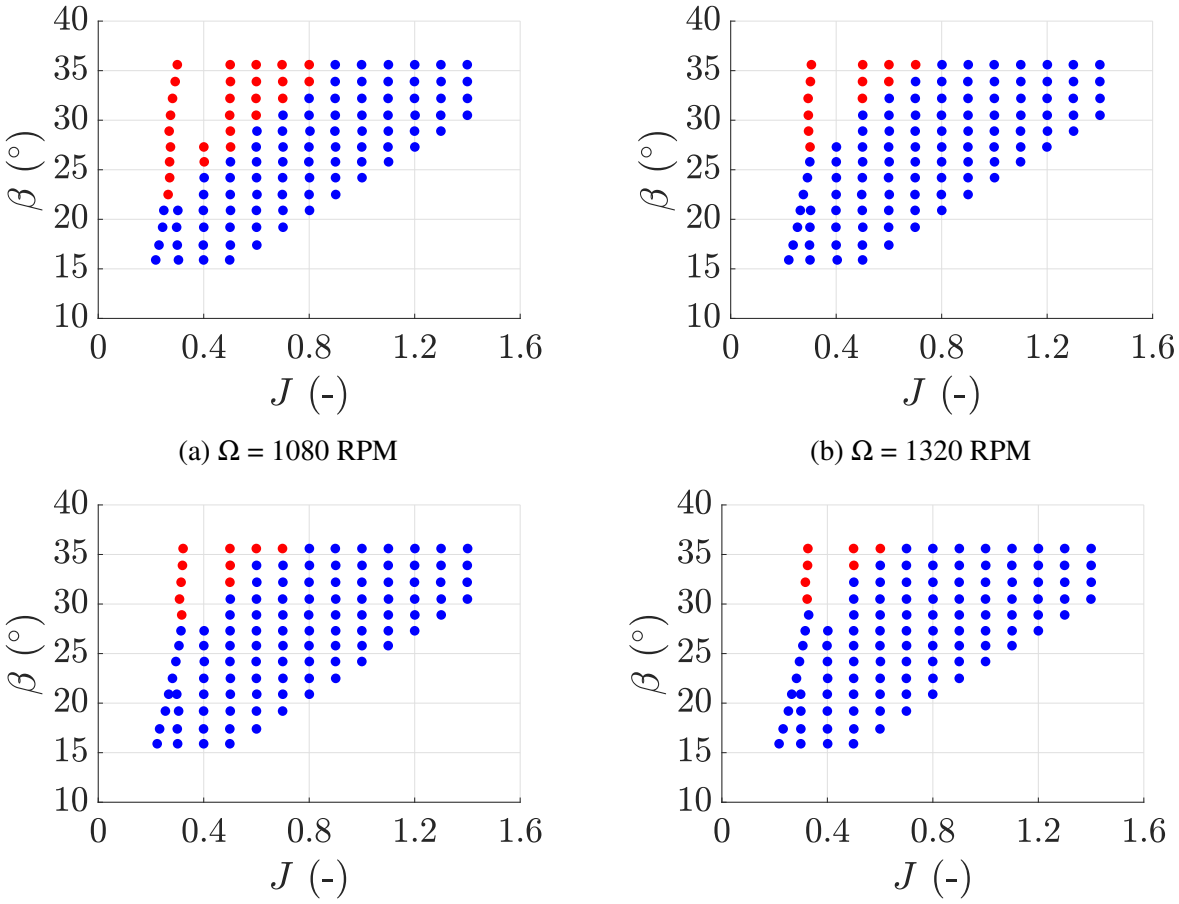

(a) Ω = 1080 RPM

(b) Ω = 1320 RPM

(c) Ω = 1560 RPM

(d) Ω = 1800 RPM

Figure 4.25: Stall identification as a function of advance ratio and blade pitch angle for fixed rotational speeds. Each dot correspond to a test point: red indicates evidence of stall, blue otherwise.

4.7 Chapter Summary

Within this chapter a novel methodology of stall identification was developed to identify the presence of stall onset through the measurement of blade strain, motor torque and wind tunnel velocity data. Due to the closed loop nature of the De Havilland wind tunnel, for conditions at which the wind tunnel fan was not operating, measurements of the recirculation induced by the propeller were utilised to assess the minimum advance ratio at which the propeller could operate for a given blade pitch angle. It was observed that for a growth in blade pitch angles, the measured wind tunnel recirculation converged, highlighting a collapse in the propeller induced velocity, thus suggesting the presence of stall.

Additionally, measurements of averaged blade flap bending and torsional strain data were analysed, displaying a departure from a linear trend for increased blade pitch angles where stall occurred. Moreover, for pre-stall conditions, the standard deviation of the strain remained relatively constant before growing up to twice as much for cases at which stall was identified. Measurements of strain time histories were also analysed, highlighting a repeatable behaviour of constant amplitude for attached conditions. Whilst for operational conditions at which the propeller was stalled, irregular patterns and variable signal amplitudes in the time histories were observed. Furthermore, analysis of strain spectra demonstrated that the spectral content of a propeller blade operating at a stalled condition will exhibit a significant non-harmonic content, where the signal energy is distributed amongst a large range of frequencies. In addition to stall identification, strain readings were also successful in identifying blade eigenmode frequencies, when compared with numerical mode calculations.

Measurements of motor torque were also logged, highlighting a more pronounced growth in torque for fully developed cases of stall, this behaviour appeared less apparent for early stages of stall onset. In summary, a novel methodology of stall identification developed to identify the presence of stall onset through the measurement of blade strain, motor torque and wind tunnel velocity data was implemented to characterise the stall boundary of the MENtOR tiltrotor blade set.

Chapter 5

A Multi-Measurement Approach To Identify Stall

This chapter presents measurements of propeller performance and blade tip deflections of the MENtOR tiltrotor blade set, operating in fixed pitch propeller mode, at varying rotational frequencies, blade pitch angles and advance ratios. A multi measurement approach has been implemented to determine the identification of the blade stall boundary through independent measurement techniques and support the validity of the stall boundary identification criteria developed in Chapter4. A description of the test conditions applied for each of the implemented experimental techniques is presented in Section 5.1. RSB measurements logged to assess propeller performance are presented in Section 5.2 and DIC measurements of blade bending and torsional tip deflections are displayed in Section 5.3.

5.1 Test Matrix

Measurements of propeller performance and blade tip deflections were obtained within the same wind tunnel entry. Testing was performed for a range of operational conditions through variation of propeller rotational frequency Ω and advance ratio $J = U_\infty/(nD)$ for a fixed blade pitch angle $\beta_{0.75R}$. Furthermore, measurements were sampled at a reduced range of blade pitch angles between $\beta_{0.75R} = 16^o$ to 35.7^o when compared to previous strain tests.

Measurements of propeller performance were logged for a range of rotational frequencies between 1080 RPM and 1800 RPM at a resolution of 120 RPM. However, data presented in this work is for rotational frequencies up to 1440 RPM to ensure measurement reliability, as dynamic measurements of the rotating shaft balance indicate the possibility of the measurement of inertial force terms such as rig/balance motion due to resonance, as described in Section 3.1.4.4. In addition to performance measurements, blade tip deflection measurements were collated through a range of rotational frequencies between 1080 RPM and 1800 RPM, in increments of 240 RPM. Moreover, due to the reduced rigidity of the rig as a result of the RSB installation, the advance

ratio was limited to 1.3 for the large pitch angle tests. A visual representation of the test matrix and measurement techniques implemented at each test point is shown in Table 5.1.

Table 5.1: Test matrix as a function of blade pitch $\beta_{0.75R}$ and advance ratio J. X = Measurement of propeller performance obtained at RPM varying from 1080 RPM to 1800 RPM in 120 RPM increments. + = Measurement of blade tip deflections obtained at RPM varying from 1080 RPM to 1800 RPM in 240 RPM increments. Blank = Point not tested.

$\beta_{0.75R}$	No WT	J=0.3	J=0.4	J=0.5	J=0.6	J=0.7	J=0.8	J=0.9	J=1.0	J=1.1	J=1.2	J=1.3
16^o	X +	X	X	+								
19.1^o	X +	X	X	+		+						
22.3^o	X +		X	X +		+		+				
25.5^o	X +		X	X +	X	+		+		+		+
28.7^o	X +			X +	X	+		+		+		+
32^o	X +			X +	X	+		+		+		+
35.7^o	X +			X +	X	+		+		+		+

5.2 Measurements of Propeller Performance

5.2.1 Glauert Blockage Correction

As testing was conducted in a closed loop return wind tunnel, this presents several challenges when testing rotary wings such as propellers, both in terms of flow recirculation and wind tunnel blockage. Despite the flow recirculation induced from the propeller and wind tunnel blockage appearing as a separate issue, they are very much intertwined. To accurately set the wind tunnel freestream velocity for a propeller system, an assessment of propeller induced recirculation around the wind tunnel loop was performed with results presented in Figure 4.1. However, due to the physical presence of the propeller disc and supporting structure within the wind tunnel, further corrections must be made to account for the variation in freestream velocity due to the reduction in cross sectional area. An assessment of well established wind tunnel correction models [87–90] for propeller testing was carried out by Fitzgerald [91] highlighting the suitability of the Glauert correction over that of comparable methods developed.

Glauert's correction method [87] is a well established correction based on momentum theory that establishes the required velocity correction for propeller configurations where the ratio of propeller disc area (A) to wind tunnel cross sectional area (A_{CS}), also commonly referred to as the blockage factor (ε), is no longer negligible. Typically, blockage factors greater than 10% require the need for velocity correction. During this experimental investigation the blockage factor was computed to equal, $\varepsilon = 0.237$ (23.7%). A visualisation of the blockage area can be appreciated from Figure 5.1. Using momentum theory, Glauert's correction can be simply expressed as the the ratio of equivalent freestream velocity (U') to a reference freestream velocity (U_∞), using the equation below, where $\tau_4 = \mathrm{T} \,/\, \left(\rho A U_\infty^2\right)$.

$$\frac{U^{'}}{U_{\infty}} = 1 - \frac{\tau_4 \varepsilon}{2\sqrt{1+2\tau_4}}$$

It must be stressed that Glauert's correction is not solely based upon the blockage factor of the propeller but also the thrust condition at which the propeller is operating. Therefore, by definition, a propeller operating at a larger thrust will require a larger velocity correction due to the increased velocity in the propeller slipstream. A more complete description of Glauert's correction and its limitations can be found in Barlow et al. [92].

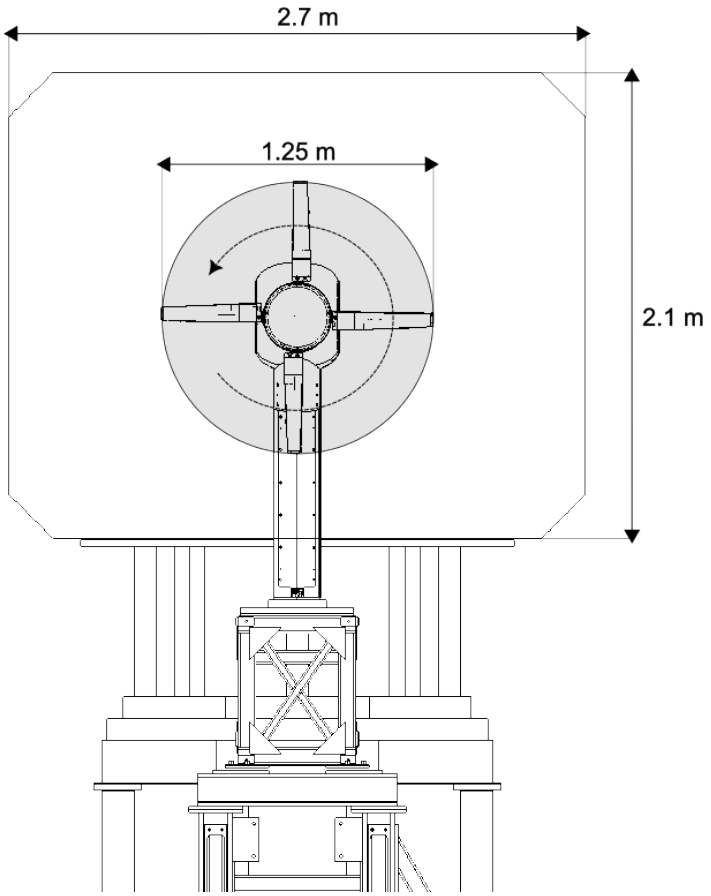

Figure 5.1: Upstream view of UKNRR situated in De Havilland wind tunnel, highlighting the propeller disc area (A) with respect to the wind tunnel cross sectional area (A_{CS}).

To evaluate the impact of Glauert's wind tunnel blockage correction on the reference freestream velocity, a comparison of the reference advance ratio, J, is compared to the equivalent advance ratio $J' = U'/nD$ is presented in Figure 5.2. As expected, for all rotational frequencies presented, there is a clear drop in magnitude of the equivalent velocity when compared to that of the reference. It is clear there is a linear relationship between the equivalent and reference velocity, therefore the correction can be thought of as an offset in J for the same thrust condition. To highlight this clearly, focusing on the $\beta_{0.75} = 16^{\circ}$ curve at approximately $J \approx 0.2$ for all rotational

frequencies which represents the "No WT" case, hence not a constant value of J.. At this condition of operation the propeller loading is at it largest and therefore corresponds to the maximum value of the Glauert correction. At 1080 RPM, the maximum shift in advance ratio corresponds to 0.05 for $J = 0.2$ and the corresponding equivalent advance ratio, $J' = 0.15$. Furthermore, as expected, a growth in advance ratio reduces the propeller loading and therefore the ratio of J'/J reduces, representing a reduction in the equivalent velocity correction.

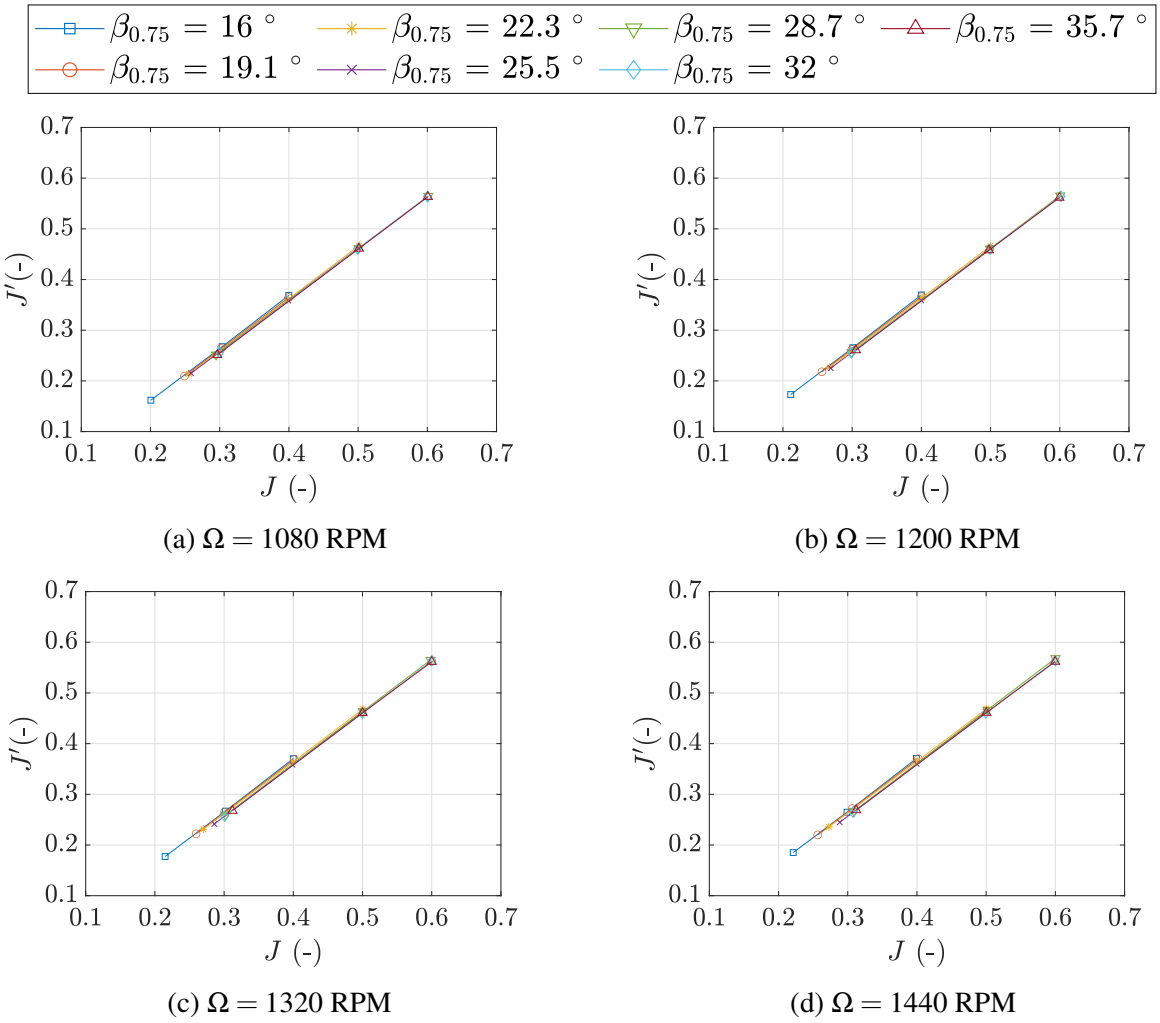

(a) $\Omega = 1080$ RPM

(b) $\Omega = 1200$ RPM

(c) $\Omega = 1320$ RPM

(d) $\Omega = 1440$ RPM

Figure 5.2: Comparison of the equivalent propeller advance ratio (J') computed using Glauert's wind tunnel blockage correction to the reference propeller advance ratio (J) for an rotational frequency range of $\Omega = 1080 - 1440$ RPM.

5.2.2 Measurement of Propeller Thrust

Assessment of propeller blade loading is critical for characterisation of propeller performance, as thrust performance provides meaningful insight to the operational boundaries of the blades. Thrust performance data has been presented in coefficient form (C_T) to ensure that data presented is not influenced by density or temperature variations, using the standard propeller coefficient notation shown below.

$$C_T = \frac{T}{\rho n^2 D^4}$$

Prior to analysis of the performance results, it should be highlighted that upon inspection of highly loaded thrust conditions, there appears to be a discrepancy in the absolute value of the thrust measurement. During the setup of the UKNRR, both dynamic (rotating) and static load measurements were assessed with the blades-on and blades-off. It was observed during dynamic operation for highly loaded cases, there was an unexpected deviation from expected thrust values. However, dynamic cases at lightly loaded conditions and static cases displayed expected results, ensuring the balance calibration remained valid. Upon closer inspection of the rotor hub, it was identified that due to a poor hub design, the pitch links were determined to be an influencing factor on the load path of the blades, therefore skewing the thrust measurement at large thrust conditions. Ultimately, without an entire re-design of the rotor hub or measurement of pitch link loads independent from the RSB, there is no way to assess the magnitude of the load contribution and correct appropriately. Despite, the increased uncertainty at cases of large thrust, the RSB still manages to capture the expected thrust trends.

Measurements of thrust coefficient as a function of advance ratio for several blade pitch angles, at four different rotational frequencies are presented in Figure 5.4. Data with and without the Glauert blockage correction is presented, where data with a dashed line corresponds to the Glauert correction. As anticipated, there is a visible shift of the corrected $C_T - J$ curves to lower values of J. Focusing on the 1080 RPM case, shown in Figure 5.3a, it is clear for values of $\beta_{0.75} \leq 22.3^\circ$, $C_T - J$ curves are equally spaced and display a reduction in thrust coefficient for increasing advance ratio, as expected for attached conditions. However, for the case of $\beta_{0.75} = 25.5^\circ$, for values of $J = 0.4 - 0.5$, there is a flattening of the $C_T - J$ curve, highlighting the reduction of thrust generation which can only be attributed to presence of flow separation. At larger values of $\beta_{0.75}$, the continued levelling of the $C_T - J$ curve with increasing values of J, further highlights the presence of stalled flow, thus confirming that at large pitch angles and low advance ratio conditions a deeper stall occurs. Furthermore, this indication of stall in the thrust measurement has been adequately captured using the strain gauge stall identification criteria presented in Chapter 4.

It is clear for all rotational frequencies presented, in agreement with the strain gauge identification criteria, for cases of $\beta_{0.75} \leq 22.3^\circ$ there is no stall observed. However, for conditions

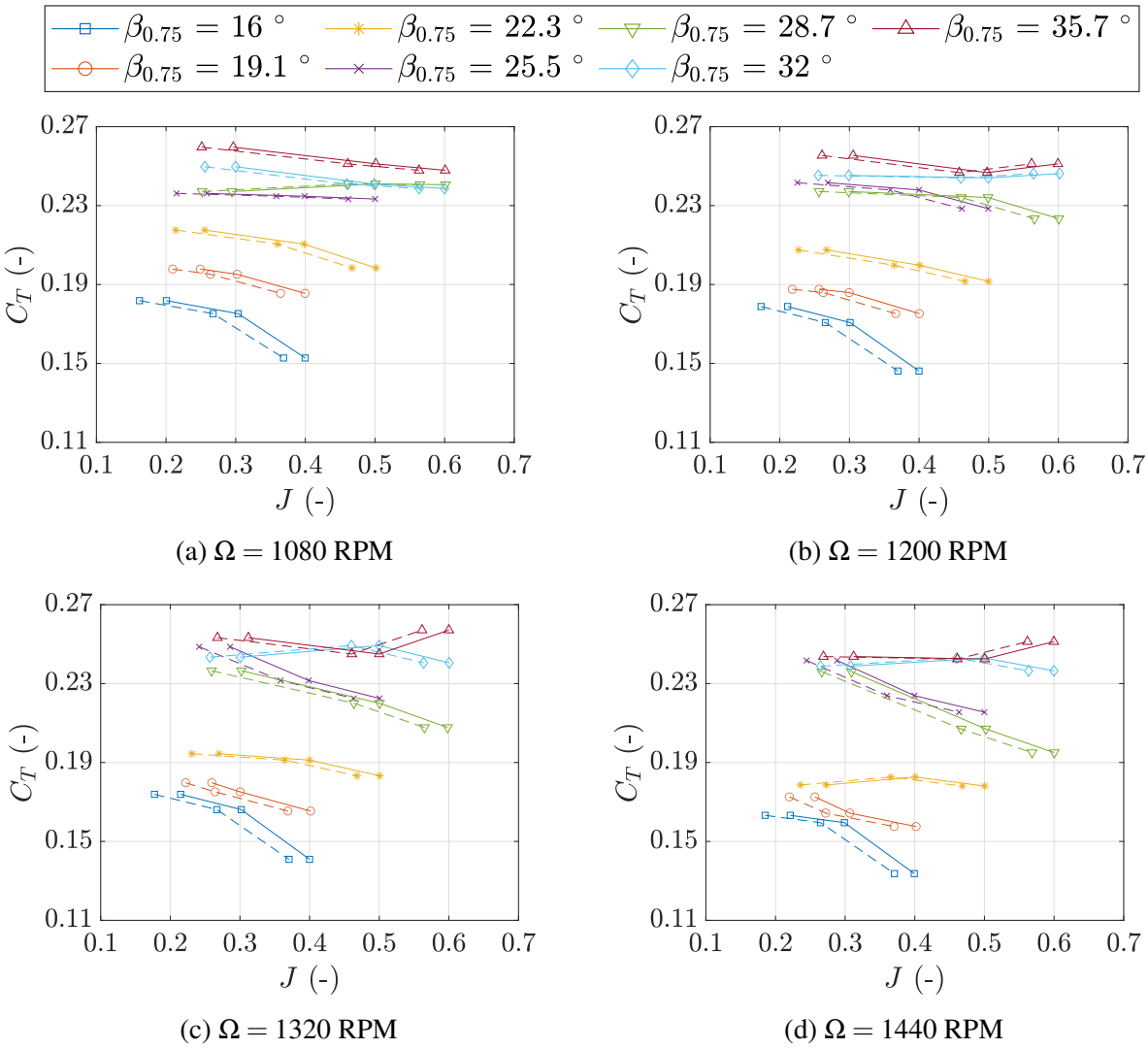

(a) $\Omega = 1080$ RPM

(b) $\Omega = 1200$ RPM

(c) $\Omega = 1320$ RPM

(d) $\Omega = 1440$ RPM

Figure 5.3: Measurements of thrust coefficient C_T as a function of advance ratio J for a rotational frequency range of $\Omega = 1080 - 1440$ RPM. Dashed lines represent the equivalent propeller advance ratio (J') computed using Glauert's wind tunnel blockage correction.

at which there are large blade pitch angles and advance ratio's, thrust measurements indicate further presence of stall. At 1200 RPM, for $\beta_{0.75} = 25.5°$ at $J = 0.6$ the drop in C_T with respect to the $J = 0.5$ condition indicates that the blades are stalled at $J = 0.5$. However the increase in J reduces the effective AoA, thus promoting reattachment of the flow. Furthermore, until now the identification of the stall boundary using strain gauges has proven robust. However, for $\beta_{0.75} = 28.7°$ at $J = 0.6$, there is a reduction in C_T with respect to $J = 0.5$ suggesting similar to the $\beta_{0.75} = 25.5°$ condition that the flow reattaches, this appears to contradict the strain gauge data from which stall was identified. Nonetheless, for cases at which $\beta_{0.75} > 28.7°$, strain and thrust data concur on the blade stall boundary.

Furthermore, at 1320 and 1440 RPM, the minimum J values ("No WT" case) for $\beta_{0.75} > 22.3°$ all collapse on one another suggesting that the propeller is operating in a more developed stall when compared to the lower rotational frequencies and blade pitch angles. In agreement

with the strain gauge measurements, the stall boundary identification from the thrust data for both the 1320 and 1440 RPM conditions accurately captures the stall behaviour of the blade. It is therefore, apparent that the criteria developed using strain gauge behaviour to identify the presence of stall appears a viable method to assess the blade operational boundaries. As no large advance ratio cases at which negative thrusting behaviour could be captured were tested, this remains an area for further validation. However, given the accurate characterisation of the stall boundary, there is no clear reasoning why strain gauges could not be successful at defining the opposing end of the operational envelope.

5.2.3 Measurement of Propeller Torque

Up until this point within this thesis, readings of torque have been obtained via measurements from the motor controller feedback. However, installation and commissioning of a RSB has allowed for a second measurement source of torque data. Measurements of C_Q from the RSB have also been compensated for by means of aerodynamic tare measurements, to account for the torque of the entire rotor system in a blades-off condition. Furthermore, despite the Glauert blockage correction not being dependent on the torque measurement, the values of thrust for which the corresponding torque is measured are. Therefore, the velocity correction obtained can also be applied to the $C_Q - J$ curves measured by the RSB, both the corrected and uncorrected $C_Q - J$ curves are displayed in Figure 5.4, where the dashed line corresponds to torque data with the Glauert correction applied.

When considering the 1080 RPM case, for values of $\beta_{0.75} \leq 19.1°$, the behaviour of the $C_Q - J$ curves is as expected, where curves flatten with increasing J and are approximately equally spaced. This is to be expected as strain, thrust and motor torque data has provided no indication of stall at any of these blade pitch angles. Moreover, when analysing the $\beta_{0.75} = 22.3°$ case, thrust and torque data do not indicate any presence of stall for any advance ratio, yet the strain gauge data suggests otherwise for the "No WT" case corresponding to $J = 0.26$. This is likely a result of the blades operating at a condition of weak stall or stall onset which is detectable to the blade strain gauges but due to the relatively small change in thrust and torque, it is not appreciable on the global load measurements of the propeller. However, this discrepancy in stall identification between the strain gauge and RSB measurements occurs only for this condition of weak stall. For $\beta_{0.75} = 25.5°$, there is a noticeable increase in gradient of the $C_Q - J$ curve at $J = 0.4$ before flattening at $J = 0.5$, indicating a significant increase in passive drag due to regions of separated flow. An identical behaviour is displayed for $\beta_{0.75} = 28.7°$ although for an increased advance ratio. Furthermore, at the largest blade pitch angles $\beta_{0.75} > 32°$, the $C_Q - J$ curves display noticeable gradient changes, even at large values of J, clearly identifying stalled operating conditions.

Focusing on the 1200 RPM condition, the behaviour of the $C_Q - J$ curves appear to agree very well with the stall identification points as determined via the strain gauges. However, two

points of disagreement occur, $\beta_{0.75} = 22.3°$ for the "No WT" case and $\beta_{0.75} = 28.7°$ at $J = 0.6$, for both of which no sign of stall is appreciable from the $C_T - J$ and $C_Q - J$ curves.

Furthermore, both 1320 and 1440 RPM cases have demonstrated an agreement between the identification of stall using C_T, C_Q and strain measurements. Nonetheless, despite an agreement for all rotational frequencies presented, it is clear that for cases at which the stall is at very early stages of development, C_T and C_Q do not capture this behaviour. Therefore, this further supports the rationale that strain gauges instrumented on the blade appear to be more successful at determining the early onset of stall development.

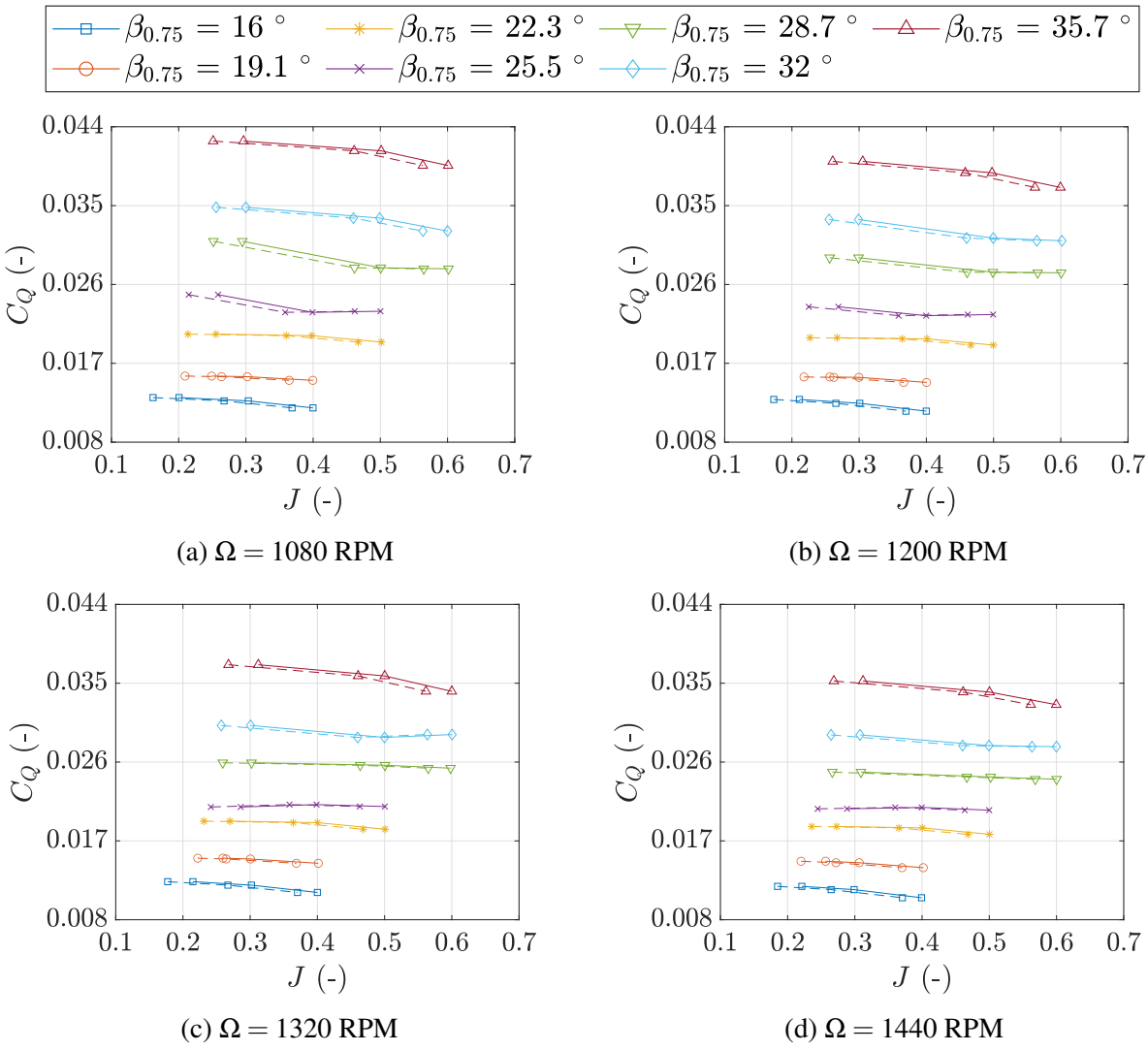

(a) $\Omega = 1080$ RPM

(b) $\Omega = 1200$ RPM

(c) $\Omega = 1320$ RPM

(d) $\Omega = 1440$ RPM

Figure 5.4: Measurements of torque coefficient C_Q provided by the Rotating Shaft Balance (RSB) as a function of advance ratio J for a rotational frequency range of $\Omega = 1080 - 1440$ RPM. Dashed lines represent the equivalent propeller advance ratio (J') computed using Glauert's wind tunnel blockage correction.

To evaluate the reliability of the torque behaviour between the two measurement sources, a comparison of the C_Q obtained from the motor controller feedback and the RSB is compared, without Glauert's blockage correction, for all common test points and presented in Figure 5.5.

Where the dashed line corresponds to the motor torque coefficient and the solid line represents torque coefficient obtained from the RSB. At first glance, both torque measurement sources show very similar trends, with a discrepancy in absolute values under certain operating conditions. Differences in absolute values are particularly prominent for highly thrusting conditions, probably owing to the increased magnitude of the loads that are transferred through the pitch links, and this probably affects the measurements on the other axes too, especially thrust measurements. Therefore, it should acknowledged that the confidence in the RSB measurements is somewhat diminished under certain conditions, especially in high loading cases. However, even if the absolute values might be affected by some level of uncertainty, the trends shown are expected to accurately capture the performance changes needed for stall identification with a large degree of confidence.

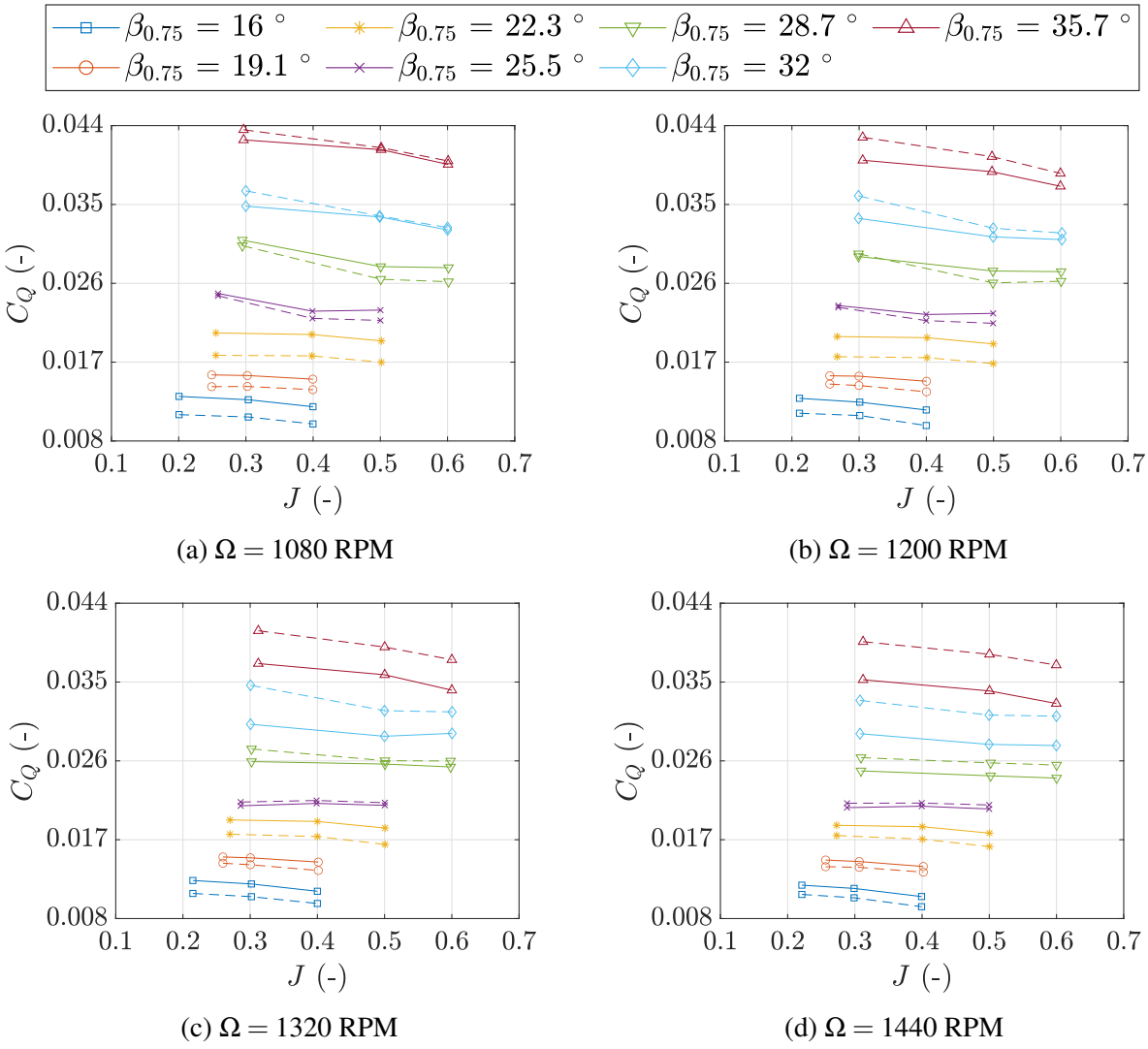

(a) $\Omega = 1080$ RPM

(b) $\Omega = 1200$ RPM

(c) $\Omega = 1320$ RPM

(d) $\Omega = 1440$ RPM

Figure 5.5: Comparison of torque coefficient C_Q measured by the Rotating Shaft Balance (RSB) and motor controller feedback as a function of advance ratio J for a rotational frequency range of $\Omega = 1080 - 1440$ RPM. Dashed lines represent the motor controller feedback torque.

5.3 Measurements of Propeller Blade Tip Deflection

5.3.1 Assessment of Blade Rigid Deflection

During the installation of the rotor blades onto the pitch shafts, it was observed that there was a very small amount of negative interference between the blade root and the pitch shaft, ultimately altering the swashplate kinematics during operation. This flexibility is best described as a rigid flapping motion of the blade, resulting in a contribution to the measured blade tip flap bending deflection (δ). As the rotational frequency is increased and the blade becomes loaded, the blade moves to an extreme on the pitch shaft, at which point the blade reaches the end of travel. However, this means to accurately assess the measured tip deflection, the rigid flap displacement (δ_R) must be ascertained.

$$\delta = \delta_{Measured} - \delta_R$$

To assess the contribution of the rigid flap bending deflection (δ_R), measurements of blade tip flap bending deflection ($\delta_{Measured}$) at J = “No WT" were logged for a range of rotational frequencies between 480 and 1800 RPM, as shown in Figure 5.6. A second order line of best fit, with a resolution of 120 RPM, was applied to the experimental data, as the expected deflection should following a parabolic trend with increasing rotational frequency, due to the blade aerodynamic loading increasing with the square of the rotational frequency. It should be noted, to improve the reliability of the second order fit, additional test points at lower rotational frequencies from the test matrix ($\Omega < 1080$) were measured.

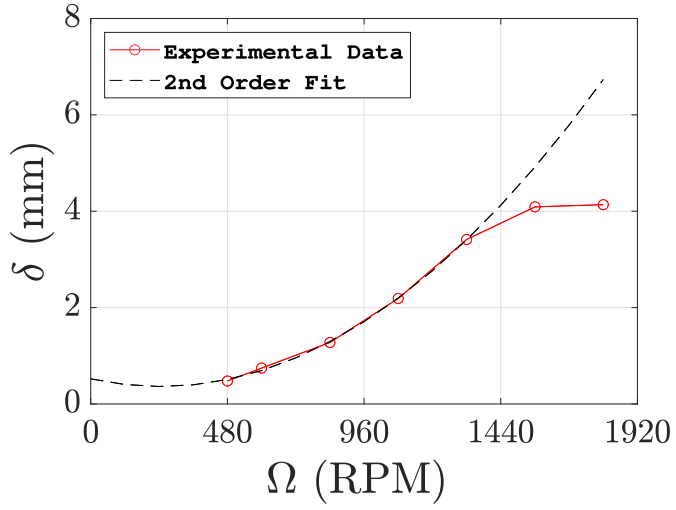

Figure 5.6: Experimental measurements of blade tip flap bending deflection at J = “No WT" case, as a function of rotational frequency with a 2nd order fit applied to assess the rigid body deflection of the propeller blades during operation at $\beta_{0.75R} = 16°$.

As previously explained in Section 3.1.4.4, the rig resonance that occurs at approximately 1500 RPM, is understood to alter the position of the rotor hub for rotational frequencies greater than 1500 RPM. Therefore, altering the performance of the entire propeller system. Moreover, the rigid deflection data also appears to be influenced by this movement of the hub, as experimental data points for Ω = 1560 RPM and 1800 RPM display a deviation from the expected parabolic behaviour that should occur as a consequence of the aerodynamic loading, that increases with the square of the rotational frequency. This expected trend of blade tip deflection has previously been captured experimentally [20].

This decrease in the flap bending deflection measurements highlight that there is either an unexpected reduction in blade loading, further indicating that the rig resonance is responsible for a change of 1/rev flapping behaviour, resulting in a deviation of the measurement when phased locked at a single measurement location, or more likely, movement of the rotor hub resulting in a lateral hub rotation (Γ_R). Consequently, only experimental data points collated at a rotational frequency less than 1560 RPM were used to generate the second order fit coefficients, so that the expected parabolic behaviour is not compromised by data points known to deviate from the expected behaviour. It is clear until a rotational frequency of 1560 RPM, the agreement of experimental and fitted data is very good. Therefore, the rigid flap displacement (δ_R) was determined as the mean of the data points from 0 to 480 RPM, resulting in $\delta_R = 0.44$ mm. All blade tip flap bending data points tested had this value removed to account for rigid deflection. Moreover, to quantify the effect of lateral hub rotation at Ω = 1560 RPM and 1800 RPM, the difference in expected and measured flap bending deflection was used to compute the in-plane rotation, using the equation below.

$$\Gamma_R = \tan^{-1}\left(\frac{\delta_{Fit} - \delta_{Measured}}{R}\right)$$

The hub rotation was calculated to be $\Gamma_R = 0.076^\circ$ and 0.238°, for 1560 and 1800 RPM, respectively. It is important to stress, due to the hub movement that occurs for rotational frequencies greater than 1500 RPM, absolute values of flap bending deflection data presented above this rotational frequency can not be used reliably to provided accurate deflection values. However, the trends of the data can be used to further understand both the aerodynamic and aeroelastic behaviour of the blades, including the identification of stall.

5.3.2 Blade Tip Flap Bending Deflection

Measurements of propeller blade tip flap bending (δ) at a single azimuthal position of $\psi = 270^\circ$, are presented in Figure 5.7 as a function of $\beta_{0.75R}$ for various advance ratios. Identical to the strain and performance data, the "No WT" curve was not obtained at constant advance ratio as this depends on the blade pitch angle. Measurements of flap bending displacement of the blade tip at the 25% tip chord location are shown to reduce with an increased advance ratio, when

operating at a constant rotational frequency. As already explained in the strain and performance results, this can be explained by the reduction in aerodynamic loading the blade is subjected to, due to a decrease in effective angle of attack. Furthermore, when considering the rotational frequency of 1080 RPM (shown in Figure 5.7a), the stall onset for the "No WT" curve can be appreciated at $\beta_{0.75R} = 22.3°$, where there is a slight reduction in gradient between this pitch angle and the prior test point of $\beta_{0.75R} = 19.1°$, indicating a departure of linear behaviour, which as shown in previously in Chapter 4, is an indicator of flow separation.

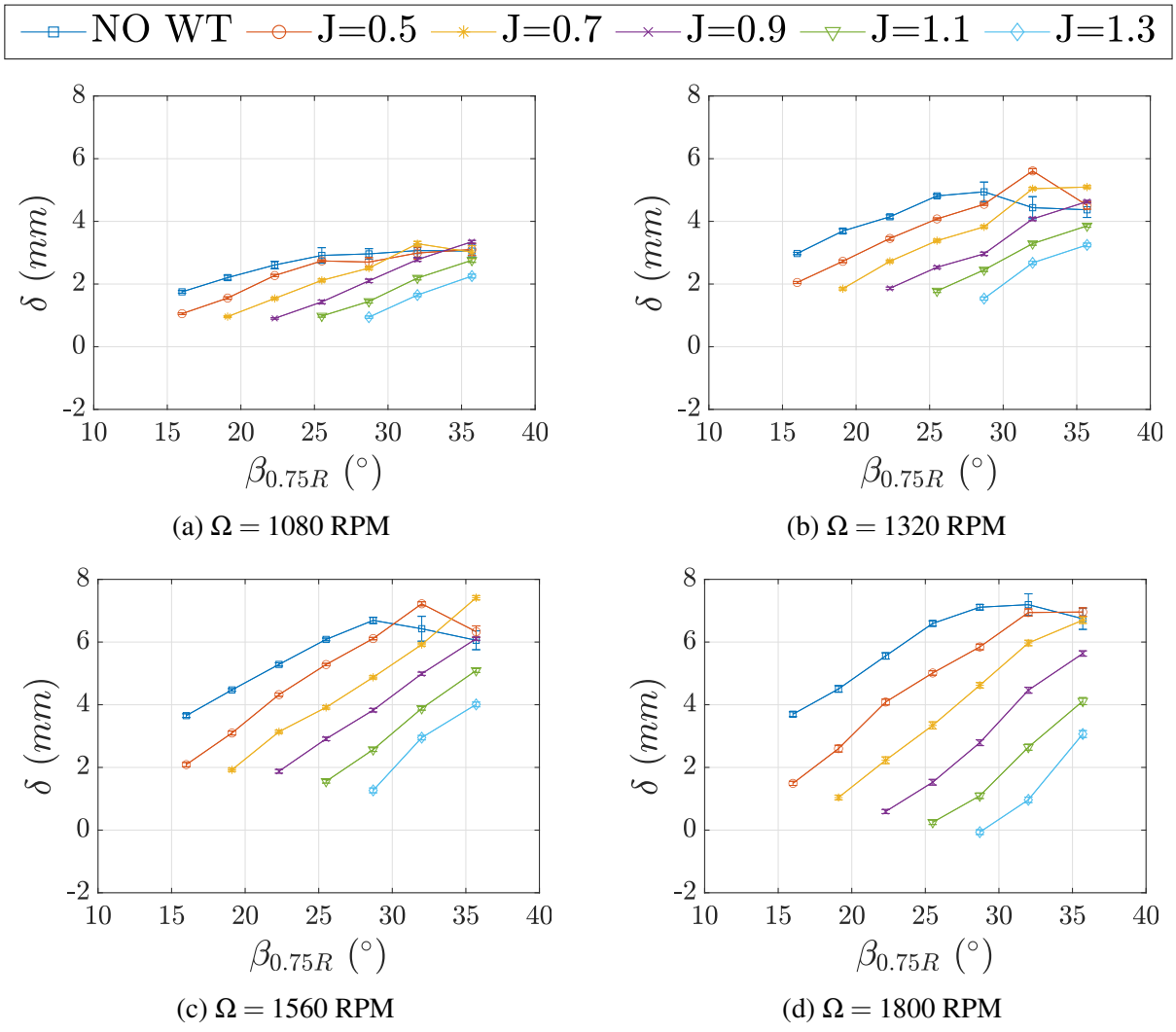

(a) $\Omega = 1080$ RPM

(b) $\Omega = 1320$ RPM

(c) $\Omega = 1560$ RPM

(d) $\Omega = 1800$ RPM

Figure 5.7: Blade tip flap bending deflection (δ) at $0.25c_{tip}$ as a function of the blade pitch angle for rotational frequency range of 1080, 1320, 1560 and 1800 RPM. Standard deviation of the measurements has been added as error bar.

To further support the presence of stall, the standard deviation of the bending deflections (displayed on Figure 5.7 as error bars) presents an increase, highlighting a growth in the measurement unsteadiness, a further indication of stalled flow. This growth in unsteadiness is more apparent for increased pitch angles, as deeper stall develops, ultimately enhancing the flow unsteadiness. In addition, measurements of blade tip flap bending deflection identify the presence

of stall at $\beta_{0.75R} = 22.3°$, in agreement with the measurements flap bending strain and propeller performance. Moreover, as the advance ratio is increased, there is a noticeable delay in stall angle for larger blade pitch angles. This is apparent when continuing to focus on the 1080 RPM plot, for cases J = 0.5 and J= 0.7, with stall identified at $\beta_{0.75R} = 28.7°$ and 32°, respectively. However, it is clear for J > 0.9, the blade tip flap bending deflection remains linear as a function of $\beta_{0.75R}$ and the flow unsteadiness does not grow, reaffirming that for large J values the flow remains attached. Furthermore, the behaviour of the blade tip flap bending deflection is similar for increased RPM values. However, it is clear that propeller operating at lower RPM values, displays a reduction of blade tip flap bending deflection at smaller values of $\beta_{0.75R}$, thus promoting stall sooner. At larger RPM conditions, flap bending measurements indicate a delay in the manifestation of stall. This is apparent at 1320 RPM, when focusing on the "No WT" curve at $\beta_{0.75R} = 28.7°$, where the departure from linear behaviour and significant rise in standard deviation can be appreciated when compared to the equivalent blade pitch angle for the 1080 RPM case. With regards to the flap bending deflection measurements at $\Omega = 1560$ and 1800 RPM, the criteria of stall identification from blade tip flap bending deflection measurements remains consistent. However, as previously mentioned, at rotational frequencies larger than 1500 RPM, the rotation of the rotor hub introduces a bias into the absolute value of the flap bending displacement. Therefore, Figures 5.7c and 5.7d, must be interpreted with a larger degree of caution. It is however reinforced that increasing J for a given RPM and increasing RPM for a given J, delays the onset of stall. Moreover, the 1800 RPM case (Figure 5.7d) at J = 1.3, presents a finding of negative flap bending, that was also identified in the strain measurements displayed in Figure 4.8. Despite reduced confidence in the measurements at 1560 and 1800 RPM, this behaviour of blade tip flap bending deflections further supports that at an approximate advance ratio of $J = 1.3/1.4$, the propeller blade tip is operating in a negative thrusting condition. Thus, identifying the upper operational boundary of the propeller design envelope. It should be noted that similar to stall, negative tip flap bending can pose many unfavourable aerodynamic conditions on an operating propeller, an obvious example of this is an excessive structural stress on the blade as a direct result of a portion of the blade thrusting in the opposite direction from the remainder of the blade. Ultimately, reducing blade aerodynamic performance whilst increasing the probability of structural failure. To be clear, operation in the negative thrusting condition does not mean structural failure will occur as blades are designed to operate with a safety factor. However, it should be reinforced that operation outwith the specified design envelope is not common practice and is not advised.

5.3.3 Blade Tip Torsional Deflection

In addition to measurements of propeller blade tip bending (δ), measurements of propeller blade tip torsional twist ($\Delta\theta$) are presented in Figure 5.8, where results are displayed as a function of $\beta_{0.75R}$ for various advance ratio conditions. Prior to the discussion of the torsional results, it is

important to clarify that for measurements of torsional twist presented, a negative value of $\Delta\theta$ corresponds to a nose down rotation. For all rotational frequencies presented in Figure 5.8, it is clear that an increased blade pitch angle results in an increased nose down torsional twist. This twist behaviour at the blade tip further supports the behaviour of the flap bending deflection, as an increasing nose down twist will result in a reduction in the blade aerodynamic loading due to a reduced effective angle of attack. This behaviour at the blade tip is likely a consequence of a negative propeller twisting moment generated by the centre of pressure acting at a location aft of the blade centre of gravity. As such the blade tip twists in a nose down direction, reducing the effective angle of attack.

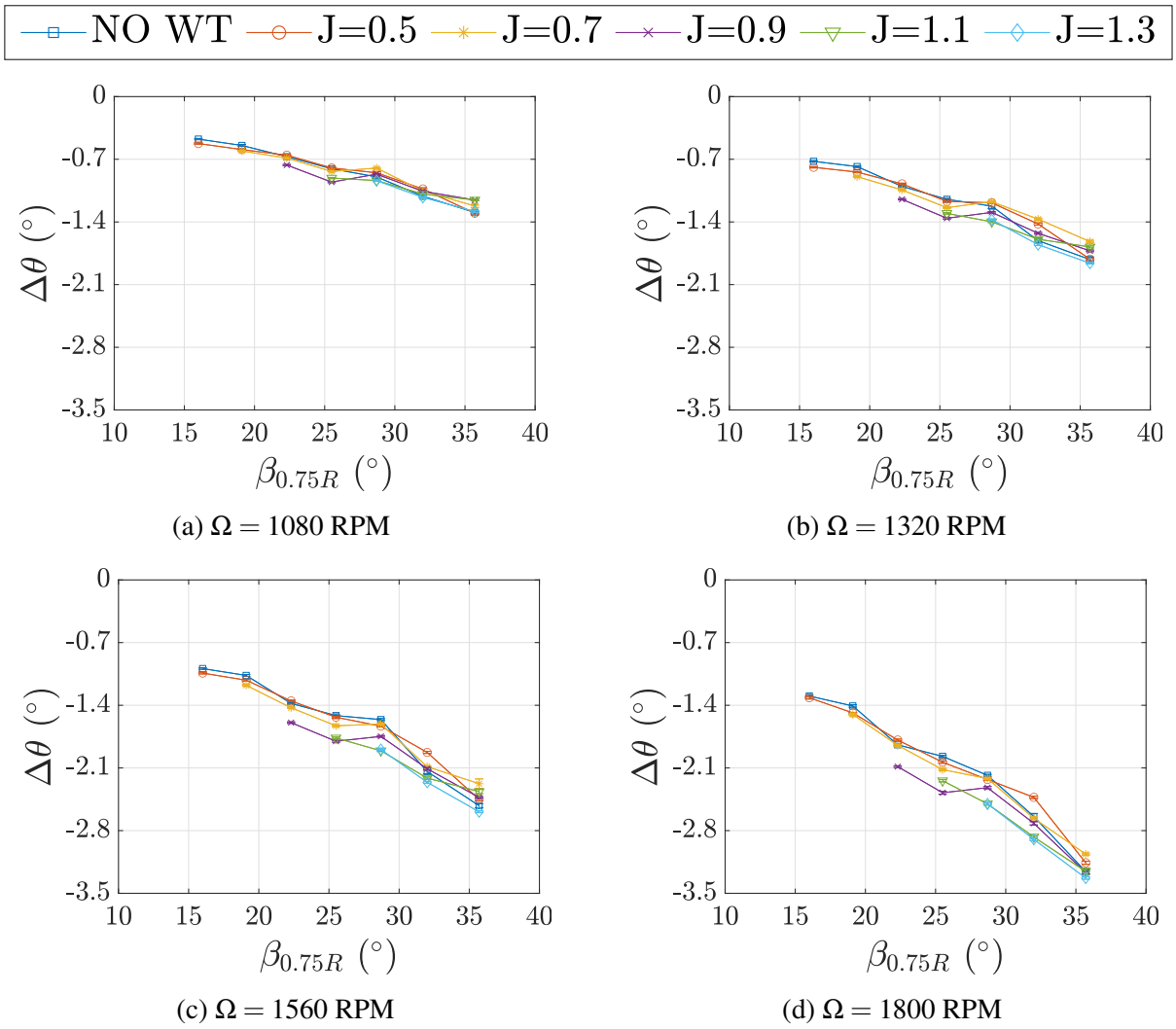

(a) $\Omega = 1080$ RPM

(b) $\Omega = 1320$ RPM

(c) $\Omega = 1560$ RPM

(d) $\Omega = 1800$ RPM

Figure 5.8: Blade tip torsional deflection ($\Delta\theta$) as a function of the blade pitch angle for rotational frequencies of 1080, 1320, 1560 and 1800 RPM. Standard deviation of the measurements has been added as error bar.

Despite this apparent reasoning, it should be stressed that measurements of torsional twist at the blade tip are not representative across the entire blade span. Therefore, due to the increased blade thickness and sectional aerodynamic chord length towards the tip, an increased sectional

torsional stiffness is expected, thus preventing the entire blade from twisting nose down. Furthermore, for all rotational frequencies presented, measurements of blade tip twist appear to grow linearly with increasing blade pitch angle with no clear deviations marking the onset of stall. Considering all rotational frequencies, measurements obtained between $\beta_{0.75R} = 22.5° - 28.7°$, highlight a slight deviation. However, upon comparison to the strain measurements of the most outboard torsional strain gauge (T2), shown in Figure 4.10, there is no clear overlap between torsional strain measurements and blade tip torsional twist. This observation highlights that the behaviour of both torsional strain and optical tracking torsional measurements, is not a very reliable method to identify stall onset as it is significantly more difficult to appreciate operating conditions at which stall is present. This can be explained by the increased torsional stiffness of the blade with respect to that of flap bending stiffness, thus the increase in torsional deflections are driven by the increased rotational frequency plus advance ratio and not solely the presence of separated flow. This observation in the results can be further supported by very small measurements of the standard deviation for the corresponding conditions, suggesting there is very little unsteadiness in the blade twisting behaviour, even at conditions where stall has been identified as present.

However, when considering the natural frequencies of the blade modes in free-free conditions, shown in Table 3.6, it is clear that the blades are very stiff in both bending and torsion, with the first bending mode at 261.3 Hz and first torsion at 933.4 Hz. Therefore, as shown throughout this thesis, measurements of the aeroelastic response of the blades used to identify stall are primarily displayed within flap bending measurements. Furthermore, despite many test points operating in deep stall, there was no triggering of aeroelastic phenomena such as stall flutter, which typically manifests as a purely torsional oscillation. Therefore, it is clear that the MENtOR blades are too stiff both in torsion and flap bending to excite the relevant blade modes for an aeroelastic response.

5.4 Chapter Summary

Measurements of propeller performance and blade tip deflections were presented within this chapter as part of a multi measurement approach to identify the onset of blade stall and support the validity of the stall boundary identification criteria previously developed. Measurements of propeller thrust and torque were able to capture test conditions at which stall was fully developed, correlating well with the identified test conditions that were shown to exhibit stall using the stall boundary identification criteria. At operational conditions where stall onset is at early stages of development and more subtle, the presence of stall onset is more apparent in blade strain measurements therefore supporting the applicability of the stall boundary identification criteria to identify the blade stall boundary. Furthermore, measurements of propeller blade tip deflections were shown to capture the onset of stall. Flap bending measurements were shown

to appear more reliable in the detect of stall when compared to that of the blade torsional deflections. Similar to performance measurements, the presence of stall onset is more apparent in blade strain measurements. However, the test conditions of fully developed stall can be clearly identified. In summary, a multi measurement approach was implemented using two independent measurement techniques, both supporting the validity of the stall boundary identification criteria.

Chapter 6

A Single Bladed Rotor Operating At High Advance Ratio

This chapter presents a towing tank investigation into the strain and load characterisation of a single bladed rotor operating in both hovering and edgewise flight conditions at high advance ratios. Following the identification of stall through measurements of strain in axial flight conditions, a separate investigation is presented within this chapter to assess the viability of utilising measurements of the blade strain distribution to identify regions of reverse and separated flow in edgewise conditions. A description of the test matrix for both hover and edgewise conditions is presented in Section 6.1. Measurements of averaged rotor loads and blade strain distribution are presented for hover in Section 6.2. Averaged and phase resolved measurements of rotor loads and blade strain for edgewise conditions are presented within Section 6.3. A comparison of both experimental measurements are performed to assess the viability to define regions of separated and reverse flow.

6.1 Test Matrix

Tests were conducted at both hover and advance flight, at advance ratios (μ) ranging between 0.40 and 1.00 for two collective angles (θ) of 7^o and 25^o. The 7^o case will be used to investigate the blade response in attached flow on the advancing side of the rotor, whereas the 25^o case will be used to study the blade response in separated flow conditions around the entire azimuth.

Hover testing was completed at three different rotational speeds of 16, 20 and 24 RPM. Load data and strains were captured to evaluate the impact of rotational speed on blade structural response at hover. A small study into rotor hover efficiency was performed. This will act as a benchmark from which blade response in forward flight can be compared against. Testing

Elements of this chapter were presented in Croke et al. "Experimental Investigation Of Rotor Blade Structural Response In Hovering and Advance Flight At Low Reynolds Number Conditions" at the Vertical Flight Society's 80th Annual Forum & Technology Display, Montréal, Québec, Canada, Canada, May 07-09, 2024.

at hover was performed for both collective angles of 7^o and 25^o. Furthermore, testing was performed at five high advance ratio conditions, ranging from $\mu = 0.40$ to 1.00 in equally spaced increments of 0.15, as shown in Table 6.1.

Table 6.1: Single rotor blade investigation test matrix as a function of blade pitch θ and advance ratio μ. Each test was performed at a constant rotational frequency of 20 RPM. X = Point tested, Blank = Point not tested.

θ	$\mu = 0.00$	$\mu = 0.4$	$\mu = 0.55$	$\mu = 0.70$	$\mu = 0.85$	$\mu = 1.00$
7^o	X	X	X	X	X	X
25^o	X	X	X	X	X	X

A constant rotor rotational speed of 20 RPM was selected due to the load limitations of the force balance. The rotor tip speed (V_{tip}) was $0.655 m/s$ with a corresponding tip Reynolds number (Re_{tip}) of $32,600$. Also, higher rotational frequencies result in larger tip speeds, therefore any increase above 20 RPM for this blade would have limited the maximum available advance ratio due to translation motion speed limitation of the towing tank. The corresponding speeds and Reynolds number at each advance ratio are shown in Table 6.2.

Table 6.2: Test matrix of advance conditions showing advance ratio, forward tow velocity and Reynolds number.

Advance Ratio μ (-)	Tow Velocity U_∞ (m/s)	Reynolds Number Re (-)
0.40	0.26	13,000
0.55	0.36	17,900
0.70	0.46	22,800
0.85	0.56	27,700
1.00	0.66	32,600

Within this chapter, standard rotorcraft notation, typical of helicopters is used. Coefficients of thrust (C_T), torque (C_Q) and moment (C_M) are defined as follows:

$$C_T = \frac{T}{\rho V_{tip}^2 A}$$

$$C_Q = \frac{Q}{\rho V_{tip}^2 A R}$$

$$C_M = \frac{M}{\rho V_{tip}^2 A R}$$

6.2 Hovering Flight

6.2.1 Rotor Loads

To establish a series of baseline data that can be used to compare to the rotor performance in forward flight, both coefficients of rotor thrust and torque were determined at hovering conditions as shown in Figure 6.1. Three rotational frequencies of 16, 20 and 24 RPM were studied to assess the dependency of the measurements on Reynolds number. Rotor thrust coefficients were shown to be effectively independent of RPM variation and were quantified at $C_T = 0.0017$ and 0.0057 for $\theta = 7^o$ and $\theta = 25^o$ respectively, for a rotational frequency equal to 20 RPM. The increase in thrust can be attributed to the increased rotor collective angle. Measurements of rotor torque coefficient were found to be $C_Q = 0.00039$ and 0.0024 for $\theta = 7^o$ and $\theta = 25^o$, respectively for a rotational frequency equal to 20 RPM. Torque measurements were shown to increase for the $\theta = 25^o$ case due to the nature of the stalled flow increasing both the induced and parasitic drag contributions. Moreover, torque measurements were also found to be slightly dependent on Reynolds number, with increasing RPM. Again, this can be attributed to the presence of stall around the entire rotor azimuth. The standard deviation of the measurement were computed to assess the aerodynamic unsteadiness. As expected, at hover, unsteadiness was found to be very low and almost non-appreciable due to equal loading around the azimuth.

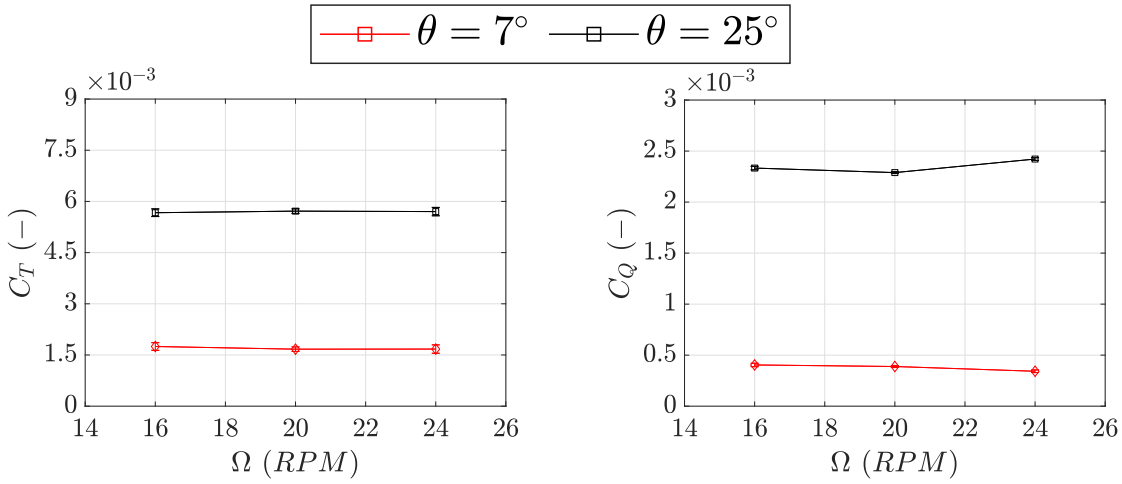

(a) C_T (b) C_Q

Figure 6.1: Comparison of rotor thrust (C_T) and torque (C_Q) coefficients at hovering conditions ($\mu = 0.00$) for blade collective angles of $\theta = 7^o$ and $\theta = 25^o$ shown as a function of rotor blade rotational frequency (Ω). Standard deviation of the measurements has been added as error bar.

An assessment of rotor hovering efficiency was undertaken by evaluating both disc loading (DL) and Figure of Merit (FoM) parameters, defined below, for all rotational frequencies tested, the results are displayed in Table 6.3.

$$DL = \frac{T}{A} \qquad FoM = \frac{C_T^{3/2}}{C_Q\sqrt{2}}$$

For the 20 RPM case, which was the chosen RPM for testing, disc loading was evaluated to be 0.72 and 2.45 for $\theta = 7^o$ and $\theta = 25^o$, respectively. Rotor FoM values for both collective angles were found to be 0.124 and 0.133, respectively. FoM results shown here must be interpreted with some degree of scepticism as the rotor disc loading for which they have been evaluated for is not constant. This means due to the increase in thrust, the induced component of the power has risen relative to the profile component of power. Nonetheless, FoM results can still be used individually to provide an insight into the rotor hovering efficiency.

For both collective settings, a very low FoM was obtained. This can be primarily explained by the presence of only a single rotor blade, thus reducing equivalent rotor solidity when compared to a conventional dual or multi-bladed rotor. A prior single bladed rotor test at low Reynolds conditions, has also demonstrated very low values of FoM, similar to the values obtained in this investigation [65]. Furthermore, numerical optimisation studies for low Reynolds blade design have shown 3 bladed rotors display FoM values as low as 0.1 under certain operating conditions [93]. Additionally, the chosen blade design, incorporated a NACA 0024 aerofoil section (max thickness of 24%) across the entirety of the span, leading to an increase in profile drag due to thicker aerofoil section than that of the commonly used NACA 0012. Moreover, the blade was not an optimised geometrically, as it did not include a taper or twist distribution along the span. Furthermore, the blade tip did not make use of a rounded edge and was abruptly ended, leading to increased tip losses. However, despite the non-optimised geometry (required for the installation of strain gauges at such a small scale), the blade design was used to investigate unconventional and simplified rotor geometries that are likely to be incorporated into drones, small Unmanned Air Vehicle (UAVs) and MAVs. Typically, for a rotor of this size, high-fidelity blade design is not feasible unless for military or planetary applications.

Table 6.3: Comparison of rotor disc loading (DL) and figure of merit (FoM) at hovering conditions ($\mu = 0.00$) for blade collective angles of $\theta = 7^o$ and $\theta = 25^o$ shown as a function of rotor blade rotational frequency (Ω).

Ω	$\theta = 7^o$		$\theta = 25^o$	
	Disc Loading	Figure of Merit	Disc Loading	Figure of Merit
16	0.479	0.128	1.553	0.129
20	0.715	0.124	2.447	0.133
24	1.031	0.141	3.516	0.125

6.2.2 Structural Response

Measurement of blade strain distribution at varying rotational frequencies for both attached and stalled collective angles are displayed in Figure 6.2. Both collective angles display similar behaviour with a growth in measured strain for an increasing rotational frequency. This increase in strain can be explained by an increased generation of thrust at larger rotational frequencies. It should be noted that the thrust data presented in Figure 6.4a is presented in coefficient form. Therefore, the absolute value of thrust is not easily appreciated, as the compensation for increased dynamic pressure is applied. However, this increase in thrust is captured via the strain gauges instrumented within the blade, as for the $\theta = 25^o$ case the maximum strain magnitude is larger than the equivalent for a collective of $\theta = 7^o$. For both the $\theta = 7^o$ and $\theta = 25^o$ cases the strain distribution follows the expected pattern with the largest strain at the blade root and the smallest strain outboards towards the blade tip. This can be explained as the blade is fixed at the root with no longitudinal or lateral cyclic, thus the beam is representative of a cantilever beam.

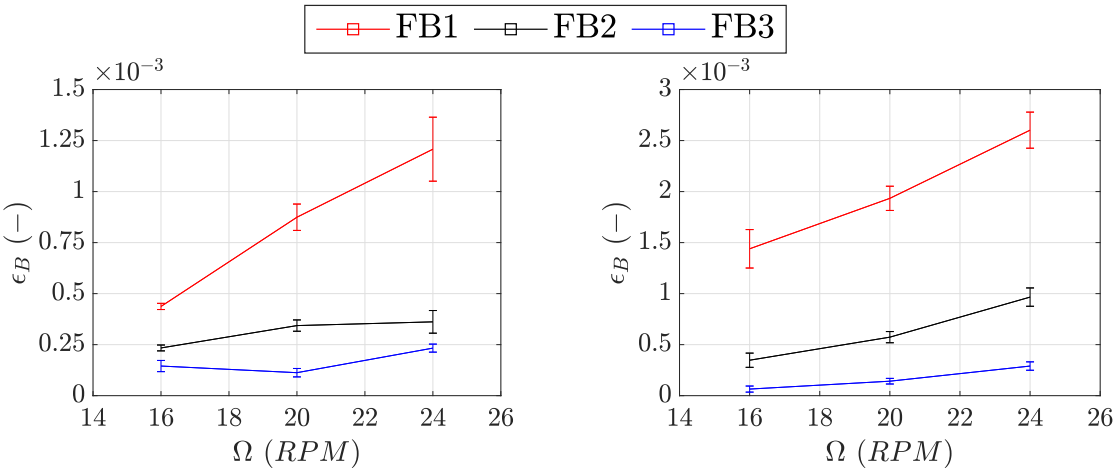

(a) $\theta = 7°$ (b) $\theta = 25°$

Figure 6.2: Mean strain (ε_B) measurements for a given collective setting as a function of rotational frequency presenting the strain distribution of FB1, FB2 and FB3. Error bars added to show the standard deviation of the measurements.

6.3 Edgewise Flow Conditions

6.3.1 Rotor Loads

Before analysis of rotor strain behaviour can be fully appreciated, insight of the rotor aerodynamic environment in question can be very useful. To provide some insight into this environment, rotor blade performance is evaluated using coefficients of thrust, torque and pitching moment. Analysis of the data in coefficient form allows for meaningful quantification of blade performance, as blade performance can be directly compared to that of other rotor blades of various scales and design parameters. Therefore, to adequately characterise the blade in forward flight, rotor thrust, torque demand and blade pitching moment around the feathering axis as a function of azimuthal position are presented in Figure 6.3.

Figures 6.3a and 6.3b show rotor thrust coefficient at $\theta = 7^o$ and $\theta = 25^o$, respectively. For both collective angles, thrust measurements display the same trend of behaviour despite the $\theta = 25^o$ case being stalled around the entirety of the azimuth, due to an excessive angle of attack. Firstly, focusing on the advancing side of the rotor disc ($0^o < \psi < 180^o$), as expected, the reduced collective angle results in lower measurements of peak thrust for a given advance ratio when compared to the $\theta = 25^o$ case. It is also observed for both collectives tested, that as the advance ratio is increased, the magnitude of the thrust also increases. Despite the similarities in the behaviour of the thrust data for both collectives, there is a noticeable difference in the azimuthal position at which the peak loading occurs. For $\theta = 7^o$ peak loading occurs at approximately $\psi = 90^o$ whereas at $\theta = 25^o$ peak loading occurs at approximately $\psi = 75^o$.

Shifting the focus to the retreating side of the rotor disc ($180^o < \psi < 360^o$), where regions of reverse flow occur, it can be observed for both collective angles that there in a minima of rotor loading at approximately $\psi = 250^o$. Due to the large advance ratios that were tested, the blade in the retreating section of the disc is subjected to increased reverse flow effects for $\mu > 0.4$. This can be appreciated clearly from the negative thrust measurements, meaning the blade is thrusting in the opposing direction from the advancing side of the rotor disc. Moreover, for increasing advance ratios the magnitude of the negative thrust grows due to the increased region of the blade surface area that is subjected to the reverse flow. For example, at an advance ratio of 1, the entire blade is entrained in reversing flow when at $\psi = 270^o$ on the retreating side of the rotor disc. In addition, increased advance ratio conditions see outboard portions of the blade enter and exit the reverse flow region over a larger span of azimuthal angles. This can be better appreciated when considering $\mu = 0.55$ and $\mu = 0.70$ cases shown in Figure6.3a. For the $\mu = 0.55$ case, the identifiable reverse flow region where thrust is negative, occurs when the blade is positioned within the azimuthal range of $200^o < \psi < 300^o$. At the larger advancing condition, $\mu = 0.70$, negative thrusting is observed for an azimuthal range of $180^o < \psi < 330^o$ thus highlighting that not only does the magnitude of the thrust vary but also the onset locations

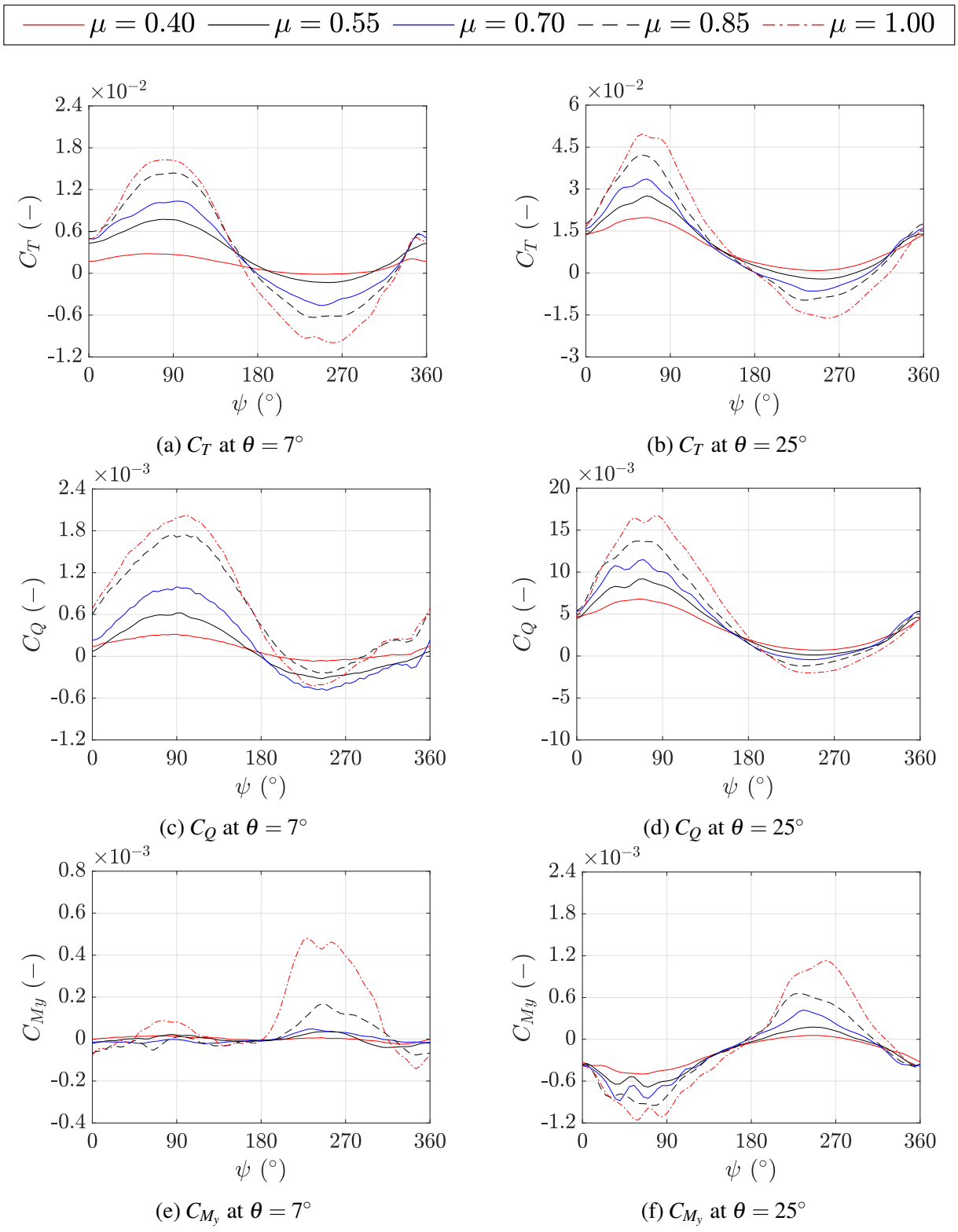

(a) C_T at $\theta = 7°$

(b) C_T at $\theta = 25°$

(c) C_Q at $\theta = 7°$

(d) C_Q at $\theta = 25°$

(e) C_{M_y} at $\theta = 7°$

(f) C_{M_y} at $\theta = 25°$

Figure 6.3: Coefficients of thrust (C_T), torque (C_Q) and feathering moment (C_{M_y}) of a rotor blade in advance flight ($\mu = 0.40 - 1.00$) at a collective angles of $\theta = 7°$ and $25°$ shown as a function of rotor blade azimuthal position (ψ).

at which reversal of thrust occurs. For conditions at which $\mu > 0.70$, the trend of growth in magnitude and the azimuthal range at which reverse flow occurs continues. This behaviour has also been identified for the larger collective setting as shown in Figure 6.3b.

Similar to the thrust behaviour, measurements of blade torque (shown in Figures 6.3c and 6.3d) detail the required rotor power for both collective angles. For the $\theta = 25^o$ case, there is a significant torque increase with respect to the $\theta = 7^o$ case.

$$C_P = \underbrace{\frac{kC_T^2}{2\mu}}_{\text{Induced Power}} + \underbrace{\frac{\sigma C_{d_0}}{8}(1+4.6\mu^2)}_{\text{Profile Power}} + \underbrace{\frac{C_D\mu^3}{2A}}_{\text{Parasitic Power}}$$

This can be explained by analysing the contributions of each of the power components as shown in the equation above. An increase in induced power is a consequence of the large increase in blade thrust as a result of an increased collective. Profile power increases due to the growth in advance ratio and parasitic power is increased due to the presence of stalled flow. Flow separation results in a large increase in blade drag which stems from the development of a separated region trailing the blade. Thus when all components are considered, the significant growth in rotor torque is appreciable. It should also be noted, that similar to the measurements of thrust, the azimuthal range at which motor torque measurements identify the reverse flow grows, further supporting that for larger advance ratio conditions the azimuthal angle range for which the blade is subject to flow reversal is increased. However, as the torque is not solely dependent on the thrust, the effect is harder to appreciate.

Furthermore, Figures 6.3e and 6.3f display the coefficient of pitching moment around the blade feathering axis at $\theta = 7^o$ and $\theta = 25^o$, respectively. Considering the $\theta = 7^o$ case on the advancing side of the rotor disc, it is observed that the pitching moment coefficient is approximately zero for all advance ratio conditions. A pitching moment coefficient of approximately zero is to be expected on the advancing side of a rotor operating in attached flow conditions as the blade aerodynamic centre is co-located with the blade geometric quarter chord. However, on the retreating side of the blade this is not the case, due to transfer of the aerodynamic centre from the blade geometric quarter chord to the blade geometric three quarter chord, thus promoting a positive pitching moment, which corresponds to a nose up rotation. Moreover, the peak pitching moment coefficient is observed at approximately $\psi = 250^o$, coinciding with the minimum thrust on the retreating side. Identical to the thrust behaviour, an increase in advance ratio corresponds to a growth in peak pitching moment coefficient due to the growth in the reverse flow region. This is highlighted when comparing the identified reverse flow region azimuthal range for the $\mu = 0.55$ ($200^o < \psi < 300^o$) and $\mu = 0.70$ ($180^o < \psi < 330^o$) cases, highlighting an agreement with the identified range obtained via the rotor thrust measurements. Focusing on the $\theta = 25^o$ case, where the flow is separated around the entire azimuth, the blade pitching moment coefficient is observed to be negative on the advancing side, with a minima at approximately $\psi = 75^o$, where for a growth in advance ratio the peak magnitude increased. Alternatively, on

the retreating side of the blade, the behaviour is similar. However, due to the reversal of the thrust direction, measurements of pitching moment coefficient were found to be of similar trend and maximum amplitude but with an opposing sign. The maximum pitching moment coefficient on the retreating side was observed at approximately $\psi = 250^o$.

To further quantify the rotor aerodynamic environment, Figure 6.4 presents mean rotor thrust and torque coefficient measurements for both collective settings as a function of advance ratio. The standard deviation of the measurements have been plotted as error bars to highlight the behaviour of the loading oscillations. The $\theta = 25^o$ case demonstrates larger mean thrust and torque loads at all advance ratios when compared to the $\theta = 7^o$ case. It can also be observed that for both collectives, the thrust coefficient remains relatively constant with increasing advance ratio. When analysing the torque coefficient, it is clear for both collective angles, there is a growth in mean torque with advance ratio. This can be attributed to the fact that the growth in advance ratio increases the profile and parasitic drag of the rotor. Moreover, this increase is more apparent for the $\theta = 25^o$ case due to the presence of stalled flow. Finally, with regards to rotor loads, both collectives indicate a growth in thrust and torque oscillations as a consequence of increasing advance ratio, which can be attributed to larger unsteadiness as a consequence of increasing regions of reverse flow. Again, the $\theta = 25^o$ case exhibits very large oscillations with respect to the $\theta = 7^o$ case, due to the presence of stalled flow and increased rotor loading.

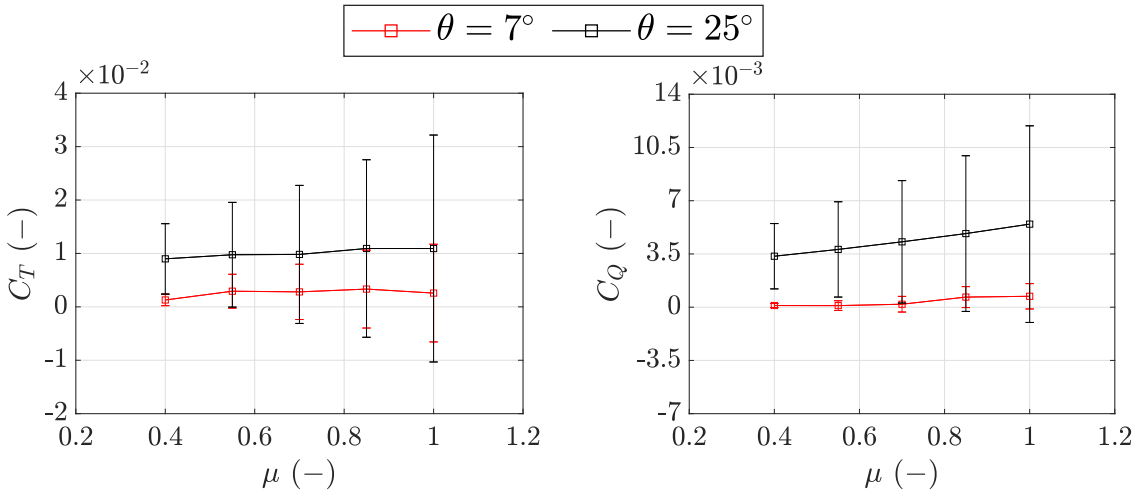

(a) C_T (b) C_Q

Figure 6.4: Mean coefficients of thrust (C_T) and torque (C_Q) measurements for both collective settings as a function of advance ratio. Error bars added to show the standard deviation of the measurements.

6.3.2 Structural Response

Now that the rotor aerodynamic environment has been described and quantified, measurements of rotor strain can be presented. Measurements of rotor strain as a function of azimuthal position, for a range of advance ratios at two different radial locations, are presented in Figure 6.5.

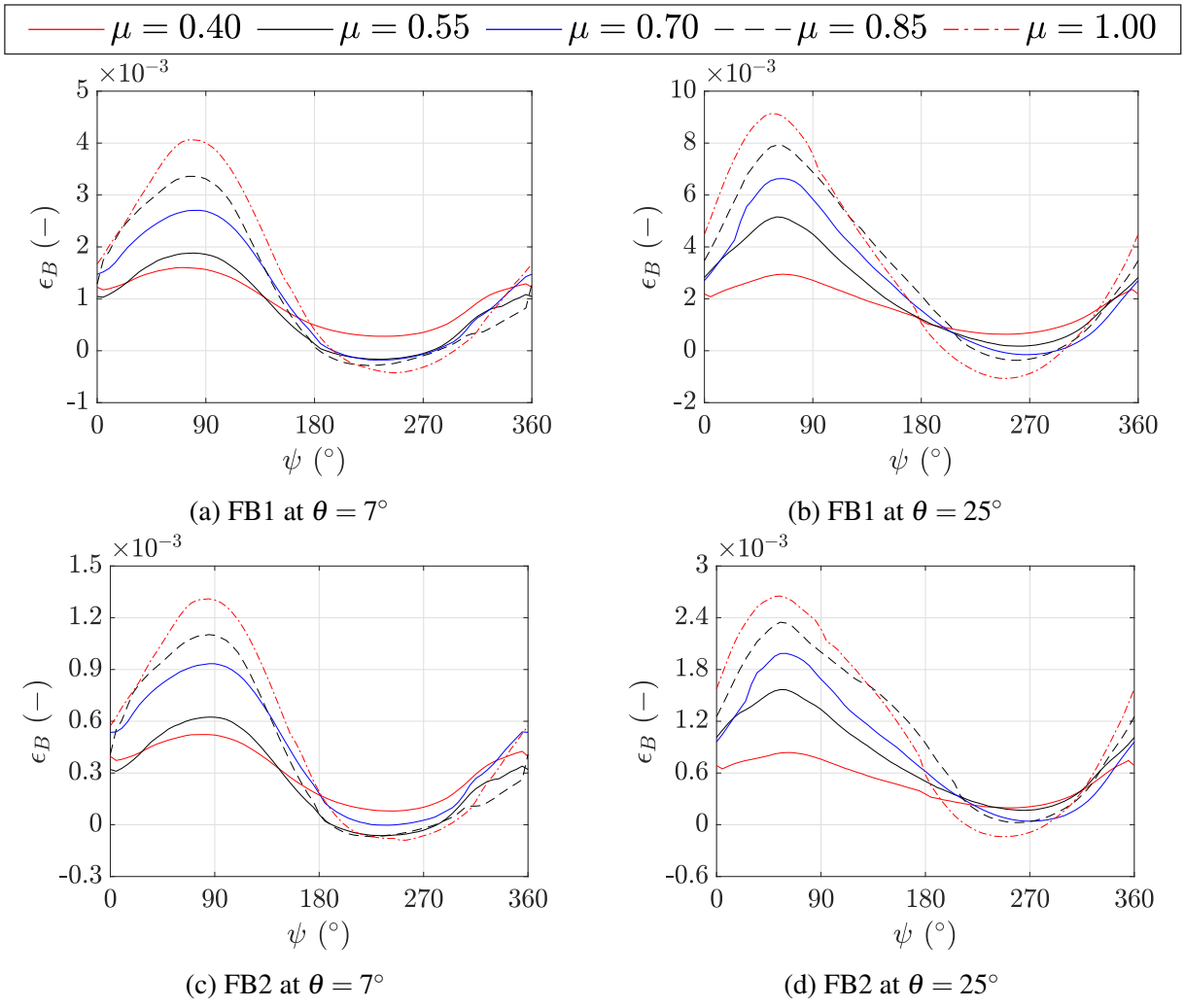

(a) FB1 at $\theta = 7°$

(b) FB1 at $\theta = 25°$

(c) FB2 at $\theta = 7°$

(d) FB2 at $\theta = 25°$

Figure 6.5: Strain (ε_B) at FB1 ($y/R = 0.25$) and FB2 ($y/R = 0.50$) in advance flight ($\mu = 0.40 - 1.00$) at collective angles of $\theta = 7°$ and $\theta = 25°$ shown as a function of rotor blade azimuthal position (ψ).

Figures 6.5a and 6.5c show for the $\theta = 7^o$ case, measurements of rotor blade strain from FB1 and FB2 bridges to highlight the strain distribution along the blade span. It is apparent that the strain behaviour across both bridges on the advancing side of the rotor disc follows the behaviour exhibited by the thrust. For both FB1 and FB2 bridges, the peak strain occurs at approximately $\psi = 90^o$, identical to the peak loading shown in the thrust data. Also, just like the thrust data, an increase in advance ratio leads to a growth in peak strain magnitude. Shifting the focus to the retreating side, the minima of strain appears to also align with the behaviour shown in the thrust data, with the strain minima occurring at approximately $\psi = 250^o$ for both FB1 and FB2.

Focusing on FB1, it is clear for $\mu > 0.4$ there is an occurrence of negative strain on the retreating side of the disc, coinciding with the thrust minima location. Negative strain, indicates that the blade is being loaded in the opposing direction from the thrust axis, which is further indication of strong reverse flow effects. As the blade is non-twisted and non-tapered, the variation of strain magnitude across different bridges is useful to provide insight into loading distribution across the blade. However, it is important to note that the strain, although very dependent on loading, is not to be confused with a measure of loads, as the blade strain is also dependent on structural properties such as torsional and bending stiffness. When comparing FB1 to FB2, it is clear that FB1 has a larger magnitude of strain at any azimuthal location. This is to be expected as the blade is secured to the rotor hub at the root, ensuring a fixed collective angle with no longitudinal or lateral cyclic. Therefore, in terms of strain distribution, the blade is representative of a cantilever beam and the strain would be expected to drop further outboard towards the tip.

Furthermore, similar to the thrust measurements shown previously, measurements of flap bending strain distribution appear to also highlight the increased azimuthal range at which reverse flow regions develop. These reverse flow regions are more apparent in measurements of FB1 due to the inboard location of the strain gauge bridge. Considering the $\mu = 0.55$ case, the identified reverse flow region occurs between, $190^o < \psi < 300^o$, demonstrating a close agreement with the $200^o < \psi < 300^o$ identified from load measurements. Similarly, at the largest advance ratio case tested, $\mu = 1.00$ the strain identified reverse flow region ($180^o < \psi < 310^o$) was compared to load based azimuthal ranges ($170^o < \psi < 300^o$). Highlighting the strong applicability of using strain measurements to capture the load based reverse flow regions, further demonstrating the ability to use strain measurements to reliably identify reverse flow in edgewise conditions. It should be noted, that both FB1 and FB2 strain measurements for the $\mu = 0.4$ case remain positive, highlighting no presence of strong reverse flow effects, agreeing with prior thrust measurements. Figures 6.5b and 6.5d show for the $\theta = 25^o$ case, measurements of rotor blade strain from FB1 and FB2 bridges. Identical to the $\theta = 7^o$ case, locations of maximum and minimum strain plus the behaviour of strain variation across the blade span at different bridge locations remains the same. However, due to the presence of stalled flow around the entire rotor azimuth, there is an unsteadiness in the strain measurement that can be visibly acknowledged (particularly in Figure 6.5d) by the variation in the smoothness of the strain on the advancing side of the rotor disc.

Similar to analysis of the load data, Figure 6.6 presents mean rotor strain measurements of individual bridges for both collective settings as a function of advance ratio. In addition, the standard deviation of the measurements have been plotted as error bars to highlight the behaviour of bridge strain unsteadiness. It is clear for the $\theta = 25^o$ case that the mean strain of any bridge is larger than that of the $\theta = 7^o$ case. This behaviour will primarily be a consequence of larger thrust loads. However, the presence of stalled flow will also have an influence on

measured strain due to the large increase in rotor drag. Moreover, structural parameters such as stiffness will also influence the measured strain. Again, identical to measurements of rotor loads, strain measurements unsteadiness is shown to grow with increased advance ratio, which can be explained as a consequence of increasing regions of reverse flow.

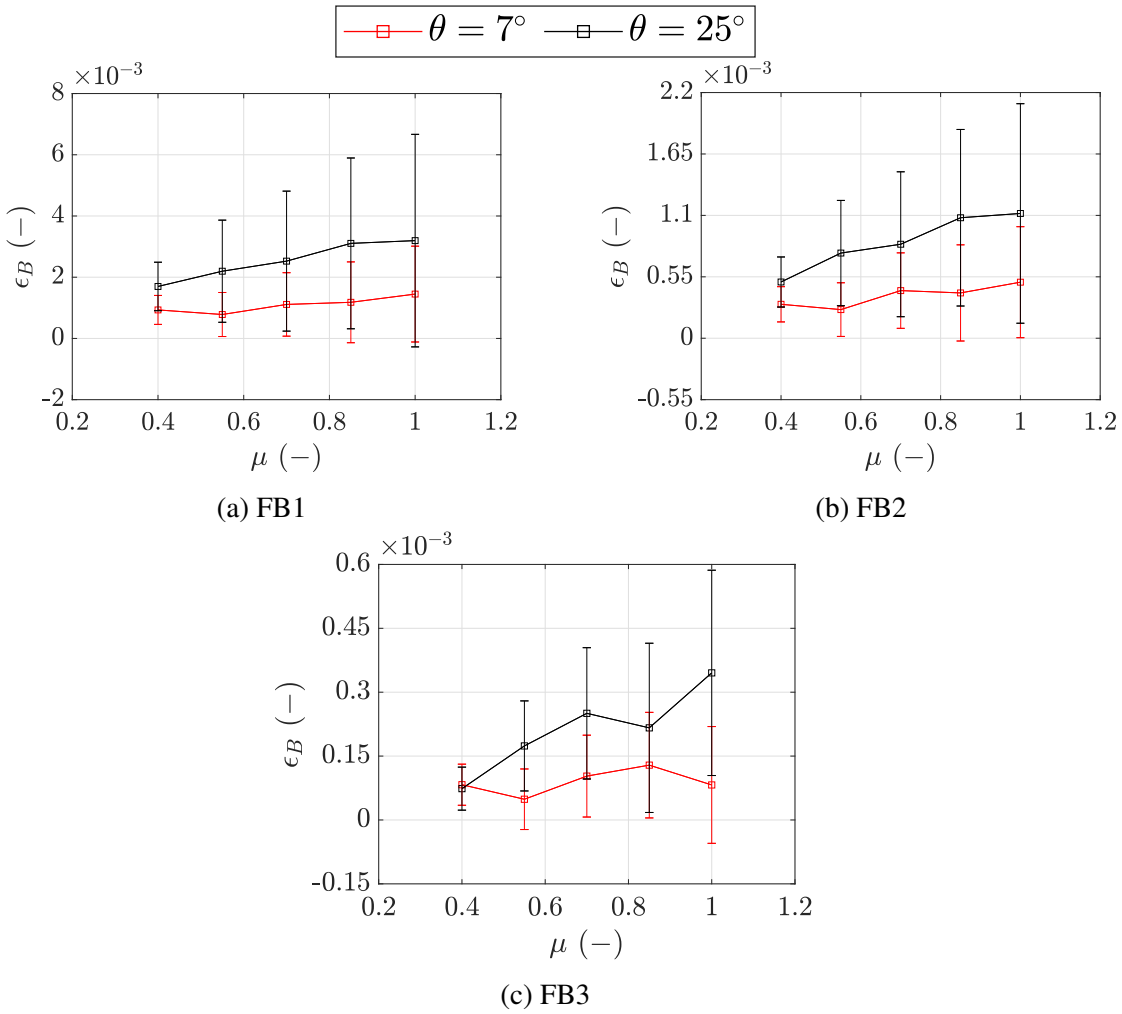

(a) FB1

(b) FB2

(c) FB3

Figure 6.6: Mean strain (ε_B) measurements for both collective settings as a function of advance ratio for individual bridges FB1, FB2 and FB3. Error bars added to show the standard deviation of the measurements.

To visualise the strain distribution across the blade more clearly, Figure 6.7 presents mean rotor strain measurements for different bridges for a given collective. As previously mentioned, it is clear that closer to the blade root there is a growth in mean strain and a reduction towards the blade tip. For both collective angles, the oscillation in the measured strain at FB1 is significantly larger due to the location of the bridge on the blade, as the most inboard bridge at 25% of the blade span this bridge is subjected to reverse flow at the lower advance ratios tested.

Finally, to further highlight the presence of stalled flow. Figure 6.8 presents the spectral content of FB1 at advance ratios of 0.4 and 1.00 for both collective angles. The spectra is shown as the non-dimensional frequency to highlight the dominant 1/rev signal and the surrounding

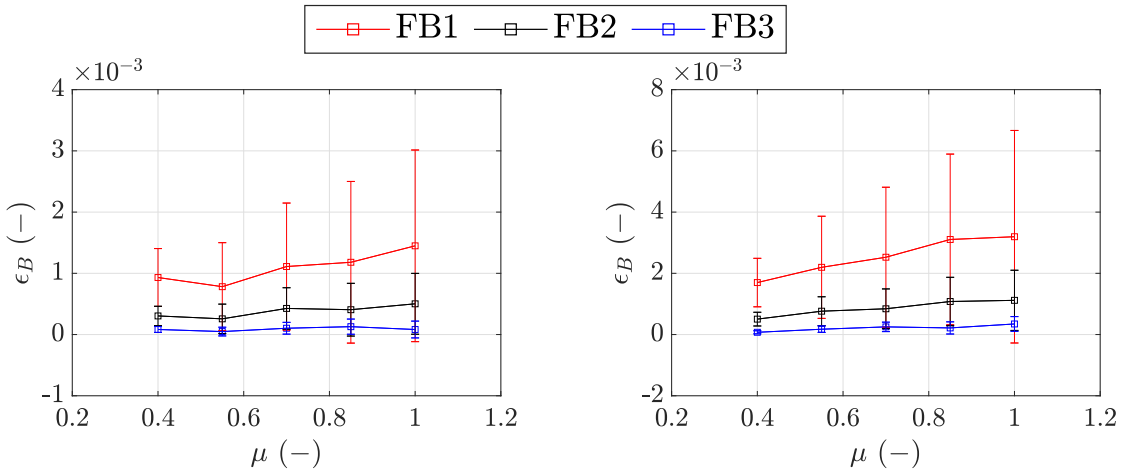

(a) θ at 7° (b) θ at 25°

Figure 6.7: Mean strain (ε_B) measurements for a given collective setting as a function of advance ratio presenting the strain distribution of FB1, FB2 and FB3. Error bars added to show the standard deviation of the measurements.

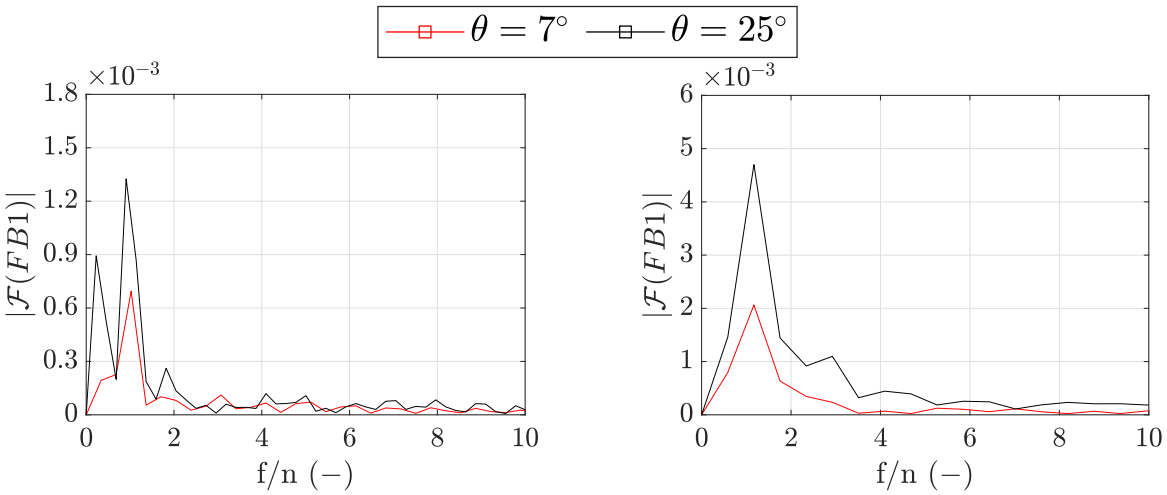

(a) $\mu = 0.40$ (b) $\mu = 1.00$

Figure 6.8: Amplitude of the Fourier transform (as a function of the non dimensional frequency f /n) of the strain measurements for FB1 at $\theta = 7°$ and $\theta = 25°$ for advance ratios of 0.4 and 1.00.

broadband of the signal. It is clear from the $\theta = 7^o$ case shown in Figure 6.8a that there is very limited broadband content within the signal and is dominated by a single rotor harmonic (1/rev). In contrast, the $\theta = 25^o$ case shows a large distribution of signal energy across a range of non-harmonic frequencies. This can be explained by stall induced vortical structures shedding into the wake, at frequencies that do not likely synchronise with the rotor harmonics. Figure 6.8b further confirms this behaviour as the $\theta = 25^o$ case continues to display a large distribution of signal energy across a range of non-harmonic frequencies. Moreover, as expected, the magnitude of signal energy is larger for the $\theta = 25^o$ case.

6.4 Chapter Summary

Following the identification of stall through measurements of strain in axial flight conditions, an investigation was performed to assess the viability of utilising measurements of the blade strain distribution to identify regions of reverse and separated flow in edgewise conditions at two collective conditions of $\theta = 7^o$ (attached) and $\theta = 25^o$ (separated). Reverse flow regions were identified through phase resolved measurements of rotor thrust, torque and pitching moment around the rotor azimuth, highlighting strong reverse flow effects for $\mu > 0.4$. Growth in reverse flow effects were observed for increasing advance ratio conditions due to the growth in the reverse flow region on the retreating side of the blade, where increased negative thrusting magnitudes and increased azimuthal ranges of negative thrust were observed. Phase resolved measurements of blade flap bending strain were also shown to exhibit the same behaviour, whilst also being able to capture the entry and exit of the reverse flow region for various advance ratios. Averaged measurements of loads and strain were also compared for both collective conditions, to assess the impact of the presence of separated flow around the entire rotor disc. The $\theta = 25^o$ collective setting displayed a noticeable growth in both thrust and torque for all advance ratio conditions, when compared to the $\theta = 7^o$ collective setting. Further to this, a growth in load unsteadiness was also observed as a consequence of stalled flow around the entire azimuth. Similarly, average strain measurements displayed an identical trend to load measurements, with larger strains observed towards the blade root. In summary, measurements of flap bending strain distribution have been demonstrated to successfully identify the presence of reverse and separated flow of a rotor operating in edgewise conditions.

Chapter 7

Conclusions and Future Work

This chapter highlights key findings presented from an experimental investigation into blade stall identification in both axial and edgewise flight conditions using a novel stall identification criteria. Recommendations of future work on how this criteria could be extended to aeroelastic instabilities such as stall flutter are discussed. Finally, key considerations on the development of rotary-wing test rigs are identified.

7.1 Conclusions

Blade stall identification in axial conditions was investigated through a wind tunnel investigation of tiltrotor blade stall in fixed pitch propeller mode. Testing was performed within the De Havilland 9ft x 7ft closed return wind tunnel, capable of reaching a maximum freestream velocity of $70m/s$ and made use of the United Kingdom National Rotor Rig, recently commissioned at the University of Glasgow to allow for testing of propeller blade sets up to 3000 RPM at Mach tip scaled conditions of 0.6. A custom 1.25m diameter tiltrotor blade set was instrumented with two fully bridged axial and two shear strain gauges to monitor the flap bending and torsional strain at several radial locations. To characterise the blade operational envelope, testing was conducted at multiple blade pitch angles ($\beta_{0.75R} = 15.9^\circ - 35.6$), advance ratios ($J = \text{No WT} - 1.4$) and rotational frequencies ($\Omega = 1080 - 1800$ RPM) ensuring a high resolution of data points.

To advance blade stall identification experimental methods and allow for the characterisation of blade operational boundaries in the absence of conventional stall identification techniques such as load measurement or flow visualisation, a novel blade stall identification criteria was developed using measurements of blade strain, wind tunnel velocity and motor data.

The propeller was identified as operating in a stalled condition when the following markers were observed: collapse of the induced velocity around the wind tunnel loop for increasing pitch angles when the wind tunnel fan is not in operation; departure from linear behaviour of the flap bending strain vs blade pitch curves; marked increase of the standard deviation of the flap bending strain, up to twice the pre stalled conditions; presence of non-harmonic content in the

strain spectra, up to 20 % in amplitude of the corresponding harmonic content; non-consistent oscillation amplitude in the strain time history and a more pronounced increase in torque for fully developed stall (even if not so evident at stall onset).

Further to the identification of stall, blade strain measurements were shown to capture blade eigenmode frequencies when analysed on a logarithmic scale, particularity the lower frequency the first flap bending mode. The first flap bending mode was experimentally identified between 90-100 Hz, which is very close to the numerically estimated first flap bending frequency of 113 Hz. To further support the ability to identify blade eigenmodes, strain spectra data display a peak of the non-harmonic content just past the 3/rev for the 1800 RPM case and just past the 5/rev for the 1080 RPM case, which translate to the same dimensional frequency of approximately 90–100 Hz, which suggests that the blade structural response to the broadband content of the stall induced vortical shedding mainly manifests as an excitation of the first flap bending mode.

In addition to the development of a blade stall identification criteria, flap bending bridges appeared to be more reliable in detecting stall onset than the torsional bridges, as torsional bridges only showed large variations in deeper stall conditions. Axial strain gauges used to form flap bending bridges were shown to identify the first three eigenmodes clearly, all of which are bending modes. Furthermore, torsional bridges which are composed of shear strain gauges are shown to capture the fourth eigenmode (torsion-bending) very accurately but cannot be used to identify the lower frequency bending modes, again supporting the notion that flap bending bridges provide a better insight into blade stall identification, as the blade first flap bending mode typically occurs at a lower eigenfrequency. Similarly, a more pronounced increase in torque was clear for cases of fully developed stall. However, increased torque measurements were not overly apparent at stall onset, meaning that torque information alone could not solely be used to identify the presence of stall in its early stages. It was also observed that as the blade pitch angle was increased, development of stall was observed to be more sudden in nature when varying the RPM (and therefore the blade critical Reynolds number) as opposed to a more gradual onset when the advance ratio was increased. It should be noted that the quantitative changes between pre and post stall conditions reported within this thesis are expected to be a function of propeller geometry, blade structural properties and operating conditions, thus no absolute threshold values for stall detection can be advised that are applicable for all propellers. However, the set of criteria defined in this thesis is expected to be generally applicable for stall detection on conventional propellers.

To further strengthen the validity of the stall boundary identification criteria developed, measurements of propeller performance and blade tip deflections were presented within this thesis as part of a multi measurement approach to identify the onset of blade stall. Measurements of propeller thrust and torque were shown to capture test conditions at which stall was fully developed, correlating well with the identified test conditions that were shown to exhibit stall using the stall boundary identification criteria.

Measurements of propeller blade tip deflection, both flap bending and torsional twist, were obtained using DIC to characterise the blade tip deformation during operation for both attached and stalled conditions. Measurements of flap bending deflection for highly loaded test cases such as No WT at 1800 RPM, were shown to exhibit deflections as large as 7 mm. Alternatively, at large advance ratios of 1.3 at 1800 RPM, blade tip deflections were shown to become negative, highlighting a negative thrusting condition as a consequence of a negative effective angle of attack. Flap bending deflections were shown to follow an identical behaviour trend to that of the flap bending strain results, displaying a deviation from linear behaviour as a function of blade pitch angle and a growth in the standard deviation of the deflection measurement for conditions at which stall has been identified using both performance and blade strain data, further supporting the ability to identify the presence of stall using flap bending deflection measurements. Conversely, measurements of torsional twist provided no clear ability to identify the onset of stall or stalled conditions.

Research activity regarding blade stall identification was extended to edgewise flight conditions by means of a towing tank investigation of a 0.625m diameter single bladed rotor. A custom blade was manufactured and instrumented with fully bridged axial strain gauges to monitor the flap bending strain at three radial locations. Measurements of rotor thrust and torque were acquired using a 6-DOF load cell to characterise the rotor aerodynamic environment. The rotor was tested at two fixed collective angles of $\theta = 7^o$ and 25^o in both hover and edgewise flight conditions for advance ratios ranging between 0.4 to 1.00 where strong reverse flow effects are present on the retreating side of the blade.

During hover, thrust measurements were found to be independent of the influence of Reynolds number, whereas the torque was shown to be somewhat dependant. For $\theta = 25^o$, both thrust and torque measurements were shown to increase when compared to the $\theta = 7^o$ case. Moreover, the non-optimised blade design and operation as a single rotor displayed relatively poor FoM values of 0.124 for $\theta = 7^o$ and 0.133 for $\theta = 25^o$.

For advancing flight conditions where $\mu > 0.4$, phase resolved measurements of thrust and torque were used to identified regions of reverse flow, occurring at approximately $\psi = 250^o$ for both collective angles. Furthermore, at increased advance ratio conditions, outboard portions of the blade enter and exit the reverse flow region over a larger span of azimuthal angles, as a consequence of the growth of the reverse flow area. For $\mu = 0.55$ and $\mu = 0.7$, the identified reverse flow regions were observed at $200^o < \psi < 300^o$ and $180^o < \psi < 330^o$, respectively. Phase resolved measurements of blade flap bending strain were obtained at three locations across the blade span, demonstrating identical azimuthal minima and maxima locations as load data. For $\mu = 0.55$, a strain identified reverse flow region was observed at $190^o < \psi < 300^o$, demonstrating the ability of strain data to successfully capture the blade reverse flow region and stall in edgewise flight conditions, this agreement of strain and load reverse region boundary identification was shown to extend across all advance ratios tested. Spectra results of the strain displayed

a dominant 1/rev signal can be clearly identified for both collective angles. Similarly to stalled cases in axial conditions, a large distribution of signal energy across a range of non-harmonic frequencies for the $\theta = 25^o$ case, is observed due to the presence of stalled flow.

In summary, this body of work presents a novel blade stall identification methodology, which is primarily based on the measurement of blade structural response. The objectives set out at the beginning of this thesis were met through the development of experimental rotary-wing test rigs and extensive wind tunnel and towing tank testing campaigns. For both axial and edgewise flight conditions, validity of the identified stalled and reverse flow regions has been supported through the implementation of a multi-measurement approach, utilising experimental methods such as load measurement and stereoscopic digital image correlation. In addition to the development of a novel stall identification methodology, this research has also clearly addressed the need for a comprehensive state-of-the-art aerodynamic and aeroelastic experimental dataset for a blade design with well defined geometric and structural properties.

7.2 Future Work and Considerations

7.2.1 Stall Flutter Identification Criteria

At certain operational conditions where there is a presence of stall, an aeroelastic instability termed stall flutter can occur. Propeller stall flutter has been and still very much is an important phenomenon within the propeller community, as new blade designs and the use of composite materials could potentially lead to an operational condition where stall flutter is excited. As stall flutter onset can be extremely abrupt, this can lead to instant blade failure and the destruction of the propeller rig or airframe. At present there is very limited experimental data that can be utilised regarding stall flutter as a consequence of undefined blade geometries and structural properties. However, there has not been a significant experimental effort to address this gap of propeller stall flutter. This can be attributed to the complexities of performing aeroelastic testing on scaled blades within a wind tunnel. It is therefore crucial that an experimental investigation focused on the identification, observation and measurement of the propeller stall flutter phenomenon and its characteristics is undertaken, using state-of-the-art experimental methods.

7.2.2 Considerations of Key Challenges and Constraints To Develop A Large Scale Rotary Test Rig

The design of a large scale rotor rig testing facility is a complex task which involves many subject matter experts and a commitment of significant financial resource. The United Kingdom National Rotor Rig (UKNRR) was a project that incorporated a joint industry and academic approach to develop a portable large scale rotor rig which would allow for investigations at unconventional rotor configurations such as transition from edgewise to axial flight modes and

deep stall conditions. To aid any future rotor rig development efforts, existing or from scratch, the following considerations have been highlighted to outline the key challenges faced during the development of the UKNRR and its conversion to a fixed pitch propeller, with the aim of expediting and assisting with any difficulties that were encountered during this project. Furthermore, recommendations of future design choices are addressed.

7.2.2.1 Tiltrotor Mechanisms

The UKNRR was initially designed with the aim that the rotor plane could be altered during operation, through the transition corridor between edgewise flight and conventional propeller axial conditions. To achieve this, the initial design and manufacture incorporated a gearbox which was responsible for the rotation of the main rotor shaft. However, due to excessive vibratory issues resulting from the operation of the gearbox, resulting structural and operational safety concerns led to the decision of the removal of the gearbox and therefore to operate the rig as a conventional fixed pitch propeller using a single drive train, without the capability to transition the rotor plane. For applications were disc angles within the conversion corridor are of interest, a more practical and safer solution, that would allow for testing at these rotor orientations would be continued use of a single drive train mechanism. However, with the capability to orient the main rotor shaft at fixed angles. This solution would therefore allow for testing to be conducted without the use of a gearbox and the required supporting ancillary systems such as the gearbox control cabinet, hydraulic brake, lubrication pack and lubrication chiller. It is also worth noting, this solution would completely remove the ability to test rotor performance at various pitch rates. However, typical pitch rates encountered would be a maximum of approximately five degrees per second, where unsteady aerodynamic effects on the blades would not be of significant concern.

7.2.2.2 Hub Design

The UKNRR hub was designed to operate as a conventional helicopter rotor hub, comprising of a swashplate to alter the blade pitch collective angle and both longitudinal and lateral cyclic pitch angles. Blade pitch shafts were unrestricted and therefore allowed the blades to articulate in flapping, lead-lag and torsional motions, which under certain operating conditions lead to excessive loading on the pitch horns and pitch links. To conduct testing in propeller mode using the UKNRR, flap and lag stops were installed to fix the blade pitch shaft position, ultimately restricting blade lead-lag and flapping motions. Similarly, swashplate collars were installed to restrict movement of the swashplate along the main rotor shaft to fix the blade collective pitch angle. However, swashplate collars if not mounted appropriately result in an introduction of a cyclic input, which is not be be expected of a propeller system and is complex to accurately measure. Therefore, for applications where testing in conventional propeller mode is of importance, a conventional propeller hub with no requirement for stops or a swashplate should be

made use of. This will significantly simplify the setup and operation of a rotary rig of this scale by removing the complexities introduced by an articulating rotor hub, specifically removal of complex kinematics and simplification of the rotor load path.

7.2.2.3 Load Measurement

Measurements of rotor blade loading are crucial for obtaining a meaningful measure of rotor aerodynamic performance. Rotor loading was obtained on the UKNRR via a bespoke rotating shaft balance situated within the rotor hub. Rotating shaft balances are typically complex and unique to individual rigs, due to the fact that they must be integrated correctly within the rotating frame of the wind tunnel model. As the balance rotates, this imposes the requirement for the balance to be dynamically calibrated, ensuring that any load contributions from centrifugal forces are accounted for correctly and do not impact the measurement. Despite, their complexity, a rotating shaft balance is very useful for measuring a localised loads such as that of a propeller/rotor. Static balances that are situated in the stationary frame must be mounted so that there is an interface between the stationary and rotating components. Typically this means that static balances must have a larger range and therefore usually a larger resolution to measure the loads of interest. Nonetheless, for large scale rotary rigs this additional mass is often not significant and this is why there is now a noticeable shift back towards conventional static balances to obtain load measurements of rotary systems. Despite the concern of obtaining a meaningful load measurement, there are more subtle but equally important considerations when choosing to make use of a rotating shaft balance, such as, the stability and reliability of the load path of the system. An clear example of this concern is often found in fully articulated rotor hubs, where under certain operating conditions, excessive loads are passed through the pitch horns and pitch links, ultimately altering the true measurement value obtained from the rotating shaft balance. Furthermore, data that is acquired on the rotating frame must be transferred back to the stationary frame, imposing the requirement of a telemetry system or slip ring system, resulting in many complications to ensure reliable data acquisition and data quality.

7.2.2.4 Common 1/rev Signal

Data acquisition of rotating systems can be complex when integrating multiple measurement systems together. This difficulty is driven by the need for a common clock or time stamp between the individual systems. A common example of this is the synchronization of an analogue 1/rev signal obtained via a hall effect sensor and a digital force measurements acquired from the rotating shaft balance. As the hall effect sensor requires the close presence of a magnet to break its magnetic field to recognise a peak in voltage, the magnet is typically mounted on the rotating frame, with an additional magnet, of opposite polarity, situated at an azimuthal position offset of 180° to maintain hub balancing. A potential difference is applied to the circuit via a power supply and therefore to avoid swapping of batteries and the need to continually check

hub mass balancing, the hall effect sensor is placed on the stationary frame. As there are two measurement signals, one digital and one analogue, the digital signal introduces a latency to the acquisition system and even for what appear small latency values of microseconds, this can result in significant phase delay of the digital signal with respect to the analogue time signal, typically $\psi = 5 - 20°$. The preferred solution to this problem would be the introduction of a 1/rev signal on the rotating frame that is acquired using the same acquisition system as the rotating shaft balance. This would mean that the analogue to digital conversion would occur synchronously and the force data and 1/rev signal would have a common time stamp. Such a solution would require the hall effect sensor to possess a stable power supply, similar to that of the telemetry system, in addition to a further acquisition channel to log the 1/rev signal.

7.2.2.5 Pressure Transducers

Load measurements and blade strains have been demonstrated to successfully show the presence of stall, both globally across the rotor plane and at blade spanwise locations. However, the ability to precisely identify the exact chordwise and spanwise location at which flow separation occurs across a range of operational conditions has proven difficult. Particularity due to a limited resolution of suitable strain gauge locations and the significant time that would be required to implement optical methods suitable for assessing flow separation at this scale. Therefore, it would be recommend that future blades are designed with the view to incorporate pressure transducers within the blade structure at various spanwise and chordwise locations. Measurements of both chordwise and spanwise pressure distributions in addition to measurements of blade strains and rotor loads would provide further insight into the development of stall and rotor blade response at stalled conditions.

Appendix A

Rotating Shaft Balance

A.1 Sample Load Reduction Calculation

Conversion of raw voltage measurements to force and moments is achieved using the following calculation procedure. To ensure the correct measurement of voltages applied to the balance gauges which correspond to the true applied load, a zeroing procedure must be applied. System zeros (S_O), that account for RSB drift and voltage residual are obtained when the rotor azimuthal position is set to $\psi = 0^\circ$. In addition, a weight tare (W_0) is conducted for each collective setting to correctly account for variation in C.G location and weight term around the rotor azimuth. Removal of zeros from raw measured voltages (V_{raw}) provides fully bridged strain gauge output voltage (V_0) corresponding to each channel, in an [8 × 1] vector.

$$V_0 = V_{raw} - S_0 - W_0 = \begin{bmatrix} V_{SFF} \\ V_{SFR} \\ V_{NFF} \\ V_{NFR} \\ V_{AFF} \\ V_{AFR} \\ V_{RMF} \\ V_{RMR} \end{bmatrix}$$

Channel reduction is performed to provide a six channel output, [6 × 1] vector (V_{bal}), representing the corresponding voltages in the form of a six component load system of three forces (Y , N, A) and three moments (m, l, n).

$$V_{bal} = \begin{bmatrix} V_Y \\ V_N \\ V_A \\ V_m \\ V_l \\ V_n \end{bmatrix} = \begin{bmatrix} V_{SFR} \\ V_{NFR} \\ V_{AFF} + V_{AFR} \\ V_{NFF} \\ V_{RMF} + V_{RMR} \\ V_{SFF} \end{bmatrix}$$

Conversion to RSB loads (forces and moments) from measured voltage signals was performed using a second order Taylor series expansion, making use of interaction matrices ($[T_0]$,$[T_1]$,$[T_2]$) obtained during balance calibration. Apparent loads, $\vec{L_0}$, correspond to the loading solely in the channel axis and do not account for any cross-coupling between channels. Therefore, $\vec{L_0}$, is obtained through the multiplication of the direct factor matrix, $[T_0]$, and six channel voltage output vector (V_{bal}).

$$\vec{L_0} = \left[T_0\right] \cdot V_{bal}$$

First order loads are determined through multiplication of apparent loads ($\vec{L_0}$) and the negative first order interaction matrix ($[T_1]$).

$$\vec{L_1} = -\left[T_1\right] \cdot \vec{L_0}$$

Second order loads are obtained using first order loads ($\vec{L_1}$) and second order channel interactions ($[T_2]$), to account for second order terms that are a function of the applied load.

$$\hat{L_2} = \begin{bmatrix} Y_2 \\ N_2 \\ A_2 \\ m_2 \\ l_2 \\ n_2 \end{bmatrix} = \vec{L_1} - \begin{bmatrix} T_2 \end{bmatrix} \begin{bmatrix} V_Y^2 \\ V_Y \cdot V_N \\ V_Y \cdot V_A \\ V_Y \cdot V_m \\ V_Y \cdot V_l \\ V_Y \cdot V_n \\ V_N^2 \\ V_N \cdot V_A \\ V_N \cdot V_m \\ V_N \cdot V_l \\ V_N \cdot V_n \\ V_A^2 \\ V_A \cdot V_m \\ V_A \cdot V_l \\ V_A \cdot V_n \\ V_m^2 \\ V_m \cdot V_l \\ V_m \cdot V_n \\ V_l^2 \\ V_l \cdot V_n \\ V_n^2 \end{bmatrix}$$

A.2 Calibration Matrices

Values of interaction matrices obtained during balance calibration in propeller and rotor mode are presented in Figure A.1.

```
31802     (Bal.Flag 1)
BALANCE CALIBRATION NO.   31802  IN SI UNITS,NORMALISED TO 1VOLT      PRODUCED ON MON, DEC  7 2015
BIS401/01 8 COMPONENT ROTARY SHAFT BALANCE(A7459).                   (-prop -90)
BIS401/01. FULL CALIBRATION.
CALIB ASSY DRG No A7463. +5V. INDIVIDUAL MONITORS.

 DIRECT FACTORS                  FIRST ORDER INTERACTIONS
  X    DX/DR           BY X        BN X        BA X        BM X        BRMX        BYMX        BASX      X
  Y   5.15510363     -1.00000000 -0.01122666 -0.00006992  0.00208805 -0.00162253  0.03599162  0.00000000  Y
  N   5.40307745     -0.01089116 -1.00000000  0.00299665  0.03599926  0.00269415  0.00138798  0.00000000  N
  A   1.17607404      0.00513469 -0.03739404 -1.00000000 -0.00225856 -0.00484144 -0.00227815  0.00000000  A
  M   0.19583036      1.37139161 -29.0481765  0.07527250 -1.00000000 -0.05355788 -0.02252025  0.00000000  M
  RM  1.15870617     -0.49993420 -0.10688078  0.05233081 -0.00406126 -1.00000000  0.01878563  0.00000000  RM
  YM  0.17187839     -28.9281326 -0.22307206  0.12244871 -0.07512455 -0.03678806 -1.00000000  0.00000000  YM
  AS  0.00000000      0.00000000  0.00000000  0.00000000  0.00000000  0.00000000  0.00000000 -1.00000000  AS
 SUMCHECK=       -51.08163890
 SECOND ORDER INTERACTIONS
   X         Y          N          A          M          RM         YM         AS         X
  CXY Y   0.00000000  0.00000000  0.00000000  0.00000000  0.00000000  0.00000000  0.00000000   CXY Y
  CXY N   0.00000000  0.00000000  0.00000000  0.00000000  0.00000000  0.00000000  0.00000000   CXY N
  CXY A   0.00000032  0.00000095  0.00000067  0.00000010 -0.00000018 -0.00000036  0.00000000   CXY A
  CXY M   0.00000023  0.00000131 -0.00000473  0.00000023  0.00000243 -0.00000010  0.00000000   CXY M
  CXY RM  0.00000000  0.00000000  0.00000000  0.00000000  0.00000000  0.00000000  0.00000000   CXY RM
  CXY YM  0.00000000  0.00000000  0.00000000  0.00000000  0.00000000  0.00000000  0.00000000   CXY YM
  CXN N   0.00000000  0.00000000  0.00000000  0.00000000  0.00000000  0.00000000  0.00000000   CXN N
  CXN A  -0.00000072  0.00000048  0.00000069  0.00000012  0.00000025 -0.00000007  0.00000000   CXN A
  CXN M   0.00000000  0.00000000  0.00000000  0.00000000  0.00000000  0.00000000  0.00000000   CXN M
  CXN RM  0.00000000  0.00000000  0.00000000  0.00000000  0.00000000  0.00000000  0.00000000   CXN RM
  CXN YM  0.00000099  0.00000404 -0.00000720  0.00000000 -0.00000114 -0.00000002  0.00000000   CXN YM
  CXA A   0.00000000  0.00000000  0.00000000  0.00000000  0.00000000  0.00000000  0.00000000   CXA A
  CXA M   0.00001050  0.00000146  0.00000235 -0.00000005 -0.00000457 -0.00000152  0.00000000   CXA M
  CXA RM -0.00000214 -0.00000190 -0.00000174  0.00000063 -0.00000078  0.00000060  0.00000000   CXA RM
  CXA YM  0.00001311  0.00002154  0.00000224  0.00000213  0.00000852  0.00000027  0.00000000   CXA YM
  CXM M   0.00003567  0.00000763 -0.00000373  0.00000029  0.00007134 -0.00000134  0.00000000   CXM M
  CXM RM  0.00002081 -0.00002149  0.00000522 -0.00000967  0.00003429  0.00000333  0.00000000   CXM RM
  CXM YM  0.00000000  0.00000000  0.00000000  0.00000000  0.00000000  0.00000000  0.00000000   CXM YM
  CXRMRM  0.00000000  0.00000000  0.00000000  0.00000000  0.00000000  0.00000000  0.00000000   CXRMRM
  CXRMYM  0.00004617 -0.00001274  0.00000035 -0.00000210  0.00004621  0.00000651  0.00000000   CXRMYM
  CXYMYM -0.00005171 -0.00001106  0.00000541 -0.00000042 -0.00010344  0.00000194  0.00000000   CXYMYM
 SUMCHECK=         0.00011641
```

(a) Propeller mode

```
31801     (Bal.Flag 1)
BALANCE CALIBRATION NO.   31801  IN SI UNITS,NORMALISED TO 1VOLT      PRODUCED ON FRI, NOV 27 2015
BIS401/01 8 COMPONENT ROTARY SHAFT BALANCE(A7459).
BIS401/01.  FULL CALIBRATION.
CALIB ASSY DRG No A7463. +5V EXCITATION.

 DIRECT FACTORS                  FIRST ORDER INTERACTIONS
  X    DX/DR           BY X        BN X        BA X        BM X        BRMX        BYMX        BASX      X
  Y   5.15456628     -1.00000000 -0.00864440 -0.00045783  0.00233810 -0.00154626  0.03581867  0.00000000  Y
  N   5.39811153     -0.01318287 -1.00000000  0.00257644  0.03633198  0.00306322  0.00118913  0.00000000  N
  A   1.17465004      0.00419592 -0.03675576 -1.00000000 -0.00224616 -0.00530828 -0.00250972  0.00000000  A
  M   0.19426872      1.29452780 -29.2738781  0.06530437 -1.00000000 -0.02622107 -0.02641922  0.00000000  M
  RM  1.15833480     -0.49992474 -0.10528026  0.05237013 -0.00402326 -1.00000000  0.01859433  0.00000000  RM
  YM  0.17280313     -28.7917158 -0.18210461  0.10707636 -0.07088866 -0.04618889 -1.00000000  0.00000000  YM
  AS  0.00000000      0.00000000  0.00000000  0.00000000  0.00000000  0.00000000  0.00000000 -1.00000000  AS
 SUMCHECK=       -51.22117494
 SECOND ORDER INTERACTIONS
   X         Y          N          A          M          RM         YM         AS         X
  CXY Y   0.00000000  0.00000000  0.00000000  0.00000000  0.00000000  0.00000000  0.00000000   CXY Y
  CXY N   0.00000000  0.00000000  0.00000000  0.00000000  0.00000000  0.00000000  0.00000000   CXY N
  CXY A   0.00000000  0.00000000  0.00000000  0.00000000  0.00000000  0.00000000  0.00000000   CXY A
  CXY M   0.00000000  0.00000000  0.00000000  0.00000000  0.00000000  0.00000000  0.00000000   CXY M
  CXY RM  0.00000000  0.00000000  0.00000000  0.00000000  0.00000000  0.00000000  0.00000000   CXY RM
  CXY YM  0.00000000  0.00000000  0.00000000  0.00000000  0.00000000  0.00000000  0.00000000   CXY YM
  CXN N   0.00000000  0.00000000  0.00000000  0.00000000  0.00000000  0.00000000  0.00000000   CXN N
  CXN A   0.00000000  0.00000000  0.00000000  0.00000000  0.00000000  0.00000000  0.00000000   CXN A
  CXN M   0.00000000  0.00000000  0.00000000  0.00000000  0.00000000  0.00000000  0.00000000   CXN M
  CXN RM  0.00000000  0.00000000  0.00000000  0.00000000  0.00000000  0.00000000  0.00000000   CXN RM
  CXN YM  0.00000000  0.00000000  0.00000000  0.00000000  0.00000000  0.00000000  0.00000000   CXN YM
  CXA A   0.00000000  0.00000000  0.00000000  0.00000000  0.00000000  0.00000000  0.00000000   CXA A
  CXA M   0.00000000  0.00000000  0.00000000  0.00000000  0.00000000  0.00000000  0.00000000   CXA M
  CXA RM  0.00000000  0.00000000  0.00000000  0.00000000  0.00000000  0.00000000  0.00000000   CXA RM
  CXA YM  0.00000000  0.00000000  0.00000000  0.00000000  0.00000000  0.00000000  0.00000000   CXA YM
  CXM M   0.00000000  0.00000000  0.00000000  0.00000000  0.00000000  0.00000000  0.00000000   CXM M
  CXM RM  0.00000000  0.00000000  0.00000000  0.00000000  0.00000000  0.00000000  0.00000000   CXM RM
  CXM YM  0.00000000  0.00000000  0.00000000  0.00000000  0.00000000  0.00000000  0.00000000   CXM YM
  CXRMRM  0.00000000  0.00000000  0.00000000  0.00000000  0.00000000  0.00000000  0.00000000   CXRMRM
  CXRMYM  0.00000000  0.00000000  0.00000000  0.00000000  0.00000000  0.00000000  0.00000000   CXRMYM
  CXYMYM -0.00005209 -0.00001097  0.00000546 -0.00000042 -0.00010420  0.00000194  0.00000000   CXYMYM
 SUMCHECK=        -0.00016028
```

(b) Rotor mode

Figure A.1: RSB interaction matrices ($[T_0]$,$[T_1]$,$[T_2]$) obtained during RSB calibration procedure.

Bibliography

[1] A. Filippone and G. N. Barakos. Rotorcraft systems for urban air mobility: A reality check. *The Aeronautical Journal*, 125(1283):3–21, 2021.

[2] W Appleton, A Filippone, and N Bojdo. Interaction effects on the conversion corridor of tiltrotor aircraft. *The Aeronautical Journal*, 125(1294):2065–2086, 2021.

[3] R.J. Higgins, G.N. Barakos, and A. Filippone. A review of propeller stall flutter. *The Aeronautical Journal*, 126(1304):1678–1717, 2022.

[4] R J. Higgins. *Investigation of Propeller Stall Flutter*. PhD thesis, University of Glasgow, Glasgow, Scotland, April 2021.

[5] Ross J. Higgins and George N. Barakos. Whirl and stall flutter simulation using CFD. In *43rd European Rotorcraft Forum, Milan, Italy*, 12-15 Sep 2017.

[6] Ross Higgins, Antonio Jimenez-Garcia, George N. Barakos, and Nicholas Bown. A time-marching aeroelastic method applied to propeller flutter. In *AIAA Scitech 2019 Forum*, 07-11 Jan 2019.

[7] Ross J. Higgins, Antonio Jimenez-Garcia, George N. Barakos, and Nicholas Bown. High-fidelity computational fluid dynamics methods for the simulation of propeller stall flutter. *AIAA Journal*, 57(12):5281–5292, 2019.

[8] R. J. Higgins, G. N. Barakos, and E. Jinks. Estimation of three-dimensional aerodynamic damping using CFD. *The Aeronautical Journal*, 124(1271):24–43, 2020.

[9] Ross J. Higgins, George N. Barakos, Edward Jinks, and Nicholas Bown. A propeller blade design for experimental stall flutter investigations. In *47th European Rotorcraft Forum, Virtual Meeting*, 06-09 Sep 2021.

[10] Ricardo Santos Pereira. *Dynamic Stall, Handbook of Wind Energy Aerodynamics*. Springer International Publishing, 2022.

[11] Barnes W McCormick. Propeller dynamic and aeroelastic effects. NASA CR-80N22348, National Aeronautics and Space Administration, NASA Lewis Research Center, OH, USA, 1980.

[12] R Katzmayr. Deflection of propeller blades while running. Techincal Memorandum 145, National Advisory Committee for Aeronautics, Washington, D.C, USA, 1922.

[13] Friedrich Seewald. Flutter in propeller blades. Techincal Memorandum 642, National Advisory Committee for Aeronautics, Washington, D.C, USA, 1931.

[14] Fred E. Weick. Determination of propeller deflection by means of static load tests on models. Techincal Note 275, National Advisory Committee for Aeronautics, Langley Field, VA, USA, 1928.

[15] Fred E. Weick. Full-scale wind-tunnel tests of a series of metal propellers on a VE-7 airplane. Techincal Report 306, National Advisory Committee for Aeronautics, Washington, D.C, USA, 1929.

[16] Theodore Theodorsen. Propeller vibrations and the effect of the centrifugal force. Techincal Note 516, National Advisory Committee for Aeronautics, Langley Field, VA, USA, 1935.

[17] Fritz Liebers. Propeller tip flutter. Techincal Memorandum 683, National Advisory Committee for Aeronautics, Washington, D.C, USA, 1932.

[18] Fritz Liebers. Contribution to the theory of propeller vibrations. Techincal Memorandum 568, National Advisory Committee for Aeronautics, Washington, D.C, USA, 1930.

[19] Fritz Liebers. Resonance vibrations of aircraft propellers. Techincal Memorandum 657, National Advisory Committee for Aeronautics, Washington, D.C, USA, 1932.

[20] Edwin P. Hartman and D Biermann. The torsional and bending deflection of full-scale aluminium-alloy propeller blades under normal operating conditions. Techincal Report 644, National Advisory Committee for Aeronautics, Langley Field, VA, USA, 1938.

[21] E Z. Stowell and A F. Deming. Noise from two-blade propellers. Techincal Report 526, National Advisory Committee for Aeronautics, Langley Field, VA, USA, 1936.

[22] Edwin P. Hartman and D Biermann. The effect of compressibility on eight full-scale propellers operating in the take-off and climbing range. Techincal Report 639, National Advisory Committee for Aeronautics, Langley Field, VA, USA, 1938.

[23] Hermann Borck. Dependence of propeller efficiency on angle of attack of a propeller blade. Technical Memorandum 54, National Advisory Committee for Aeronautics, Langley Field, VA, USA, 1921.

[24] J.F. Shannon and J.R.Forshaw. Propeller blade vibration: Nature and severity of vibration at edgewise resonance as influenced by coupling effects due to blade twist. Reports & Memoranda 2561, Aeronautical Research Council, London, England, UK, 1941.

[25] F. Clifton and L.H.G Sterne. Strain gauge test of a fluttering propeller in a wind tunnel. Reports & Memoranda 2072, Aeronautical Research Council, London, England, UK, 1943.

[26] L.H.G Sterne and R.H Brown. The elimination of flutter from a propeller. Reports & Memoranda 2047, Aeronautical Research Council, London, England, UK, 1943.

[27] L.H.G Sterne. Spinning tests on fluttering propellers. Reports & Memoranda 2022, Aeronautical Research Council, London, England, UK, 1945.

[28] Theodore Theodorsen and Arthur A. Regier. Effect of the lift coefficient on propeller flutter. Wartime Report LSF30, National Advisory Committee for Aeronautics, Langley Field, VA, USA, 1945.

[29] A.B Haines and P.B Chater. 24ft tunnel tests on a rotol wooden spitfire propeller: Test results and data for single radius calculations. Reports & Memoranda 2357, Aeronautical Research Council, London, England, UK, 1946.

[30] L.H.G Sterne, H.G Ewing, and J Kettlewell. Strain gauge investigation of propeller flutter. Reports & Memoranda 2472, Aeronautical Research Council, London, England, UK, 1947.

[31] H G. Ewing, J Kettlewell, and D.R Gaukroger. Comparative flutter tests on two, three, four and five-blade propellers. Reports & Memoranda 2634, Aeronautical Research Council, London, England, UK, 1948.

[32] John E. Baker and Russell S. Paulnock. Experimental investigation of flutter of a propeller with clark Y section operating at zero forward velocity at positive and negative blade-angle settings. Techincal Note 1966, National Advisory Committee for Aeronautics, Langley Air Force Base, VA, USA, 1949.

[33] John E Baker. The effects of various parameters, including mach number, on propeller-blade flutter with emphasis on stall flutter. Techincal Note 3357, National Advisory Committee for Aeronautics, Langley Air Force Base, VA, USA, 1955.

[34] W.H Gray and A.E Allis. The torsional deflection of several propellers under operating conditions. Research Memorandum L51A19, National Advisory Committee for Aeronautics, Langley Field, VA, USA, 1951.

[35] John H. Wood and John M Swihart. The effects of blade-section camber on the static characteristics of three NACA propellers. Research Memorandum L51L28, National Advisory Committee for Aeronautics, Langley Field, VA, USA, 1952.

[36] Arthur E. Allis and John M Swihart. The effects of blade-section camber on the stall-flutter characteristics of three NACA propellers at zero advance. Research Memorandum L53B17, National Advisory Committee for Aeronautics, Langley Field, VA, USA, 1953.

[37] Atwood R. Jr Heath. Some torsional-damping measurements of laminated beams as applied to the propeller stall-flutter problem. Research Memorandum L53A19, National Advisory Committee for Aeronautics, Langley Field, VA, USA, 1953.

[38] Harvey H. Hubbard, Marvin F. Burgess, and Maurice A. Slyvester. Flutter of thin propeller blades, including effects of mach number, structural damping, and vibatory-stress measurements near the flutter boundaries. Techincal Note 3707, National Advisory Committee for Aeronautics, Langley Field, VA, USA, 1956.

[39] Vernon L. Rogallo and Paul F. Yaggy. A wind tunnel investigation of the stall flutter characteristics of a supersonic type propeller at positive and negative thrust. NASA Technical Memorandum 3-9-59A, National Aeronautics and Space Administration, Moffett Field, CA, USA, 1959.

[40] Vernon L. Rogallo. Propeller blade loading control patent. US Patent 3-144-999, United States Patent Office, Washington, D.C, USA, 1964.

[41] P.E Burton. Straingauge test report on a spin test carried out on a type(c) r.305/3-82-f/6 propeller on the spinning tower at the R.A.E Farnborough. Test Report 093.1.592, Dowty Rotol Limited, Gloucester, England, UK, 1979.

[42] Thomas C O'Bryan. Flight measurements of the vibratory and torsional stresses on a supersonic-type propeller for forward mach numbers up to 0.95. Research Memorandum L56D20a, National Advisory Committee for Aeronautics, Langley Field, VA, USA, 1956.

[43] Thomas C O'Bryan. Flight measurements of the vibratory bending and torsional stresses on a modified supersonic propeller for forward mach numbers up to 0.95. Techincal Note 4342, National Advisory Committee for Aeronautics, Langley Field, VA, USA, 1958.

[44] Thomas C O'Bryan. Flight measurements of the vibratory stresses on a propeller designed for an advance ratio of 4.0 and a mach number of 0.82. Techincal Note 4410, National Advisory Committee for Aeronautics, Langley Field, VA, USA, 1958.

[45] JB Whitlow Jr and GK Sievers. Fuel savings potential of the NASA advanced turboprop program. In *Aviation Fuel Conservation Symposium,Washington, D.C, USA*, 10-11 Sep 1984.

[46] James F Dugan, Brent A Miller, Edwin J Graber, and David A Sagerser. The NASA high-speed turboprop program. NASA Technical Memorandum 81561, National Aeronautics and Space Administration, NASA Lewis Research Center, OH, USA, 1980.

[47] Roy D Hager and Deborah Vrabel. Advanced turboprop project. NASA Special Publication 495, National Aeronautics and Space Administration, NASA Lewis Research Center, OH, USA, 1988.

[48] Roy H. Lange. A review of advanced turboprop transport aircraft. *Progress in Aerospace Sciences*, 23(2):151–166, 1986.

[49] O. Mehmed, K.R.V Kaza, F. Lubomski, and R.E. Kielb. Bending-torsion flutter of a highly swept advanced turboprop. NASA Technical Memorandum 82975, National Aeronautics and Space Administration, NASA Lewis Research Center, OH, USA, 1981.

[50] PN Bansal, PJ Arseneaux, AF Smith, JE Turnberg, and BM Brooks. Analysis and test evaluation of the dynamic response and stability of three advanced turboprop models. NASA Contractor Report 174814, National Aeronautics and Space Administration, NASA Lewis Research Center, OH, USA, 1985.

[51] Arthur F Smith. Analysis and test evaluation of the dynamic stability of three advanced turboprop models at zero forward speed. NASA Contractor Report 175025, National Aeronautics and Space Administration, NASA Lewis Research Center, OH, USA, 1985.

[52] Arthur F Smith. Analysis and test evaluation of the dynamic response and stability of three advanced turboprop models at low forward speed. NASA Contractor Report 175026, National Aeronautics and Space Administration, NASA Lewis Research Center, OH, USA, 1985.

[53] O Mehmed and KRV. Kaza. Experimental classical flutter results of a composite advanced turboprop model. NASA Techincal Memorandum 88792, National Aeronautics and Space Administration, NASA Lewis Research Center, OH, USA, 1986.

[54] Arthur F Smith and Bennett M Brooks. Dynamic response and stability of a composite prop-fan model. NASA Contractor Report 179528, Hamilton Standard Divsion United Technologies Corporation, Windsor Locks, CT, USA, 1986.

[55] Arthur F Smith and Bennett M Brooks. Dynamic response of two composite prop-fan models on a nacelle/wing/fuselage half model. NASA Contractor Report 179589, Hamilton Standard Divsion United Technologies Corporation, Windsor Locks, CT, USA, 1986.

[56] K Kaza, O Mehmed, M Williams, and L Moss. Analytical and experimental investigation of mistuning in propfan flutter. In *28th Structures, Structural Dynamics and Materials Conference, Monterey, CA, USA*, 06-08 Apr 1987.

[57] Oral Mehmed. Propfan model wind tunnel aeroelastic research results. *NASA Lewis Research Center, Lewis Structures Technology, 1988. Volume 1: Structural Dynamics*, 1988.

[58] Gary Podboy and Martin Krupar. Laser velocimeter measurements of the flow field generated by a forward-swept propfan during flutter. In *23rd Fluid Dynamics, Plasmadynamics, and Lasers Conference, Orlando, FL, USA*, 06-09 Jul 1993.

[59] W.J.F. Koning, B.G. Allan, E.A. Romander, and W. Johnson. Comparing 3D and 2D CFD for mars helicopter ingenuity rotor performance prediction. In *49th European Rotorcraft Forum, Buckeburg, Germany*, 05-07 Sep 2023.

[60] Graham Bowen-Davies and Inderjit Chopra. Investigation of the unsteady reverse flow airloads at high advance ratios. In *41st European Rotorcraft Forum, Munich, Germany*, 01-04 Sep 2015.

[61] Felipe Bohorquez, Paul Samuel, Jayant Sirohi, Darryll Pines, Lael Rudd, and Ron Perel. Design, analysis and hover performance of a rotary wing micro air vehicle. *Journal of the American Helicopter Society*, 48(2):80–90, 2003.

[62] Felipe Bohorquez and Darryll Pines. Hover performance of rotor blades at low reynolds numbers for rotary wing micro air vehicles. In *21st AIAA Applied Aerodynamics Conference, Orlando, FL, USA*, 23-26 June 2003.

[63] Benjamin R Hein and Inderjit Chopra. Hover performance of a micro air vehicle: rotors at low reynolds number. *Journal of the American Helicopter Society*, 52(3):254–262, 2007.

[64] Manikandan Ramasamy, Bradley Johnson, and J Gordon Leishman. Understanding the aerodynamic efficiency of a hovering micro-rotor. *Journal of the American Helicopter Society*, 53(4):412–428, 2008.

[65] Oliver Wild, Matthew J Murphy, and Anya R Jones. Comparison of instantaneous aerodynamic loads on sharp and blunt trailing-edged blades of high advance ratio rotors. In *AIAA Scitech 2023, National Harbor, MD, USA*, 23-27 January 2023.

[66] Oliver Wild and Anya R Jones. Reverse flow aerodynamics of low reynolds number rotors with blunt trailing-edged blades at high advance ratios. In *AIAA Scitech 2022, San Diego, CA, USA*, 3-7 January 2022.

[67] Oliver D. Wild and Anya R. Jones. Vortex identification and quantification on blunt trailing-edge rotor blades in reverse flow. *AIAA Journal*, 61(7):2982–2997, 2023.

[68] Andrew H Lind, Jonathan N Lefebvre, and Anya R Jones. Time-averaged aerodynamics of sharp and blunt trailing-edge static airfoils in reverse flow. *AIAA journal*, 52(12):2751–2764, 2014.

[69] Andrew H Lind and Anya R Jones. Vortex shedding from airfoils in reverse flow. *AIAA Journal*, 53(9):2621–2633, 2015.

[70] Andrew H Lind, Luke R Smith, Joseph I Milluzzo, and Anya R Jones. Reynolds number effects on rotor blade sections in reverse flow. *Journal of Aircraft*, 53(5):1248–1260, 2016.

[71] Andrew H Lind and Anya R Jones. Unsteady aerodynamics of reverse flow dynamic stall on an oscillating blade section. *Physics of Fluids*, 28(7), 2016.

[72] Andrew H Lind and Anya R Jones. Unsteady airloads on static airfoils through high angles of attack and in reverse flow. *Journal of Fluids and Structures*, 63:259–279, 2016.

[73] Andrew H Lind, Lauren N Trollinger, Field H Manar, Inderjit Chopra, and Anya R Jones. Flowfield measurements of reverse flow on a high advance ratio rotor. *Experiments in Fluids*, 59:1–15, 2018.

[74] K.W. McAlister, L.W. Carr, and W.J. McCroskey. Dynamic stall experiments on the NACA 0012 airfoil. NASA Techincal Publication 1100, National Aeronautics and Space Administration, NASA Ames Research Center, CA, USA, 1978.

[75] Anubhav Datta, Hyeonsoo Yeo, and Thomas R Norman. Experimental investigation and fundamental understanding of a full-scale slowed rotor at high advance ratios. *Journal of the American Helicopter Society*, 58(2):1–17, 2013.

[76] Daniele Zagaglia, Alexander D. Croke, Richard B. Green, and George N. Barakos. Development of the uk national rotor rig for aeroelastic testing of rotary wings. In *49th European Rotorcraft Forum, Bückeburg, Germany*, 05-07 Sep 2023.

[77] A Tatar, J Wu, D Zagaglia, B Titurus, D Rezgui, RB Green, and G Barakos. Modal characterisation of a rotor/propeller rig for tip-mach scaled wind tunnel testing. In *47th European Rotorcraft Forum, Virtual Meeting*, 06-09 Sep 2021.

[78] Mark A. Woodgate, Thomas A. Fitzgibbon, and George Barakos. The use of computational fluid dynamics in the investigation of stall onset on tilt-rotor blades. In *AIAA Aviation 2021, Virtual Meeting*, 2-6 August 2021.

[79] J. Wu, D. Rezgui, and B. Titurus. Bending-torsion flutter of a highly swept advanced turboprop. Internal Report, University of Bristol, Bristol, UK, 2022.

[80] Bart Peeters, Herman Van der Auweraer, Patrick Guillaume, and Jan Leuridan. The polymax frequency-domain method: A new standard for modal parameter estimation? *Shock and Vibration*, 11:395–409, 08 2004.

[81] Murray McKechnie and George Barakos. Numerical investigation of propeller stall flutter. In *50th European Rotorcraft Forum, Marseille, France*, 10-12 Sep 2024.

[82] Datatel Telemetry. *Helicopter Main Rotor Telemetry User Manual*. Datatel Telemetry, 2015.

[83] H Smith. Rotary shaft balance data reduction specifications. ARA Techincal Note EA2015.30.6, Aircraft Research Association, Bedford, UK, 2015.

[84] T.A. Cook. A note on the calibration of strain gauge balances for wind tunnel models. RAE Techincal Note Aero-2631, Royal Aircraft Establishment, Farnborough, UK, 1959.

[85] M Giuni. *Formation and early development of wingtip vortices*. PhD thesis, University of Glasgow, Glasgow, Scotland, 2013.

[86] S Skinner. *Study of a C-wing configuration for passive drag and load alleviation*. PhD thesis, University of Glasgow, Glasgow, Scotland, 2018.

[87] Hermann Glauert. *The elements of aerofoil and airscrew theory*. The University Press, 1926.

[88] E.C Maskell. A theory of the blockage effects on bluff bodies and stalled wings in a closed wind tunnel. Reports & Memoranda 3400, Aeronautical Research Council, London, England, UK, 1963.

[89] PR Ashill and RFA Keating. Calculation of tunnel wall interference from wall-pressure measurements. *The Aeronautical Journal*, 92(911):36–53, 1988.

[90] J.E Hackett, D.J. Wilsden, and D.E Lilley. Estimation of tunnel blockage from wall pressure signatures: a review and data correlation. NASA Contractor Report 15-2241, National Aeronautics and Space Administration, NASA Ames Research Center, CA, USA, 1979.

[91] Ryan Elizabeth Fitzgerald. *Wind tunnel blockage corrections for propellers*. MSc Thesis, University of Maryland, College Park, 2007.

[92] J.B. Barlow, W.H. Rae, and A. Pope. *Low-Speed Wind Tunnel Testing*. Wiley, 1999.

[93] W.F.J Koning, B.N Perez, H.V Cummings, E.A. Romander, and W. Johnson. Overview of rotor hover performance capabilities at low reynolds number for mars exploration. In *50th European Rotorcraft Forum, Marseille, France*, 10-12 Sep 2024.